Universidad:
UNIVERSIDAD DE LA LAGUNA

Titulo:
SOLAR POLES MAGNETISM

Autor:
ADUR PASTOR YABAR

Directores:
MANUEL ARTURO COLLADOS VERA
MARÍA JESÚS MARTÍNEZ GONZÁLEZ

Año:
2017

DEPARTAMENTO DE ASTROFISICA

Universidad de La Laguna

Solar Poles Magnetism

Thesis submitted by
D. Adur Pastor Yabar
As a requirement for the degree of
Doctor by University of La Laguna

INSTITUTO Đ ASTROFISICA Đ CANARIAS
April 2017

Examination date: May, 2017
Thesis supervisor: Dr. Manuel Collados Vera
Dr. María Jesús Martínez González

ISBN: xx-xxx-xxxx-x
Depósito legal: TF-xxxx/2017
Some of the figures included in this document have been already published in *The Astrophysical Journal*.

a la ratita presumida

Resumen

El descubrimiento del magnetismo en la superficie solar data de hace algo más de 100 años y, desde entonces, la comprensión de su comportamiento, así como su inter-relación con la termodinámica solar, ha ocupado una posición central en los estudios acerca del Sol. Este esfuerzo ha permitido, entre otros muchos hallazgos, el descubrimiento del comportamiento cíclico del magnetismo sobre la superficie solar, lo que se conoce como ciclo magnético solar. Este ciclo engloba una serie de características de comportamiento cuasi-periódico, entre las cuales, por la relación con este trabajo, se destacan aquí las asociadas a las regiones polares.

Las regiones polares son aquellas zonas del Sol con latitudes por encima de $\pm 60°$, es decir, los alrededores de los polos norte y sur. El magnetismo en los polos solares, a diferencia de otras regiones del Sol sin manchas en la superficie, obedece al ciclo de actividad solar de 11 años. En concreto, posee una polaridad de campo magnético dominante en periodos comprendidos entre dos máximos de actividad magnética consecutivos, dando al campo global una apariencia de dipolo magnético. En los máximos de actividad, esta apariencia dipolar desaparece para reaparecer con la polaridad invertida hasta el siguiente máximo solar. Es evidente, pues, que la comprensión del ciclo magnético solar requiere del entendimiento del magnetismo en las regiones polares. Además, éstas constituyen la principal fuente de líneas de campo abiertas, es decir, del magnetismo de la heliosfera, por donde se acelera el viento solar, que constituye un flujo continuo de partículas hacia el vecindario solar.

El estudio del magnetismo se basa en la espectropolarimetría, es decir, la interpretación del espectro polarizado de la luz. Dada la baja intensidad del campo magnético global —tres órdenes de magnitud más pequeño que el campo magnético en una mancha solar—, las señales de polarización son pequeñas y difíciles de detectar por encima del ruido de los presentes instrumentos. Estas dificultades observacionales han sido las causantes de que haya relativamente pocos trabajos sobre el magnetismo global y el magnetismo en los polos en particular. Los primeros trabajos de los años 50 se basaron en la observación de la polarización circular ya que, en general, es un orden de magnitud más intensa que la polarización lineal. Obtener el vector de campo magnético requiere de la caracterización completa del estado de polarización de la luz. Esto hace que sólo se tenga acceso a la componente del campo magnético en la línea de visión.

En la última década, la nueva instrumentación más sensible, ha hecho posible el estudio del vector campo magnético completo en las regiones polares del Sol por medio de observaciones espectropolarimétricas de los cuatro parámetros de Stokes. Este paso ha permitido ampliar nues-

tra comprensión sobre el magnetismo en estas regiones. Así, se ha observado que la topología del campo no es morfológicamente diferente de la que se observa en cualquier otro punto de la superficie solar fuera de las regiones activas. No obstante, presenta ciertas particularidades. Aquellos campos magnéticos que dan lugar a la polaridad dominante se congregan en entidades de tamaño superior al de las demás estructuras de las regiones polares o del resto de la superficie solar fuera de las regiones activas. Además, el número de estas estructuras con la misma polaridad que la de la región polar varían con el tiempo en escalas del ciclo magnético solar. Así, su número es mayor cerca de periodos de mínimo de actividad magnética solar, momento en el que las regiones polares exhiben la mayor intensidad de campo neto. En cambio, en máximos de actividad magnética solar, cuando la polaridad dominante en las regiones polares está en pleno cambio, su número se reduce de forma drástica.

Sin embargo, el estudio en profundidad del magnetismo en los polos también ha arrojado nuevas dudas. Una de ellas concierne a la topología de los campos magnéticos que aparecen con polaridad más o menos balanceada. Estos campos magnéticos son horizontales, es decir, paralelos a la superficie solar, para algunos autores (Ito et al., 2010; Jin et al., 2011; Shiota et al., 2012; Kaithakkal et al., 2013) mientras que otros autores encuentran que dichos campos muestran distribuciones más o menos isótropas (Blanco Rodríguez & Kneer, 2010). Otro aspecto a considerar es que la mayoría de estos estudios se han realizado durante una fase de mínimo del ciclo de actividad magnética (2009), salvo el estudio de Shiota et al. (2012) que se extiende desde un mínimo (2008) hasta la fase de incremento de actividad posterior (2012). Durante fases de máximos de actividad y fases de actividad decreciente, no hay estudios espectropolarimétricos. Por ello, una parte importante de la tesis busca la caracterización de la topología magnética de las regiones polares solares en la fase ascendente del ciclo solar, así como durante el máximo de 2015 y la posterior fase descendente.

En esta tesis abordamos el estudio del magnetismo en los polos desde el punto de vista global y, a su vez, observamos este magnetismo a las escalas más pequeñas accesibles, es decir, unas centenas de kilómetros en la superficie del Sol. El punto de vista global nos permite entender y profundizar el estudio del magnetismo en los polos y su relación con el ciclo de actividad. Para ello hacemos uso del satélite *Solar Dynamics Observatory*, uno de cuyos instrumentos a bordo, *Helioseismic Magnetic Imager*, opera desde inicios de 2010 observando, entre otros, la componente longitudinal del campo magnético de forma frecuente y sin pausa, con una estabilidad técnica y una señal a ruido excelentes.

El análisis a grandes rasgos de estos datos muestra el comportamiento del campo magnético global esperado para la fase del ciclo solar cubierto. En 2010, poco después del mínimo de actividad magnética solar de 2009, se observa que ambas regiones polares tienen una intensidad de campo magnética promedio de aproximadamente 1 G y de polaridad opuesta en cada región polar, negativo en el norte y positivo en el sur. Según transcurre el ciclo, el Sol se acerca hacia un máximo de actividad magnética (2015) y, en las regiones polares, se observa un paulatino debilitamiento del valor promedio hasta su cancelación. Por último, según se deja atrás este máximo y el Sol se encamina hacia un nuevo mínimo de actividad magnética, se observa el crecimiento de la nueva polaridad en cada región polar. Como suele observarse para otros ciclos, este proceso de paulatino debilitamiento, cambio de polaridad y posterior crecimiento de la nueva

polaridad ocurre de forma asimétrica, es decir, las distintas fases no ocurren simultáneamente en ambos polos, sino que cada uno tiene sus propios tiempos.

Un análisis más detallado muestra una señal oscilatoria de pequeña amplitud (0.2 G) y de corto periodo (∼30 días) respecto al total de la serie temporal (6 años). La pequeña amplitud de la señal explica que esta oscilación aparezca y desaparezca de las latitudes más altas según estén en una fase orbital de la Tierra que favorezca o perjudique su observación. Observamos además que esta oscilación no es sólo propia de las latitudes más altas sino que está presente en todas las latitudes y a lo largo de toda la serie temporal. El análisis de Fourier de estas series temporales por cada banda de latitud permite determinar que la periodicidad de esta señal no es la misma para todas las latitudes sino que presenta el mismo periodo que el valor de la rotación solar para cada latitud considerada. Descartadas las regiones activas como origen de tal señal, exploramos la posibilidad de que esta oscilación pueda deberse a la presencia de una componente no axisimétrica en el campo magnético global. Modelamos esta posibilidad por medio de un dipolo magnético inclinado y obtenemos que la señal oscilatoria observada es compatible con un ángulo de 21-40° entre el eje de rotación solar y el eje magnético.

Para un estudio más exhaustivo en cuanto a la topología del campo magnético en las regiones polares, acudimos a dos telescopios terrestres. Por una parte el instrumento *Tenerife Infrarred Polarimeter* en la *Vacuum Tower Telescope* nos permite la observación de los cuatro parámetros de Stokes en el infrarrojo cercano. El uso de longitudes de onda más largas nos permite una sensibilidad mayor a los campos magnéticos, ya que el efecto Zeeman es proporcional a la longitud de onda. Por contra, la resolución espacial mejora a longitudes de onda más cortas, de modo que con estas observaciones nos limitamos a resolver escalas de aproximadamente 1000 km en la superficie solar. Para llevar la resolución espacial al límite de lo que es posible en la actualidad, acudimos a la *Swedish Solar Telescope* para observar con el instrumento *CRisp Imaging SpectroPolarimeter*. Estos datos son de menor sensibilidad polarimétrica con lo que se limita el acceso a los campos más débiles, pero a cambio, pueden ser resueltos a escalas tan pequeñas como 200 km.

El estudio realizado con las líneas infrarrojas nos permite determinar que las regiones polares, al igual que las regiones de Sol en calma observadas en el centro del disco y en el limbo ecuatorial, están repletas de campo magnético, teniendo cerca de un 80% del campo observado con señales de polarización por encima del nivel de ruido. En líneas generales encontramos que los diferentes parámetros relacionados con el campo magnético considerados en este estudio muestran, tanto en el limbo norte como en el oeste, un comportamiento similar entre sí, pero diferente del encontrado en el centro del disco. Este comportamiento puede responder al cambio en la línea de visión respecto a la vertical a la superficie solar. Únicamente la densidad de flujo magnético en la línea de visión muestra un comportamiento distinto en la región polar norte. Tanto para el campo observado en el centro del disco como para el del limbo oeste, se encuentra que el valor medio de la densidad de flujo magnético en la línea de visión viene dado por las estructuras magnéticas con señales de polarización más fuertes mientras que el resto muestran equilibrio de polaridades. En la región solar norte, son las señales de polarización débiles las que definen el valor medio de la densidad de flujo magnético.

A pesar de la abundancia de señales magnéticas en el campo de visión, no para todas ellas conseguimos obtener la topología de los campos magnéticos debido a ambigüedades inducidas por el ruido. Por tanto el análisis de la topología se realiza sobre aquellas señales de polarización con campo magnético por encima de 600 G. Por encima de este límite, consideramos que el vector campo magnético está bien determinado. En el centro del disco se observa que estos campos son eminentemente verticales, en consonancia con los resultados observacionales previos obtenidos por otros autores, así como lo que se deduce de la teoría para concentraciones intensas de campo magnético, donde la presión magnética favorece la orientación vertical de los campos.

El estudio de la topología magnética en los limbos en el sistema de referencia línea de visión, muestra un comportamiento bi-modal. Por una parte, algunos campos magnéticos son compatibles con campos verticales en el sistema de referencia local. Esta compatibilidad se confirma al cambiar estos campos magneticos al sistema de referencia local. En éste, se tiene que además de poseer una configuración de campos verticales, las estructuras magnéticas tienen una forma similar a una marquesina. El núcleo de la estructura está caracterizado por los campos magnéticos más intensos y verticales. Alrededor de ese centro, se observa un halo de campos menos intensos y con campos expandiéndose de, o concentrándose hacia, el núcleo de la estructura. Los demás campos magnéticos, no pueden ser debidos a estructuras verticales individuales si bien no podemos especificar, con estas observaciones, su topología exacta.

Este comportamiento bi-modal ha sido observado con anterioridad por Ito et al. (2010); Blanco Rodríguez & Kneer (2010); Jin et al. (2011) y Shiota et al. (2012). En todos ellos, una de las componentes está caracterizada por campos verticales, mientras que sobre la topología de la otra, unos (Ito et al., 2010; Jin et al., 2011; Shiota et al., 2012) la encuentran caracterizada por campos horizontales y otros (Blanco Rodríguez & Kneer, 2010) por campos más bien isótropos. En nuestro caso la componente de campos no verticales, se caracteriza por campos fuertes (por encima de 600 G) cuya característica principal es que no son compatibles con estructuras individuales de campos verticales. La determinación de su topología exacta requiere de observaciones adicionales, aunque la presencia de bucles magnéticos no resueltos, podría dar lugar a esta segunda componente de campos magnéticos.

Las observaciones con el instrumento CRISP en la SST nos permiten tener acceso a un área de la superficie solar mayor a la vez que tenemos una resolución espacial y una sensibilidad polarimétricas altas, aunque al observar en el visible, la sensibilidad magnética en este estudio es menor que en el anterior. En este caso vemos que la cantidad de píxeles con señales polarimétricas significativas es mucho menor que en el estudio anterior. El estudio de los diversos parámetros relacionados con el campo magnético muestran un comportamiento similar cuando las dos regiones observadas cerca del limbo solar se comparan con los del centro del disco. Este comportamiento está en coherencia con los trabajos previos (Ito et al., 2010; Blanco Rodríguez & Kneer, 2010; Jin et al., 2011; Shiota et al., 2012).

La topología del campo magnético se obtiene para un conjunto limitado de campos magnéticos. Para definir este subconjunto desarrollamos una comprobación sobre la evolución de la χ^2 para inversiones con diferentes valores forzados de inclinación. De esta forma, obtenemos que los campos magnéticos en el centro del disco presentan un azimut homogéneo y la distribución de

inclinaciones está cercana a una distribución isótropa, con una cierta preferencia por campos horizontales. En los limbos, no obstante, vemos que los campos para los cuales se puede determinar una topología corresponden a un subconjunto de los observados en el centro del disco, en particular, en los limbos obtenemos la topología de los campos verticales. Si bien no obtenemos información suficiente sobre su topología, sí que vemos que los campos sobre los que no analizamos su topología comparten propiedades similares a los que en la VTT no son verticales. Es decir, tienen amplitudes de polarización circular por encima del ruido que son compatibles con campos de más de 600 G y menos de 1000 G y su señal de polarización lineal está por debajo del nivel de ruido.

Por último, para cada una de las estructuras magnéticas de las que obtenemos su topología calculamos el flujo magnético total a través de la superficie del Sol así como su distribución espacial en la región polar norte. Obtenemos que las estructuras se reparten a lo ancho de toda la región polar, aunque las que acarrean más flujo se ubican a latitudes más bajas. Este escenario es consistente con Shiota et al. (2012) en cuanto al flujo individual de las estructuras y en cuanto a cuáles de ellas son las que determinan la polaridad de la región polar. Otra característica importante observada es el hecho de que estas estructuras, que aportan la identidad magnética a la región polar norte, se sitúan en latitudes por debajo de 70°. Esto último es compatible con el escenario generalmente aceptado para el cambio de polaridad de la región polar. En este escenario, se tiene que el agente que gobierna el cambio de la polaridad de la región polar es el flujo magnético proveniente de latitudes medias-bajas. De esta forma, las latitudes más altas ya habrían cancelado su polaridad previa al máximo de 2015 y los bordes inferiores del polo ya tendrían su nueva polaridad dominante.

En resumen, por un lado se presenta un estudio detallado, desde un punto de vista del magnetismo polar a gran escala y su evolución, en escalas de tiempo del ciclo solar. Y por otro lado, realizamos un estudio más exhaustivo en cuanto a la topología de los campos magnéticos observados en las regiones polares del Sol a costa de la evolución temporal de los mismos.

Códigos de la UNESCO: 120602 FISICA SOLAR, 120604 EL SOL

x

Abstract

The presence of magnetism in its surface was discovered more than 100 years ago. Since then, most of the solar research has focused on unveiling the magnetism of the Sun as well as understanding its interplay with the thermodynamics of the solar atmosphere. This longstanding effort has allowed the discovery of several properties. One of those is the cyclic behaviour of the solar surface magnetism, namely the solar magnetic cycle. This cycle includes some properties concerning the quasi-periodic behaviour of the solar surface magnetism. Because of its relation with this thesis work, we briefly overview those related with solar polar regions.

Solar polar regions are those areas above/below $\pm 60^{\circ}$ solar latitudes, i.e. solar surface around solar poles. The magnetism at these regions follows the solar magnetic activity cycle, in contrast to other solar surface areas free of active regions. For instance the average magnetic field over each polar region exhibits a dominant polarity in between two consecutive maxima. This dominant polarity is found to be of opposite polarity at the North and South polar regions and hence, they resemble a magnetic dipole-like configuration. At magnetic activity maxima this dipolar-like appearance disappears and it builds up again after the maximum, but with the polarity reversed. It is thus compulsory to understand the magnetism at the polar regions in order to fully comprehend the solar magnetic cycle. Furthermore these regions are the main area to which the open solar magnetic field lines are rooted to. These magnetic fields are essential in the behaviour of the heliosphere and the acceleration of the solar wind.

The study of the magnetism is based on the inference of physical properties from the polarisation of the light. Due to the weakness of the global magnetic field —three orders of magnitude weaker than that at solar sunspots— the polarisation signals are weak and hard to detect above the sensitivity of the current instrumentation. This is the reason behind the relatively small number of solar global magnetism studies as well as the few polar magnetism studies. Dating in mid fifties, the first polarimetric studies used circular polarisation signals as they are usually one order of magnitude stronger than linear polarisation signals. However, retrieving the full magnetic field vector requires the complete characterisation of the polarisation state of the light. The use of the circular polarisation only gives information about the LOS magnetic field component.

In the last years, the understanding of the solar poles magnetism has stepped forward thanks to new and more sensitive instruments. These instruments have made possible studying the whole magnetic field vector at the solar polar regions by means of full spectropolarimetric ob-

servations. For instance, it has been observed that the magnetic field topology is not different, morphologically, from that of any other solar surface magnetism outside active regions. However, at high latitudes there are some special features. First, the magnetic fields that set the dominant polarity of solar polar regions are gathered in larger in size magnetic field structures than the rest of structures found at polar regions or from the magnetic structures found at solar surface outside active regions. Second, the number of these structures that give the magnetic polarity to the polar region varies with time at solar cycle timescales. Close to minima of activity, these structures are the largest, when solar poles present their strongest averaged magnetic field strength. In contrast, close to maxima of solar magnetic activity, when solar polar regions are reversing their polarity, they are hardly seen.

This deeper characterisation of the solar polar regions magnetism has lead to some new questions. For instance, the magnetic field topology of those structures in polarity balance, is yet unclear. Some authors found them to be horizontals, i.e. parallel to the solar surface (Ito et al., 2010; Jin et al., 2011; Shiota et al., 2012; Kaithakkal et al., 2013) while others found them to be isotropic (Blanco Rodríguez & Kneer, 2010). Another question arises from the fact that most of the full spectropolarimetric studies were performed during or close to a minimum of solar magnetic activity (2009). Only Shiota et al. (2012) has performed such kind of study outside minima, covering from a minimum of activity (2008) to the posterior rising phase (2012). Out of these stages there are no full spectropolarimetric studies. This is the reason why part of the thesis looks for the magnetic field topology characterisation during the rising phase of the solar activity cycle and the posterior maximum of 2015 and decreasing phase.

In this thesis we tackle the study of the solar poles magnetism from a large scale point of view as well as at the smallest spatial scales available, i.e. a few hundred kilometres on the solar surface. The global point of view is used to deepen the understanding of the solar poles magnetism as well as its relation with the solar magnetic cycle. To do so we use the Helioseismic Magnetic Imager instrument onboard the Solar Dynamics Observatory satellite that has been observing the Sun since 2010. One of the data products offered by the instrument team is the LOS magnetic field component, that has been observed during the whole mission with a signal-to-noise ration and an excellent instrument stability.

The analysis of this dataset shows the expected magnetic field behaviour for the solar magnetic activity cycle covered. In 2010, short after the minimum of activity (2009), both polar regions exhibit their strongest averaged magnetic field strength ($\sim$ 1 G), which is negative at the North and positive at the South. As the Sun gets closer to the maximum of magnetic activity (2015), polar regions show a gradual decrease of their averaged value until it completely cancels. After the maximum, the Sun faces a new solar activity minima and polar regions start to build up their new polarity. As it is usually observed, this process takes place in an asymmetric way, i.e. each polar region elapse through these stages independently.

A more detailed study shows an oscillatory signal with small amplitude (0.2 G) and short period ($\sim$ 30 days) with respect to the whole sequence available (6 years). The small amplitude of the signal explains why this oscillation appears and disappears at the highest latitudes. Every six months, the Earth movement along the orbit favours or hides the observation of each

polar region. Furthermore we found that this oscillation is present all over the solar surface, not only at the highest latitudes and that it is present for the whole time series. The Fourier analysis of these time series reveals that the period of this oscillation is not the same for all the latitudes but it is the same as the solar surface rotation for each latitude. After discarding active regions as the source of such oscillatory signal, we investigate the possibility of the presence of a non-axisymmetric component in the global magnetic field. This possibility is modelled by means of a tilted rotating magnetic dipole and we found that the observed signal is compatible with an inclination of $21^\circ - 40^\circ$ between the solar rotation axis and the magnetic axis.

In order to deepen in the characterisation of the magnetic field topology at the polar regions we used two ground based telescopes. On the one hand, the Tenerife Infrarred Polarimeter, installed at the Vacuum Tower Telescope allows the observation of the full Stokes vector at the near-infrarred. As Zeeman effect is proportional to the wavelength, the larger the wavelength the larger sensitivity to magnetic fields. However, the spatial resolution improves for decreasing wavelength so with this data we limit ourselves to spatial scales of around 1000 km in the solar surface. In order to improve the spatial resolution we used the CRisp Imaging SpectroPolarimeter instrument installed at the Swedish Solar Telescope. These data have less polarimetric sensitivity but they allow spatial scales of around 200 km.

The study with the infrarred lines shows that polar regions, as the quiet Sun regions observed at disc centre and at the West limb, is full of magnetism with polarimetric signals above the noise in $\sim 80\%$ of the field-of-view. In general the various parameters related with magnetic fields show a similar behaviour at both, the North and West limb data, which is different to that observed at disc centre. This common behaviour at both limb data can be due to the change of the line-of-sight with respect to the vertical to the solar surface. Only the line-of-sight magnetic flux density shows a particular behaviour at the North region. At disc centre and West region, the average line-of-sight magnetic flux density is given by strong polarimetric signals while the other magnetic fields show a polarity balance. At the North region, it is those magnetic fields outside strong polarimetric signals the ones that set the averaged line-of-sight magnetic flux density.

Even when most of the field-of-view has magnetic field signals, we cannot retrieve the magnetic field topology for all of them. This is so due to the presence of ambiguities associated to the noise. Hence we analyse the magnetic field topology over those polarimetric signals that with magnetic field strength over 600 G. Above this threshold we consider that the magnetic field vector is well determined. At disc centre we observed that these fields are verticals, in agreement with previous observational studies as well as the theoretical results, where the magnetic pressure favours a vertical configuration.

The study of the magnetic field topology close to the limbs at the line-of-sight reference frame shows a bi-modal behaviour. On the one hand, some magnetic fields are compatible with vertical fields at the local reference frame. This compatibility is confirmed when changing the topology of these fields to the local reference frame. In addition, when we performed this change, we also found that these fields have vertical fields forming canopy-like structures. The core of the structures shows the strongest and most vertical fields. Around them, there is an hale of magnetic fields expanding from, or converging to, the core of the structure. On the other hand, the

other fields cannot be vertical as it is clear from their polarimetric signals at the line-of-sight. However, we have presented a qualitative scenario with unresolved magnetic loops, that can give rise to these polarimetric signals.

This bi-modal behaviour has already been observed by Ito et al. (2010); Blanco Rodríguez & Kneer (2010); Jin et al. (2011) and Shiota et al. (2012). All of them found that one component is characterised by vertical magnetic fields, but for the other component, some authors found to be due to horizontal fields (Ito et al. 2010; Jin et al. 2011 and Shiota et al. 2012) while other authors found them to be more isotropic (Blanco Rodríguez & Kneer, 2010). We found that this latter component has strong magnetic fields and whose magnetic topology is not compatible with vertical magnetic fields. We have found that the presence of spatially unresolved magnetic loops could qualitatively explain the polarimetric signals found for these fields. The determination of their exact magnetic field topology, however, requires of additional observations.

The observations with the CRISP instrument at the SST allow covering a wider polar region as well as a higher spatial resolution and high magnetic sensitivity. However, at the visible, the magnetic sensitivity is lower than at the infrarred study. This time the number of polarimetric signals detected is significantly smaller than in the previous study, hardly reaching an 8% of the field-of-view with polarimetric detections. The study of various parameters related with the magnetic field show a similar behaviour at both limb datasets when compared to disc centre. This picture of no particular behaviour at the polar region rather than that proper of limb observations is consistent with previous works Ito et al. (2010); Blanco Rodríguez & Kneer (2010); Jin et al. (2011) and Shiota et al. (2012).

As in the previous study, not for all the polarimetric signals, a magnetic field topology can be retrieved. At disc centre, those magnetic fields, for which the magnetic field topology is retrieved, show a homogeneous azimuth with an inclination distribution close to isotropic, though with a preference for horizontal fields. At the limbs, the magnetic fields for which the topology can be inferred are a subset of those at disc centre, namely, the vertical ones. This time we have no bi-modal behaviour for the magnetic fields whose topology is determined. However there are several polarimetric signals that share similar polarimetric properties to those of the non-vertical fields of the VTT. First their Stokes V profiles are compatible with the presence of magnetic fields ranging from 600 G to 1000 G. Second, they do not show linear polarisation signals above noise.

Finally, for each of the structures for which the topology is settled, we calculated the total magnetic flux going through the solar surface as well as their spatial distribution at the North region. We found that the structures are scattered all over the polar region with those carrying the largest flux located below solar latitudes of 70°. This picture is in agreement with that found by Shiota et al. (2012) concerning the amount of flux carried by these structures and which ones set the polarity of the polar region. They are the ones with magnetic flux above 10^{17} Mx. We have also found that these structures giving the polarity to the polar region are concentrated below solar latitudes of 70°. This result is in agreement with the generally accepted model of polar polarity reversal. In this scenario the polarity reversal is driven by the amount of flux coming from lower latitudes. Hence, latitudes below 70° had already reversed their polarity

while the polarmost areas are yet neutral in average.

In summary, we present a detailed study from a large-scale point of view as well as its evolution in solar time-scales. We also address the small-scale study of the magnetic structures to which this global behaviour is rooted to, though at the expense of a worse temporal and spatial coverage. We particularly focus our study in the magnetic topology of these fields.

UNESCO codes: 120602 SOLAR PHYSICS, 120604 THE SUN

Contents

1

Introduction

1.1 The Sun as a star

A star is an accumulation of mass, big enough to turn on and maintain nuclear fusion reactions in its interior. Stars are born from the accretion of gas from a molecular cloud and depending, mainly, on the initial mass of the star, their life present different properties. These differences in the life of stars are quite well visible in the Hertzsprung-Russell diagram (HR, see Fig. 1.1). In this diagram, the spectral type of stars is on the horizontal axis and the absolute visual magnitude on the vertical axis. As visible on the diagram, the various stars are not randomly distributed but they are located in particular areas. This distribution is closely related to the stellar type and their life stage. The most prominent population is along the so-called main sequence (see Fig. 1.1). This branch corresponds to the initial life stage of stars, when the nuclear reactions that take place on the core of the stars, fuse hydrogen to helium. This stage is the longest one in the life of stars.

Although all the stars belonging to the main sequence are characterised by the fusion of hydrogen to helium in their interiors, they exhibit a great variety of physical properties. These differences are the reason for the extense distribution of the stars in this life stage. Hence, the most massive stars show the smallest absolute magnitudes (i.e. the most luminous, upper in the diagram). And the other way around, the less the initial mass of the star the bigger its magnitude, i.e. the less luminous, lower in the diagram. This phase on the star life finishes when no more hydrogen is available in the core of the stars. When these reactions end, stars move to the next phase, i.e. giants (for the less massive stars) or supergiants (the more massive stars). In this period heavier than hydrogen atoms are occasionally fused in their interiors and hydrogen is fused to helium in layers above the core. At this step, the surface temperature decreases (rightwards in the diagram) and the luminosity increases (upper in the figure).

Once the nuclear reactions in the interior of the star conclude, the star dies expelling the external layers of the star, giving rise to a supernovae (massive stars) or a planetary nebulae (less massive stars). At the same time, the core of the more massive stars collapse forming black

holes (the most massive stars) or neutron stars (the rest of massive stars) and the less massive stars forming white dwarfs. The latter are not stars in the sense that they do not maintain nuclear reactions in their interiors, but they emit significant amount of luminosity coming from the thermal energy stored and are located at the bottom leftmost part of the HR diagram.

The Sun is an intermediate-low mass star and it is estimated to be in the middle of its life in the main sequence phase. It belongs to the main sequence as a G type star (black arrow in Fig. 1.1 marks —roughly— the position of the Sun in the HR diagram) and it has been in this stage for approximately 4.5 Gyr. The source of thermal energy at this stage comes from the fusion of hydrogen atoms into helium in the core. The generation of this energy together with the dominant transport mechanism delimits different layers on the interior of the Sun (see Fig. 1.2).

The innermost part of the Sun (from the centre to about 25% of the $R_\odot$) is the core. In this part, the temperature and density are high enough to perform nuclear fusion reactions. This process is dominated in this type of stars by the proton-proton chain reaction. Around the core, a radiative envelope covers up to an approximately 70% of the $R_\odot$. In this layer, the energy generated in the core is effectively carried outwards by radiation. At around 70% of the $R_\odot$

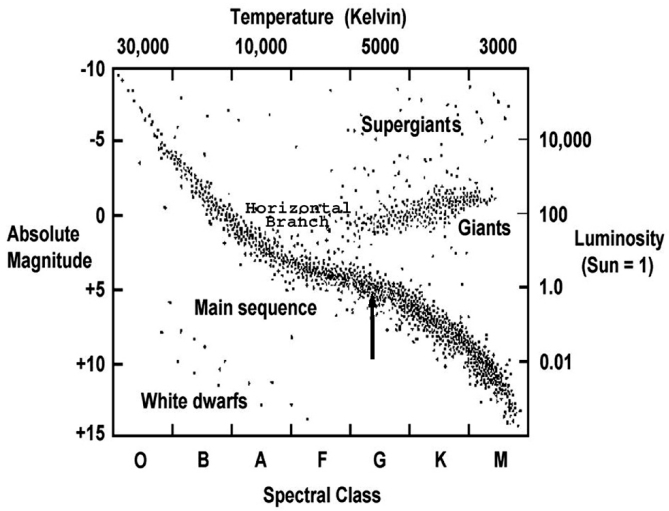

FIGURE 1.1— Hertzsprung-Russell (HR) diagram for stars in the solar neighbourhood, with stellar spectral classification on the x-axis and absolute magnitude in the y-axis. The relation between spectral classification and effective temperature is made explicit with the temperature axis in the upper part. The same relation is stablished between absolute magnitude and luminosity with the rightmost axis. Over this diagram, depending on the stellar type and age, most of the stars are distributed in the *main sequence*, *giants*, *supergiants* and *white dwarfs*. The approximate position of the Sun in the HR diagram is highlighted with a vertical arrow. Image courtesy of the *Chandra X-ray observatory*, `http://chandra.harvard.edu/edu/formal/variable_stars/bg_info.html`.

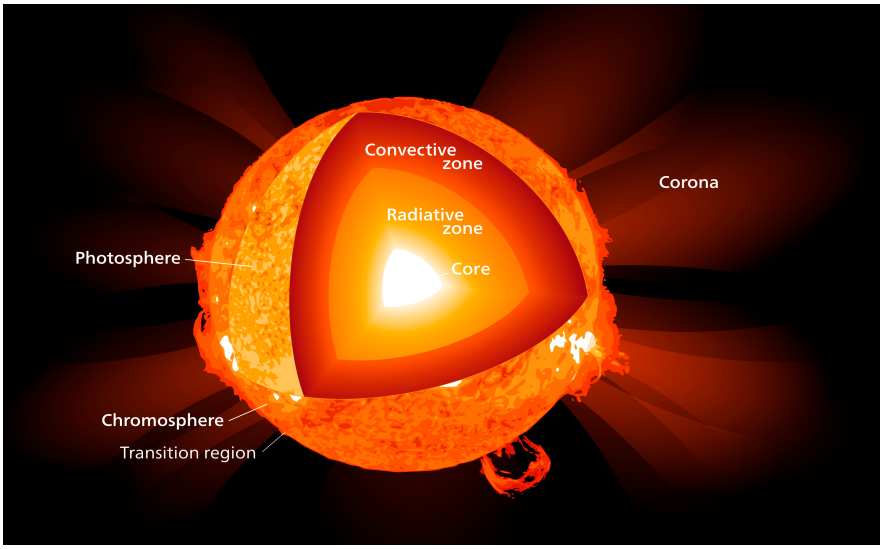

FIGURE 1.2— Stratification of the different layers of the Sun. The innermost part (up to 25% of the solar radius —$R_\odot$— is the core, where fusion reactions take place. This core is surrounded by a radiative layer that spreads to 70% $R_\odot$. Then a convective layer carries the interior energy to the surface of the Sun. Above the surface the solar atmosphere continues until the heliosphere, the volume where the solar wind pressure is dominant above the pressure done by intergalactic particles. According to the different physical properties, the solar atmosphere is divided in the photosphere, chromosphere, transition region and corona. Picture modified from that courtesy of `https://commons.wikimedia.org/wiki/File:Sun_poster.svg`.

the temperature of the plasma has decreased enough such that helium and then, hydrogen start to be not fully ionised. There, the opacity of the plasma to radiation increases and radiation becomes inefficient as an energy transport mechanism. Above this point to the surface, the energy is carried (mainly) by convection. Up to this layer, the temperature and density of the plasma has monotonically decreased from innermost layers outwards. This situation holds until at a given layer the opacity of the plasma drops enough to radiation become, again, the main energy transport mechanism. This frontier is referred to as the solar surface, above which the solar atmosphere spreads to the interplanetary medium. It is this layer, the solar atmosphere, from which most of the information about the Sun comes from.

The solar atmosphere is characterised by steep changes in the thermal and density properties of the plasma. Due to this strong stratification we usually distinguish four layers in it. The deepest one is the photosphere, covering the first ≈500 km of the solar atmosphere. The temperature of the plasma at this slab decays with height from ≈6000 K to ≈4000 K. Above it, there is the chromosphere, an approximately 1400 km thick layer characterised by a sudden increase in the temperature from ≈4000 K up to ≈20000 K. The mechanism through which upper layers are hotter than expected for a gas with decreasing density with height is yet an open issue. Above

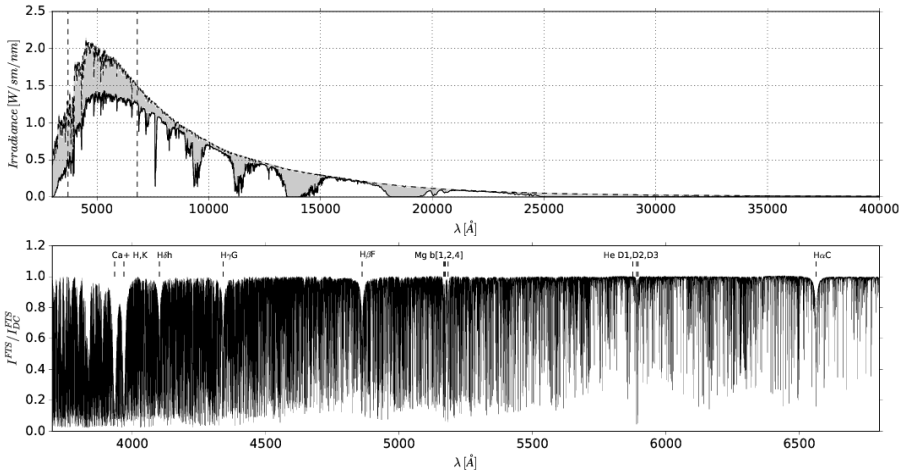

FIGURE 1.3— Upper panel: dashed black line represents the solar emission spectrum from 3300Å to 40000Å as seen from outside the Earth atmosphere. Black solid line is the same spectrum seen from sea-level. Grey shadow holds the absorbed radiation by the Earth atmosphere, which is mainly due to Earth atmosphere molecular absorption (O_2, H_2O, CO_2). The data used for the plot is courtesy of the American Society for Testing and Materials (ASTM) for the Terrestrial Reference Spectra for Photovoltaic Performance Evaluation `http://rredc.nrel.gov/solar/spectra/am1.5/#a`. Bottom panel: normalised Fourier transform spectrum (FTS) from 3300Å to 6700Å (this spectral region is marked in the upper panel with vertical dashed lines), from Neckel (1984). This high resolution spectrum exhibits many solar absorption lines (with also some Earth atmosphere absorption lines). The spectral position of some of the Fraunhofer solar spectral lines are marked with vertical dashed lines above the normalised continuum together with their identification.

the chromosphere, a ≈1000 km thick layer referred to as transition region is distinguished by a very steep increase in the mean temperature from ≈20 kK to ≈300 kK. This increment becomes even bigger above the transition region, in the corona, where the temperature reaches millions of Kelvin. This last layer spreads through the heliosphere without a clear boundary. Though the atmosphere of the Sun is quite stratified with height, these outer layers of the Sun are highly dynamic and so are their boundaries.

There are different ways to study the physics of the Sun. One of the few sources of information coming from deep on the Sun interior are the neutrinos. These particles are very low matter interacting particles generated during nuclear reactions. Due to their low interaction character, they escape directly from the Sun's core (Bahcall, 1969) to the open space. Another source of information comes from the continuos flux of particles that are accelerated in the upper atmosphere. This outwards from the Sun flux of particles is referred to as the solar wind. These particles are measured in-situ from the Earth and satellites (Snyder et al., 1963) and are an important source of information. An additional source of information (and the one we have made use of in this thesis) is the light coming from the Sun. The emergent light spectrum from the Sun has a nearly black body shape (see uppermost panel of Fig. 1.3) over which, myriads

of spectral lines are present. The first detection of some of these spectral lines was done in early 19th century by Fraunhofer (see lowermost panel of Fig. 1.3). Both continuum shape and spectral lines contain valuable information of the thermodynamic and magnetic properties of the plasma (see Ch. 3). An important field of study that uses the light incoming from the Sun is Helioseismology, that infer valuable information about the solar interior by studying the propagation of waves through the solar interior.

The Sun is our nearest star and it can be studied in a higher detail than any other star, allowing a deeper understanding on the nature of stars. In addition, there are three more reasons to focus on the Sun. The first one is that it is the main agent in the Sun-Earth interaction. The second reason is that the Sun is itself a huge laboratory. In particular, in its interior there are physical conditions that are not reachable in any laboratory in the Earth. Finally, the Sun is the main energy source for the life on the Earth.

1.2 Solar quiet sun magnetism

An interesting feature of the Sun that has not been mentioned yet and that this thesis is related to is the presence of magnetic fields in its atmosphere. The presence of a global magnetic field on the Sun was suspected by the shape of coronal streamers during solar eclipse observations, in particular, at solar minima (Ranyard, 1879; Bigelow, 1889). During these epochs, the shape of these streamers reminds to that of field lines produced by a magnet and hence, a dipolar global magnetic field for the Sun was proposed. However, the first detection of magnetic fingerprints in the solar atmosphere took place in other structures: sunspots.

Sunspots are distinguished because in white light they appear darker than their surroundings. This high contrast property allowed the study of sunsopts well early in History. Though one of the earlier registers of sunspot detection date to the second Century BC by Chinese astronomers, it was not until 17th century that a huge step forward took place. It was with the invention of the telescope and the observation of the Sun with it (Thomas Harriot, 1610). The continuous observations of the Sun led to the proposal of the existence of a solar cycle of 11 years (Schwabe 1842). During the elapse of the cycle the number of sunspots varied with a maximum of magnetic activity, a decaying phase, a minimum of magnetic activity and a subsequent rising phase.

Another step forward took place by the 20th Century when the study of the spectrum of the light coming from sunspots showed a sharp bright part in some spectral lines (Young 1892). Some years later, it was discovered the way magnetic fields modify the properties of spectral lines (Zeeman, 1897). These two facts together suggested the magnetic character of sunspots. The observation of the Zeeman effect in spectra from solar spots (Hale, 1908) settled the magnetic nature of sunspots. This first detection of magnetic signatures in the solar surface opened a new (magnetic) view of the Sun and other stars (see Ferrario et al., 2015, for a comprehensive review about the magnetism in stars). Following their previous studies, (Hale, 1913) looked for the proposed presence of a general magnetic component in the Sun. They found that the Northern hemisphere (from equator to latitude 50°) during 1912 and 1913, exhibited positive polarity. The Southern hemisphere, in contrast, was characterised by a negative polarity for this

same time interval. This detection resembled well with the general magnetic field inferred from coronal streamers as tracers of a bipolar object and their initial hypothesis of the solar general magnetic field similar to that of a magnetised sphere.

The subsequent study of the solar magnetism revealed two different behaviours. On the one hand, the most evident structures, such as sunspots, pores, and *plage* are associated to the emergence of active regions. These structures are huge magnetic concentrations that generally appear in the solar surface as bipolar structures. This component was the first one detected and studied. It is so because their large-scale (several seconds of arc) strong magnetic fields (of the order of thousands of Gauss) facilitate their detectability. On the other hand, the second component is referred to as the quiet Sun, originally named after the apparent absence of magnetic fields in it. Its nature has progressively evolved from a free of magnetism character to the nowadays view: an almost fully magnetic quiet Sun. According to these two components, the quiet Sun involves the solar surface magnetism outside active regions and, in particular, the polar regions. This evolution of the quiet Sun magnetic character is not casual. Quiet Sun observations are subtle to intrinsic observational difficulties and limited in the theoretical analysis. Hence, the progressive improvement of observation facilities and theoretical modelling has revealed an increasingly rich magnetism of the quiet Sun.

From an observational point of view, quiet Sun magnetic field structures are characterised by intrinsically small spatial scales. Then, the study of such magnetism requires: On the one hand, big apperture telescopes to reach high enough spatial resolution. On the other hand, it is necessary to have very good atmospheric conditions during observations to properly resolve them. Another observational restriction to deal with is the intrinsic weakness of its polarisation signatures. This makes necessary to use highly sensitive polarimetric measurements and high signal-to-noise ratios (SNR).

From a theoretical point of view, the analysis of quiet Sun observations it is also a difficult task. It is not only that the polarimetric signals are weak but also that the polarimetric signals exhibit a wide variety of shapes. The shape of Stokes V profiles are an example of this point. A single magnetic field generates bi-lobed, anti-symmetric profiles. In the quiet Sun, however, the presence of very asymmetric profiles as well as the presence of one- or multi-lobed (more than two lobes) is usual (Sigwarth et al., 1999; Sánchez Almeida & Lites, 2000; Khomenko et al., 2003). Hence, different theoretical models are required in order to explain them. For instance, perfectly antisymmetric Stokes V profiles can be modelled with the presence of a magnetic field constant along the line-of-sight (LOS) and a constant LOS velocity. An example of such a profile is shown in left panel of Fig. 1.4. In order to reproduce the wide variety of Stokes V shapes observed at the quiet Sun (asymmetries, non bi-lobed profiles), the required model is more complex. For instance, middle panel of the figure shows how the presence of gradients in the LOS velocity and in the magnetic field give rise to asymmetric profiles. Rightmost panel shows a scenario where the presence of multiple magnetic fields in the same resolution elements can entail multi-lobed profiles.

A big effort has been made in order to understand and fully characterise this weak magnetism permeating the solar atmosphere. Historically, these studies have been made from two different

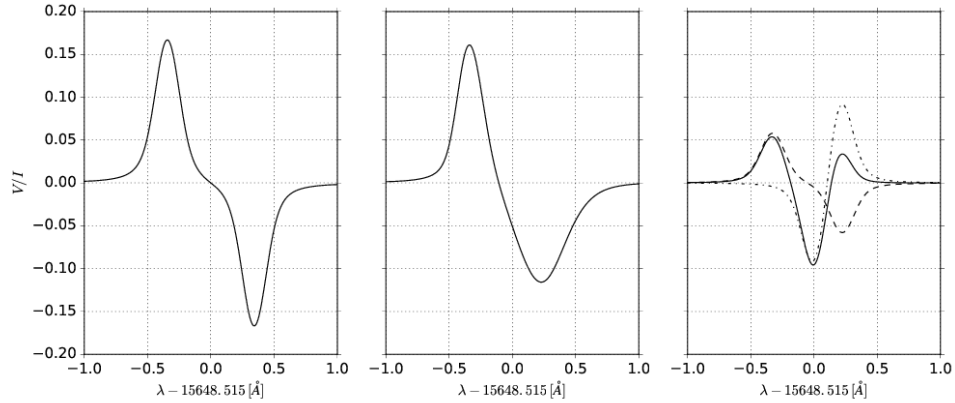

FIGURE 1.4— Left panel: circular polarisation spectrum synthesised for the VALC (Vernazza et al., 1981) semi-empirical atmosphere with a magnetic field of 1000 G pointing to the observer. Middle panel: same synthesis as in the previous one but now the magnetic field strength (LOS velocity) varies linearly from the bottom part of the atmosphere 0 G (-2 km/s) to 1000 G (2 km/s). Right panel: synthesis using the VALC model with two components in the resolution element. For the stronger (dashed lines) a magnetic field of $800G$ along the LOS pointing to the observer and a LOS velocity of $-1km/s$ are introduced. For the second component (dashed-dotted) a VALC model with a magnetic field of $300G$ directed on the LOS but of opposite polarity to the former is chosen. In addition a LOS velocity of $2km/s$ is set. The combination of both with a filling factor of 0.3 and 0.7 gives the solid line. For the synthesis we have used the Stokes Inversion based on Response function (SIR) code (Ruiz Cobo & del Toro Iniesta, 1992).

perspectives. On the one hand, there have been studies focused on the topological study of this magnetism. On the other hand, some works look at the long-term temporal evolution of this magnetism. This second point of view aims to shed new insight about the source of this magnetism and the relation of these fields with the magnetism of active regions. The source associated to active regions is agreed to be due to the action of a global dynamo whose action is behind the global magnetic field behaviour. This global dynamo explains observed features such as the cyclic behaviour of solar magnetism, the non random emergence of sunstpots, etc. Yet, the source for the quiet Sun magnetism is unclear.

The topological study of the quiet Sun magnetism has involved a huge observational effort overcoming the intrinsic difficulties of this magnetism. From these studies, a bi-modal behaviour is observed for the quiet Sun. On the one hand there are magnetic structures with strong magnetic fields (kG) (Stenflo, 1973). These strong fields are characterised by vertical fields and downflow motions. Their spatial distribution over the solar surface is not homogeneous but they are distributed forming a network like shape. Moreover, these fields were found to be co-spatial with those responsible of the network shape exhibited by the Ca II H and K emission over the solar disc (Leighton et al. 1962; Noyes & Leighton 1963 and Simon & Leighton 1964). The determination of the *true* magnetic field strength of this network fields was not reliably inferred until the work by Stenflo (1973). He found that network elements were characterised by kG fields

and spatial scales of the order of 100 km. These magnetic structures lead to the theoretical introduction of the thin flux tube model (Spruit & Roberts, 1983) and the flux tube vision of the network Stenflo & Harvey (1985).

On the other hand the other component exhibits weaker magnetic fields than the Network. These magnetic fields are permeating all the quiet Sun area and its topology is not clear yet. The first detection of magnetic signals outside the Network was done by Livingston & Harvey (1971). They found the presence of very faint magnetic signals inside the boundaries of the network component. This magnetism is usually referred to as Inner/Inter-Network fields (hereinafter, IN). Some years later two main properties of the IN magnetism were settled (Zirin, 1985): 1- Longitudinal magnetic fluxes of IN fields are at least one order of magnitude smaller than those of network regions. 2- They appear allover the surface and are dragged by surface flow motions to the boundaries of the granules. If they are long-lived enough, plasma motions can take these fields to network boundaries, merging them with network fields by cancelation or coalescence.

It was also with the first spectropolarimetric analysis of the IN magnetism that the characterisation of the intrinsic magnetic field strengths of these fields was attempted. However, while visible observations (Grossmann-Doerth et al., 1996; Sigwarth et al., 1999; Sánchez Almeida & Lites, 2000; Socas-Navarro & Sánchez Almeida, 2002; Domínguez Cerdeña et al., 2003; Socas-Navarro et al., 2004) led to magnetic fields of the order of kG, the infrared ones (Keller et al., 1994; Lin, 1995; Lin & Rimmele, 1999; Khomenko et al., 2003; Martínez González et al., 2007a) gave hG fields. The discrepancy was solved by Martínez González et al. (2006) and nowadays the community agrees that IN elements are characterised by hG magnetic field strengths.

The intrinsic weakness of the IN fields together with the small-scale variation as well as their short lifetime (a mean lifetime of $\sim$3 minutes, Zhou et al. 2010) is still a challenge from an observational point of view. A sample of these difficulties is the open question about the orientations of the IN magnetic fields. Some works (Orozco Suárez et al., 2007b,a; Lites et al., 2007, 2008; Borrero & Kobel, 2013) get inclinations (the angle between the magnetic field vector and the vertical to the surface) predominantly around 90° while other studies point to more isotropic distributions (Martínez González et al., 2008; Asensio Ramos, 2009; Stenflo, 2010; Faurobert & Ricort, 2015).

The above-mentioned works used the Zeeman effect (see Sec. 3.1) in order to investigate the properties of the quiet Sun magnetism. It is also possible to tackle this quiet Sun magnetism characterisation from another point of view: the Hanle effect. These studies (Stenflo, 1982; Faurobert-Scholl et al., 1995; Faurobert et al., 2001; Stenflo et al., 1998; Berdyugina & Fluri, 2004; Trujillo Bueno et al., 2004; Bommier et al., 2005; Derouich et al., 2006) recover weak magnetic fields when assuming a microturbulent distribution of magnetic fields.

Concerning the temporal studies of the quiet Sun magnetism at solar cycle time-scales, there are typically three ways to tackle this study. Most of the effort in such kind of studies has been done studying the long-term time variation of some magnetic proxies, such as the emission in Ca II H/K. These studies (Ortiz et al., 2002; Ermolli et al., 2003; McIntosh et al., 2011; Yeo et al., 2014) seem to agree that the emission from the network component does show a variation

with the cycle. This variation comes from the fact that active regions supply a big amount of flux to the surroundings during their decay. As the number of active regions vary with the solar cycle, so does this flux contribution to network fields. Yet it seems that at least a fraction of the network fields, as inferred from its emissivity in different magnetic proxies, does not vary with the cycle. This gives rise to the distinction between what some authors name the "active/enhanced" network, whose temporal behaviour is related with the solar cycle, and the network, which is independent (Ermolli et al., 2013).

Another way to address this question is the analysis of long-term spectropolarimetric observations. The study of the magnetic properties based on the probability density function of the magnetic field (Buehler et al., 2013; Lites et al., 2014) or on the power spectrum of internetwork magnetic fields spatial distribution (Faurobert & Ricort, 2015) shows no evidence of a solar cyclic behaviour of the IN magnetism. In the other hand, Jin et al. (2011) found a cyclic behaviour of quiet Sun magnetic structures. They found that the strongest quiet Sun signals exhibit a temporal behaviour correlated with the solar cycle evolution. In contrast, intermediate magnetic structures show an anti-correlation with the solar cycle.

This temporal study has also been made using spectropolarimetric data by means of Hanle signals. Stenflo (2003) studied the time evolution of Hanle signals in atomic lines and he found that they present variation with the solar cycle. Kleint et al. (2010, 2011) and Bianda et al. (2014) also use the Hanle effect to determine magnetic fields using C_2 molecules. They study the temporal evolution of these signals during the last minimum and the subsequent rising activity phase, and found no evident variation. However, their analysis of observations taken for the Atlas of the Second Solar Spectrum (Gandorfer 2000), which took place during a maximum of activity, is compatible with some variability during the solar cycle.

The landscape of the quiet Sun magnetism shows an increasingly with time complex scenario in which the magnetism is occupying a more relevant role. These fields form small scale structures characterised by weak/intermediate magnetic field strengths compared to active region structures. However, they cover most of the surface most of the time. Hence this component can potentially play a relevant role in the energy budget of the solar atmosphere. For instance, the amount of flux rate emergence related with IN magnetic fields is bigger (3.7×10^{24} Mx day^{-1} Gošić et al. 2016) than that of active regions even at maxima of activity (6.2×10^{21} Mx day^{-1} Schrijver & Harvey 1994). Lately there have been observational reports that emphasise the potential role of the quiet Sun magnetism in the energetics of the solar atmosphere. In these works, chromospheric counterparts of quiet Sun photospheric magnetic events have been observed, such as loop emergence, (Martínez González & Bellot Rubio, 2009) and magnetic bubble emergence (Ortiz et al., 2014).

It has been mentioned above that polar regions are considered as part of quiet Sun magnetism. It is so because active regions appear close to equator latitudes ($\pm 40°$, in what is known as activity belt). Because of this reason, it can be reasonably expected that the influence of active regions at low latitudes and at polar regions can be different.

1.3 A Polar view of the quiet sun

Polar caps are considered as those regions with a solar latitude above 60°. Their observation is only feasible at high heliocentric angles, the angle between the vertical to the solar surface and the line-of-sight (hereinafter, LOS). This fact adds some additional observational and analysis difficulties to the already difficult quiet Sun magnetism studies. Observations at increasing heliocentric angle are characterised by foreshortening, lowered contrast and reduced observed intensity. In addition, the analysis of these observations must take into account projection effects when solving the radiative transfer. These intrinsic difficulties have made the spectropolarimetric analysis at these latitudes to be scarce.

The first magnetic detections at polar regions date of the middle fifties by Babcock & Babcock (1952), who presented the study of solar full-disc magnetographs. They found that at each polar region (above/below $+/-70°$) the LOS magnetic field component exhibits a non-null mean value $\langle B_{LOS} \rangle \in (1, 5)$ G. The sign of these mean values was found to be opposite in each pole. This scenario was coherent with the general magnetic field proposed from coronal streamers shape and agree with the first detection of the general magnetic field (Hale, 1913). Observations of the magnetism at polar regions continued (Babcock & Babcock, 1955) showing that this value was not constant. This variation was due to: 1- The modulation by the tilt between the rotation axis of the Sun and the ecliptic. 2- The polar fields reversal (Babcock, 1959). This second change took place during a maximum of activity. However, they did not find any rotational variation in the magnetic field from polar regions. This periodic variation would be present if a misalignment between the rotational axis and the general magnetic axis were present. Two facts support such a misalignment. 1- Coronal morphology, especially during solar minima, exhibits a misalignment between coronal streamers "tracing" magnetic fields and the solar rotation axis (Bruno et al., 1982). 2- Hale et al. (1918) and Seares et al. (1918) found a misalignment of $\sim 7°$ between the general magnetic field and the solar rotation axis. However, these results based on the displacements of Zeeman components have remained controversial due to the very limited instrumentation used.

The continuous study of the LOS magnetic field component at the polar regions (Stenflo, 1970; Severny, 1971; Svalgaard et al., 1978; Howard & Labonte, 1981; Tang & Wang, 1991; Lin et al., 1994) together with the observation of polar faculae behaviour on solar cycle timescales (Waldmeier, 1955; Sheeley, 1964; Tanaka, 1964; Sheeley, 1964) settled the nowadays standard polar magnetism behaviour, in which it is clear the time evolution relation of the magnetism at these regions and the solar cycle. In this scenario the magnetic flux of the active regions of the following polarity is preferentially dragged to higher latitudes. This decaying active region magnetic flux is of opposite polarity to the dominant polarity of the each hemisphere polar region. Hence, this supply of opposite sign polarities cancels the previous polarity and builds up the new one. This cyclic related behaviour constitutes the first difference with the quiet Sun magnetism at lower latitudes.

The introduction of spectropolarimetry allowed discovering that high latitude quiet Sun shows a bimodal magnetic topology behaviour. This is similar to the topology of quiet Sun at lower latitudes. However, there exist some differences. On the one hand, there are some magnetic

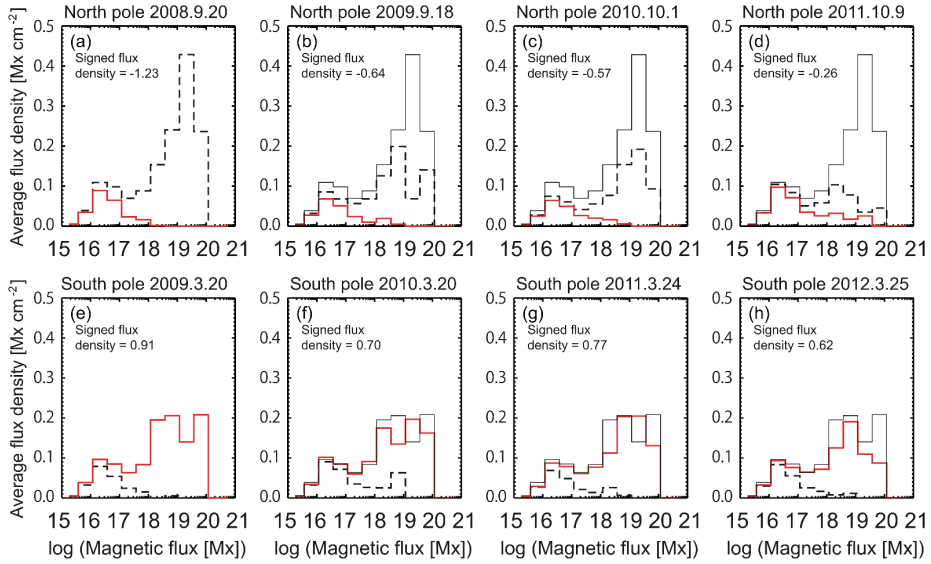

FIGURE 1.5— Top row: time evolution from 2008 to 2012 (from left to right) of the average flux density of polar vertical magnetic patches. Positive flux is displayed in dashed lines and negative one in red. The positive distribution for the first year is overplotted in thin solid line in the other three panels. The same representation is used in the second row of panels for the South pole. This time, the thin solid line of years 2010 to 2012 refers to the negative flux (red line) found in 2009. Image source: Fig. 3 from Shiota et al. (2012).

fields whose strength is of the order of kilogauss (Homann et al., 1997; Okunev & Kneer, 2004; Blanco Rodríguez et al., 2007; Tsuneta et al., 2008; Blanco Rodríguez & Kneer, 2010; Ito et al., 2010; Jin et al., 2011; Shiota et al., 2012; Kaithakkal et al., 2013; Quintero Noda et al., 2016). These fields show, when accounting for geometrical effects, a vertical to the surface orientation. This is similar to the observed behaviour of strong fields at low latitudes. However, at these high latitudes it is not clear if these fields are associated to upflows (Okunev & Kneer, 2004; Blanco Rodríguez et al., 2007), downflows (Blanco Rodríguez & Kneer, 2010) or both (Quintero Noda et al., 2016). In addition, in the latter work, the authors study the LOS velocity distributions with optical depth finding that the larger the optical depth, the smaller the amplitude of the LOS velocity.

This strong magnetic field component shows, in contrast to low latitudes, a bimodal behaviour. The strongest magnetic fields are associated to larger in size magnetic flux concentrations. These structures show the same polarity as the dominant one at the polar region (Ito et al., 2010; Shiota et al., 2012; Kaithakkal et al., 2013). These fields associated to large in size flux concentrations follow the solar cycle (Shiota et al., 2012). When polar regions exhibit the strongest LOS magnetic flux, these fields are the most numerous. When polar regions are reversing their polarity these fields are almost absent. This component seems to be characteristic of high latitudes as

there is no counterpart found at low latitudes (Ito et al., 2010; Shiota et al., 2012). The other strong magnetic fields, though associated to smaller in size structures than the cycle dependent ones, exhibit similar behaviour to low latitudes quiet Sun. These fields are characterised by a polarity balance (Ito et al., 2010; Shiota et al., 2012) and no cycle dependent behaviour (Shiota et al., 2012). These features are nicely gathered in Fig. 1.5 taken from Shiota et al. (2012). In the figure, the vertical component for both polar regions is shown. The North region (first row) shows a dominant negative polarity (dashed lines) in 2008, which gradually decreases during the following years (the solid thin line is the initial distribution of negative flux). Notice that only the strongest fluxes vary whilst the weaker fluxes tail remains quite constant in time. The South region (second row) exhibited a more steady behaviour with a very faint decrease of the amount of negative flux (red line).

On the other hand, the second component of the magnetism at high latitudes is characterised by weaker magnetic fields (hG, Tsuneta et al., 2008; Blanco Rodríguez & Kneer, 2010; Ito et al., 2010; Jin et al., 2011; Shiota et al., 2012). The morphology of these magnetic fields is not clear yet. Some authors (Tsuneta et al., 2008; Ito et al., 2010; Jin et al., 2011; Shiota et al., 2012) derive horizontally dominated distributions. These fields are found to share properties with the weak component at lower latitudes (Ito et al., 2010; Jin et al., 2011; Shiota et al., 2012). Shiota et al. (2012) studied a four-year temporal evolution of this component at high and low latitudes. In both disc positions, it was found that these fields show no related behaviour with the cycle phase. Blanco Rodríguez & Kneer (2010) in contrast found that the orientations of these fields are compatible with a random distribution.

In summary, polar regions are outside the main area of direct influence of active regions and hence, they belong to the so-called quiet Sun magnetism. In fact, the topology of the magnetic signals detected at these high latitudes seem to be similar to those proper of low latitude quiet Sun. However, there are important differences between the polar quiet Sun magnetism and the quiet Sun magnetism at low latitudes. One of such differences is the clear relation that polar magnetic fields show with the solar cycle. Another important difference is the disparate influence that active region can play in the magnetism of the quiet Sun at low and high latitudes. It is also seen that most of the solar open magnetic field lines to the Heliosphere are rooted to polar regions (van de Hulst, 1953; Babcock & Babcock, 1955). In addition and according to dynamo theories, polar regions magnetism is thought to be a major agent in the development of the solar cycle. However, the study of the physical properties of this magnetism is scarce due to the intrinsic problems associated to these regions. This thesis aims to continue deepening into the understanding of the magnetism at polar regions. In particular, this work is focused on the magnetism at the photosphere by means of spectropolarimetric techniques. To do so, a whole coverage, from a large scale point of view to the highest spatial resolution has been carried out. In order to perform such a task the ideal observations would consist of:

- high temporal coverage,
- high spatial coverage,
- high spatial resolution,

- high polarimetric sensitivity, and
- a better observation angle (rather than looking from the ecliptic).

In practice, it is not possible to achieve all these requirements at the same time. In order to cover most of them, different datasets have been used. Regarding a favourable viewing angle, currently it is not possible to perform spectropolarimetric observations from outside the ecliptic at all. Such observations would alleviate the influence of projection effects, both, for the observation and the posterior analysis. In this sense, some yearsahead, the Solar Orbiter mission plans to observe the polar regions from outside the ecliptic up to 25/34°.

High temporal and spatial coverage with sufficient polarimetric sensitivity can be reached with data coming from Helioseismic Magnetic Imager (HMI; Scherrer et al., 2012; Schou et al., 2012) onboard Solar Dynamics Observatory (SDO; Pesnell et al., 2012). This kind of work allows the study of the polar magnetism behaviour through the solar cycle timescale. However, in such a study the high polarimetric sensitivity reached and high spatial resolution are lost. In order to palliate these lacks, high spectropolarimetric sensitivities are needed. This target is successfully achieved by the Spectro-Polarimeter (SP; Lites et al., 2013) of the Solar Optical Telescope (SOT; Tsuneta et al., 2008) on board the Hinode mission (Kosugi et al., 2007). This combination reaches higher spectropolarimetric sensitivities than those achieved by HMI and higher spatial resolution. It is not possible to further improve these two issues simultaneously, but they can be done separately. Better spectropolarimetric sensitivities together with acceptable spatial resolution can be reached at near infrared spectral lines. This point can be fulfilled with the Tenerife Infrared Polarimeter II (TIP-II; Collados et al., 2007) instrument installed at Vacuum Tower Telescope (VTT; Schroeter et al., 1985). The best spatial resolution with acceptable spatial coverage and polarimetric sensitivity is achieved with visible spectral lines coming from CRisp Imaging SpectroPolarimeter (CRISP; Scharmer, 2006) located at the Solar Swedish Telescope (SST; Scharmer et al., 1999).

This thesis is structured in six chapters. Chapter 2 presents the facilities, type of data used from each of them as well as the reduction process applied. Chapter 3 briefly outlines the method applied to infer meaningful quantitative physical information from the data. Chapter 4 presents the global polar magnetism study performed with HMI@SDO data. Chapter 5 explores the properties of the magnetism at polar regions as observed in the near infrared. In chapter 6 analyses polar magnetism as reavealed by the joint action of CRISP@SST. Finally, the conclusions of this work are presented in Chapter 7.

2

Observations

This thesis aims to deepen into the understanding of the magnetism at the solar polar regions. Polarimetry and, more interestingly, spectropolarimetry, are the most extended techniques to infer quantitative information on magnetic fields. For this reason, the different instrumentation used in this thesis have polarimetric capabilities. The various facilities have been used according to the different specific objectives of the thesis, namely:

1. Long-term behaviour of the solar polar magnetism
2. Magnetic properties of the weakest polarisation signals
3. Polar region large scale study at high-resolution, high-polarimetric sensitivity

In the next sections we briefly describe the instruments and the kind of data employed as well as some additional steps in the data products up to ready-to-analyse data status.

2.1 Solar global magnetism from full-disc magnetograms

There are different possibilities to tackle the long temporal study of the solar global magnetism. Historically, such type of studies at polar regions have been performed by means of full disc LOS magnetograms taken from ground based facilities, mainly the Wilcox Solar observatory (Hoeksema, 1991) and the Mount Wilson Solar Observatory (Seares, 1917). In the last decades, the access to space data has enabled a new opportunity for this research. The solar and Heliospheric Observatory (SOHO; Domingo, 1995; Domingo et al., 1995b,a) satellite and, afterwards, the Hinode satellite shed new insights in the understanding of the polar magnetism (Varsik et al., 2002; Benevolenskaya, 2004; Krivova & Solanki, 2004; Tsuneta et al., 2008; Ito et al., 2010; Shiota et al., 2012). In the last few years two new facilities have been deployed with the polar magnetism as part of their main scientific targets. The Synoptic Optical Long-term Investigations of the Sun is located since 2007 at the Kitt Peak observatory. The other one is the SDO that is a space borne mission operative since early 2010's. From these possibilities we have chosen the latter due to its time coverage, high time cadence, moderate magnetic sensitivity and

spatial resolution and its technical stability during the whole mission.

The SDO is a NASA mission launched on February 11, 2010. The main goal of the mission is to understand the sources driving the solar variability and their impact on the Heliosphere and the Earth. To do so, it carries three different instruments that continuously observe the whole solar disc:

- *Atmospheric Imaging Assembly* (AIA; Lemen et al., 2012): This is an imaging instrument focused on the study of the solar corona. To that aim it takes every 12 seconds images at some ultraviolet and extreme ultraviolet wavelengths: 94 Å, 131 Å, 171 Å, 193 Å, 211 Å, 304 Å, 335 Å, 1600 Å and 1700 Å.
- *EUV Variability Experiment* (EVE; Woods et al., 2012): This instrument is focused on the study of the solar extreme-ultraviolet (EUV) irradiance in order to understand the most energetic phenomena of the solar atmosphere such as solar flares or coronal mass ejections.
- *Helioseismic and Magnetic Imager* (HMI): This instrument is an improvement of the Michelson Doppler Imager (MDI; Scherrer et al., 1995) instrument onboard SOHO. The main goal is to study global modes oscillations and the magnetic field at the solar photosphere.

From the above-mentioned mission and instrument goals, it is clear the suitability of the HMI@SDO data for the study of the long-term time evolution of the photospheric magnetism at the Sun, in particular in the polar regions. The instrument is a filtergraph (tunable filter) that sequentially measures in six wavelength positions around the photospheric FeI 6173 Å spectral line. Doing so it allows measuring the Stokes parameters of the whole disc. The full-disc data products are the Doppler shift, the line-of-sight magnetic field, the continuum intensity, and the magnetic field vector. The LOS magnetic field component can be obtained from the vector magnetic field. However, as it is retrieved using a different method, we explicitly distinguish both. A sketch of the optical layout of this telescope/instrument is presented in Fig. 2.1.

The entrance window is a 50 Å passband window centred in the line of interest. The rest of the light is reflected. The next two optical devices are two lenses that form the telescope. It has a clean aperture of 14 cm ensuring a diffracted image of $0\farcs92$. However, as the pixel size of the detector is $0\farcs504$, the final spatial resolution achieved is $1''$. After the telescope, there are two calibration-focus wheels (*Calibration unit* in Fig. 2.1) for the calibration of the instrument. In between these two wheels, there are two optical systems. The first one is the beam modulator (*Light modulator* in Fig. 2.1), responsible of performing the polarimetric modulation. The second system is the image stabilisation system, a tip-tilt mirror that keeps fixed the solar disc image in the forthcoming optical path. In order to get the corrections to be applied by the tip-tilt, there is a polarised beam-splitter which sends one of the orthogonal polarisation states to a limb sensor and the rest of the light continues through the optical system.

Next, there is a new passband filter which tightens the transmitted wavelengths to 8 Å around the spectral line. Afterwards a Lyot filter further selects the transmitted bandpass to 612 mÅ.

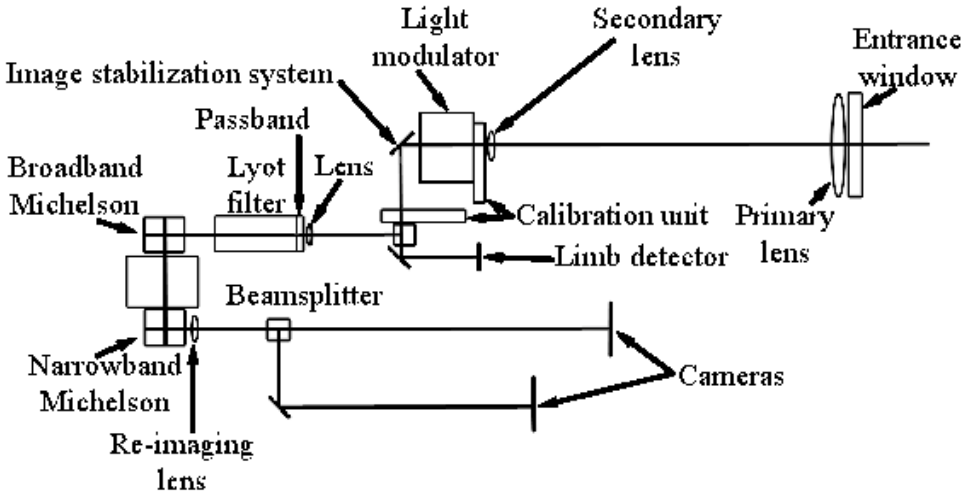

FIGURE 2.1— Sketch of the optical layout of the instrument HMI@SDO. The figure is adapted from `http://hmi.stanford.edu/proposal_April_2002/C.2_body.pdf`.

HMI takes data in six different wavelengths around the 6173 Å FeI line. This final tuning, i.e, the selection of the observed wavelength, is done with two Michelson interferometers. The first one is the broadband interferometer, with a FWHM passband of 172 mÅ and the second interferometer is the narrow one with a FWHM passband of 86 mÅ. The selection of the wavelength is done by the joint action of these two interferometers. The narrowband one selects the final width of the transmitted spectral wavelengths. The broadband one is used to attenuate the non-desired periodically transmitted peaks of the narrowband interferometer.

Finally, a beamsplitter sends the outgoing light to two different cameras. One of the cameras is used for 45 seconds cadence products and the second camera is used for 720 seconds cadence data. From the filtergrams measured, various parameters are recovered, including: LOS Doppler velocity, LOS magnetic field, full magnetic field vector, continuum proxy, line width, line depth, and LOS magnetic field component synoptic maps.

With this instrument we have studied the time evolution of the LOS magnetic field component. This parameter is calculated from a set of twelve filtergrams due to the two modulations needed ($I + V$ and $I - V$) at each of the six wavelength positions. The algorithm is based on the centre of gravity method (Semel, 1967; Rees & Semel, 1979). This method measures the relative displacements of the centre of gravity of the $I + V$ and $I - V$ modulations. In the following, we use the definition:

$$I_{\pm}(\lambda) = \frac{I(\lambda) \pm V(\lambda)}{2}, \tag{2.1}$$

for the measured intensity profiles for the modulation where Stokes I and V are summed or subtracted. The centre of gravity for each component is given by the Doppler velocity which will be common for both measurements $I_{\pm}(\lambda)$ and the magnetic displacement of each component which will be in opposite directions for each measurement:

$$\Delta\lambda_{\pm} = \frac{\int_{-\infty}^{+\infty} (I_c - I_{\pm}(\lambda)\,\lambda)\,d\lambda}{\int_{-\infty}^{+\infty} (I_c - I_{\pm}(\lambda)\,)\,d\lambda}, \tag{2.2}$$

where I_c is the continuum intensity and $\Delta\lambda_{\pm}$ is the measured wavelength displacement of the centre of gravity of the $I_{\pm}(\lambda)$ profile. Due to the fact that the Doppler and magnetic displacements influence in different ways, these displacements are related with the LOS velocity ($\Delta\lambda_V$) and with the magnetic field strength ($\Delta\lambda_B$):

$$\begin{aligned} \Delta\lambda_V &= \frac{\Delta\lambda_+ + \Delta\lambda_-}{2} = \frac{v}{c}\lambda_0 \\ \Delta\lambda_B &= \frac{\Delta\lambda_+ - \Delta\lambda_-}{2} \\ &= \frac{e_0}{4\pi mc}\lambda_0^2 g_{eff} B\cos\theta, \end{aligned} \tag{2.3}$$

The last equality assumes that the magnetic splitting is in the weak field regime of the Zeeman effect (see for instance Section 3.1 of Landi Degl'Innocenti & Landolfi, 2004). e_0 is the electron charge, m is the mass of the electron and c is the speed of light. λ_0 is the zero velocity wavelength of the spectral line, g_{eff} is the effective Landé factor of the atomic transition associated to the spectral line, B is the magnetic field strength, and θ the magnetic field inclination with respect to the LOS direction. Hence, once estimated the centres of gravity of the $I_+(\lambda)$ and $I_-(\lambda)$ profiles, one can recover the LOS velocity and the LOS component of the magnetic field.

The HMI team estimates the values $\Delta\lambda_{\pm}$ from the coefficients of a Fourier expansion:

$$\begin{aligned} a_{\pm}^n &= \frac{2}{T}\int_{-T/2}^{T/2} I_{\pm}(\lambda)\cos\frac{2\pi n\lambda}{T}\,d\lambda \\ b_{\pm}^n &= \frac{2}{T}\int_{-T/2}^{T/2} I_{\pm}(\lambda)\sin\frac{2\pi n\lambda}{T}\,d\lambda, \end{aligned} \tag{2.4}$$

where T is the period of the function (six points in wavelength). In practice, Eq. 2.4 is substituted by the discrete Fourier expansion:

$$\begin{aligned} a_{\pm}^n &= \frac{2}{T}\sum_{i=0}^{5} I_{\pm}(\lambda_i)\cos\frac{2\pi n\lambda_i}{T}\Delta\lambda \\ b_{\pm}^n &= \frac{2}{T}\sum_{i=0}^{5} I_{\pm}(\lambda_i)\sin\frac{2\pi n\lambda_i}{T}\Delta\lambda, \end{aligned} \tag{2.5}$$

where $\Delta\lambda = 68.8$ mÅ, the nominal separation between two consecutive wavelength positions, and $T = 6\Delta\lambda$. The index i runs over the six wavelength positions and $I_{\pm}(\lambda_i)$ is the measurement

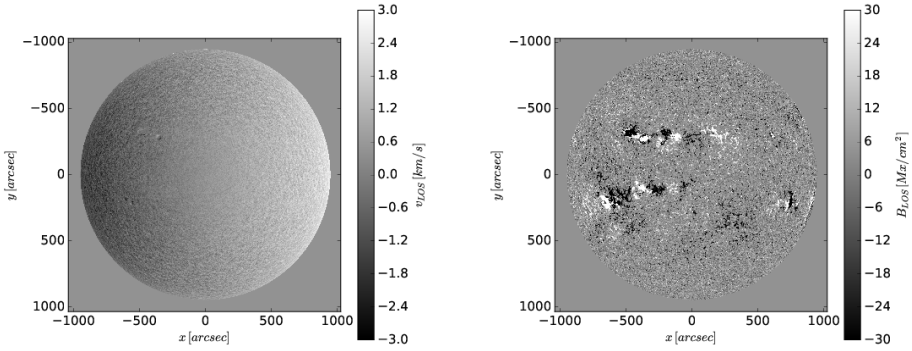

FIGURE 2.2— HMI dopplergram (left) and magnetogram (right) for 24th May 2013. The dopplergram is in km/s and the magnetogram in Mx/cm^2. x and y directions are given in seconds of arc. The East is on the left and the North at the top.

of each of the modulations at the i-th wavelength position.

The wavelength offset from the spectral line centre for each of the modulation states is given by:

$$\Delta\lambda_{\pm}^{n} = \frac{1}{d_n} \arctan\left(\frac{b_{\pm}^{n}}{a_{\pm}^{n}}\right), \tag{2.6}$$

where $d_n = 2\pi n/T$. The offered data up to date is for n=1. This estimation of the wavelength displacement together with Eq. 2.3 results in the calculation of the LOS velocity and the LOS component of the magnetic field. Figure 2.2 shows an example of an HMI full-disc dopplergram and a full-disc magnetogram. These data products are ready to use and no further processing is needed.

2.2 The weakest polar magnetic signals from the high sensitivity spectro-polarimetry

The above-mentioned data allows a study covering very long time sequences with a very steady and controlled environment. However, it lacks the polarimetric sensitivity and spatial resolution that can be reached in other facilities. An additional research addressed in this work concerns the study of the weakest magnetic signals. For this purpose, and taking into account that the sensitivity to Zeeman signals is enhanced with wavelength (see for instance Ch. 3.1.2), we have used near infrared data. In particular, we have used data coming from TIP-II@VTT that allow a very high polarimetric sensitivity while keeping a moderate spatial resolution.

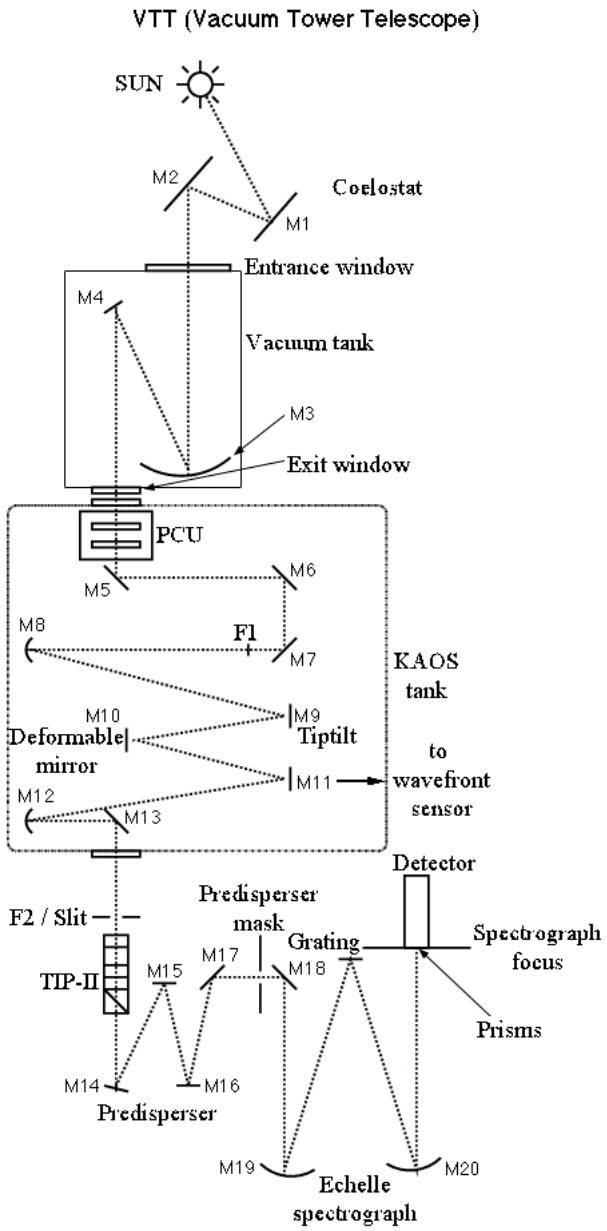

FIGURE 2.3— Sketch of the optical layout for the VTT telescope when using the TIP-II polarimeter.

2.2.1 The Vacuum Tower Telescope

Built in 1986, the VTT telescope is located at the *Observatorio del Teide* in Tenerife, Spain. Its operation is shared by three German institutions: *Kiepenheuer-Institut für Sonnenphysik* (KIS), *Leibniz Institute for Astrophysics Potsdam* (AIP), and the *Max Planck Institute for Solar System Research* (MPS). The telescope is located inside a 38 meters height tower with a coelostat on the top. A coelostat is formed by two flat mirrors used to compensate the movement of the Sun on the sky, and sends the incoming solar light to a fixed system, i.e., the telescope. In contrast to altazimuth mountings, coelostats do not introduce image rotation since their movements are aligned with the movements of the Sun. These two mirrors have 80 cm diameter. The entrance pupil of the system (70 cm) is given by mirror M3 (see Fig. 2.3), the primary mirror of the telescope. This mirror is slightly off-axis (0°85) and forms, together with the secondary mirror, M4, the telescope itself. The secondary mirror is flat and is also off-axis with an angle of 0°85. Both, M3 and M4, are inside a vacuum tube.

Outgoing the vacuum tube in the light propagation direction, the first optical system is the Polarimetric Calibration Unit (PCU) that enters the optical path when polarimetric calibration is needed. Next is the Kiepenheuer Adaptive Optics System (KAOS; von der Luehe et al., 2002). An adaptive optics system (AO) looks for alleviating the effect of the turbulence of the Earth's atmosphere. Its optical setup begins with three folding mirrors (M5, M6, M7) with an angle of 45°. Then, there is a collimator (M8, off-axis by 1°5) and the tip-tilt mirror (M9), with an angle of incidence of 3°. This mirror has three actuators that allow the correction of global movements of the FOV. The next mirror is M10 with an angle of incidence of 3°. This is a deformable mirror that compensates in real time the inhomogeneities in the wavefront due to the effect of the atmosphere. Following the optical path, there is M11, which is a dichroic mirror (3°), which splits the beam in two and adequately tilts in order to perform scans of a bi-dimensional area of the solar surface when using the long-slit spectrograph. A small fraction of the light beam goes to a Shack-Hartmann wave-front sensor that calculates the correction to be performed by the deformable mirror. Most of the light is reflected on the dichroic and continues its path to the instruments through the imaging mirror (M12) and the folding M13 mirror.

Following this system, there is the (secondary) focus of the telescope, F2, where the slit is placed. The light that does not go through the slit to the spectrograph is reflected and is used for three different slitjaw images: Ca II-H/K, continuum and Hα. When the TIP-II polarimeter is used, the modulator and the polarising beamsplitter are located behind the slit. In this observing mode, from this point and until the detector there are two beams for the same slit with orthogonal linear polarisation states. Mirrors M14, M15 and M16 form the predisperser, a classical low resolution spectrograph composed of a collimator, a reflective grating and a camera mirror. In our case we have substituted the grating by a flat mirror. This way, the predisperser assembly acts as a simple 1:1 re-imaging system in our setup. Following the predisperser, M17 sends the light to the predisperser mask that removes non desired orders and/or wavelengths. After the mask comes M18 that sends the beam to the Echelle spectrograph, with a collimator (M19) a refractive grating and a camera mirror (M20). Finally, the light is recorded on the detector.

The spectrograph (from the slit to the detector) can be rotated in order to orientate the slit on the solar surface as desired. In this work we have made emphasis on having the slit in such a

way that the it crosses the solar limb when observing at the limb. With this strategy we have the reference of where the limb is. Additionally, the position of the limb helps to determine the observing coordinates with a good precision. This is interesting since the transformation from the LOS magnitudes to the local reference frame (LRF) strongly depends on the accurate positioning of the data. In this sense, the telescope pointing has some uncertainties of few seconds of arc. However, more important is the fact that the AO allows moving the slit in a $\pm 60''$ area. This capability is interesting when observing the polar regions as the AO system needs a contrasted feature in the FOV (pore, facula, granulation —in good seeing conditions—) in order to be able to work properly. Thus, once AO is locked on structures near the pole, it allows some freedom to move the field of view on the entrance focal plane of the spectrograph and adequately centre our observational target on the slit.

The instruments available at the VTT are:

- *Triple Etalon SOlar Spectrometer/Visible Imaging Polarimeter* (TESOS/VIP; Tritschler et al., 2002): A tunable filtergraph formed by three Fabry-Pérot etalons in a telecentric configuration. In its original setup, it is a spectrometer with a spectral resolution $R = 300000$ at 5000 Å and covers the spectral range between 4500 Å and 7500 Å. There is a second configuration (VIP) with which full Stokes imaging polarimetry can be done. This instrument is located in an optical lab and requires the deviation of the beam after the M13 mirror.

- Echelle spectrograph: As explained above, this instrument is a classical long-slit high-resolution ($R > 750000$) spectrograph with a collimator, refractive grating and a re-imaging mirror. There are several different gratings in order to maximise the throughput of the system. In joint action with the low-resolution predisperser, three spectral regions can be observed simultaneously. There also exists the possibility to observe only with the predisperser, covering a wider spectral range with lower spectral resolution.

- *Laser Absolute Reference Spectrograph* (LARS; Doerr, 2015): This is an instrument designed to achieve high signal-to-noise ratio and a very accurate wavelength calibration. It uses the Echelle spectrograph fed with an optical fiber, illuminated with a $3''$ region on the Sun. The precision in the wavelength calibration is reached by means of a laser frequency comb.

- *HELioseismic Large Region Interferometric Device* (HELLRIDE; Staiger, 2012): This is a Fabry-Pérot spectrometer focused on the measurement of Doppler shifts of many solar lines in quasi-simultaneous mode. This is done with two etalons and a matrix of 16 filters. As TESOS/VIP, this instrument does not use the spectrograph and the beam is deviated before reaching it.

- TIP-II: It uses the Echelle spectrograph and adds IR polarimetric capabilities with a polarimeter and an infrared detector. This instrument was moved to the GREGOR telescope during the 2014 season. Since this is the main instrument used in this work, we describe it in more detail below.

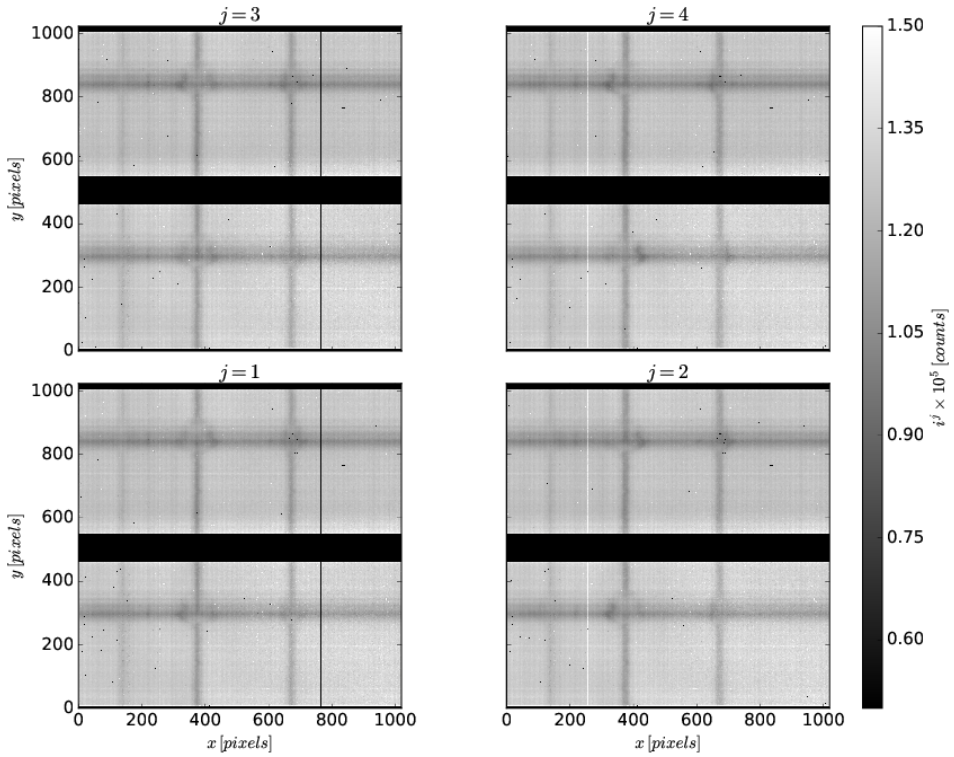

FIGURE 2.4— Example of modulated images observed with TIP-II. Dark current has been subtracted and Flat-field correction has been applied. Wavelength direction is in the x direction and position on the slit in the y direction. Each image has two intensity beams of the same slit position due to the dual beam configuration of the instrument. The demodulation has not been applied and the four images refer to each intensity measurement of the modulation scheme. It is worth noticing the presence/absence, in $j = 2$ or $j = 4$ of each sigma component of the transition that forms the spectral line around the 390 column. In the upper beam, for $j = 4$ ($j = 2$) the absorption is observed in the blue (red) sigma component while at the lower beam the red (blue) one is absorbed. This is so because each sigma component carries information about orthogonal polarisation states, and hence the polarised beamsplitter clearly separates these two.

2.2.2 TIP-II

TIP-II is a polarimeter designed and assembled at the Instituto de Astrofísica de Canarias. It has two optical systems, the polarimeter and the infrared detector (inside a cryostat). The latter is located after the spectrograph and the polarimeter is just after the slit. The polarimeter has two ferroelectric crystals and a beamsplitter. The ferroelectric crystals act as retarders and are used to modulate the light in four different linear combinations of the Stokes parameters (Collados et al., 2007) at each slit position. Changing the voltage applied to each of the crystals, the

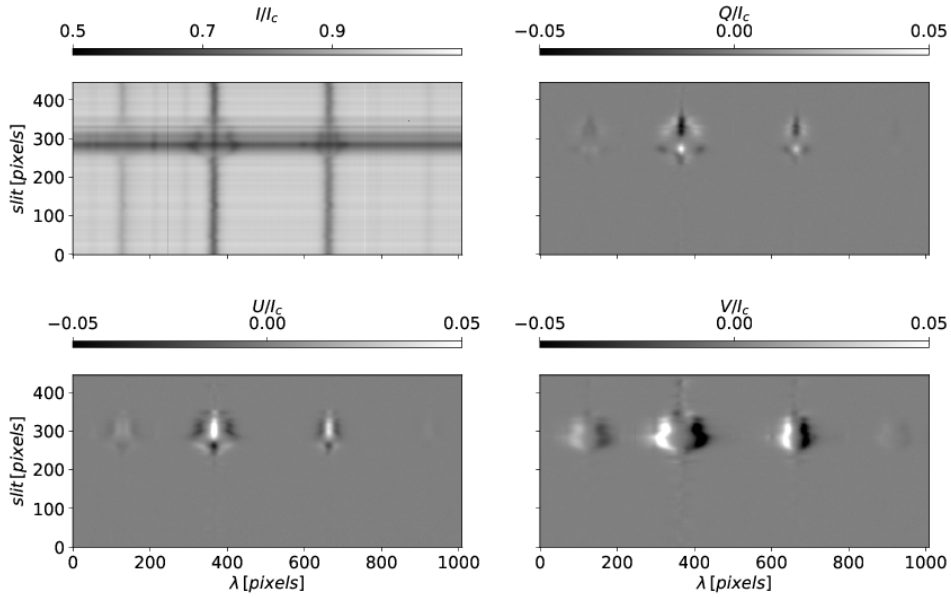

FIGURE 2.5— Stokes spectral images for the modulated images shown in Fig. 2.4.

fast axis is changed between two given positions and the modulation of the light is performed. The beamsplitter is used in order to analyse the light and to separate the beam in orthogonal polarisation states. The use of two beams is convenient at ground-based observations since it permits reducing the cross-talk between Stokes parameters due to seeing-induced intensity fluctuations (Collados, 1999), which can be of the order of the polarisation signals.

For each slit position the acquisition of the data is done with four sequential images. Each of these corresponds to the intensity measured with a different linear combination of the Stokes parameters. Figure 2.4 shows the four dual-beam intensity images for a slit position with TIP-II. The combination of these images allows recovering the four Stokes profiles for each slit position, what is referred to as the demodulation of the data.

The demodulation process is the method needed to go from images given by the modulator (linear combination of Stokes parameters) to the Stokes parameters themselves. Ideally, this method would consist on the inversion of the modulation that is introduced by the modulator. However, most of the telescopes were not designed for polarimetric observations and hence they have many optical devices that actually introduce spurious polarisation signals. In order to remove this instrumental polarisation, the demodulation process consists of two steps. In the first one, the polarimetric calibration unit is used to know how all the successive optical devices

behave polarimetrically. For the optical devices preceding the polarimetric calibration unit, a theoretical model is often used. It is so because the optical devices before the polarimetric calibration unit are usually big enough to make impossible a calibration on a daily basis. Hence, a telescope model is developed and tested in telescope calibration days. Once both steps are combined, it is possible to retrieve from the measurement of the various modulated images the Stokes parameters of the light reaching the telescope (see for instance Fig. 2.5).

2.2.3 Data reduction

Most instrument developers supply software in order to process raw data to ready-to-analyse data products. This software tackles the dark current subtraction, the flat-fielding correction, the bad-pixels correction and the demodulation of the data. The result of running these routines shows, however, some features that have to be considered before proceeding with the data analysis.

The first step is to refer all the datasets to a common continuum intensity. In particular, to the continuum intensity at disc centre. To do so, we take advantage of the observation strategy in which each dataset taken was preceded and followed by a flat-field measurement. Hence, this allows refering all the datasets to disc centre intensity and as well as removing intensity variations as the Sun moves on the sky.

A second additional reduction step requires a modification of the supplied standard routines. After the demodulation process there is typically a residual cross-talk between the different Stokes parameters. The correction process is detailed in Schlichenmaier & Collados (2002). Here we give a very brief summary and highlight where the changes are performed. The cross-talk from Stokes I to Q, U and V is estimated from the non-zero continuum value of Q, U and V. The deviation of Stokes Q, U and V continuum from zero is assumed to come from Stokes I. Hence Stokes Q, U and V are corrected with as much Stokes I as needed to settle the polarimetric continuums at zero level.

In order to correct the cross-talk from Stokes V to Q and U, those pixels where the amplitude of Stokes V is larger than the amplitude of Q or U are used. For these pixels the least square coefficients of the fit of Stokes V to Q and U are calculated. The mean value of these coefficients is the cross-talk to be corrected for. To do so at each point Stokes Q (U) is subtracted of Stokes V times the V to Q (U) cross-talk coefficient. The modification involves the estimation of the cross-talk between Stokes Q, U and V. This change is necessary since spurious polarimetric signals at the limb can reduce the accuracy of the cross-talk coefficients. These spurious signals are due to the strong intensity variations that can be found close to the limb. Hence, big amplitude polarimetric signals can be produced entering the cross-talk coefficient determination. The implemented solution is to follow the same procedure as in the standard routine but performing these cross-talk coefficients calculation just inside the solar disc.

In a third step, we correct for residual intensity trends and fringes that persist after flat-fielding correction. The estimation of these fringes is done by means of a polynomial fit of the mean intensity profile of the flat-field ($\bar{I}$). However, the presence of spectral lines in $\bar{I}$ can, potentially,

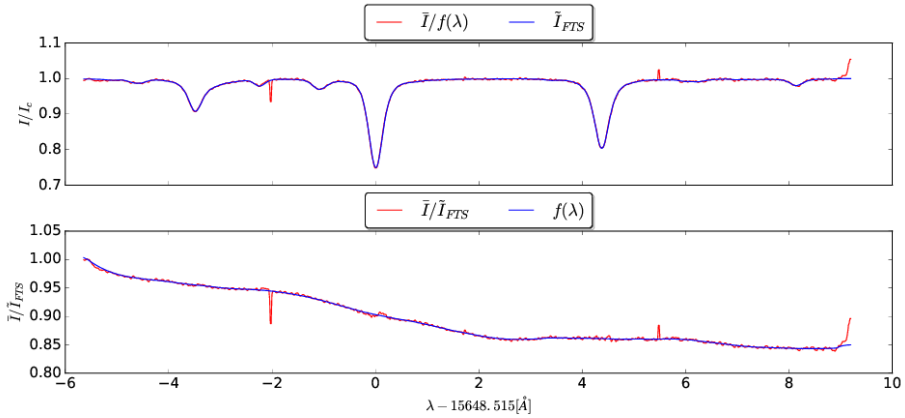

FIGURE 2.6— Top panel: comparison between the degraded FTS spectrum $\tilde{I}_{FTS}(\lambda)$ (blue) and the mean intensity profile observed $\bar{I}$ corrected for the continuum oscillations $f(\lambda)$ (red). Bottom: ratio between $\bar{I}$ and $\tilde{I}_{FTS}(\lambda)$ (red) and the fitted function $f(\lambda)$ (blue).

influence this fit. In order to remove the spectral lines, $\bar{I}$ is compared to the spectrum of a Fourier transform spectrometer (I_{FTS}, Livingston & Wallace 1991). This atlas is a very high signal to noise ratio spectrum with no significant spectral broadening, no spectral stray light and with very accurate continuum level. Following Allende Prieto et al. (2004), the I_{FTS} is modified to be comparable to our $\bar{I}$ as: $\tilde{I}_{FTS}(\lambda) = \alpha + (1-\alpha)\Gamma(\sigma) \star I_{FTS}(\lambda)$, where α is a white-light stray light factor and in order to take into account the different spectral resolution, $I_{FTS}(\lambda)$ is convolved with a gaussian $\Gamma(\sigma)$. The values of α and σ are unknown and have to be calculated. However, the values of α and σ depend on the proper determination of the intensity fringes. Simultaneously, the intensity fringes estimation depends on the subtraction of the spectral lines. In order to solve this problem an iterative method is followed:

1. We look for the best fit of the $\tilde{I}_{FTS}(\lambda)$ to $\bar{I}/f(\lambda)$. In this fitting procedure, α and σ are the free parameters. $f(\lambda)$ is a guess to the fluctuations of the continuum. In the first iteration, this $f(\lambda)$ is given by a linear fit to $\bar{I}$

2. We divide $\bar{I}$ by the $\tilde{I}_{FTS}(\lambda)$ recovered in the previous step. This gives an estimation of the intensity fringes without spectral lines

3. $\bar{I}/\tilde{I}_{FTS}(\lambda)$ is fitted with a polynomial of up to order 10. $f(\lambda)$ is set to the best fit of these polynomial functions (as deduced from the minimum χ^2)

4. This new estimation of $f(\lambda)$ feeds the new cycle. When convergence is achieved, $f(\lambda)$ contains the fluctuations to correct with.

The convergence is reached when the reduced χ^2 between $\bar{I}/f(\lambda)$ and $\tilde{I}_{FTS}(\lambda)$ is below 0.01 or more than 100 cycles have been performed. Figure 2.6 shows an example of the result. Upper panel compares $\bar{I}/f(\lambda)$ and $\tilde{I}_{FTS}(\lambda)$, red and blue, respectively. Lower panel depicts $\bar{I}/\tilde{I}_{FTS}(\lambda)$

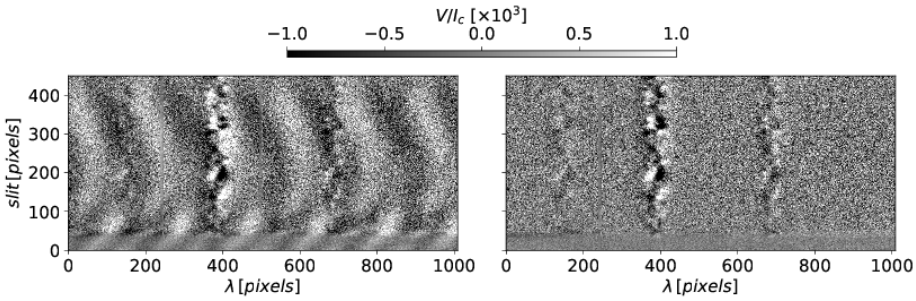

FIGURE 2.7— Stokes V spectral map for the slit position number 10 for a North polar region dataset before (left) and after removing polarimetric interference fringes (right).

and $f(\lambda)$ in red and blue colours, respectively. The correction $f(\lambda)$ is applied to each of the Stokes parameters. For the data analysed in Ch. 5 the values retrieved are: $\alpha \sim 5\%$ and $\sigma = 14$ mÅ.

It is possible to perform the wavelength calibration from the above-mentioned process. It is so because after the final fit, we can get the atlas wavelengths and hence, the wavelength calibration of the data. Since the atlas uses an absolute wavelength calibration, our wavelength calibration is also absolute.

In the reduced datasets some interferometric fringes persist (see left panel of Fig. 2.7). Their subtraction was performed individually for each Stokes Q, U and V parameters. Each spectra of each Stokes parameter of the dataset is fitted to a pair sinus/cosinus. In order to fit the interferometric fringes, several periods between 1 to 4 Å are proposed. This procedure must take into account the presence of polarimetric signals. To do so, wavelengths belonging to spectral lines signatures are avoided in the fitting. These spectral points are selected from the decreased intensity observed in the Stokes I spectrum as well as from the maximum Stokes Q, U and V signals observed. An example of this fringe subtraction is presented in the right panel of Fig. 2.7.

Another additional step performed previous to the analysis of the data consist in the application o a technique to the reduce the non correlated noise. This step is done using a principal component analysis (PCA, Loève, 1955). This technique decomposes a set of observations in an orthogonal basis of vectors. In this basis, the first eigenvector gathers most of the variance of the data. The next vectors are built following the same strategy but with an additional constraint. Each new eigenvector must be orthonormal to the previous vectors of the basis. This basis is able to collect most of the correlated variance in the first few eigenvectors. This technique can be applied to spectropolarimetric data in order to reduce uncorrelated noise of the profiles (Martínez González et al., 2008). To do so we get the PCA decomposition of each dataset, and recover the Stokes profiles with the first 40 eigenvectors for each Stokes parameter. This number is larger than the usual number of profiles used when using PCA decomposition (Ruiz Cobo & Asensio Ramos, 2013; Quintero Noda et al., 2015). The selection of this number is done

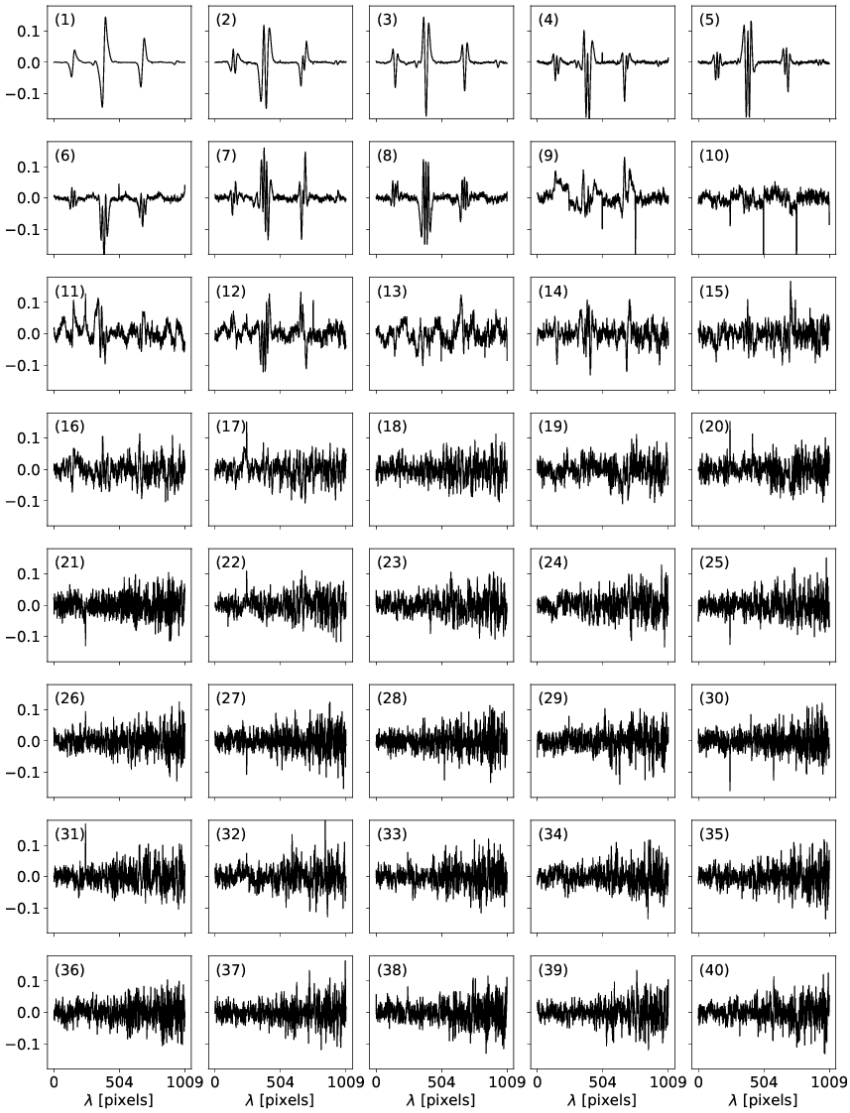

FIGURE 2.8— Set of the first forty eigenvectors of Stokes V for North polar region dataset taken on 14th September 2013. The number of the eigenvector runs from 1 to 40 from left to right and from top to bottom.

so that we ensure that most of the information encoded in the profiles is preserved even at the expanse of preserving also some amount of noise. To do so we look at the eigenvalues maps until noisy maps are recovered. Figure 2.8 shows the first 40 eigenvectors of stokes V for one of the TIP-II datasets analysed in Sec. 5.4. The first eigenvector (leftmost and uppermost panel) has a typical Stokes V profile and a very flat continuum. The second eigenvector (uppermost panel of the second column) has a typical linear polarisation profile or, the derivative of the former. The same applies to the rest of the eigenvectors. This is suggestive of a Taylor series expansion, though the interpretation of eigenvectors in terms of physical quantities is not always straightforward (Skumanich & López Ariste, 2002)

2.3 Solar poles magnetism: high spatial resolution observations

The third objective we address in this thesis is the analysis of a significant fraction of the solar polar cap at high spatial resolution. This objective can not be reached with any of the previously described observations. On the one hand, HMI covers the whole polar areas but the spatial resolution and polarimetric sensitivity is not high enough to fulfil this objective. In the other hand, TIP-II data from VTT exhibit the highest magnetic sensitivity but lacks the spatial resolution and spatial coverage. In contrast, these requirements can be reached with the CRISP instrument at SST, at the expense of a lower magnetic sensitivity than at IR wavelengths. In particular the FeI line at 6173 Å is an excellent candidate due to its continuum devoid of blended lines and its high magnetic sensitivity (its Landé factor is 2.5).

2.3.1 The Solar Swedish Telescope

The SST is a 1-meter telescope located in the *Observatorio Roque de los Muchachos*, La Palma (Spain). It was built in 2002 and it is operated by the Institute for Solar Physics of the *Royal Swedish Academy of Sciences*. The sketch of the telescope is presented in Fig. 2.9. The first optical device is an optical lens (L1) with two main objectives: 1- it is the imaging element of the system and 2- it is the entrance window to the vacuum tube. This lens is followed by two flat mirrors (M1, M2) with an incidence angle of 45°. In contrast to the coelostat of the VTT, these two mirrors are placed in an altazimuth mount. Due to this setup, a rotation of the image of the Sun is introduced by the system when compensating for the Sun's movement on the sky. The beam is focused at the bottom of the tube (BT), where a full disc image is formed. This image is used as a second order pointing system, after a theoretical estimation of where the Sun should be given the date, hour and location of the telescope. There is a small mirror in this focal plane that selects the FOV and sends this light to a chromatic corrector (SC). This correction compensates for the different focal length of the lens (L1) with wavelength. This light is then sent to the optical bench. The first two optical elements in the optical bench are two mirrors. Their purpose is to compensate the movements and the inhomogeneities of the incoming front wave due to atmospheric disturbances. First, a flat mirror (TT) with three actuators compensates for the FOV's global movements. Second, a deformable mirror (DM) compensates for high order seeing effects. Depending on their orientation, these two elements also select the instrument to be used:

- *TRI-Port Polarimetric Echelle-Littrow* (TRIPPEL Kiselman et al., 2011): It is a Littrow

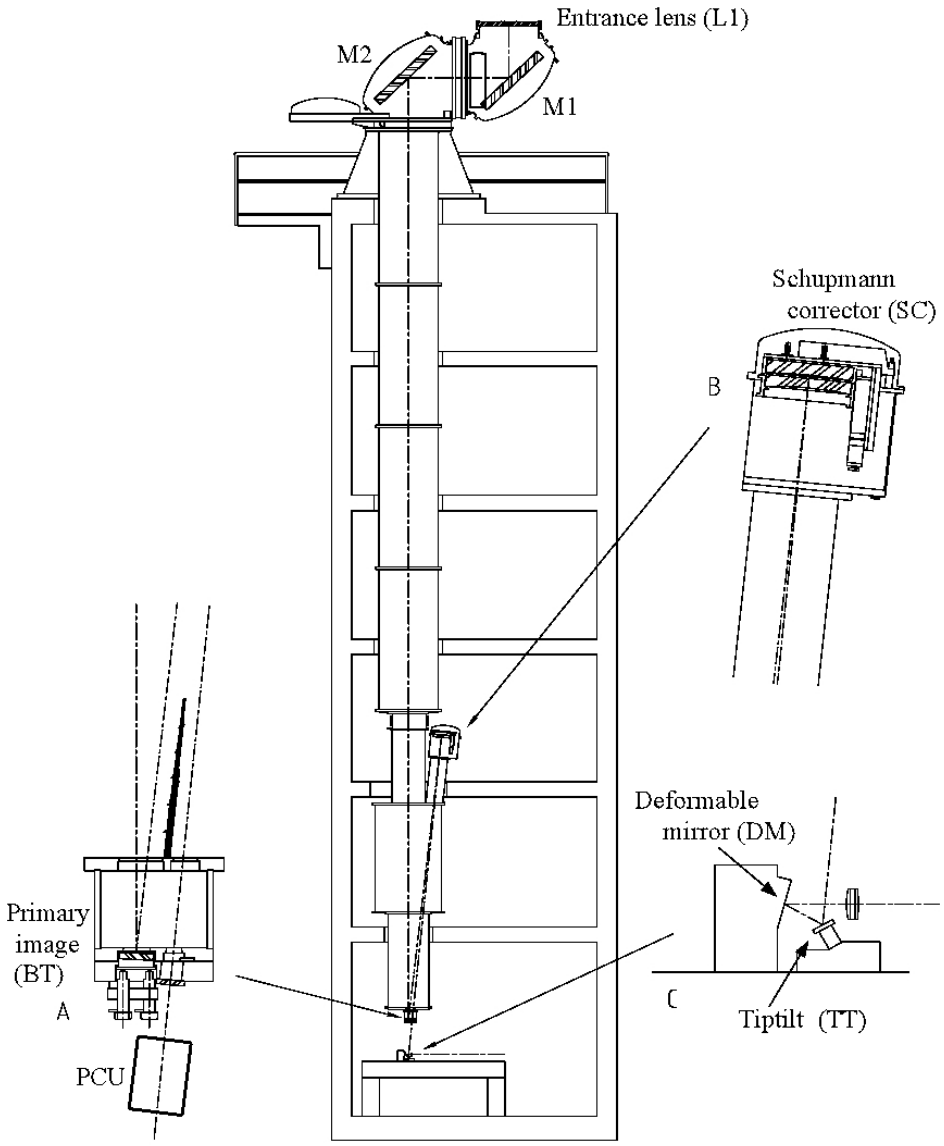

FIGURE 2.9— Drawing of the optical layout of the SST telescope up to the AO system. Image slightly modified from that courtesy of *The Institute for Solar Physics of the Royal Swedish Academy of Sciences* `http://www.isf.astro.su.se/NatureNov2002/Telescope_Full.html`.

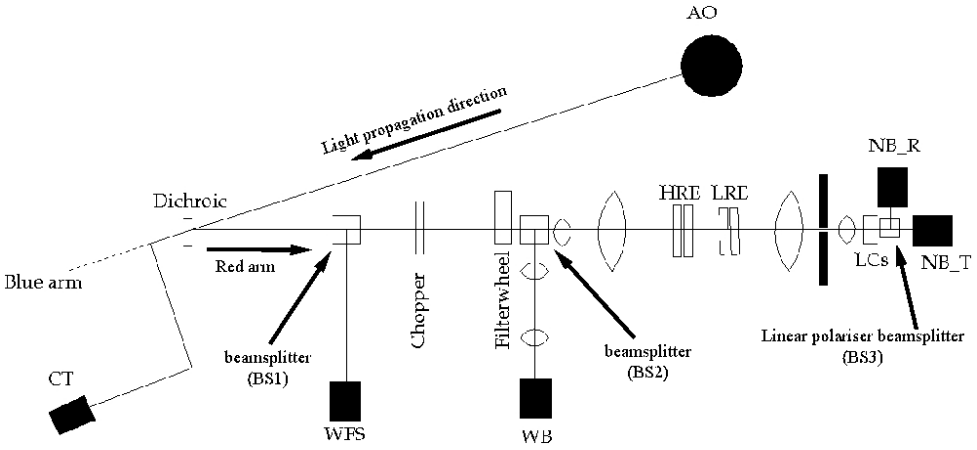

FIGURE 2.10— Sketch of the optical layout of the SST optical bench. Image slightly modified from that courtesy of *The Institute for Solar Physics of the Royal Swedish Academy of Sciences*. `http://dubshen.astro.su.se/wiki/index.php?title=CRISP`.

spectrograph specially designed to allow simultaneous observations at three separate wavelengths with a spectral resolution of $R \sim 200000$. It covers a wavelength range between 3800 Å and 11000 Å and at the moment it has no polarimetric capabilities.

- *CRisp Imaging SpectroPolarimeter* (CRISP Scharmer, 2006): It is an imaging spectropolarimeter with two telecentric etalons for wavelength tuning. Its working spectral range covers from 5100 Å to 8600 Å. This instrument is described in more detail below, given that it is the one that has been used to acquire data for this work.
- *CHROMospheric Imaging Spectrometer* (CHROMIS): This instrument is also an imaging spectropolarimeter with two telecentric etalons for wavelength tuning. It is designed to work at blue wavelengths (380-500 nm). It can work simultaneously with CRISP.

2.3.2 CRISP

The optical layout of this instrument is depicted in Fig. 2.10. After the AO system mirrors, the light is sent to a dichroic that splits the beam in two, depending on the wavelength. The dichroic reflects the red light to the CRISP instrument and the blue light (in our setup) is used by an imaging system to estimate the global shift corrections: Correlation Tracker (CT on the figure). The red light, once reflected by the dichroic, is split again (BS1), sending a fraction of the light to a wavefront sensor (WFS on the figure) and the rest is transmitted to the following devices. The wavefront sensor is a Shack-Hartmann with 85 subapertures. This system estimates and sends the corrections to the deformable mirror (AO). In addition, it allows moving the locking point of the AO in order to reach the targets of interest.

The next element in the light path to the instrument is the chopper. This is a rotating plate with holes that rotates synchronised with the exposure and read-out of the detector. The standard

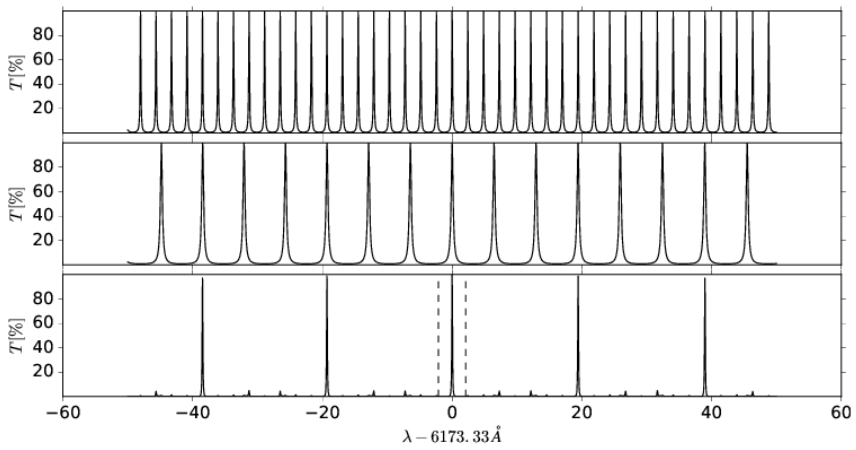

FIGURE 2.11— Separate contribution to the wavelength dependence transmission profile of the CRISP instrument. Top panel: transmission profile of the HRE, notice that they are thiner but their period is also shorter. Middle: transmission profile of the LRE. Its main goal is to avoid the contribution of HRE peaks close to the chosen one. Bottom: joint transmission of the two etalons. In vertical dashed lines, the FWHM of the prefilter is highlighted. Transmissions are theoretical, and given in percentage.

exposure time is 18 ms, with a readout time of 15 ms. The chopper rotates with a speed that ensures no illumination of the detectors while reading. The chopper is followed by a broadband filter with a transmission passband (filterwheel on the figure), depending on the spectral line selected, varying from 0.3 nm to 0.9 nm. This element is responsible for eliminating undesired transmission peaks of the instrument. After this filterwheel, a beamsplitter (BS2) reflects a fraction of the light to a broadband camera (WB). The images from this camera are used by the Multi-Object Multi-Frame Blind-Deconvolution code (MOMFBD; van Noort et al., 2005) together with the narrowband images to estimate the blurring induced by seeing and correct for it.

The light that is transmitted by the beamsplitter (BS2) is sent to two etalons (HRE and LRE on the figure) enclosed in a thermally controlled environment. These two etalons are responsible for the selection of the quasi-monochromatic wavelength observed. Figure 2.11 shows the transmission profile of this system. The first etalon is the High Resolution etalon (HRE) that selects a very narrow spectral range (ideally monochromatic, upper panel in Fig. 2.11). As an interferometric device, given the separation between the two reflecting surfaces of the etalon, there are a huge number of wavelengths transmitted. In order to eliminate the nearest undesired peaks, there is a second etalon whose transmission profile is shown in the middle panel of Fig. 2.11. The combined transmission profile is presented in the bottom panel of Fig. 2.11. Though the combined action of both etalons reduces the number of transmitted wavelegths, there are yet periodic transmission peaks at undesired wavelengths. The selection of a single transmission peak is performed by the prefilter located previous to the etalons in the optical path (see Fig. 2.10). The transmitted beam presents a wavelength dependent transmission profile with a

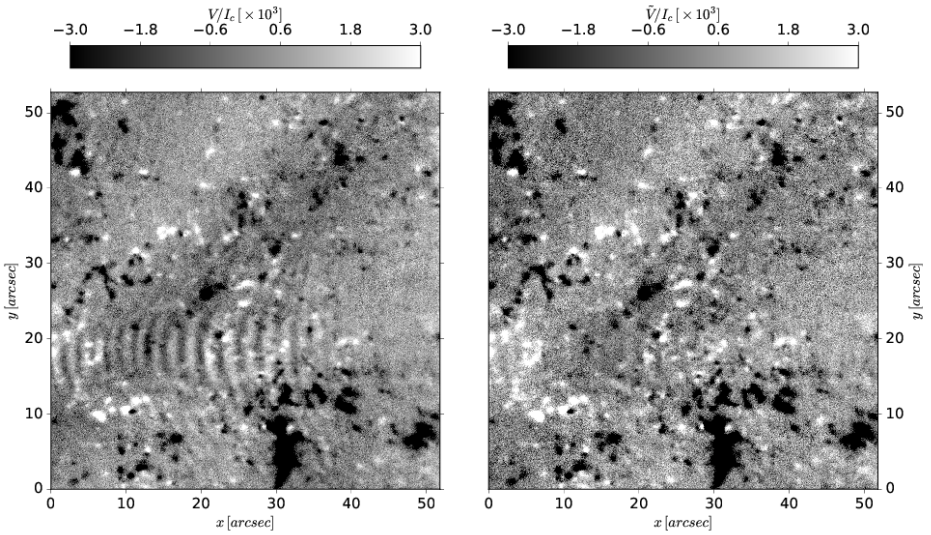

FIGURE 2.12— Left: monochromatic Stokes V image at $-100m\AA$ for the 07:19 scan acquired the 19th August 2015 for the Fe I Å spectral line using the method described on the text. Right: The same image after the fringe correction. Residual short frequency fringes still remain after fringe correction.

full-width at half-maximum (FWHM) of 49.2 mÅ for the 6173 Å spectral line (shown in dashed vertical lines in the bottom panel in Fig. 2.11).

Finally, just in front of the detectors, there are two more elements: 1- the liquid crystals that modulate the incoming light in order to measure the Stokes parameters and 2- a polarising beam-splitter splits the light into two orthogonal linearly polarised beams that are sent to two different narrowband cameras. This observation setup is designed to reduce the seeing induced cross-talk.

This instrument is a tunable imager and hence, each image is a monochromatic image of a two dimensional area of the solar surface. The various measurements along the spectral line profile are achieved in a sequential manner. In addition, as we are interested on polarimetric observations, at each wavelength position four linear combinations of the Stokes parameters are taken. Once these four images are recorded at a wavelength position the etalon separation is changed shifting in wavelength the transmission peak to the next wavelength position. This way, it is possible to get the four linear combinations of the Stokes parameters for a set of chosen wavelengths covering the spectral line of interest. The step from handling linear combinations of Stokes parameters to get the Stokes parameters independently is done by means of the demodulation process (see last paragraph of Sec. 2.2.2).

2.3.3 Data reduction

The reduction of CRISP data was carried out using the CRISPRED pipeline (de la Cruz Rodríguez et al., 2015). This software takes into account the dark current subtraction, flat-field correction and demodulation process. CRISP data is usually handled using the MOMFBD code, that reduces the Earth-atmosphere effect on the data. However, since we are interested on looking for very weak polarisation signals and MOMFBD increases the noise, we avoid this step in the reduction of our data. The alternative step taken is a de-stretching method kindly implemented by de la Cruz Rodríguez. Another step of the standard reduction is to take into account the non flat transmission profile of the prefilter. Standard reduction also deals with small imperfections of the reflecting surfaces of the etalons, which are translated in a wavelength offset that are field dependent. This is taken into account with the so called cavity maps. These maps are a product of the standard reduction routines that carry the wavelength offset for each pixel of the FOV. Yet, a final inspection of the reduced data showed some residual artifacts that require to be corrected.

The first one is the presence of polarimetric interference fringes. These fringes are seen in the individual monochromatic images (see for instance left image of Fig. 2.12). The shape of these fringes is different for each polarimetric Stokes parameter but are not wavelength dependent.

For their correction, for each polarimetric Stokes parameter, the continuum monochromatic image is used to build a "fringe-map". This "fringe-map" is used to correct the other wavelength images of the spectral line. At the continuum there are no solar polarisation signatures and the identification of the fringes is easier and more accurate. In order to build this "fringe-map", the Fourier transform of the bi-dimensional monochromatic image at the continuum is used. After the transformation, the coefficients associated to those fringes clearly stand out above the rest of the frequencies. Thus, filtering those frequencies make it possible to build a "fringe-map" for each Stokes parameter.

Although the shape of the fringes for each polarimetric Stokes parameter is similar for the various monochromatic images taken to sample the spectral line, their amplitude varies. Interference fringes are then corrected using the previously built "fringe-map" of each polarimetric Stokes parameter times a wavelength-dependent factor. This factor is estimated by a least square fitting of the fringe map to each monochromatic image. This fitting avoids those pixels of the monochromatic images that show solar polarisation signatures. The criterion used to discriminate those pixels with polarimetric signals from those that not, is a one sigma criterion, where sigma is the standard deviation at the continuum. In this coefficient determination all the pixels whose spectral polarimetric parameter exhibits a maximum amplitude above 1 sigma are not considered. Fig. 2.12 shows an example of the fringe subtraction result in a monochromatic Stokes V image of the Fe I spectral line at disc centre. Though not completely removed, the presence of fringes is strongly alleviated.

Another feature to deal with is the cross-talk between the Stokes parameters. Two different approaches are followed to tackle this problem. On the one hand, the contribution from Stokes I to Stokes Q, U and V is estimated from the linear fit of Stokes I at continuum wavelengths with the Stokes Q, U, V at this same wavelength:

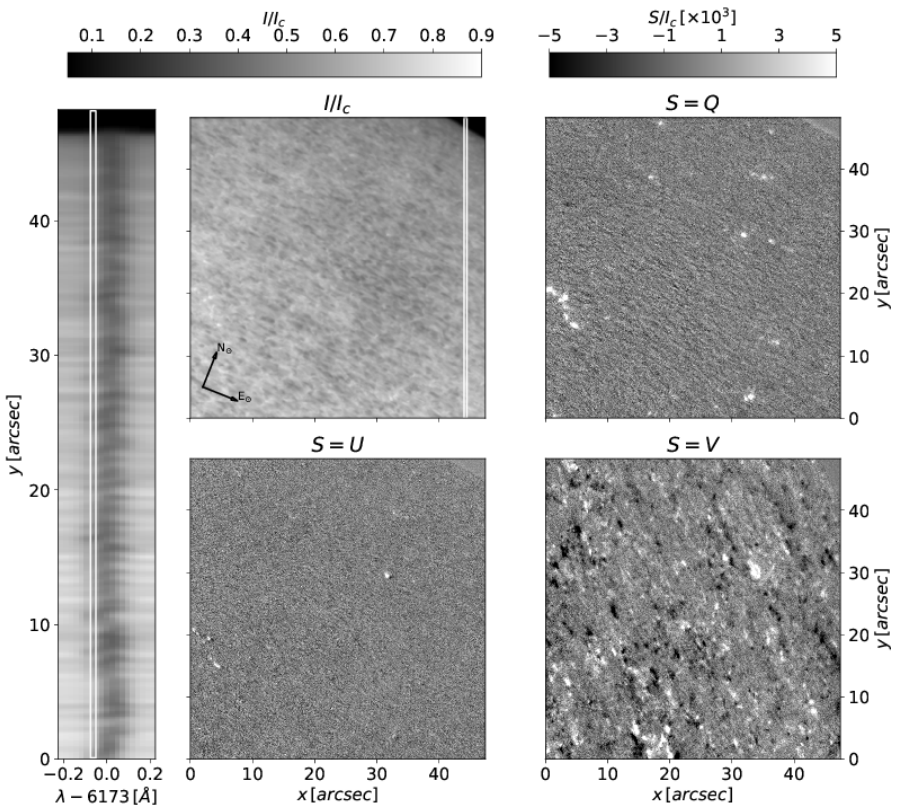

FIGURE 2.13— CRISP is a tunable filter that takes monochromatic images of bidimensional areas of the solar surface. The spectral information is recovered in a sequence of tuned monochromatic images. On the left, the 19 wavelength positions for a vertical cut along the x position at $44''.75$ (highlighted in the Stokes I image). The images on the right are the Stokes I (middle top), Q (right top), U (middle bottom) and V (right bottom) images for the wavelength $-75m\mathring{A}$ from the line core.

$$S_{cont}(x,y) = b_s\, I_{cont}(x,y); \qquad for\ S = Q,U,V. \tag{2.7}$$

The Stokes Q, U, V corrected from Stokes I cross-talk are:

$$S'(x,y,\lambda) = S(x,y,\lambda) - b_s\ I(x,y,\lambda); \qquad for\ S = Q,U,V. \tag{2.8}$$

On the other hand, the Stokes V to Stokes Q and Stokes V to Stokes U cross-talk correction is performed as described in Schlichenmaier & Collados (2002):

$$S'(\lambda) = S(\lambda) - d_s\ V(\lambda); \qquad for\ S = Q,U, \tag{2.9}$$

where d_s is calculated from those pixels that fulfil:

1. they exhibit solar polarisation signals. In this case, the maximum amplitude of the Stokes V profile must be above 3 sigma threshold

2. the maximum absolute amplitude of Stokes V is larger than 5 times the maximum absolute amplitude of Stokes Q (U)

These two requirements are fulfilled by a set of N pixels. For each pixel, a least-square fitting of Stokes V profile to Stokes Q (U) profile is performed. This gives a set of N (d_s^n $n = 0, N$) coefficients. The average value of this set of coefficients gives the cross-talk coefficient $d_s =< d_s^n >$ from Stokes V to Q (U).

The final reduction step handles with the continuum intensity reference for the various FOVs. The Sun moves on the sky as the observations are carried out. Hence there is an intensity variation due to the different intensity reaching the telescope. In contrast to the case with the VTT data (see first paragraph of Sec. 2.2.3), at the SST we do not have a flat-field before and after each scan. This time we use the various datasets taken, which spread over the polar region and East limb, to calculate the calibration factor. To do so we compare the centre-to-limb variation (CLV) of the observations with a synthetic CLV of the 6173 Å continuum. This allows the estimation of a time dependent factor, required to set all the observed FOVs to the same intensity reference. In order to avoid particular behaviours of each FOV, the time variation of this factor is fitted to a third order polynomial. This step ends with the various FOVs taken along the morning, settled to the intensity reference, given by the disc centre continuum.

Figure 2.13 shows the reduced data of a North pole dataset. On the left, the spectral image corresponding to Stokes I is shown. This spectral image comes from the column at $x = 44\farcs75$. The four monochromatic images at the right are the Stokes I, Q, U and V at the spectral position -75 mÅ from the line centre.

In Ch. 1 we mentioned the three research-lines pursued in this thesis in order to continue deepening the understanding of the magnetism at polar regions. Excluding data from HMI@SDO, which already offers physical properties of the Sun, the other instruments supply Stokes parameters profiles. Hence, it is necessary to infer physical parameters (such as temperature, velocity, magnetic field strength, ...) from the observed Stokes parameters. This step is itself a state of the art technique out of the scope of the thesis project. The next chapter gives a brief summary of this step to pass from Stokes profiles to physical magnitudes for our particular case. The reader is referred to specialised bibliography (see for instance del Toro Iniesta & Ruiz Cobo, 2016, and references therein) for a detailed treatment about the step from Stokes profiles to solar atmosphere physical properties.

3

From observations to physical properties

3.1 The radiative transfer equation (RTE)

Observationally driven, this thesis is based on the interpretation of the electromagnetic radiation (ER) coming from the Sun. As we have seen in Ch. 1, the ER from the Sun shows a spectral energy distribution (SED). The information of the various physical parameters is encoded in the SED, both in its shape as well as in the several spectral lines visible superimposed in it. These features encode information of the physical properties about the matter where the ER comes from. The radiative transfer characterises the interactions between the matter and ER and how physical properties of the former are imprinted on the latter.

Figure 3.1 shows a schematic representation of the general scenario through which the ER-matter interaction takes place. An ER beam (I) propagates and reaches a slab of matter characterised by some physical properties such as temperature, velocities, ... In this slab, of thickness d, ER interacts with matter. It is in this interaction that the physical properties of the slab can, potentially, leave an imprint on the ER. The ER outgoing from the slab (I$'$) depends on the incoming one (I), the losses that take place inside the slab and the sources to the ER in the direction of the outgoing beam. This picture is mathematically expressed by means of the RTE:

$$\frac{dI_\lambda}{ds} = -\kappa_\lambda I_\lambda + \epsilon_\lambda, \tag{3.1}$$

where I_λ is the spectral energy distribution, s is the geometrical path through the slab and κ_λ is the total opacity per unit length. Opacity times the radiation I_λ gives the absorption inside the slab. ϵ_λ is the emission inside the slab that contributes in the direction of propagation of I_λ and it is expressed in units of energy per unit surface, unit solid angle, unit wavelength interval, unit time, and unit length. Losses are given by absorption and scattering processes whilst emission, scattering in the direction considered and stimulated emission contribute positively to the energy outgoing from the slab.

It is convenient to express Eq. 3.1 in terms of the optical depth: $d\tau_\lambda = -\kappa_\lambda ds$ and then τ_λ is the number of mean free paths of light with wavelength λ of the layer ds. Introducing $S_\lambda = \epsilon_\lambda/\kappa_\lambda$,

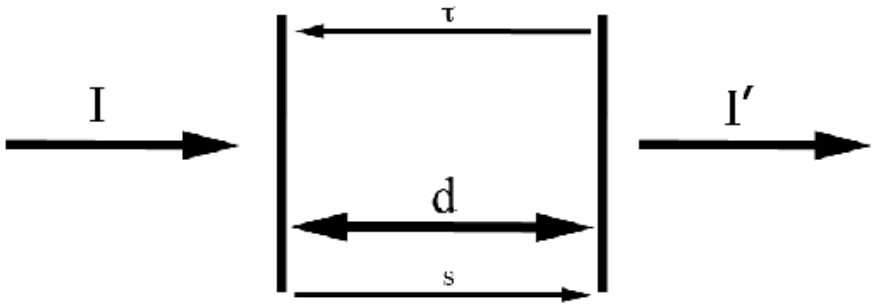

FIGURE 3.1— Schematic view of the matter-electromagnetic radiation interaction. An incoming ER beam I encounters a slab of material characterised by a set of physical quantities $T, v, B, \ldots$. Inside this slab of thickness d the incoming ER interacts with the material and is modified. The outgoing ER beam I' can potentially have some characteristic imprints that depend on the physical properties of the slab.

the source function, then S_λ is the specific intensity emitted in a mean free path and Eq. 3.1 can be rewritten:

$$\frac{dI_\lambda}{d\tau} = I_\lambda - S_\lambda. \tag{3.2}$$

As it was mentioned in Ch. 1, the density of the Sun decreases with increasing distance to its centre. When the density is low enough, the ER escapes from the Sun. This layer is the solar surface. Above it, there is the solar atmosphere, that plays a similar role to the slab in the previous example. Most of the physical imprints on the ER come from these layers, where the ER interacts for the last time with the solar atmosphere. Spectroscopy is the study of the spectral energy distribution and the spectral lines in it. This technique allows the inference of some physical properties of the solar atmosphere such as temperature or plasma velocity. However, to infer quantitative information of the magnetic field populating the Sun's atmosphere it is convenient to carry out spectropolarimetry, i.e. the study of the polarised spectrum.

3.1.1 RTE for polarised radiation

A useful property of the light when studying the magnetism is the polarisation of the light. From a classical point of view, ER behaves as a transversal electromagnetic wave propagating in a direction $\mathbf{\Omega}$ (as deduced from Maxwell equations, see for instance Born & Wolf, 1999). These waves are characterised by the oscillation of the electric and magnetic quantities on the plane perpendicular to $\mathbf{\Omega}$. These three vector magnitudes, electric and magnetic fields and $\mathbf{\Omega}$ form a right-handed orthogonal system. So, the description of any, electric or magnetic, field fully describes the ER wave. Let us define $\mathbf{e}$ a right-handed reference frame with $\hat{\mathbf{e}}_\mathbf{3}$ aligned with the propagation direction $\mathbf{\Omega}$ of the ER and $\hat{\mathbf{e}}_\mathbf{1}$ and $\hat{\mathbf{e}}_\mathbf{2}$ in the plane perpendicular to it (see Fig. 3.2). An electromagnetic wave can be described as the superposition of monochromatic plane waves of the form:

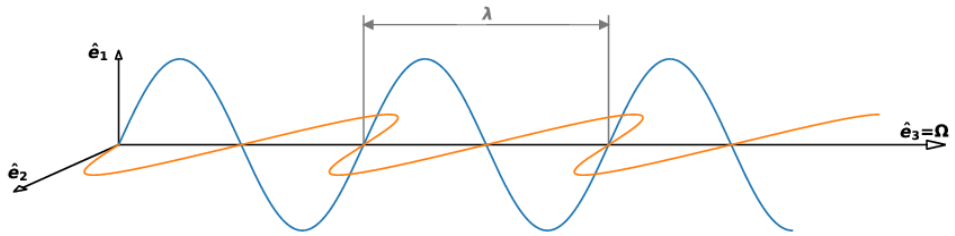

FIGURE 3.2— Sketch of the electric field component oscillation (in blue and orange) of a monochromatic wave with period λ, i.e. the wavelength. The oscillation of the electric field vector takes place in the plane defined by $\mathbf{e}_2$ and $\mathbf{e}_3$ to light beam propagation direction: $\mathbf{\Omega} \equiv \mathbf{e}_3$. $\mathbf{e}_1$ is the reference for the azimuth ϕ definition and, together with $\mathbf{e}_2$, forms a right-handed coordinated system .

$$\begin{aligned} \mathbf{E}_1(\mathbf{r}, \mathbf{\Omega}) &= a_1 e^{i(\phi_1 - \omega t + \mathbf{k}\cdot\mathbf{r})} \hat{\mathbf{e}}_1 \\ \mathbf{E}_2(\mathbf{r}, \mathbf{\Omega}) &= a_2 e^{i(\phi_2 - \omega t + \mathbf{k}\cdot\mathbf{r})} \hat{\mathbf{e}}_2, \end{aligned} \tag{3.3}$$

where $\mathbf{r}$ stands for a position vector in space. $a_{1,2}$ are the component amplitudes and $\phi_{1,2}$ their phases. ω is the angular frequency and $\mathbf{k}$ is the wavevector. Equations 3.3 describe the behaviour with time of the electric field for a given point in the plane perpendicular to the ER propagation direction $\mathbf{\Omega}$. Depending on the relations between a_1, a_2 and $\delta = \phi_1 - \phi_2$, the trajectory described by the electric field in the plane perpendicular to the propagation direction can be linear, circular or elliptical:

- If the phase difference δ is 0 or π, then the electric field at a given point in space describes a linear path with time. In this case, the ER is said to be linearly polarised.
- Another particular situation is when $a_1 = a_2$ and the phase difference is $\delta = \pi/2$ or $\delta = 3\pi/2$. In this case, the electric field vector describes a circle in time and the ER is said to be circularly polarised.
- In the most general case the amplitude relation and phase difference are different from the previous ones. Then the trajectory with time described on the plane perpendicular to the ER propagation at a given point is an ellipse.

In the Stokes formalism the polarisation state of the light is fully described with four parameters defined as:

$$\begin{aligned} P_0 &= a_1^2 + a_2^2 \\ P_1 &= a_1^2 - a_2^2 \\ P_2 &= 2\, a_1\, a_2\, \cos\delta \\ P_3 &= 2\, a_1\, a_2\, \sin\delta, \end{aligned} \tag{3.4}$$

where P_j are the so-called Stokes parameters. These are four parameters obtained with three variables, i.e. the four Stokes parameters are not independent. They fulfil the additional condition that $P_0^2 = P_1^2 + P_2^2 + P_3^2$.

When dealing with ER at visible or near infrared frequencies, many of these waves will be detected during a measurement and a time average (or the total of the total photon ensemble) is obtained. Hence, Eq: 3.4 is re-written as:

$$\begin{aligned} I &= < a_1^2 > + < a_2^2 > \\ Q &= < a_1^2 > - < a_2^2 > \\ U &= < 2\, a_1\, a_2\, \cos\delta > \\ V &= < 2\, a_1\, a_2\, \sin\delta >, \end{aligned} \tag{3.5}$$

where $< \ldots >$ stands for the ensemble average. In this situation, the relation between the four Stokes parameters becomes $I^2 - Q^2 - U^2 - V^2 \geq 0$. This expression can be re-written in order to define the polarisation degree of the ER: $p = \sqrt{Q^2 + U^2 + V^2}/I$. p takes values from 0 to 1 with 0 for completely unpolarised light (an example of this type is the natural light) and 1 for fully polarised light. The Stokes parameter I represents the total intensity of the light. Stokes Q and U are two parameters used to characterise the linear polarisation of the light. Stokes V is used to describe the circular polarisation. The combination of these three (Q, U and V) parameters allows the characterisation of any state of polarisation.

Positive Stokes Q is usually used to define the origin of azimuth's. Negative Stokes Q occur at an azimuth of 90°, positive Stokes U at 45° and negative Stokes U at 135°. Positive Stokes V (circular) polarisation is defined in clockwise direction from ER propagation direction, while the negative Stokes V is given in the counterclockwise. In short, the Stokes parameters for the description of polarised light can be expressed as:

$$\begin{aligned} I &= \updownarrow + \leftrightarrow \\ Q &= \updownarrow - \leftrightarrow \\ U &= \swarrow\!\!\nearrow - \nwarrow\!\!\searrow \\ V &= \circlearrowleft - \circlearrowright \end{aligned} \tag{3.6}$$

The usefulness of the polarisation when considering the magnetic field inference lies in the fact that magnetic fields are one of the few physical properties that can leave characteristic polarimetric signatures on the light.

It is possible to generalise the RTE (Eq: 3.2) to take into account the polarisation properties of the ER (see Landi Degl'Innocenti & Landolfi, 2004, for a detailed derivation and expression for each term):

$$\frac{d\,\mathbf{I}_\lambda^\dagger}{d\,\tau} = \bar{\boldsymbol{\kappa}}_\lambda \left(\mathbf{I}_\lambda^\dagger - \mathbf{S}_\lambda^\dagger\right), \tag{3.7}$$

where $\mathbf{I}_\lambda^\dagger$ is now a pseudo-vector of four parameters (I, Q, U, V), $\mathbf{S}_\lambda^\dagger$ is the source function (S_I, S_Q, S_U, S_V). $\bar{\boldsymbol{\kappa}}_\lambda$ is a four times four matrix called absorption matrix that polarimetrically

characterises the medium. The absorption terms are located in the diagonal and the dichroic and anomalous dispersion terms in the non-diagonal terms. The properties of this absorption matrix depend on the magnetic field regime. For the photospheric cases considered in this thesis, the observed polarisation signatures are generated in the Zeeman regime.

3.1.2 Zeeman-induced polarisation

In this regime, the atomic energy levels can be perturbed by the presence of a magnetic field. This perturbation leaves imprints on the polarisation of the light that can be used to infer quantitative information about the magnetic field.

In the absence of a magnetic field, the energy levels of an atom are characterised by their level N, their angular momentum L, their spin momentum S, and their total angular momentum J=L+S. According to the quantum theory, these magnitudes can only take discrete values, gathered in the quantum numbers n, l, s, and j, respectively. These quantum numbers define the electronic atom energy levels. Spectral lines are formed, either in emission or absorption, when an atom suffers an energy disturbance so that its energy changes in between two of these energy levels (see Fig. 3.3 for a sketch). These energy transitions are called bound-bound transitions and are governed by selection rules. For a radiative transition between a lower energy level (X_l) and an upper energy level (X_u), the selection rules in the electric dipole approximation are: $\Delta l = l_u - l_l = \pm 1$ and $\Delta j = j_u - j_l = 0, \pm 1$ with no transitions allowed between $j_u = j_l = 0$.

The energy levels are degenerated into $2j + 1$ sub-levels with the same energy. This degeneracy is broken in presence of a magnetic field. In such a scenario, each energy level splits in $2j + 1$ energy sub-levels characterised by the magnetic quantum number m. This number takes values from $-j$ to $+j$ in integer steps. The energy difference induced is related with the strength of the magnetic field and the atomic properties of the energy sublevel. Once split, the radiative energy transitions allowed are given by: $\Delta m = m_u - m_l = -1, 0, 1$ (which complement the selection rules above mentioned). Depending on the value of Δm the transitions between sublevels are classified in: σ_b (blue component) when $\Delta m = 1$, σ_r (red component) when $\Delta m = -1$ and π when $\Delta m = 0$ (see Fig. 3.3).

The splitting of the energy levels in different sub-levels due to the presence of magnetic fields depend on the strength of the latter. Depending on the field strength, there are different regimes such as Hanle, Zeeman or Paschen-Back regime. For the magnetic fields expected at the solar surface layers and the spectral lines studied in this thesis, the expected regime is the Zeeman one. In this regime, the induced energy difference between the various energies of each sublevel is:

$$\Delta E_m = h \frac{e_0 B}{4\pi m_e c} g\, m \qquad \forall m, \tag{3.8}$$

where h is the Planck constant, e_0 is the charge of an electron, B the magnetic field strength, m_e the mass of the electron and c the speed of light in vacuum. $m_{u,l}$ is the quantum number m of the sublevels involved in the transition and $g_{u,l}$ is the Landé factor of each energy sublevel:

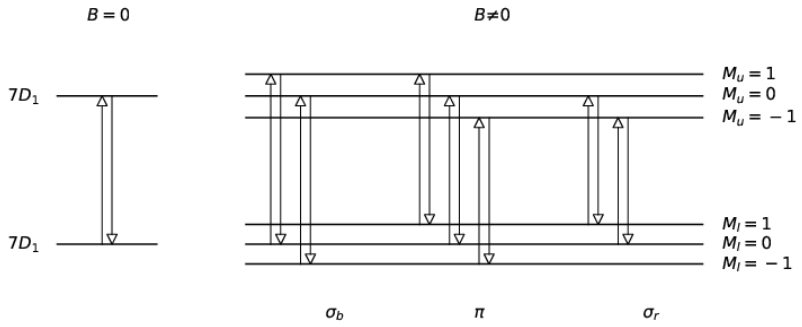

FIGURE 3.3— Schematic energy level situation for the Fe I 15648.515 Å line used in Ch. 5. Energy increases upwards. Left part is the case for the radiative transition without magnetic field and the case with a non-zero magnetic field is at the right part. The lower level is characterised by J=1 that gives rise to a degeneracy with 3 sublevels M=-1,0,1 (right). The upper level has J=1 and it is three times degenerated (M=-1,0,1, as seen on the right). The transitions at the right part are grouped according to the transition they belong to: σ_b, σ_r and π .

$$g = 1 + \frac{1}{2}\frac{J(J+1) + S(S+1) + L(L+1)}{J(J+1)} \tag{3.9}$$

The allowed transitions between the various energy sublevels that appear in presence of a magnetic field takes place for a slightly different wavelength, depending on the atomic properties of each sublevel:

$$\Delta\lambda_{m_u,m_l} = \frac{\lambda_0^2 e_0 B}{4\pi m c^2}\left(g_l m_l - g_u m_u\right) \qquad \forall \Delta m = \pm 1, 0, \tag{3.10}$$

where λ_0 is the wavelength associated to the energy transition without magnetic field. The characterisation of the sensitivity of an atomic transition to the presence of magnetic fields is encoded in the effective Landé factor:

$$\bar{g} = \frac{1}{2}(g_u + g_l) + \frac{1}{4}(g_u - g_l)\left(j_u(j_u+1) - j_l(j_l+1)\right) \tag{3.11}$$

An interesting property of the Zeeman effect is that it is proportional to λ_0^2 (Eq. 3.10). Hence the longer the wavelength the more appropriate for the detection and study of weak fields. Since the temperature can also broaden spectral lines, the interesting quantity to measure the effect of magnetic fields is the ratio of the Zeeman splitting to the Doppler Broadening $\Delta\lambda_D = \frac{\lambda_0}{c}\sqrt{\frac{2k_B T}{m} + \xi^2}$. T is the temperature of the plasma, k_B is the Boltzmann constant, and ξ is the microturbulence velocity. This ratio is linear with wavelength and favours longer

wavelengths when studying weak magnetic fields. For instance, a spectral line at 15000 Å will present, for the same magnetic field strength and the same effective Landé factor for the transition, a three times larger wavelength splitting between the various components than exactly that same line at 5000 Å, making easier the magnetic field detection. This is the reason why we measure IR wavelengths to study the weakest magnetic signals.

3.2 From Stokes vector to physical properties

The set of equations (3.7) can be solved for the Stokes vector provided the stratification of the various physical parameters such as temperature, LOS velocity, ... However, we are interested in proceeding the other way around. We have the observations of various Stokes profiles and we want to infer physical properties about the medium the light comes from. This is called the inverse problem and, for the case of the RTE, there are some already developed codes available. In particular, we have chosen the Stokes Inversion based on Response functions code (Ruiz Cobo & del Toro Iniesta, 1992, SIR). This code is suitable for photospheric spectral lines since it implements an approximation that notably reduces the computational time at the same time that it solves the RTE. This approximation is called Local Thermodynamic Equilibrium (LTE). In this situation, the various populations of atoms and ionisation stages are given by the Saha and Boltzmann equations. In addition the source function is given by the Planck function (in Eq. 3.7 $S_\nu = (B_\nu(T), 0, 0, 0)^\dagger$).

Since the dependence of the physiscal parameters in the RTE is non-linear, the inverse problem has to be solved using numerical iterative methods. The code needs an initial model atmosphere in order to solve the RTE. Assuming hydrostatic equilibrium, the input parameters of the supplied model are the temperature, microturbulent velocity, LOS velocity, magnetic field vector (intensity, inclination and azimuth), and macroturbulent velocity. All of them but the latter are height-dependent. In addition, the synthesis of Stokes profiles can be done for two supplied atmospheres sharing the same resolution element and a factor (the filling factor) that establishes the relative weight of each atmosphere. Once the model is defined, this code solves the RTE for the polarised light under Zeeman-induced polarisation (Sec 3.1.1). It includes additional features such as the spectral Point Spread Function or the Stray Light profile. The former takes into account the transmission profile of the dispersive system. The latter is a Stokes profile that is added to the outgoing profiles of the RTE solution. It can be used to take into account wavelength dependent contributors.

The inversion module of the code uses a curve-fitting problem solver (for instance a Levenberg-Marquardt algorithm) to minimise a norm. This step looks for obtaining the set of model parameters that make the best fit of the model to the observations. The norm used by SIR is given by the reduced χ^2:

$$\chi^2 = \frac{1}{n} \sum_j \sum_{i=0,3} (I_{i,j}^{syn} - I_{i,j}^{obs})^2 \frac{\omega_i^2}{\sigma_i^2}, \tag{3.12}$$

where n is the number of free parameters, $I_{i,j}^{syn}$ and $I_{i,j}^{obs}$ are the synthetic and observed value for each wavelength (j) and Stokes parameter (i), ω_i allows different weights of the Stokes param-

TABLE 3.1— Atomic parameters of the various spectral lines used. *El* is the atomic element, *ion* is the ionisation state of the atom, λ is the wavelength air in rest and in angstrom of the transition, c is the correction to be applied to the Van der Waals collision coefficient Γ_6, *E* is the excitation potential of the lower level, *log(gf)* is the logarithm of the product between $g = 2J + 1$ and the oscillator strength f. Then, the terms of the lower and upper levels are included in the table. The last two columns are the Barklem velocity exponential α and the cross-section σ in units of cm^{-2}.

El	ion	λ	c	E	log(gf)	$^{2S+1}L_J\,(l)$	$^{2S+1}L_J\,(u)$	α	σ
-	-	Å	-	eV	-	-	-	-	cm^{-2}
Fe	I	15648.515	1.0	5.426	-0.669	$^7D_{1.0}$	$^7D_{1.0}$	0.229	2.744e-14
Fe	I	15652.874	1.0	6.246	-0.095	$^7D_{5.0}$	$^7k_{4.0}$	0.330	3.992e-14
Fe	I	6173.3356	1.0	2.223	-2.880	$^5P_{1.0}$	$^5D_{0.0}$	0.266	7.869e-15

eters and σ_i stands for the noise of each Stokes parameter. In the inversion process, the model atmosphere parameters are perturbed and the behaviour of the norm is studied. Solving the radiative transfer for all the heights and model parameters involved in the calculation requires to solve a huge parameter space. In order to tackle this problem, the inversion is done only at certain height positions, that are known as "nodes". The perturbed magnitudes are calculated to the rest of heights of the model by interpolation. The setup of the inversion is data dependent and it is analysed and justified in each of the studies we have performed.

An important constraint for the spectral line choice when dealing with magnetic field inference by means of the Zeeman effect is the sensitivity of the line to the magnetic field. This is an intrinsic property of each atomic transition that leads to the spectral line and is encoded in the Landé factor (see Eq. 3.11). As it has been mentioned, the sensitivity to Zeeman effect is enhanced when moving to long wavelengths. For this reason two IR FeI spectral lines have been considered. The central wavelength of these transitions are: 15648.515 Å and 15652.874 Å. These spectral lines have large Landé factors 3.0 and 1.52, respectively and are close to the longest wavelengths at which full spectropolarimetry is possible. Hence they are excellent candidates to study the magnetism by means of Zeeman effect, even for very weak fields.

These lines were observed with TIP-II polarimeter at the VTT. The setup allows a high polarimetric sensitivity with a limited spatial coverage. In addition, the spatial resolution decreases with wavelength, reaching close to $0\farcs56$ with this combination of telescope-instrument. In order to overcome these two issues, CRISP@SST polarimetric imager was also used. This combination of telescope-instrument allows covering a wider polar region area as well as an important increase of spatial resolution, of the order of $0\farcs12$. Of the available spectral lines at this facility, the FeI 6173 Å was chosen. This line has a high Landé factor (2.5) together with a clear surrounding continuum and no blends.

It is to be noticed that there is an intrinsic ambiguity in the description of the polarised light in the Zeeman induced polarisation. This ambiguity comes from the fact that the spectral signatures of a magnetic field at a LOS azimuth of α are exactly the same to that of a magnetic field with a LOS azimuth of $\alpha \pm 180°$. This ambiguity is an important issue to deal with when observ-

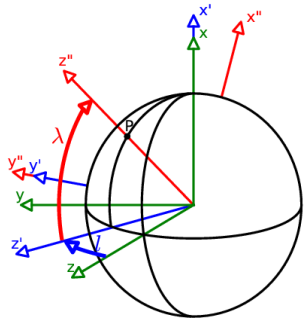

FIGURE 3.4— Sketch of the two rotations involved in the change from LOS to local reference frame. LOS reference frame S is depicted in green colour with z-axis toward the observer. First rotation (blue arrow) accounts for the longitude (l) rotation. This step defines an intermediate reference frame (S′) in which z′, the point observed and x′ are coplanar. Second rotation (red arrow) takes into account the latitude (λ) of the point and defining the local reference frame (S″) where the azimuth reference is preserved in the North solar direction and increasing eastwards.

ing far away from disc centre. It is so due to the additional fact that the inferred parameters (in particular, the magnetic field) are in the LOS reference frame. This reference system is not suitable to establish a comparison of the topologies of the magnetic fields at different regions of the solar disc. A more appropriate reference system is the LRF, i.e. referred to the vertical to the surface at each point of the solar disc.

3.3 From LOS to LRF

The step to transform the inferred parameters (magnetic field inclination and azimuth) from LOS to LRF is straightforward knowing the full magnetic vector in the LOS reference frame and the position of the pixel on the solar surface.

This change can be done with a single rotation of the heliocentric angle to the position of the pixel considered. Instead, it is worthy to proceed with two rotations in order to ensure that the azimuth reference is kept at the North solar direction and increasing eastwards. In Fig. 3.4 these two steps are sketched.

Previous to the first rotation, the magnetic field vector is transformed from a spherical coordinate system to a cartesian one (green reference frame in Fig. 3.4). This first system is defined with z-axis towards the observer, x-axis in the northward direction and y-axis eastwards. Then, the

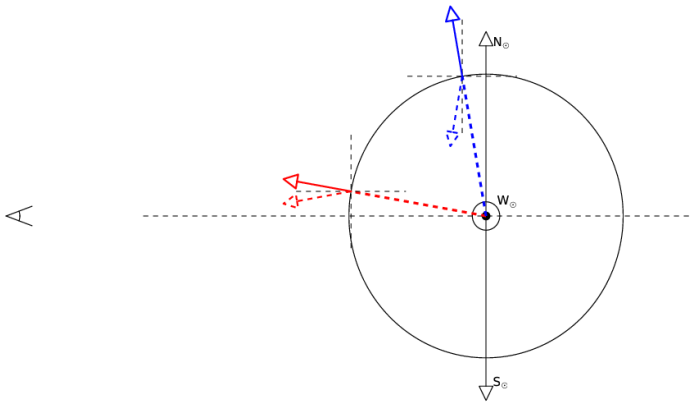

FIGURE 3.5— Simple case of the impact of the 180° LOS azimuth ambiguity when observing at high heliocentric angles, in particular close to the North limb. The observer is located at the left part of the image and the Sun is at the right. The North of the Sun is upwards, the South downwards and the West is pointing to the reader. In solid red, the case of an originally radial field is plotted. It is located at $l = 0°$ and $\lambda = 10°$. The magnetic configuration in dashed arrow is the other possible magnetic field as inferred from the other LOS azimuth due to the 180° LOS azimuth ambiguity. The same setup is used for the magnetic field close to the limb (blue arrows). Now, the disc position is $l = 0°$ and $\lambda = 80°$. .

system is rotated around the x-axis (green reference frame in Fig. 3.4) an angle given by the longitude of the point considered (P in the figure) moving the z-axis towards the y-axis (blue arrow in Fig. 3.4):

$$\mathbf{R_l} = \begin{pmatrix} 1 & 0 & 0 \\ 0 & \cos l & -\sin l \\ 0 & \sin l & \cos l \end{pmatrix}, \tag{3.13}$$

where $\mathbf{R_l}$ is the rotation matrix for a helioprojected longitude given by l. After this step z′ and x′ (blue reference frame in Fig. 3.4) are coplanar together with the point considered (P) (in a meridian plane). The next step is to rotate around y′ an angle equal to the helioprojected latitude of the point from z′ towards x′ (green arrow in Fig. 3.4):

$$\mathbf{R}_\lambda = \begin{pmatrix} \cos\lambda & 0 & \sin\lambda \\ 0 & 1 & 0 \\ -\sin\lambda & 0 & \cos\lambda \end{pmatrix}, \tag{3.14}$$

where λ is the helioprojected latitude of the point on the solar disc. The final step is to recover again the spherical coordinates of the magnetic field vector. Hence for every pixel of the FOV: $\vec{B}_{LRF} = \mathbf{R}_\lambda \, \mathbf{R_l} \, \vec{B}_{LOS}$.

As it has been mentioned, the LOS azimuth has intrinsically a 180° ambiguity. This means that it is not possible to distinguish between a magnetic field with an azimuth α from another magnetic field with $\alpha \pm 180°$ azimuth. Close to the limb, this ambiguity is critical as it can change the LRF polarity of the magnetic fields (see Fig. 3.5). For instance, let us consider a vertical to the surface magnetic field vector directed outwards from the Sun, i.e. positive polarity (in the figure, the solid blue and red arrows). We define the origin of the azimuth Northwards in the N-S direction and increasing Eastwards. A magnetic field seen at $l = 0°$ and $\lambda = 80°$ (blue arrow) would be characterised in the LOS reference frame by a LOS inclination of 80° and a 0° LOS azimuth (i.e. pointing northwards). However, due to the LOS azimuth ambiguity we can not know if the azimuth is 180° (blue dashed arrow) or 0° (blue solid arrow). On the one hand, the 180° value leads to a close to vertical field of negative polarity in the LRF. On the other hand, the 0° LOS azimuth leads to a vertical field of positive polarity. Notice the change in the polarity of the field depending on the LOS azimuth taken. This change does not take place close to disc centre (as for instance the red arrows). This field is located at $l = 0°$ and $\lambda = 10°$ and though the 180° LOS azimuth ambiguity modifies the topology it is not so extreme to even change the polarity of the magnetic field.

There are several methods developed to tackle this problem (e.g. see Metcalf et al., 2006). However, some of the first full spectropolarimetric studies at the polar region (Ito et al., 2010; Shiota et al., 2012) followed an alternative method. Because of the relevance of these works it is convenient to see first their method (as we will use it to compare our results with theirs) and then present the method we have applied.

Ito et al. (2010) and Shiota et al. (2012) solve the 180° ambiguity considering both possible LRF magnetic topologies (due to the two possible LOS azimuths). Then, each solution is classified as vertical, horizontal or undetermined for both azimuth solutions. Vertical fields are defined as: $|90 - \theta_{LRF}| \in [50°, 90°]$ in both cones, horizontal fields as: $|90 - \theta_{LRF}| \in [0°, 20°]$ and otherwise they are classified as undetermined. Now, depending on the classification of the two possibilities at each pixel, the choice for the final solution is performed following the relations:

Solution 1	Solution 2	Decision
vertical	vertical	the most vertical
vertical	undefined	the vertical one
vertical	horizontal	they are not considered in the analysis
horizontal	vertical	the horizontal one
horizontal	horizontal	it is not clear what is decided in this situation. We consider two possibilities: 1- These pixels are not analysed 2- The most horizontal solution is considered to be the real one
undefined	undefined	the pixels in this situation are not analysed

This method has some drawbacks. First, a particular configuration is imposed, where only close to vertical and close to horizontal configurations are allowed. Second, pixels classified as undetermined are not studied and can represent quite a large number. Finally, if the result is analysed statistically, it might seem to be more or less accurate, though the one by one magnetic field vector comparison show a more numerous misleading results. These three cases can be better

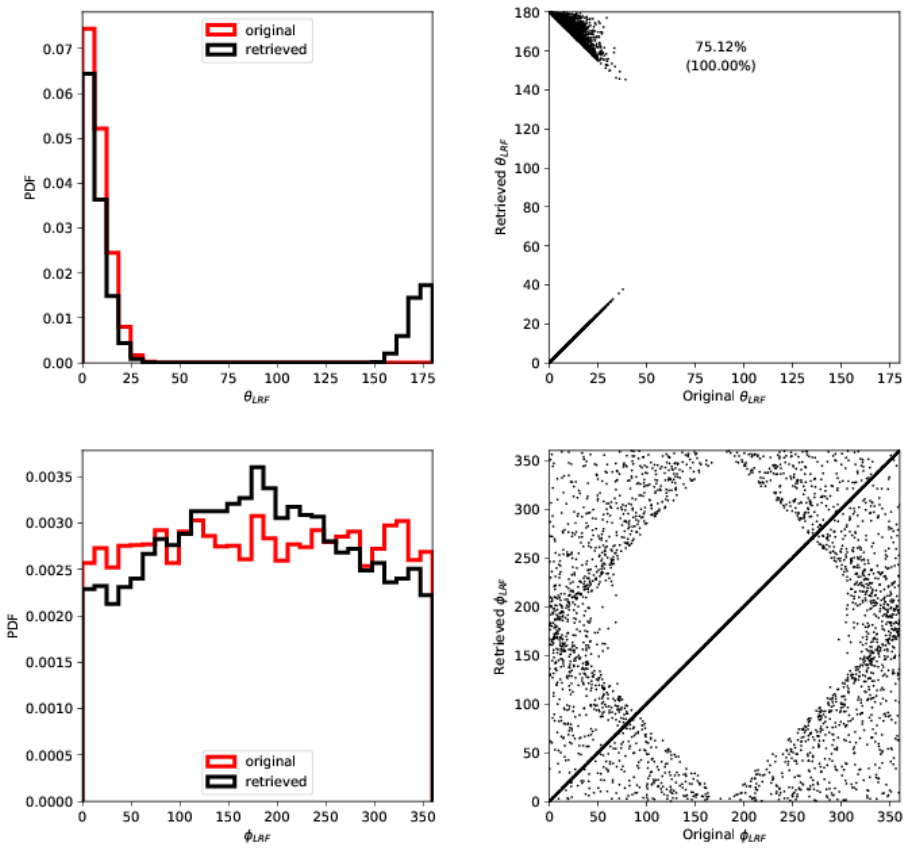

FIGURE 3.6— PDF retrieved (black) for a strongly vertical distribution (red) above $\lambda = 75°$. The original LRF inclination (top left panel) and LRF azimuth (bottom left) are shown in red. The black solid lines give the LRF topology retrieved following the same method as Ito et al. (2010); Shiota et al. (2012). The original LRF inclination (azimuth) is on the x axis of the right top (bottom) panels. The retrieved magnitude is on the y direction. The percentages on the top right panel are the fraction of pixels that retrieved the same configuration and in parenthesis the fraction of pixels for which a solution is not undetermined .

understood with the following tests.

We assume two different configurations for the LRF magnetic field topology. In the first one, we consider a strongly vertical distribution and homogeneous LRF azimuth (see red distributions of left hand panels of Fig. 3.6). In the second one, we consider a half-sinusoidal distribution for LRF inclinations and homogeneous LRF azimuths (same panels of Fig. 3.7). Now it is assumed that these distributions give the LRF magnetic field vectors for solar latitudes above $\lambda = 75°$. We transform the LRF magnetic field topology to the LOS configuration. Then, imposing the

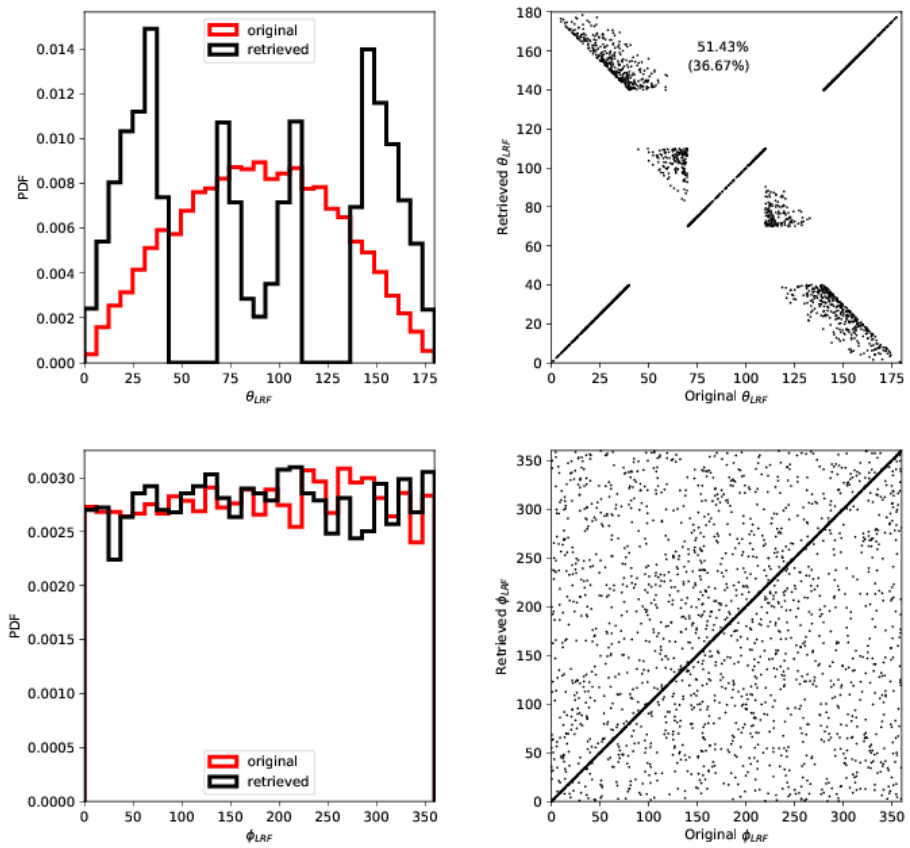

FIGURE 3.7— Same display environment as in Fig. 3.6 but now for an isotropic distribution, i.e. a magnetic field distribution given by a half-sinusoidal PDF for LRF inclinations and homogeneous LRF azimuth .

LOS 180° azimuth ambiguity, we go back to the LRF distributions the method recovers. Left panels of Figs. 3.6 and 3.7 show the original (black) and recovered (red) probability density functions (PDF) for the LRF inclinations (top) and azimuth (bottom). The right panels show the one to one comparison of the original LRF inclination (top) and azimuth (bottom) versus the recovered one.

For the vertical distribution (Fig. 3.6), it can be seen that the LRF inclination (top panels) that is recovered shows two behaviours. 75.60% of the pixels are properly recovered whilst the others are recovered with opposite polarity. The LRF azimuth (bottom panels) shows a similar distribution but with a preference for 180°, i.e. pointing southwards. With such a LRF distribution, there are no undetermined pixels.

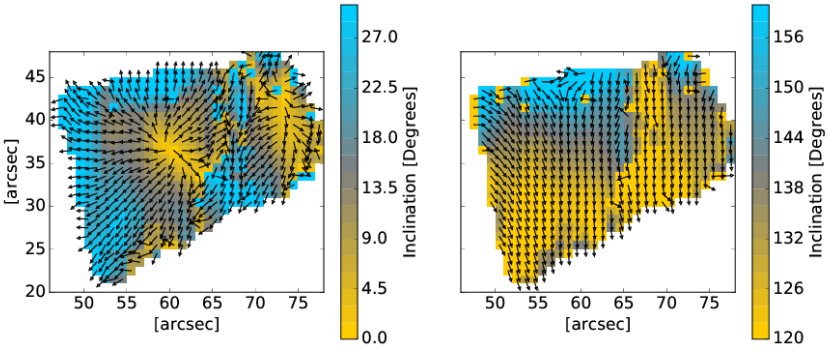

FIGURE 3.8— The two possible solutions retrieved with the numerical method that looks for spatial coherence. Color scale shows the LRF inclination and the arrows the LRF azimuth. The structure is taken from VTT observations (see Ch. 5).

The application of this method to solve the 180° ambiguity in an isotropic distribution is shown in Fig. 3.7. In this case the retrieved LRF topology overpopulates magnetic fields close to vertical and horizontal configurations. However, looking at the PDFs, though not perfectly, the result is not far from the original distribution (at least where the method recovers magnetic field orientations). This more or less statistical accuracy vanishes when the one-to-one comparison is considered (top right). It can be seen now that just half of the LRF inclinations are properly recovered, changing the polarity of the others. In addition, this configuration recovers just one third of the pixels, while the others are classified as undetermined. This low value for the magnetic fields recovered should be taken with caution. It is so because some of the undetermined cases come from those pixels whose both possible solutions for the 180° ambiguity are horizontals. Neither Ito et al. (2010) nor Shiota et al. (2012) specify the decision taken in such a situation. It is possible to follow a similar strategy as for the two vertical possible configurations (i.e. take the most vertical) and take the most horizontal possibility. In such a case, the number of pixels for which a magnetic configuration is retrieved increases to 50%. In addition, the dip close to 90° in the LRF inclination distribution retrieved is filled. Yet, of this 50% of pixels, the fraction for which the magnetic configuration is properly recovered holds at a 50%.

In this thesis we have followed an alternative method, which is similar to one followed by B. Lites (e.g. see Metcalf et al., 2006). Once the exchange from LOS to LRF is done, we have two possible local magnetic field configurations for each pixel of the FOV. Hence there are up to 2^N possible combinations, where N is the number of pixels to be disambiguated. In order to further constrain this number we additionally require that there must be some spatial coherence. To do so, we select those magnetic patches with magnetic field strengths above 1000 G. We run over all the pixels of each structure and we compare the two possible LRF configuration with its surrounding pixels. Then the azimuth that makes the LRF magnetic field most similar to the

surrounding LRF magnetic field vectors is chosen. For each structure, in this step two possible solutions for the whole structure are obtained. Then the threshold is decreased to 900 G and the same procedure is repeated. Those patches that were previously treated use the previous solution as seed. This method is repeated until a magnetic field strength threshold of 600 G is reached, for which we have detected that the uncertainties involved in the calculation (positioning, determination of magnetic parameters from inversion) make this method strongly unstable. Figure 3.8 shows the two possible magnetic field configurations retrieved with this method for a structure analysed in this thesis. Both recovered structures show spatial coherence in, the LRF inclination and LRF azimuth, and both are physically feasible. So, additional considerations are required in order to choose one, as it is done in Ch. 5 and 6.

In this chapter we have briefly seen how to extract quantitative information from the observed magnitudes. With this ability, it is possible to proceed with the analysis of magnetism at the polar regions.

4

The Sun's global magnetic field

At the beginning of the 20th Century, the first detection of magnetic signatures on the solar surface established the magnetic character of the Sun. This discovery was the initial building block of a complex solar magnetic landscape that has been set up in the successive years. The understanding of the global magnetic field behaviour as a whole is the objective of dynamo theories.

One of the most evident properties of the global magnetic field is its cyclic behaviour. This periodicity was observed well before the magnetic nature of the Sun was discovered. It was in 1842 when Schwabe proposed the existence of a solar cycle of 11 years: the sunspot cycle. This proposal was based on the observed cyclic variability of the number of sunspots present on the solar surface. During the cycle of 11 years, this parameter exhibits a minimum value in which the number of sunspots on the solar surface is the smallest (or even the surface can be devoid of these structures). This stage is followed by a rising phase, in which the number of sunspots shows a progressive increase leading to a maximum of activity, i.e. a time when the solar surface shows the highest number of sunspots in its surface. During the decreasing phase the number of sunspots is reduced again until a new minimum is reached, leading to a new cycle. The discovery of the magnetic character of sunspots settled the first feature of the global magnetic field.

However, if the magnetic polarity is taken into account, there exists another periodicity. This is referred to as the magnetic sunspot cycle, which takes into account the polarity of active regions. Hence, if the leading part of an active region is positive at a maximum, in the following maximum of the 11 year cycle is negative. This cycle period is then of 22 years, as it is necessary to have two maxima in the number of sunspots to recover the initial active region polarity configuration. This early work by Hale & Nicholson (1925) settled some additional global magnetic field features such as the Spörer's law or the Joy's law.

Regarding non-active region magnetism it was not until the middle fifties that magnetic signals outside these structures were found. Babcock & Babcock (1955) detected, for the first time, a faint magnetism at the solar poles. Interestingly, these signals were found to have opposite polarities at the North and South poles and were identified as the signature of the global dipole

of the Sun. The study of the temporal evolution of this polar magnetism (Babcock, 1959) revealed two very important results: First, he noticed that the strength of polar magnetic fields followed the activity cycle out of phase. The field strength at the poles is maximum when the activity cycle is at minimum. Second, and more important, is that he observed a reversal of the magnetic polarity in periods of activity maxima. This gives a cyclic behaviour with a period in agreement with that of the magnetic sunspot cycle: 22 years. This observational detection, together with the previously noticed in active regions, led to the proposal of the first dynamo theory (Babcock, 1961) that gathers together the observed properties of the global magnetic field at the activity belt and those at the polar regions.

Altogether, solar global magnetic field changes, at global scales, from a mostly poloidal configuration to mostly toroidal during the sunspot cycle. In epochs of very low magnetic activity, when the surface is devoid of active regions, the Sun's global magnetic field reminds a dipole. At maxima of activity, sunspots emerge at the activity belt in bipolar form, making the global structure more complex by introducing a strong toroidal component.

This globally coherent magnetic behaviour has been the subject of a long observational effort. Those studies that focused on the study of the magnetism at photospheric layers have been performed historically using magnetograms taken from ground-based facilities. For instance, Mount Wilson Solar Observatory (Seares, 1917) has been observing the Sun since early in the 20th Century. Another facility that has made important contributions is the Wilcox Solar Observatory (Hoeksema, 1991) that performs a long standing monitoring of the global magnetic field (since 1970s). In the last twenty years this effort has been extended to space-borne missions with the MDI instrument onboard SOHO satellite and its successor, the HMI onboard SDO. The former, though very fruitful in other photospheric magnetic studies, was not very suitable for the polar regions. The latter instrument offers some advantages to perform polar photospheric magnetic studies due to the improved (compared to MDI) magnetic sensitivity (8 G in the LOS magnetograms at high heliocentric angles) and improved spatial resolution ($1''$). These data have allowed us the detailed study of the footprints of the Sun's global magnetism at the solar poles.

4.1 Data

Full-disc magnetograms taken by HMI onboard SDO satellite have been used. In particular, the data series used are HMI (1.5-level) products with a cadence of 12 minutes (series HMI.V_720s). These images give the LOS magnetic field component for the whole solar disc with a spatial resolution of $1''$. The noise level of such data is close to 5G at disc centre and increases up to 8G close to the limb (Liu et al., 2012). The HMI instrument has been taking data for about 6 years: from 30th April 2010 to 14th February 2016. In this time period, the Sun has evolved from the rising phase that took place after the solar minimum of 2009 to the decaying phase after the maximum of 2014.

This study is focused on the time evolution of the global magnetic field during the 6 years of HMI data. In order to perform such a study, we have used the mean LOS magnetic field

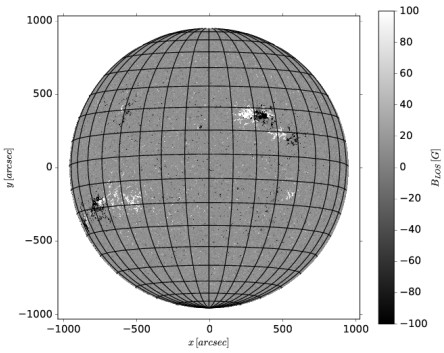

FIGURE 4.1— HMI full-disc magnetogram of the 21st of April 2011. Overplotted are the contours for the heliographic longitudes and latitudes between $-80°$ and $80°$ at steps of $10°$. The B0 angle (see the text) for this date is $-5°.15$, which means that the South pole is inside the visible disc.

component averaged over the visible longitudes. The time evolution is calculated by selecting a single magnetogram per day during the whole SDO mission. For each day we preserve the solar latitude information while the longitudes are averaged to increase the SNR of the weakest signals. The latitude information is necessary to distinguish between polar regions and the rest of the solar surface. The average over visible longitudes is necessary since the magnetism at the polar regions is very weak. This strategy requires knowing the heliospheric latitude and longitude of each point.

The calculation of the heliospheric latitude and longitude must take into account the time variation of the rotation axis orientation. This is accomplished by means of two angles. 1- The orientation of the solar axis projected on the plane of sky with respect to the vertical direction of the CCD used to record the images. This step is considered by rotating the image the angle needed to orientate the solar rotation axis aligned with the vertical direction upwards. The angle to be rotated is given by HMI team on the header of each image. It is interesting not to interpolate over the values of the magnetogram to preserve the magnetogram but perform the rotation over the solar coordinates of each pixel. The second angle to account for to get the heliographic latitudes and longitudes is the so-called $B0$ angle. This parameter gives the heliographic latitude of the disc-centre point. This angle is consequence of the inclination between the normal to the ecliptic and the solar rotation axis. The value of B0 depends on the date and is tabulated in the ephemerids. Adding this value to the helioprojected latitudes, the heliographic ones are retrieved. An example of a magnetogram with the calculated latitudes and longitudes is shown in Fig 4.1. For that date, the $B0$ value is $-5°15$. Thus the South solar rotational pole is already inside the visible disc.

Finally, the LOS magnetic field component is averaged for all visible longitudes for different latitude bin sizes. Figure 4.2 depicts the time evolution (x-axis) of the average LOS magnetic field

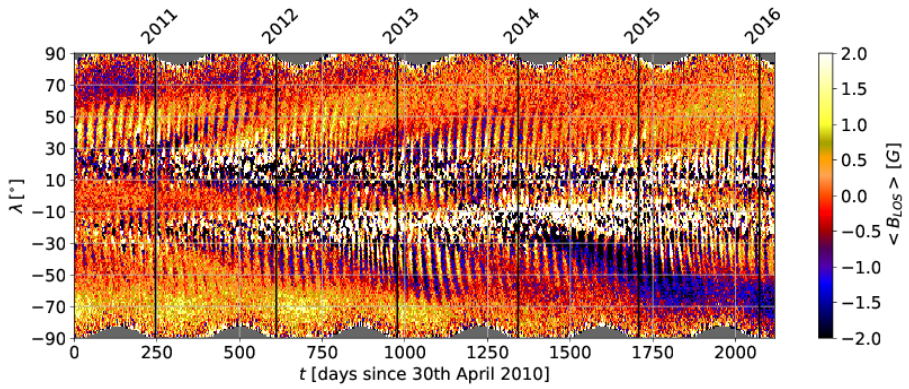

FIGURE 4.2— Time sequence of the averaged over the visible longitudes of the LOS magnetic field component for latitude bins of 1°. Time is in the x-axis in days since 30th April 2010 with a daily cadence. y-axis covers the heliographic latitudes for the time series taking into account the $B0$ angle. Colour scale is used for the averaged LOS magnetic field component, which is saturated at $\pm 2G$. Due to the inclination of the ecliptic and solar rotation axis, some solar surface areas are hidden. These regions are marked with dark gray. Vertical solid black lines mark the 1st January of each year through the time series.

component (colour scale) for a latitude bin size of 1°. In this process the noise is greatly reduced at low latitudes, close to a factor 200. At the polar regions, this improvement is strongly time dependent as the solar rotational poles enter (leave) the visible disc every year due to the solar rotation misalignment with the ecliptic. Every six months the very high latitudes are lost (seen in brown). When the pole is best visible the noise reduction is close to a factor 100. Hence, it is possible to perform a good characterisation of the global polar magnetism properties even for the very faint signals. In general the averaged magnitude has values of a few Gauss. The strongest signals (of the order of 10G) are associated to the presence of active regions in the visible disc. This value is well below the typical value for the LOS magnetic fields of active regions (around several hundred Gauss). This strong weakening of signals associated to active regions is due, mainly, to two effects. First, since we are dealing with averages over longitudes, this greatly reduces the contribution from active regions. Also, the fact that active regions usually appear in pairs of opposite polarity quite aligned in latitude implies that the longitudinal average cancels the contribution from one polarity of the active region with the other polarity of the same active region.

The time coverage of the SDO mission is long enough to detect some features associated to the global magnetic field. The most evident ones are those associated to active regions. They are seen as the strongest signals (saturated in black/white) in latitudes between ±30°. First, it can be seen that the emergence of these structures is not distributed randomly over the solar surface but they emerge in what is called activity belt. This region is defined as the area between solar latitudes ±40°. Another global magnetic field property visible in the figure gives rise to the so-called Spörer's law (Hale & Nicholson, 1925). This law refers to the variation in time of the active region emerging latitudes at different phases of the solar cycle. During the rising phase

of the sunspot cycle, active regions emerge the farthest from the equator. This is seen in the figure at the beginning of times series. Remember that, the activity minimum took place in 2009 (not covered with these dataset), and our time series begins in the rising phase of the cycle. In the figure it is seen that the first active region black/white disturbances are close to latitudes $\pm[20^\circ - 30^\circ]$. As the sun evolves to further phases of the sunspot cycle (activity maximum and decaying phase) active regions emerge closer to the equator. This is observed in the time series of the figure as a gradual drift of the emergence latitude of active regions.

Another feature related with the global magnetic field behaviour is the presence of magnetic flux surges. These surges are long-lived unipolar flux concentrations that are seen to move from the upper part of the activity belt to polar regions. This migration of magnetic flux towards high latitudes is thought to be carried by the meridional flow. This stream is a slow motion (Hathaway, 1996, and references therein) from low latitudes to high latitudes. These surges are identified in the figure as unipolar areas that move polewards. One very clear feature is seen between day 1400 and day 1900 and between -20° and -70°. This meridional circulation is thought to be essential to supply unipolar flux to the polar regions, driving the reversal of polarity in these regions (Charbonneau, 2010). The origin of this unipolar flux lies in the fact that the emergence of any active region happens with a given angle between the line that joins both polarities of the active region and the equator (usually referred to as Joy's law). This angle is such that the following polarity of the active region is at higher latitudes than the preceding part (Hale & Nicholson, 1925). In addition, in a given cycle the preceding (following) polarity of active regions is the same (Hale et al., 1919). When active regions decay, flux is supplied to the surroundings. According to standard scenario, the angle between the preceding and the following part of active regions makes possible to meridional flow to drag (preferably) the polarity of the following part to higher latitudes. This is thought to be the mechanism by which the polar regions are built in with the new polarity.

One last characteristic of the global magnetic field is the magnetic behaviour at high latitudes. The first aspect to be aware of is the presence of a dominant polarity at high latitudes. As it was already seen long ago by Babcock & Babcock (1955), the prevailing polarity at the North polar region (negative in Fig. 4.2) is of opposite sign to that of the South one (positive). This is very clearly seen at the beginning of the times series. The temporal evolution of the magnetism at the polar regions in solar cycle time-scales is a second important characteristic. As the cycle elapses from an activity minimum to a maximum, i.e. as the magnetic activity at the solar surface increases, the polar regions have an inverse behaviour. During this time, the strength of the dominant polarity decreases until a reversal of the polarity takes place. This change occurs close to maxima of activity.

4.2 Analysis

The analysis of the temporal evolution of the LOS magnetic field component averaged over the visible longitudes ($< B_{LOS} >$) between latitudes 70° and 80° for the North and South hemispheres reveal additional features hardly seen in the time series of Fig. 4.2. The result of this analysis are presented in Fig. 4.3. At the beginning of the time series both polar regions exhibit

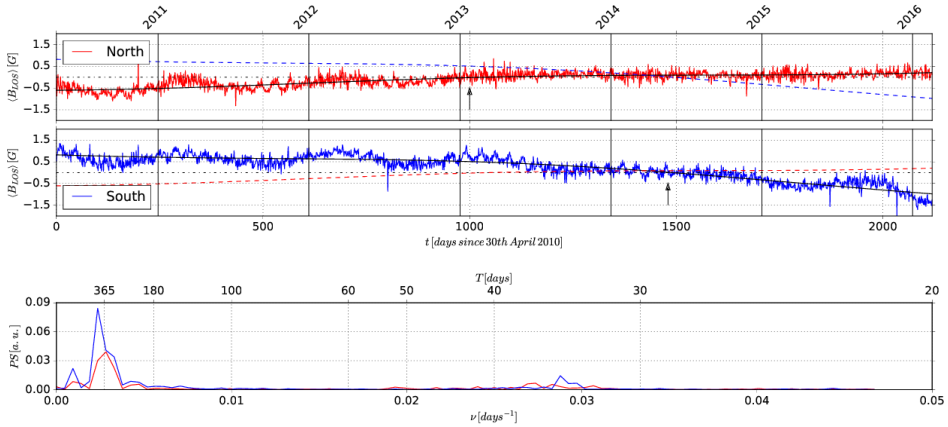

FIGURE 4.3— Top panel: the red solid line represents the time evolution of the LOS magnetic field component averaged over all visible longitudes and for latitudes between 70° and 80°. In black solid curve, the global trend is shown. Dashed blue colour shows the trend for latitudes between −70° and −80°. The black vertical arrow marks the time when the trend reaches 0 G. 0 G level is marked in black dashed-dot line. Middle panel: blue solid line shows the time evolution of the mean LOS magnetic field vector between −70° and −80°. Its trend is plotted in solid black line. Red dashed lines are used for the trend seen in the other polar region. The time when the trend crosses the origin is highlighted with a vertical arrow. 0 G level is in black dashed-dot line. Bottom panel: Fourier power spectrum associated to each of the previous time sequences after the global trend removal (following the same colour coding). Each power spectrum is normalised to its own area.

the strongest $< B_{LOS} >$. In the previous cycle, the North pole had a negative polarity and the South a positive one. The $< B_{LOS} >$ strength at each polar region is progressively reduced as the minimum leads to a rising phase and, at the maximum of approximately 2015, both polar regions have already annihilated their previous polarity. As in other solar cycles (Babcock, 1959; Svalgaard & Kamide, 2013) this decay happens asymmetrically. The North polar region shows a steady decay from mid-2010 (-0.5 G) to 2013 (0 G) (see black arrow in the upper panel of Fig. 4.3). In contrast, the South polar region initially preserves its strength with a small variation until 2013 and then abruptly decreases its strength changing its polarity by mid-2014 (see the black arrow in the middle panel of Fig. 4.3). After the maximum, the rising phase of the polar $< B_{LOS} >$ strength is also asymmetric. The South region has rapidly built up its new polarity (-1 G) whilst the North polar region remains close to zero (0.2 G).

In addition to this global behaviour two more features are present, which are hardly visible in Fig. 4.2 and are evident in Fig. 4.3. They are both of oscillatory nature. The first one is characterised by a long-period oscillation, which is observed when $< B_{LOS} >$ is not too close to zero. In the figure this can be observed, for instance, during the first 1000 days of the time series, with two maxima, at around 300 and 700 days and other two minima close to 100 and 500 days. The other oscillatory signature has a shorter period (around approximately 30 days), which is seen when the solar rotation axis is inside each of the hemispheres considered. For instance, at around day 500 since 30th April 2010 for the North and 300 days for the South.

Before analysing these oscillatory signals it is convenient to consider the satellite itself as the source for such signals. SDO is a geosynchronous satellite and thus there are at least three very clear periodic signatures induced. The first one is a 24 hours periodic signal related with the radial velocity of SDO when orbiting the Earth. The second, also very clear, induced periodic signal is related with the Earth movement around the Sun, that induces a signature with a one year period. Finally, a very weak one that can already be seen when the above two are subtracted is the Moon influence. In this case, a $\sim$ 29 days periodic oscillation is induced. All these effects are clearly seen in dopplergrams. Dopplergram and magnetogram images are obtained by means of the centre-of-gravity method (see Eqs. 2.3). This implies that one measures the wavelength displacements from two measured velocities. Then those are combined to get the LOS velocity or the LOS magnetic field component. Any of the above mentioned effects are going to enter by means of an additional velocity. As long as these velocities do not vary significantly in the 12 minutes required to build each dopplergram/magnetogram, they enter as $\Delta\lambda_+ = \Delta\lambda_+^{\odot} + \Delta\lambda_r$ and $\Delta\lambda_- = \Delta\lambda_-^{\odot} + \Delta\lambda_r$, where $\Delta\lambda_r$ stands for the wavelength shift due to these additional velocities. As the dopplergram is proportional to the addition of the previous displacements: ($v_{LOS} \propto \Delta\lambda_+ + \Delta\lambda_-$) the influence of these terms is preserved. However, for magnetograms $B_{LOS} \propto \Delta\lambda_+ - \Delta\lambda_-$ and, no systematic influence persists. It can be easily tested using the level-1.5 data dopplergrams. If the same method is applied to these data, there appear very clear peaks in the Fourier spectrum at the daily and lunar periods. Magnetograms in contrast do not show Fourier power in any of these frequencies. The weak oscillation detected from the magnetograms is characterised by a slightly lower frequency than that of the moon, well sampled with the Fourier frequency achieved.

The long term oscillation seen in Fig. 4.3 was already observed by Babcock (1959) and it is due to the inclination of the Earth orbit compared to the solar rotation axis. This inclination of the ecliptic makes the projection of the magnetic field over the LOS to vary with the orbital period. If the direction of the magnetic field does not change significantly, then an orbital modulation of the field strength is expected. Hence, there is a global trend which is modulated with the orbital period. To show this effect, we use a polynomial of order up to 7 to fit the polar trend. The product of this trend with a sinusoidal function of period close to one year (the free parameters are the amplitude, phase and period) gives the modulation. We use this guess of the modulation to subtract it from the time series and repeat the process until no improvement is reached in the fitting procedure. This way we retrieved the global magnetic trend of polar regions without the influence of the orbital modulation (shown in black solid line in the Fig. 4.3). This tilt of the ecliptic is also responsible for the signals in latitudes above 83° (see Fig. 4.2) appearing and disappearing through the orbital phase. For instance, some of the latitudes below 83° are missed in between $\sim$0 and $\sim$200 days, while they are visible from $\sim$200 to $\sim$400.

The third polar characteristic is the presence of a short period oscillation with an approximately 30 days period. This signal is extremely weak, with a peak-to-peak amplitude of $\sim$0.6 G. The fact that the oscillation appears and disappears every six months, i.e. that it is only visible when each of the poles is inside the visible disc, is due to the fact that only at these moments the area of the solar disc used for the field average is large enough. According to Liu et al. (2012) the noise of HMI-720 second cadence magnetograms vary from 4 G at disc centre to 8

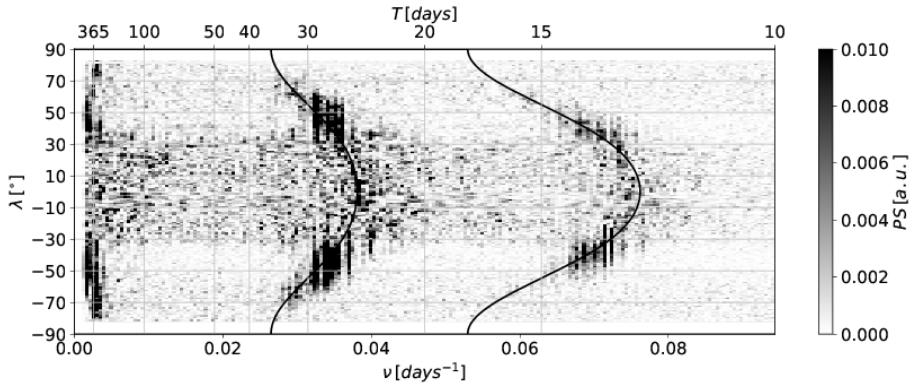

FIGURE 4.4— Power spectrum associated to the time series shown in Fig: 4.2. The bottom x-axis presents the frequencies in $days^{-1}$ and in the upper one, the corresponding period in *days*. The power spectrum for each latitude bin is in gray scale and it is normalised to its own total power. Overplotted with black solid lines are the fundamental mode and the first harmonic of the differential rotation profile.

G at the limb. When one of the poles is inside the visible disc then those pixels with solar latitudes between 70 and 80 degrees are characterised by a smaller noise, together with the fact that the number of pixels increases in a factor ~ 5, and it makes possible to observe such a small amplitude oscillation. After a Fourier analysis of the time sequence (see Fig. 4.3 bottom panel) the periods associated to the orbital and rotational oscillations are: ∼370 days and ∼34 days for the orbital and the short-period oscillation, respectively.

Interestingly, this short-period oscillation is not exclusive of the polar regions themselves but it is present all over the surface (see Fig. 4.2) during the whole time series. The presence of the oscillation itself can be clearly seen after Fourier transforming the time series and looking at the power spectrum. Figure 4.4 shows the Fourier power spectrum with latitude bins of 1 degree. To get this image, each $< B_{LOS} >$ time series is subtracted a polynomial fit of order 7 that removes the global trend, it is Fourier transformed, and the power spectrum normalised to unity. In solid black lines, the synodic frequencies (periods) of the fundamental mode and the first harmonic of the differential rotation are shown. Differential rotation is given by $\omega = A + B\sin^2\lambda + C\sin^4\lambda$, where ω is the angular velocity and λ the latitude. The constants are taken from Snodgrass & Ulrich (1990): $A = 2.972$, $B = -0.484$ and $C = -0.361$.

From what has been explained above, it is clear that there exists an observed relation between the solar surface rotation and field oscillation. In general, any magnetic structure that is dragged by solar surface rotation can potentially generate this pattern. In that sense there is an obvious candidate to play such a role, namely the ARs. To understand the effect of active regions and the quiet Sun, for each time step, a mask has been created to isolate the contribution of active and quiet components. In order to classify each point of the solar surface as "active" or "quiet", a square of 2.5×2.5 arcsec^2 has been taken centred on it. If the mean absolute value of the line-

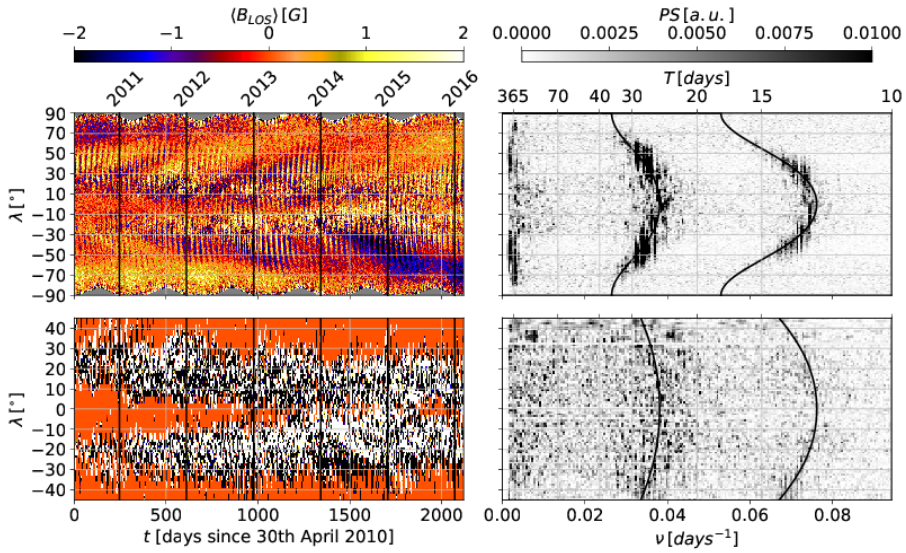

FIGURE 4.5— Left panels depict the time evolution for the QS component (top) and ARs (bottom). Colour scale is the average over the visible longitudes of the LOS magnetic field component saturated at ±2 G. The y-axis represents the heliographic latitude in degrees and x-axis the time in *days*. A vertical solid black line marks the 1st of January for each year. Right panels are the corresponding power spectra, for the QS component (top) and ARs (bottom). As in previous figures the power spectrum for each latitude bin is normalised to its own area. Solid black lines are used to mark the fundamental and first harmonic due to solar surface differential rotation.

of-sight magnetic field in this square is above/below 20 G the point is sorted as "active"/"quiet". Figure 4.5 shows the time evolution of the $< B_{LOS} > (\lambda)$ for ARs (bottom left) and for the QS (top left) components. It is remarkable that both components behave differently: active regions are contained within ±45° in latitude and they drift to the equator as the cycle evolves. Most of the surface is classified as quiet Sun and its power spectrum (right panel) shows an eye-catching concentration of the power highly located at differential rotation frequencies (both for the fundamental mode and the first harmonic). The synodic differential rotation profile is overplotted in black colour to point out the doubtless relation of the detected periodic signal with the solar surface rotation. Active regions show, however, a much more disperse power spectrum.

A disperse power spectrum for ARs is not surprising since their lifetime is short compared to solar cycle time scale. It is possible to develop a simple test to check this point. ARs are bipolar structures that emerge at the solar surface. These structures have a typical mean lifetime of several weeks during which they are dragged by the solar surface rotation. Hence ARs might generate an oscillation with the rotation period. We have performed a simulation test in which bipolar regions emerge at random longitudes, remain visible and disappear from the solar surface at the West limb by the rotation. Bipolar structures are used to simulate ARs, characterised by no net flux. During their simulated life they are dragged by the rotation of the solar surface.

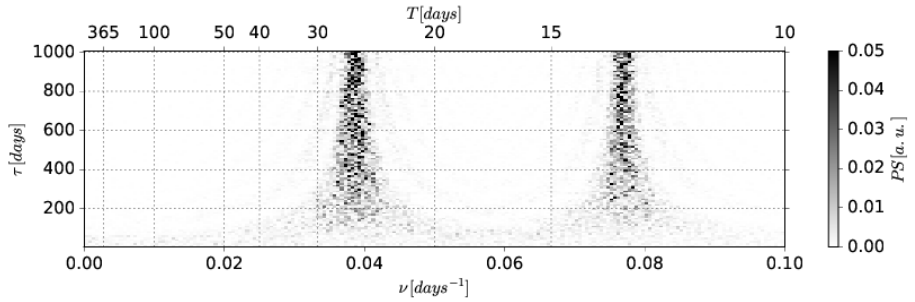

FIGURE 4.6— Simulated power spectrum of the LOS magnetic field component averaged over visible longitudes obtained after simulating the appearance of active regions on the disc and their change in position at the solar disc due to the solar rotation. τ represents the AR lifetime assumed in each simulation. The Fourier power spectrum is in gray scale and is normalised for each τ value. y-axis shows the AR lifetime used for each run of the AR emergence simulation.

The rotation period is set fixed to 26.2 days. We then calculate the average over the visible longitudes of the LOS magnetic field component. Figure 4.6 shows the Fourier power spectrum of that magnitude depending on the bipole lifetime. It is clearly seen that these structures can concentrate power significantly around the rotation frequency (and its first harmonic) when their lifetime, τ, is larger than ten times the solar rotation period, T. In the Sun, the typical mean lifetime is $< \tau > \sim 3\times$T (van Driel-Gesztelyi & Green, 2015, and references therein), though the distribution is quite broad, so we do not expect this component to be able to concentrate significant power around the rotational frequency.

From this test, we conclude that the lifetime of ARs is not long enough to generate a rotationally driven oscillation. However, there is a physical process related to ARs that has not been considered yet that could potentially lead to the observed rotational modulation of $< B_{LOS} >$. It is generally accepted that the average magnetic field at the solar poles evolves in time as a consequence of the residual magnetic field of ARs that is advected by the meridional flow from the activity belt up to higher latitudes. It is to be noted that the amount of positive flux which is advected to the north pole is larger than the negative flux advected to the south pole at the beginning of the temporal series, as seen in Figs. 4.2 and 4.5, leading to a late reversal of the latter. The detected rotationally-induced magnetic oscillation might be explained if this advection occurs at preferential longitudes and at all latitudes, and flux is advected such that half of the regions around the poles have a slightly larger magnetic field than the opposite half. We think that this coherent advection at all latitudes seems unlikely to happen coherently during the full time span of five years covered by the data we have analysed.

Another possible source for a rotationally driven periodic signature is based on a dynamo model in which the global field is not axisymmetric with respect to the rotation axis. This misalignment leads to a natural oscillation of the observed magnetic signal with solar rotation. In order to test this hypothesis, a simplified scenario of such a misalignment is considered with a bipolar

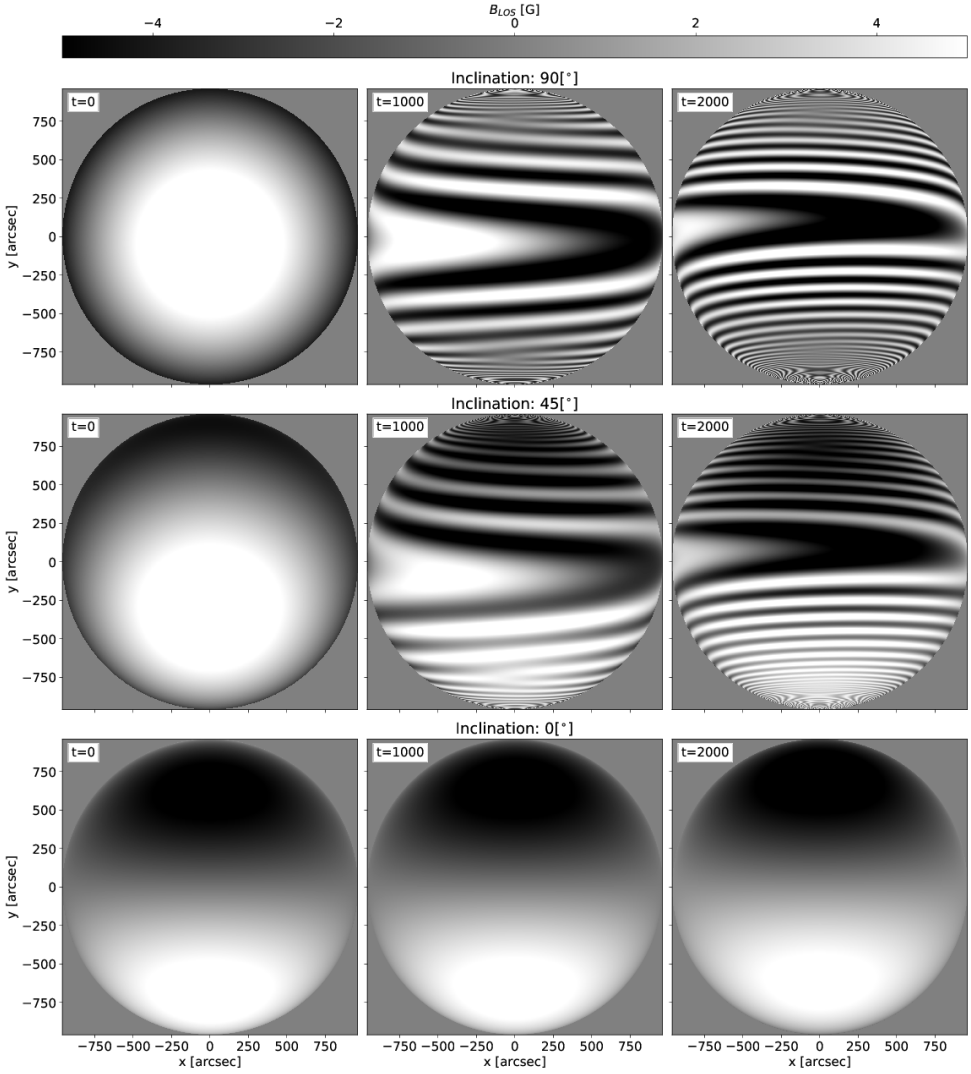

FIGURE 4.7— From top to bottom: three snapshots of the rotating magnetic dipole simulation for timestep: 0, 1000 and 2000 days with a tilt angle of 90°, 45° and 0° between the rotation and magnetic axes. The gray scale stands for the LOS magnetic field and the rotator is displayed with the North upwards and the East leftwards.

field that is tilted a certain angle to the surface rotation axis.

In order to address this scenario, we consider a rotating magnetic dipole. In this model, the global magnetic field of the Sun is given by a dipolar configuration:

$$\mathbf{B}(\mathbf{r}) = \frac{H_d}{2}\left(\mathbf{e} - 3(\mathbf{e}\cdot\mathbf{r})\mathbf{r}\right), \tag{4.1}$$

where $\mathbf{B}(\mathbf{r})$ is the spatial distribution of the magnetic field vector, H_d is the magnetic field strength at the dipole axis, $\mathbf{e}$ is an orthonormal basis for the orientation of the dipole and $\mathbf{r}$ gives the position on the stellar surface with respect to the rotation axis. We take into account the differential rotation profile of the Sun as well as the Earth orbit inclination. We have performed this simulation for different angles between the dipole and the rotator from 0° (aligned) to 90° (perpendicular). Three snapshots of the three different simulation runs are shown in Fig. 4.7 for 90°, 45°, and 0° misalignment between the axes. The first snapshot (left) shows the initial configuration. The middle panel shows B_{LOS} after 1000 days. At that moment, the North pole is inside the visible disc and the South is hidden to the observer. As only differential rotation is present, the magnetic field lines are continuously rolled up, as can be seen on the rightmost panel, where the magnetic field configuration after 2000 days is shown.

The same methodology as that applied to HMI data can be followed. For each simulation run with different initial tilt angle, we have calculated the LOS magnetic field component averaged over visible longitudes in different latitude bins. If the rotation and magnetic axes are aligned, there is no rotational modulation. In contrast, the orbital signature is very evident. When the two axes are perpendicular, the rotational modulation is maximum and the orbital one is absent. In the intermediate scenario both the orbital and rotational oscillations are present. We propose to use the ratio of the power between the orbital and rotational oscillation as a function of latitude, λ, to have an estimation of the tilt angle between the two axes. To do so we use the ratio of the power spectrum at the orbital and rotational frequencies. Due to our frequency sampling and since the power associated to each frequency can be spread around the nominal values, we consider two different ratios. On the one hand, the ratio between the maximum power found close to each nominal frequency $r_m(\lambda)$. On the other hand, the ratio of the integrated power close to the nominal orbital and rotational frequencies $r_i(\lambda)$. Mathematically:

$$\begin{aligned} r_i(\lambda) &= \frac{\int_{\nu_o-\Delta\nu}^{\nu_o+\Delta\nu} p(\nu)d\nu}{\int_{\nu_r(\lambda)-\Delta\nu}^{\nu_r(\lambda)+\Delta\nu} p(\nu)d\nu}, \\ r_m(\lambda) &= \frac{\max[p(\nu_o-\Delta\nu,\, \nu_o+\Delta\nu)]}{\max[p(\nu_r(\lambda)-\Delta\nu, \nu_r(\lambda)+\Delta\nu)]}, \end{aligned} \tag{4.2}$$

where $\nu_r(\lambda)$ stands for the rotational frequency, ν_o for the orbital one and $\Delta\nu$ is used to cover a small range of frequencies around ν_o and $\nu_r(\lambda)$. $p(\nu)$ represents the associated power spectrum. Figure 4.8 (top row) shows the decimal logarithm of the ratios as a function of the angle between the rotator and the dipole. For both parameters the ratio of the energy associated to each periodic signal shows a quite similar dependence. The amount of energy in the orbital oscillation is maximum when both axes are aligned and it decreases when increasing the misalignment

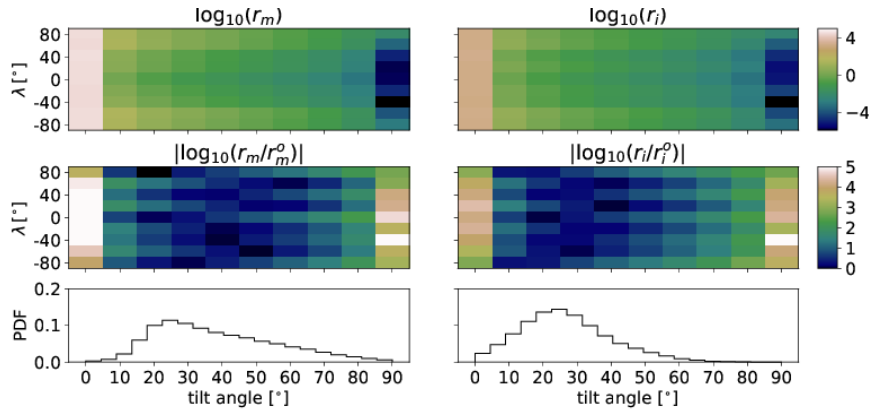

FIGURE 4.8— Upper left panel shows the latitude (y-axis) and tilt angle (x-axis) dependence of the ratio between the maximum value of the power spectrum at the orbital frequency to the maximum at the rotational one (see colour scale). The ratio is shown at logarithmic scale. The same representation is used for the ratio between the integrated power around the fundamental frequencies (see Eq. 4.2). Middle panels show the comparison between the latitudinal dependence of the simulated with the observed ratios. The use of the absolute value of the logarithm results in a zero value for an exact matched and increases otherwise. Lower panels show the probability density functions of the tilt angle that minimises $|\log_{10}(r_m/r_m^0)|$ (left) and $|\log_{10}(r_i/r_i^0)|$ (right).

between the axes.

To compare with the observations, the calculation of the ratios defined in Eq. 4.2 for the observed time series is performed over the QS component, as the simulation does not take into account contributions from ARs. Anyhow, as we have seen above, we do not expect AR to strongly influence the power detected at rotational frequencies. In order to increase the signal to noise ratio and so the power concentrations around the orbital and rotational frequencies, we use now latitude bin sizes of 20°. In the middle panels of Fig. 4.8, we compare the observed ratios defined in Eq. 4.2 (r_i^o and r_m^o with a superindex "o" for observed) with the synthetic ones (r_i and r_m).

In the rotating magnetic dipole model we are considering here, the relation between the orbital and rotational frequencies can be explained by a tilt between the magnetic and rotation axes. In order to get an estimation of this inclination angle, we fit the angle-dependence of each latitude bin to a fourth order polynomial. To do so we use a Markov-Chain Monte-Carlo method (Foreman-Mackey et al., 2013) with flat priors over the four parameters. This method gives us the posterior distributions of each of the four coefficients for each latitude bin. The combination of these four coefficients can be mixed to obtained the tilt angle that minimises $|\log_{10}(r_m/r_m^o)|$ and $|\log_{10}(r_i/r_i^o)|$. Thus we recover the probability density function (PDF) of the tilt angle for each latitude bin. The combination of these PDFs for all the latitude bins, leads to a global PDF that is shown in the bottom row of Fig. 4.8. On the one hand, the PDF for the ratios of the power maxima results in a tilt angle of 35.°52 with a 68% of probability to be between 21.°09 and 58.°62. On the other hand, for the ratios of the integrated magnitudes, the tilt angle

recovered has a 50th percentile at 25.°36 and a 68% of probability to be between 13.°48 and 39.°75. The different distributions retrieved might be indicative of the different sensitivities of each method to sources that our model do not consider. Before a more appropriate model is developed, we can give a conservative estimation of the tilt angle to be in the common region of both distributions, i.e., between 21.°09 and 39.°75.

4.3 Summary of the results

The study of daily full-disc magnetograms taken by the HMI@SDO during the 6 years of the mission has depicted a global scenario of the magnetism at these regions. During this period the solar cycle has covered the rising activity phase after the minimum of activity of 2009, going through the maximum of 2014 and also the decay of activity after it. During this time, the polar regions have followed a process with a different phase in both poles. At the beginning of the time series the polar field progressively weakened. As in other solar cycles this process has not been simultaneous at both polar regions. On the one hand, the decay phase of the North polar cap has occurred gradually reaching a null value in 2013. On the other hand, the South region has shown a quite steady, near its maximum value, until 2013 and then, its polarity has been cancelled in a quite fast ($\sim$ 1 year) process. The new accumulation of flux in the polar regions is also asymmetric, with the South region already showing the new polarity in the beginning of 2015 while the North region has a null flux since 2013.

In addition, the detection of a rotational modulation of the magnetic signal all over the surface and at all latitudes has been reported in this chapter. We have identified that this modulation is driven by the action of solar rotation motions on magnetic fields. However, not any magnetic structure can lead to the signal detected since a large spatial and long time coherence is needed to support the observed oscillation. We identify as a possible source for this signal the presence of a misalignment between the rotation axis and the global magnetic field. A simplified scenario that has been assessed here is obtained with a bipolar field that is tilted a certain angle to the surface rotation axis. This angle leads to a natural oscillation of the observed magnetic signal with solar rotation. With this model, the comparison of the power associated to the orbital and rotational frequencies points to a tilt angle of around $30° \pm 10°$.

From an observational point of view, a larger effort is needed to have longer time series with better polarimetric sensitivity to determine the weak polar signals. We have tried to extend our analysis to a larger temporal window by applying the same study to MDI@SOHO data. However, the weakness of the signals prevents us from using them to get a longer temporal series. Further analyses would be possible if the SDO mission continues recording data during the next years at least until the new minimum of activity –near 2021–, and cover a complete 11-year cycle. Extremely valuable data is also expected from the Solar Orbiter Mission (Müller et al., 2013) since this satellite is going to observe the rotational solar poles from outside the ecliptic and simultaneously detect solar wind particles close to their origin place.

Helioseismology may also help to obtain observational evidences of this orientation of the rota-

tion axis. The dependence of the rotation speed with depth is obtained after the splitting of the oscillation modes in a number of distinct frequencies. This is feasible since different modes propagate preferentially in different layers, some of them closer to the surface and some of them getting deeper into the Sun's interior. The information on the rotation axis is more difficult to achieve, though. Not only the mode splitting is required, but also the relative amplitudes of the split components need to be accurately measured. The determination of these relative amplitudes represent a hard task for helioseismology and it remains to be determined whether present space data have the necessary sensitivity for this measurement or if, on the contrary, more precise space instrumentation is required.

With this study we accomplish the objective of addressing the long-term behaviour of the polar caps. However our limited spatial resolution and low/medium magnetic sensitivity may hide properties about the morphology of polar magnetism. In the following we aim to alleviate these limitations using other facilities, though at the cost of spatial coverage and/or the temporal behaviour.

5

An infrared view of the polar magnetism

5.1 Introduction

The study presented in the previous chapter, as well as most of polar region works, has been performed using the LOS magnetic field component. It is so because the linear polarisation signals of such weak magnetism are scarce and the use of the LOS component allows us to infer some general properties. First, and despite the low resolution of the first instruments used, and the weakness of the polar magnetism, Babcock & Babcock (1955) studied the polar regions magnetism discovering a non-null polar net flux. This flux was found to be of opposite polarity in each pole. Later, the dependence of the polar magnetism with the solar cycle was discovered (Babcock, 1959). The polar region magnetism follows the solar cycle out of phase to the activity belt. During activity maxima, polar regions reverse the polarity, and during minima of activity, polar regions exhibit the strongest magnetic signatures. These early studies were preceded and co-temporal with the studies of the number of polar faculae (for an overview of these kind of studies with time, see Makarov & Makarova, 1996; Sheeley, 2008, and references therein). From these studies, it was found that the number of faculae at the polar regions followed the solar cycle. Furthermore, it was found that the abundance of these structures was out of phase with the number of sunspots (or the area covered by them). This means that close to minima of activity the number of polar faculae is maximum, whilst at maxima, they are scarce. This behaviour, which is in phase with the LOS magnetism found at polar regions, allowed establishing the close relation between the polar faculae and the dominant polarity of the polar region.

However, a detailed characterisation of the magnetism topology at these regions requires the whole magnetic field vector. To do so, we use full Stokes spectropolarimetry, that allows the inference of the magnetic field vector. The beginning of spectropolarimetric studies shed new insight in the characterisation of the magnetism at these solar regions. Homann et al. (1997) studied intensity and circular polarisation profiles of several polar faculae during an activity minimum. They found that most of these structures share the same LOS polarity than that of the polar region at that solar cycle phase. The comparison of faculae at equatorial limbs and at the polar caps showed some particularities. Indeed, those structures at polar regions

were characterised with the same polarity to that of the polar region, whilst equatorial ones showed both polarities. In addition, these structures at polar caps were found to be bigger in size ($3\farcs5 \pm 1\farcs3$) than their counterparts at the equatorial limb ($2\farcs1 \pm 0\farcs4$). Though, in both cases they harboured intrinsic magnetic field strengths in the kG regime. Further characterisation of these structures were settled by Okunev & Kneer (2004) and Blanco Rodríguez et al. (2007). Their high spatial resolution and high temporal cadence of the spectral line scan, allow the assessment of the very dynamic behaviour of faculae, that show major shape and brightness variations in short periods of time (tens of seconds). They also found that the plasma inside the faculae is characterised by hot plasma flowing outwards from the Sun. Blanco Rodríguez et al. (2007) reported the observation of polar faculae of both polarities at the two polar regions, though their number were imbalanced, with a bigger number of faculae sharing the dominant polarity of polar region than the ones with opposite polarity.

Another step forward in the understanding of the polar regions magnetism was performed with the advent of full Stokes spectropolarimetric observations. In this sense, the suit quality of observations from the spectropolarimeter onboard Hinode satellite has encouraged most of such kind of studies (Tsuneta et al., 2008; Ito et al., 2010; Jin et al., 2011; Shiota et al., 2012; Kaithakkal et al., 2013, 2015; Quintero Noda et al., 2016). Complementing the Hinode observations, to the best of our knowledge, just another full Stokes spectropolarimetric study has been performed. It was performed by Blanco Rodríguez & Kneer (2010) focused on the FeI at 1.5 μm using TIP-II installed at the VTT.

Most of these works were carried out using data spanning the same solar cycle phase, i. e. close to the minimum that took place close to 2008. To the best of our knowledge, only two works studied polar regions outside activity minima. First, Shiota et al. (2012) focused on the study of the magnetism at polar regions and its temporal evolution from 2008 to 2012. And second, Kaithakkal et al. (2015) used data from a maximum of activity (2013 and 2014), though they do not study the magnetic properties at polar regions but LOS velocities around polar faculae.

Tsuneta et al. (2008); Ito et al. (2010); Jin et al. (2011) and Shiota et al. (2012) found that the polar region magnetism appears as small (of the order of a few arcseconds) structures scattered all over the polar regions. This magnetism was found to be bimodal: some magnetic patches present vertical fields, whilst others are horizontal. In addition they found that those patches that exhibit vertical fields are characterised at the same time by a bimodal behaviour depending on the magnetic flux of the patch. On the one hand, the largest magnetic flux patches had a polarity imbalance, with the dominant polarity consistent with that of the polar region. Moreover, the study of the temporal behaviour of these fields (Shiota et al., 2012) manifests that this component is the one that varies with the solar cycle. On the other hand, the other magnetic patches, harbouring lower magnetic fluxes, presented polarity balance. Ito et al. (2010) compared a QS region at the pole and a QS region at the equatorial limb. These authors found that the magnetic patches with greatest magnetic fluxes and polarity imbalance, are inherent of polar regions, whilst the others are common at both disc positions. In the meantime Blanco Rodríguez & Kneer (2010) studied the magnetic properties at polar faculae. They also found a bimodal behaviour in magnetic field strength. On the one hand, the strongest fields (of the order of kG) were found to match the dominant polarity of each polar region. The topology of these fields

was found to be compatible with vertical fields. On the other hand, weaker fields (of the order of hG) were found to exhibit polarity balance in both polar regions with no preferred orientation.

The characterisation of the magnetism at polar regions involves understanding its topology as well as its evolution with the solar cycle. In this sense it is mandatory to continue and extend the full Stokes spectropolarimetric studies that allow the most comprehensive magnetic field characterisation. In this chapter and in the next one, we handle this issue analysing full Stokes spectropolarimetric observations of polar regions taken close to the 2014 maximum of activity.

In this chapter we use infrared data coming from TIP-II@VTT in order to study the magnetic properties of the solar polar caps. In addition, observations taken at disc centre and at the West limb are used to discern intrinsic differences between QS at low latitudes from that at high latitudes from projection effects. Infrared observations offer a higher sensitivity to Zeeman induced polarisation, hence it allows studying the weakest polarimetric signals. In this chapter we address two main objectives. First, we complement the study of the magnetic properties of polar regions, in particular outside minima of activity. And second, we perform this analysis with infrared data, which are more sensitive to weak magnetic signals. The understanding of the magnetism at polar regions is a key ingredient to explain the solar magnetism. It is so because these regions present clear magnetic activity associated with the solar cycle. Hence, it is compulsory to further study and characterise not only the magnetism of these regions as a whole but also their small scale properties.

5.2 Data

The data analysed here were taken on 14th September 2013, when the North pole can be optimally observed from ground. In the solar cycle context, this corresponds to an epoch close to the maximum of activity, i.e. to the moment when the reversal of the dominant polar polarity takes place.

TABLE 5.1— Heliographic coordinates of the central point of each scan and their spatial size.

	Disk Center	North Pole	West Limb
Heligraphic coordinates (x;y)	-35.″7; -16.″7	8.″2; 921.″3	926.″2; -79.″4
FOV	$78.''58 \times 52.''50$	$78.''75 \times 42.''00$	$78.''93 \times 15.''75$

The data were recorded using the TIP-II polarimeter installed at the VTT telescope at Observatorio del Teide (Spain). The spectral region observed was centred at 1.565 μm where there are two spectral lines that are highly sensitive to magnetic fields. The spectral sampling was 14 mÅ and the two spectral lines, 15648.515 Å and 15652.874 Å, have a Landé factor of 3.0 and 1.48, respectively. Together with the fact that Zeeman sensitivity increases with wavelength, these pair of lines are excellent to study the magnetism of quiet Sun. The setup of the instrument was such that the whole Stokes vector was recorded for a longslit of 150 μm width. The width of the slit on the sky is 0.″68 and, in order to perform the scan, the image was moved in steps

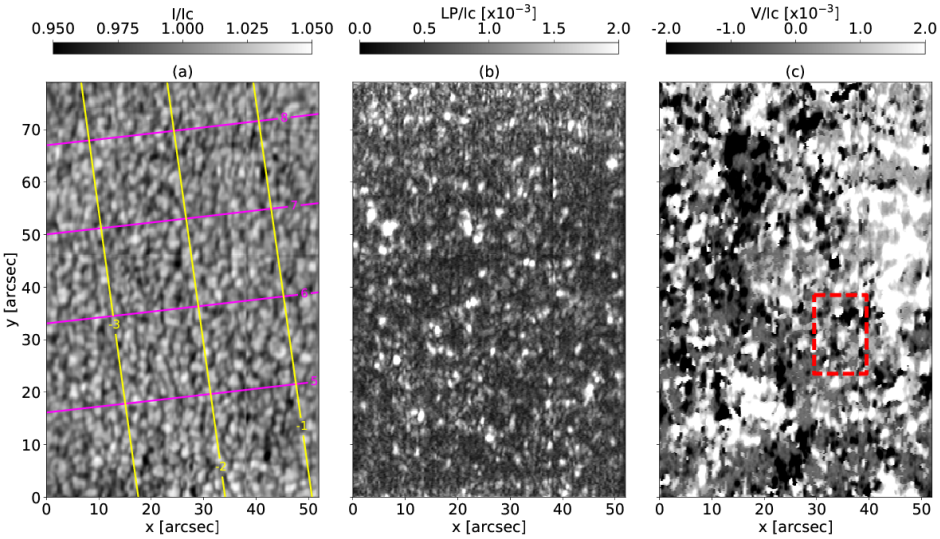

FIGURE 5.1— Panel *a*: disc centre continuum intensity map normalized to the average continuum intensity. Magenta and yellow lines mark the solar latitude and longitude, respectively. x and y axes show the observed distance on the solar disc in seconds of arc. Panel *b*: monochromatic linear polarisation map (given by $\sqrt{Q_\lambda^2 + U_\lambda^2}$) at the blue wing of the 15648.5Å line. Panel *c*: monochromatic Stokes V map at the same spectral position as for panel *b*. In red dashed square we highlight the region which is zoomed in Fig. 5.5 for a more detailed study.

of 0.″35. The slit width is slightly above the resolution by diffraction of the telescope (0.″56). So in principle, the limiting element is the slit. However the seeing lowered the spatial resolution of the observation to around 1.″1 as determined from the spatial Fourier power spectrum of the continuum intensity images.

We performed a deep mode observation with an effective exposure time of 20 seconds per slit position (giving a cadence of 23.7 seconds). The strategy followed for the observation is similar to that performed by Ito et al. (2010) and Jin et al. (2011). The idea is to study the quiet Sun component at the polar region and compare it with the quiet Sun magnetism seen at disc centre. In order to get an estimation of the projection effects, an additional dataset is taken at one of the equatorial limbs. In this step it is implicitly assumed that the quiet Sun at disc centre and at the equatorial limb are sampling the same statistical distribution. The comparison of the physical properties of each dataset allows an estimation of the projection effects when observing close to the limb. We avoided active areas using CaII K slit-jaw images, where brightening are associated to strong flux concentrations. Table 5.1 shows the position and size of each FOV. In Figs. 5.1, 5.2 and 5.3 we show the intensity map at the continuum for each FOV (panel *a*) together with two polarisation maps of the 15648.5 Å line: maps of linear polarisation (panel *b*) and signed circular polarisation (panel *c*). From these images it is possible to see the strongly magnetised character of quiet Sun regions exhibiting polarisation signals all over the FOV, even

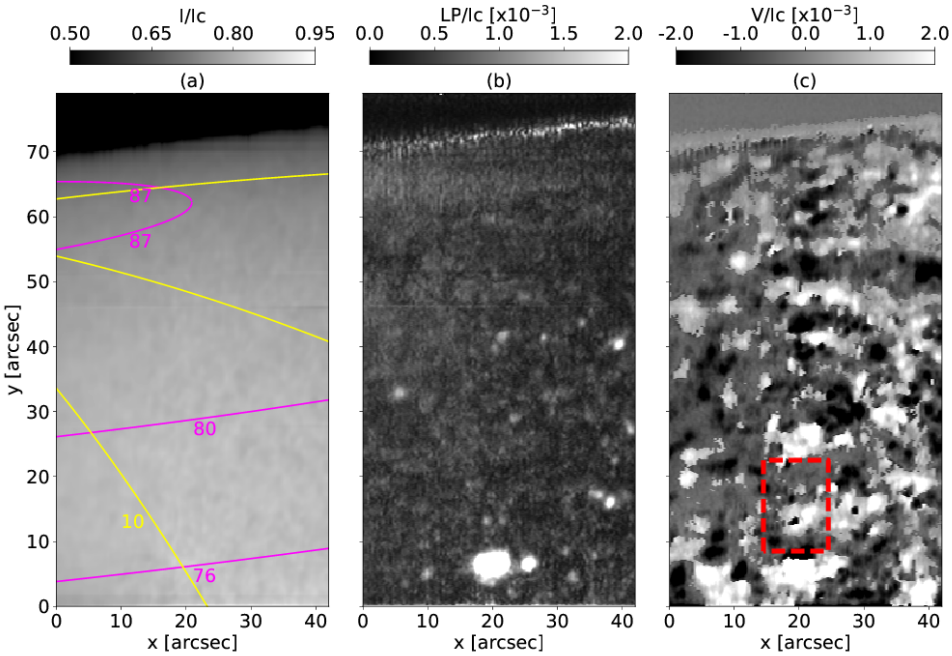

FIGURE 5.2— Same as in Fig. 5.1 but this time for the North limb dataset. As in Fig. 5.1, we highlight with a red dashed rectangle the region which is studied more in depth.

for linear polarisation signatures, which are usually more difficult to detect.

When talking about projection effects we include two differentiated main contributions. On the one hand, there are pure geometrical effects (for instance, the fact that a vertical magnetic field vector at disc centre will be seen as perpendicular to the LOS at the limb). On the other hand, limb effects are considered, which include: 1-the limb darkening, 2-the fact that close to the limb the observed spectral lines come from upper layers than when observing at disc centre, 3-changes in the radiative transfer due to the different physical magnitude stratifications in the optical path, ... These issues may drive to observed differences when studying the magnetism at disc centre and at the limb, even if the same structures are observed.

The reduction of the data is explained in detail in Sec. 2.2.3. After the reduction process, the final polarisation sensitivity is $\sigma_n^{Q,U,V}/I_c = 1 \times 10^{-4}$, where I_c is the average continuum intensity at disc centre. We consider a positive detection of polarisation signatures when any of the Stokes parameters presents at least three consecutive wavelengths over a $5\sigma_n$ criterion. Under this criterion, more than 70% of the observed FOV shows a magnetic detection in any of the three FOVs.

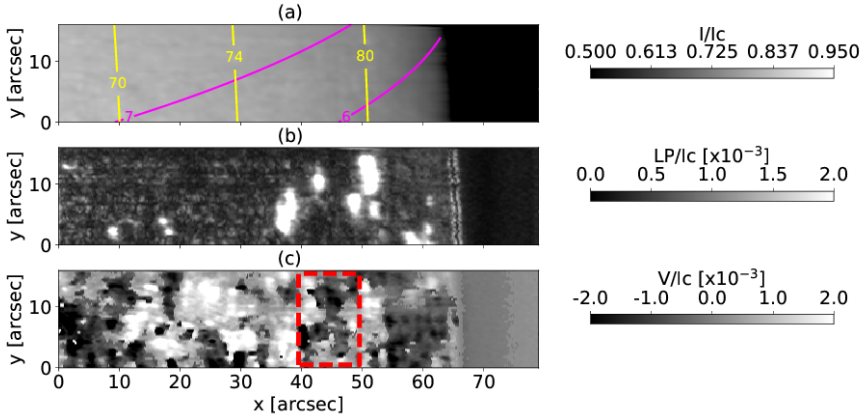

FIGURE 5.3— Same type of representation as in the two previous figures for the West limb sample. In panel *c* the red dashed rectangle highlights the region studied in Fig. 5.5.

5.2.1 Stokes amplitudes distribution

Figure 5.4 presents the Stokes amplitude distribution for the 15648 Å line at each FOV. At disc centre, the data is characterised by very weak linear polarisation signals (either Stokes Q or U), with a maximum amplitude of 0.5% the continuum intensity. Yet, 45% of the FOV exhibits Stokes Q or U above our chosen threshold of $5 \times 10^{-4}\, I_c$. Circular polarisation is characterised by a wider distribution of amplitudes that reach at most 1.8% of the continuum intensity. Circular polarisation signals are more numerous covering up to 81% of the FOV.

At the North region, the number of Stokes Q or U detections are less, covering up to a 10% of the FOV, than circular polarisation detections (80%). However, and in contrast to disc centre,

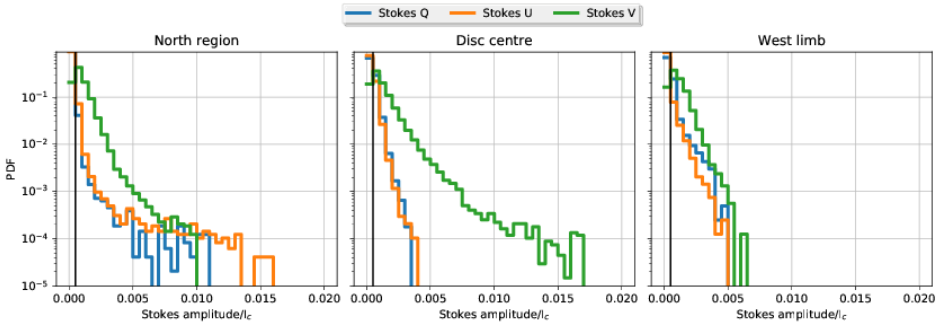

FIGURE 5.4— Maximum amplitude measured for the 15648.515Å for Stokes Q profiles (blue), Stokes U profiles (orange) and Stokes V profiles (green). The panels correspond, from left to right, to North region, Disc centre and West limb region. The vertical black line marks the signal threshold: $5 \times 10^{-4} I_c$.

there is a long tail of Stokes Q and U amplitudes, reaching a maximum of 1.7% of the continuum intensity at disc centre. At this disc position, circular polarisation maximum amplitudes are found to be weaker than those for linear Stokes amplitudes, reaching up to 1% of continuum intensity at disc centre.

At the West limb, the number of pixels with circular polarisation signals amount 86% of the FOV, though the amplitudes observed are smaller than at the other two FOVs. As for the North case, we found that at the West dataset, the largest amplitudes of Stokes V are weaker than at disc centre. In contrast, Stokes Q and U increase their relative to disc centre case, largest maximum amplitudes. At this disc position, weaker amplitudes are observed. This might be a singularity of this dataset, since at this disc position, the covered area is much smaller than in previous cases. An observational feature to be aware of is that the North region and disc centre were observed with better seeing than the West region, as can be seen from the mean r_0^{500nm} value of each FOV 13.1 cm, 15.6 cm and 6.8 cm, respectively. Usually, the worse the seeing the lower the amplitude of polarised Stokes profiles.

A weakening of the circular polarisation signals is observed when moving limbwards (Jin et al., 2011). This weakening can be due to two main reasons. The first one is that when moving to the limb, the LOS with respect to the vertical to the solar surface is different. In such a case, both the change in the radiative transfer and the different solar surface area covered by the detector pixel and the relative orientations of magnetic fields with respect to the LOS might explain this weakening. Another possibility is that the magnetic topology is such that the change of the relative orientation of the solar surface with respect to the LOS could explain this behaviour. For instance, for a vertically dominated magnetic field distribution, the change from disc centre to the limbs would disfavoured the amplitudes of Stokes V while linear amplitudes will be increased, as it is observed.

5.2.2 Stokes V profile shapes

Stokes V profiles shape is a good proxy of the model complexity of the atmosphere needed to explain the observed profiles. A perfectly antisymmetric Stokes V profile can be explained in terms of a magnetic atmosphere in which the velocity is constant with height. Those profiles that deviate from this scenario need to be explained using more complex models including gradients of the velocity and/or the magnetic field along the LOS or by more than one magnetic structure in the resolution element, i.e. by the presence of horizontal and/or vertical gradients in velocity and magnetic field.

In order to compute the number of lobes of each Stokes V profile, we look at the gradient in the wavelength dimension. The gradient of the Stokes V profiles encodes increases and decreases of Stokes V profile. In order to have a lobe, there has to be a cumulative increase (decrease) of Stokes V profile of more than 5σ followed by a cumulative decrease (increase) of Stokes V profile of more than 5σ.

Table 5.2 gather the percentages of identified lobes in each FOV. No matter the disc position of the observations, the vast majority ($\sim$77%) of the profiles have two lobes. A $\sim$13% of the

TABLE 5.2— Populations (in percentage) of the Stokes V profile shapes for each dataset. The values are expressed relative to the total number of pixels of each scan (avoiding those outside the solar disc for the limb samples).

N lobes	Disc Centre	North pole	West Limb
1	8.31	6.27	6.20
2	75.85	77.46	78.57
3	13.82	13.15	12.82
4	2.02	3.11	2.41

magnetic signals exhibit three-lobed profiles and singled-lobed are found in a ∼7% of the Stokes V profiles. Finally, a small fraction of the Stokes V profiles show four-lobed profiles. Hence, the change of the viewing angle seems to have no fundamental influence on the relative occurence of the various-lobed profiles. However, their spatial distribution do already show significant changes, as it can be seen in Fig. 5.5. At disc centre (panel *b*) single-lobe profiles (blue) are localised in the weakest Stokes V areas. Strong magnetic patches are characterised by regular Stokes V profiles. Three-lobed profiles (red) are found at the edges of magnetic patches and in between opposite magnetic patches (e.g. 36″, 45″). Four-lobed profiles (green) are found to follow the same behaviour as the three-lobed profiles. In both limb datasets (North, panel *a* and West, panel *c*) three lobed profiles are found at the edges of magnetic patches and in between opposite magnetic patches, as at disc centre, but they are also seen inside strong magnetic patches —North: (19″, 66″) and West: (46″, 5″)—. A similar behaviour is found for four lobed profiles. Single lobe profiles are found to be located in the faintest Stokes V signatures as in the disc centre case.

Another feature related with the required model complexity to reproduce the observations are Stokes V asymmetries. These magnitudes give information about the presence of velocity and/or magnetic field gradients along the LOS. Area asymmetries appear with LOS gradients and amplitude asymmetries with both, LOS and perpendicular to LOS, gradients. Following Solanki & Stenflo (1984), asymmetries are defined as:

$$\delta A = \frac{A_b - A_r}{A_b + A_r} \quad , \quad \delta a = \frac{a_b - a_r}{a_b + a_r}, \tag{5.1}$$

where δA and δa are the area and amplitude asymmetries of regular Stokes V profiles, respectively. $a_{b(r)}$ is the absolute amplitude of the blue (red) lobe and $A_{b(r)}$ represents the area of the blue (red) lobe, respectively.

The probability density functions (PDF) of the amplitude asymmetries and area asymmetries for each FOV are shown in Fig. 5.6. Disc centre is characterised by a mean value positive in both, amplitude (11.96%) and area (4.39%) asymmetries, with broad tails to larger values. This tails are markedly different for amplitude and area asymmetries. The former shows a steep decay from the mean value whilst the latter has very big tails to larger area values (either negative or positive). At the North (West) sample, the mean amplitude asymmetry is found to be

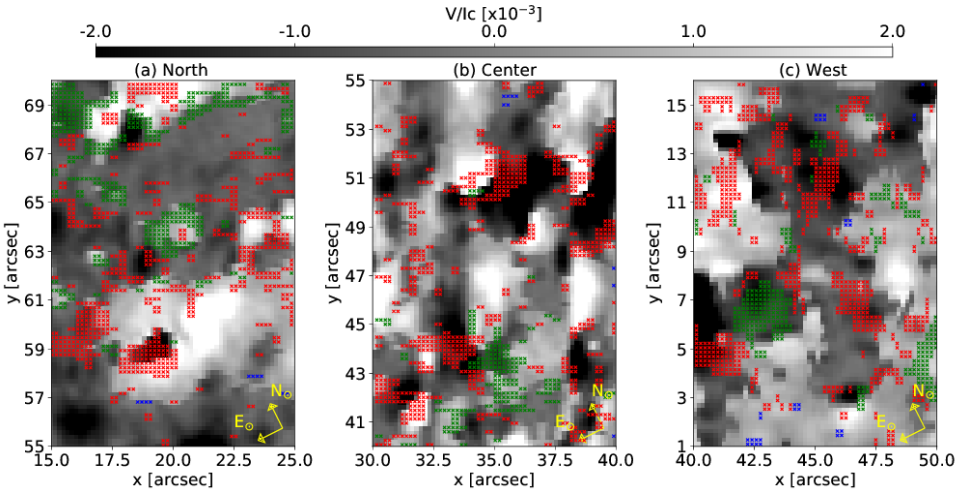

FIGURE 5.5— The background gray scale image is the monochromatic Stokes V map at the blue wing of 15648.5Å line for each FOV. Panels (a), (b) and (c) come from the red rectangles marked in Figs. 5.1, 5.2 and 5.3, respectively. Notice that the areas are chosen in such a way that the orientation for the three panels is the same. Spatial distribution of the different non-regular Stokes V profiles are marked with colour dots: we use blue colour for pixels classified as single-lobed, in red those with three lobes and green colour when four lobes are detected.

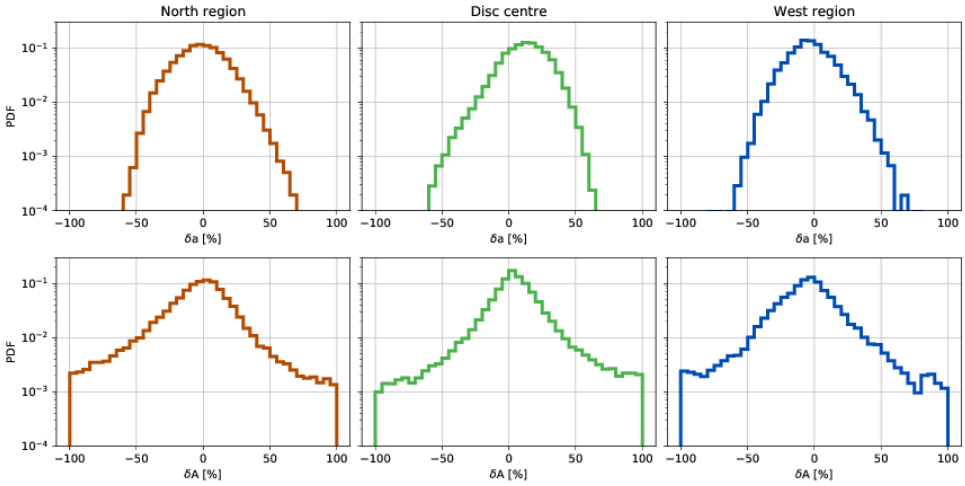

FIGURE 5.6— Top row: Probability density functions for the amplitude asymmetries. Bottom row: Probability density functions for the area asymmetries. Each column, from left to right, is for: North region, Disc centre and West region.

-1.25% (-2.89%) whilst the area asymmetry peaks at -2.57% (-4.90%). At limb positions, the distributions are reversed compared to that at disc centre. Indeed, at disc centre, the positive tail of any of the distribution dominates whilst at the limb, it is the negative tail the one that is more abundant.

The change of sign of the mean value of the amplitude and area asymmetries has already been reported for visible lines (Stenflo et al., 1987b) and infrared lines (Stenflo et al., 1987a). Buente et al. (1993) explained the change in area asymmetries by means of a vertical thin tube model, which depending on the viewing angle, is able to reproduce this behaviour. They found that the key ingredients to reproduce the observed area asymmetry behaviour with heliocentric angle is 1-the presence of downflows surrounding the flux tube, 2-the presence of inflows to the tube from the surrounding plasma, and 3-the interplay between temperature and velocity in the environment in combination with the LOS direction. This explanation can be applied to the strongest magnetic fields, i.e. those that are close to the thin tube model. This scenario would be applicable for strong enough magnetic fields, although the distributions here analysed are for the whole dataset (with regular Stokes V profile) rather than for a given subset. For the very weak fields, the vertical thin tube model might not hold, thought their topology is not clear yet. This situation is observed to be common for both limb datasets.

5.3 Inversion of Stokes profiles

To infer physical information we have performed the inversion of the observed Stokes profiles (see Sec. 3.2). We have followed two different inversion strategies for the data coming from TIP-II.

In the first inversion each resolution element is modelled by one magnetic and one non-magnetic atmosphere. Despite the inversion code allows the inference of the stratification for the various thermodynamic and magnetic parameters, we consider constant height-independent parameters but for the temperature. Departing from VAL-C (Vernazza et al., 1981) temperature stratification, we allow perturbations in up to five nodes in an independent way for each atmosphere. We additionally constrain the continuum value of both atmospheres to be the same. The remaining parameters are the LOS velocity and microturbulent velocity for each atmosphere; the magnetic field strength, inclination and azimuth of the magnetic atmosphere and the macroturbulent velocity (which is chosen to be a common parameter for both atmospheres). All of them are considered to be constant in height giving up to 18 free parameters (see table 5.3). The inversion is performed several times (up to 50 successful inversions) for each pixel with different initial values for the magnetic and dynamic parameters. To do so we set different random initial values for the magnetic field strength, inclination and azimuth and the LOS and microturbulent velocities of the input models. These values are randomly taken in the range showed in table 5.4. The result is given by the atmosphere model that best fits the observed full Stokes vector (best meaning the one with the smallest chi-square, see Eq. 3.12).

As will be shown in Sec. 5.4 there are some features like non antisymmetric two-lobe profiles, area and/or amplitude asymmetries that can not be fitted with this model. In order to estimate

TABLE 5.3— Relation of the main parameters defining the inversion strategy for the VTT.

Telescope:	VTT	VTT
SIR parameter	1 Magnetic	2 Magnetic
Number of cycles	3	5
Weight for Stokes I	1	1
Weight for Stokes Q	10	10
Weight for Stokes U	10	10
Weight for Stokes V	10	10
Nodes for temperature 1	2,3,5	2,3,5
Nodes for electr. press. 1	0	0
Nodes for microturb. 1	-1,1,1	-1,1,1
Nodes for magnetic field 1	1	1
Nodes for LOS velocity 1	1	1
Nodes for gamma 1	1	1
Nodes for phi 1	1	1
Invert macroturbulence 1	-1	-1
Nodes for temperature 2	2,3,5	2,3,5
Nodes for electr. press. 2	0	0
Nodes for microturb. 2	1	1
Nodes for magnetic field 2	0	1
Nodes for LOS velocity 2	1	1
Nodes for gamma 2	0	1
Nodes for phi 2	0	1
Invert macroturbulence 2	1	1
Invert filling factor	1	1
Continuum contrast	1	1

the influence of these populations we have performed a second inversion of the whole FOV with a different model.

In this second inversion strategy, we consider again two different atmospheres in the same resolution element. However this time both atmospheres are considered to be magnetic. An additional non-magnetic stray-light profile is used with a fixed contribution of 30%. This value is taken to be a compromise between the minimum value (20%) of Stray-light found by Beck et al. (2011) upfront the grating and the maximum value we found (50%) for which the inversion fit does not show sensitivity to the Stray-light factor. In order to get this value, we inverted, following this second inversion strategy, a set of 200 profiles with strong Stokes Q, U and/or V for Stray-light factors running from 1% to 99% in steps of 1%. The χ^2 of any of the Stokes parameters was found flat up to 50%. Above this threshold the Stokes I fit worsens with Stokes Q, U and V fits remaining flats. Just above 80% of Stray-light the χ^2 of Stokes Q, U and V become sensitive to the Stray-light, finding the worse fit the larger the Stray-light factor. The stray-light profile comes from the inversion of the whole FOV mean profile. This inversion is performed

TABLE 5.4— Minimum and maximum values for the random initialisation of the various model atmospheric parameters.

Parameter	min	max	units
B	0	2000	G
θ	0	180	degrees
χ	0	180	degrees
v_{LOS}^{mag}	-5	5	km/s
v_{mic}^{mag}	0	1	km/s
v_{LOS}^{no-mag}	-5	5	km/s
v_{mic}^{no-mag}	0	1	km/s

with much more freedom than the ones here explained since we are interested in a profile that fits very precisely the original profile but do not show features like noise or high frequency fringes.

The inversion configuration remains as in the previous strategy but this time we add three additional free parameters: the magnetic field strength, inclination and azimuth for the second magnetic atmosphere, increasing the number of free parameters up to 20. With this second model non-regular Stokes V profiles can be synthesised as well as amplitude asymmetries.

Figure 5.7 shows the comparison of the two inversion strategies for some of the VTT/TIP-II data used in this thesis. The figure shows three different examples of the two inversion strategies. In the first example (left column), Stokes I, Q and U are quite similarly reproduced but the difference resides in Stokes V. The inversion with a unique magnetic field atmosphere is unable to reproduce the three-lobed Stokes V profile while the one with two magnetic components fits it quite well. In the second case (middle column), Stokes I and V are similarly fitted and the problem arises with the velocity of Stokes Q and U compared to V. Hence the second magnetic component of the two magnetic inversion introduces a weak (62G) and inclined (98°) field with the adequate velocity to better match Stokes Q and U. Finally, in the third case (right column) the one-magnetic component inversion fits well Stokes I, Q and U but the middle lobe of the Stokes V profile can not be reproduced. The two magnetic atmospheres inversion clearly improves the fit with the addition of a rather weak (122G) and inclined (95°) magnetic field. The analysis of the results with the second strategy is presented in Appendix A. It is so because their comparison with the results of the first inversion strategy show similar results for the studied parameters in this work.

A well known issue about the magnetic field properties inference is that not always the determination of the magnetic field parameters is independent. When the magnetic field strength is not strong enough, there is a coupling between the LOS inclination, the magnetic field strength and the filling factor (Asensio Ramos et al., 2007). In this case the inverted magnitude are not these parameters independently but the LOS magnetic flux density instead: $\phi = \alpha\, B\, \cos\theta$. This situation holds as long as the Zeeman splitting is below or it is of the order of the Doppler width. In order to avoid these ambiguities when analysing the magnetic field strength and inclination,

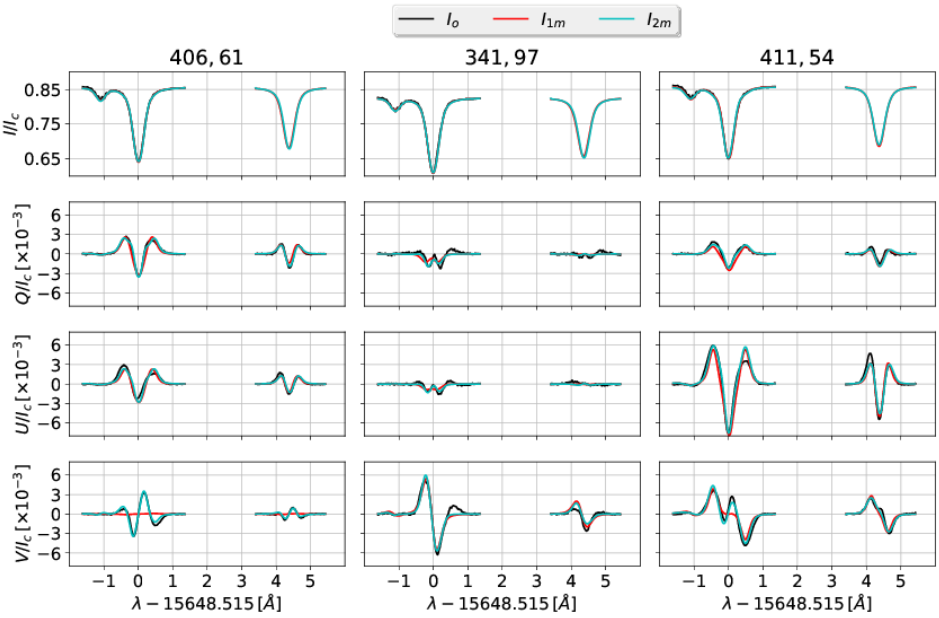

FIGURE 5.7— Inversion with the two different inversion strategies detailed in the text for three different pixels. Black solid line is the original profile, red is the inversion with a unique magnetic atmosphere and in cyan the profiles reached with two magnetic atmospheres. Middle pixel Stokes Q, U and V profiles are multiplied by a factor 5 in order to better visualise them.

we limit ourselves to those magnetic fields for which the Zeeman splitting is larger than the Doppler width. In order to set this limit we took 1000 thermodynamic model atmospheres at the disc centre and at the limb. We synthesised various 15648.515 Å spectral line profiles for increasing magnetic fields from 0 to 2000 G and calculated the distance between the maximum and minimum of the Stokes V profile. Figure 5.8 presents the result of this experiment. For disc centre it is seen that the splitting between the σ components is the same from the weakest fields up to 400 G, when the distance between lobes starts increasing. Above 500 G the splitting is unambiguously related with the magnetic field strength. In the following, the analysis for the magnetic field strength and inclination for disc centre will restrict to magnetic fields above this threshold. For limb data, the difference in the thermodynamic properties inferred make this threshold value increase a bit to around 600 G. This criterion does not consider the effect of linear signals. In the presence of linear Stokes signals, even under the above thresholds it is possible to subtract the inclination from the coupling. Though, as the lineal signals at disc centre are rather weak and at the limb data the strong linear signals coincide with strong magnetic fields, we consider that this criterion is appropriate.

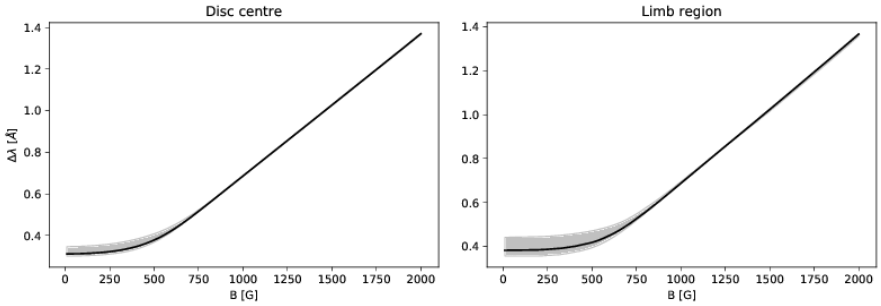

FIGURE 5.8— From left to right: Zeeman splitting dependence on magnetic field strength of the σ components of the 15648.515Å Fe I spectral line for disc centre and limb regions. The measurement of the splitting is performed for 1000 model atmospheres taken from the inversions. Grey shadowed area stands for the splitting in between the 25th and 75th percentile. Black solid line represents the 50th percentile.

5.4 Analysis based on one magnetic component inversions

5.4.1 LOS magnetic flux density

The LOS magnetic flux density (Φ) integrated over the polar region is the magnitude that usually defines the dominant polarity of the polar regions. In this case, since the area covered by our observations is very limited, this magnitude is not representative of the whole polar region as we can be subject to local inhomogeneities. The analysis of Φ is done for all the pixels with polarimetric signals above our 5σ threshold. It is so, because this magnitude is properly recovered no matter if the magnetic field strength, inclination and filling factor determination is coupled or not. In addition to the global analysis, we also look at the probability density functions (PDF) of Φ for the strongest polarimetric signals and the rest of the signals. This is so because the relative number of *strong polarity* patches in each of the FOVs is different and they can determine the shape of the PDFs. Figure 5.9 depicts the PDF of the various FOVs (columns) and in different rows, the PDF for the whole dataset, the strongest polarity patches, and the rest of the FOV.

In order to classify a structure with the label *strong polarity* we follow these steps:

1. We look for structures occupying more than 10 adjacent pixels whose absolute amplitude of Stokes Q, U or V is above $0.004\,I_c$

2. We look for structures of more than 10 adjacent pixels that have an absolute amplitude of Stokes Q or U above $5 \times 10^{-4}\,I_c$ or Stokes V absolute amplitude above $0.002\,I_c$. This different criterion for Stokes V is chosen to preserve the patchy character of the structures, as most of the FOV has signals of Stokes V. This criterion is fulfilled by all the structures at point 1 and by many more structures

3. Finally, those structures recovered in step 2 that harbour the patches identified at point 1 are classified as *strong polarity* patches

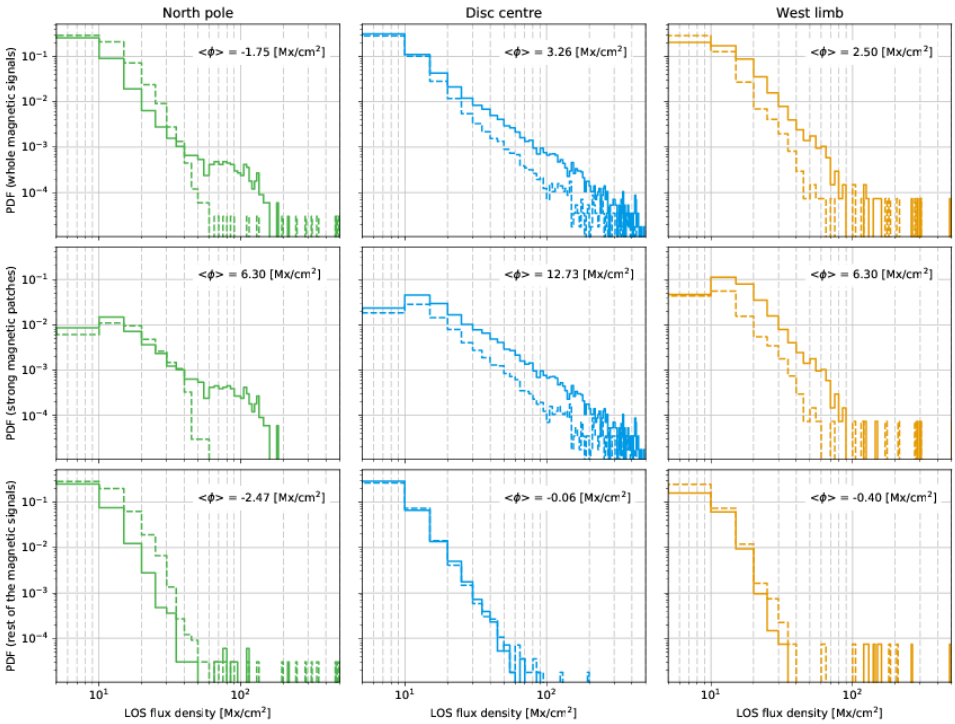

FIGURE 5.9— Probability density functions for the LOS magnetic flux density for each FOV, from left to right, North region, Disc centre and West region. The negative part of the distribution is folded to the positive one and represented with dashed lines. From top to bottom, the probability density functions for the whole dataset, that for *strong polarity* patches (see text for their identification) and for the rest of the surface.

Those regions represent the 25.97%, 8.24% and 43.31% of the magnetic signals at the disc centre, North region and West limb, respectively.

Disc centre FOV

At disc centre, the signed average LOS magnetic flux density is 3.26±0.03 Mx/cm^2. Its PDF is strongly dominated by weak LOS magnetic flux densities with 81% of the FOV exhibiting less than 10 Mx/cm^2. Yet those fields are quite balanced in polarity, with a mean LOS magnetic flux density of 0.14±0.01 Mx/cm^2. Those pixels with Φ stronger than 10 Mx/cm^2 are responsible of setting the polarity of the region, with a mean value of 16.7±0.1 Mx/cm^2. The contribution to Φ coming from *strong polarity* patches or from the rest of the surface is completely different. On the one hand, those patches classified as *strong polarity* (mid-mid panel) set the mean polarity of the region, with $< \Phi >= 12.7 \pm 0.1$ Mx/cm^2, even when they are representative of a 25% of the FOV. On the other hand, the rest of the surface (bottom-mid) is quite balanced in polarity

with a LOS magnetic flux density mean average of -0.05±0.02 Mx/cm^2.

West region FOV

West limb LOS magnetic flux density PDF is also dominated by very weak values, with 81% of the magnetic pixels characterised by a LOS magnetic flux density below 10 Mx/cm^2. Those fields are close to polarity balance ($< \Phi >_{<10} = 0.19 \pm 0.02$ Mx/cm^2) and the polarity of the observed area is due to the contribution of the rest of magnetic fields $< \Phi >_{>10} = 11.5 \pm 0.2$ Mx/cm^2. As in the previous case, when looking at the separated contribution from the *strong polarity* patches (mid-right panel) and the rest of the fields (bottom-right), it is clear that the polarity of the region is defined by *strong polarity* patches.

North region FOV

At the North pole, the PDF of Φ is again strongly dominated by weak values, 85% of the FOV is characterised by $\Phi < 10$ Mx/cm^2. The mean value of Φ over the whole region is negative $< \Phi >= -1.75 \pm 0.04$ Mx/cm^2. This sign is the dominant polarity of the North polar region previous to the maximum of 2014. Dating in 2013, these observations took place close to the maximum of 2014, when polar regions are close to their polarity reversal. For these solar heliographic latitudes, as it can be seen in Fig. 4.3, the observed Φ averaged over the visible longitudes is slightly positive and it is close to the polarity reversal. The change of the dominant polarity in polar caps is a long process during which both polarities coexist at the same time in the polarmost areas (Benevolenskaya, 2004). In this situation, a limited coverage of the polar region makes us to be subject to local inhomogeneities.

However, in contrast to disc centre or West limb datasets, for the North pole, the polarity of the region is established by weak polarity signals (mid-left panel) instead of the *strong polarity* concentrations (bottom-left). Whether this effect is due to the limited area covered or if it is proper of the polar region cannot be discerned with just this observation. At first, the West limb dataset cover a smaller area (one third of that at the polar region) and exhibits a more balanced polarity behaviour for those areas outside the dominant polarity patches. Yet, at the West limb, the whole distribution is much more sensitive to dominant polarity patches (the latter are representative of ∼43% of the magnetic pixels) than the polar region, where *strong polarity* patches give rise to 8% of the magnetic signals. Any large scale local event is discarded from the various AIA filters, which show no special features either before, during or after the observed polar target. At this point it is possible to conjeture an interesting scenario where *strong polarity* patches would carry the new polarity to be built up by the polar region for the new cycle, whilst the old polarity would be given by a weaker and more diffuse magnetic components. This scenario can be checked using Hinode data (in particular HOP79, HOP 81), which has been regularly recording data at polar regions during the last decade. The Solar Orbiter will also supply invaluable observations and magnetic information on this solar cycle phase from an exceptional observing angle.

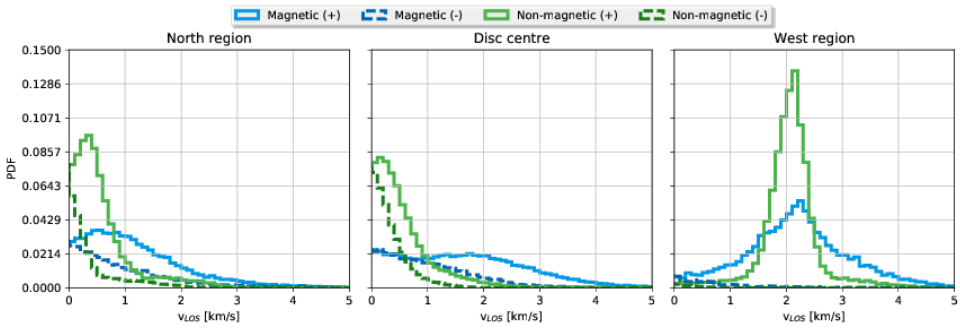

FIGURE 5.10— Velocity probability density functions of the non-magnetic (green) and the magnetic (blue) atmospheres. The negative part is folded to represent it at the positive range and they are plotted in dashed lines. From left to right the distributions hold for North region, Disc centre and West region.

5.4.2 LOS velocities

The LOS velocities for both the non-magnetic atmosphere and the magnetic one are presented in Fig. 5.10. LOS velocities follow the standard astrophysical notation with negative values towards the observer. In any of the observed disc positions, there is a sharp different behaviour between the magnetic and non-magnetic components. The magnetic component exhibits a wider distribution than the non-magnetic one.

Disc centre FOV

At disc centre, the non-magnetic LOS velocity PDF is very symmetric, though slightly red-shifted (an average of 0.257±0.005 km/s). This mean downflow can be due to the fact that the presented distributions are for those pixels that show polarimetric signals. In the quiet sun magnetic fields are weak enough to have a dynamic behaviour dictated by plasma motions. The quiet sun shows horizontal motions from the interior of upflowing granules to the boundary of downflowing intergranules. Magnetic fields are then accumulated at the edges of granules, where they coalesce or annihilate. In this sense, as the represented magnitudes are those where magnetic signals are detected, we might be sampling a subset of the quiet Sun with a preference for downflows.

The LOS velocity distribution of the magnetic atmosphere at disc centre shows a bi-modal behaviour. We fit a two gaussian model with a Levenberg-Marquardt algorithm, one of the modes is found to peak at 0.049±0.002 km/s, whilst the other, peaks at 1.730±0.002 km/s. On the one hand, the first peak is related with magnetic fields present both at upflows and downflows and whose orders of magnitude are similar. On the other hand, the second peak is related with downflows associated to the boundaries of granules and supergranules as it is seen from the mean intensity found for these fields, which is one standard deviation smaller than the mean of the whole dataset. This behaviour has been already observed (Khomenko et al., 2003, and references therein): that magnetic fields that are concentrated in the intergranules usually exhibit plasma downflows. Figure 5.11 presents the LOS magnetic velocity map for the magnetic and

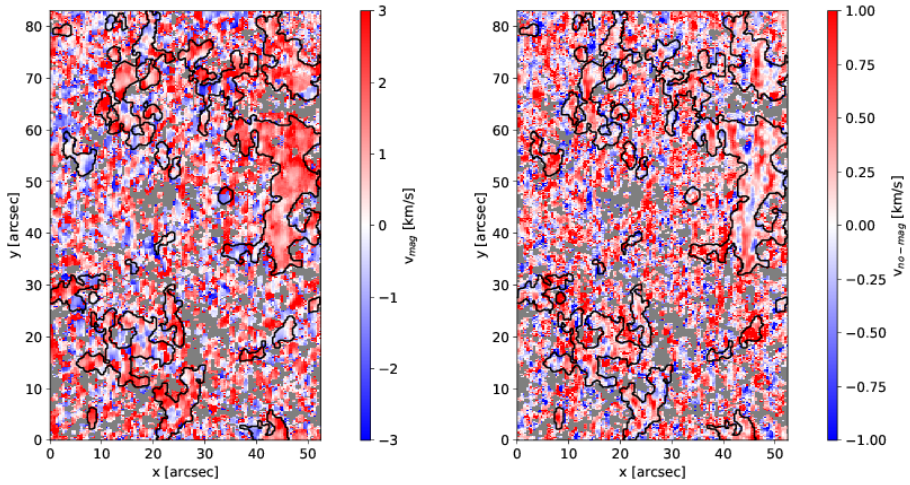

FIGURE 5.11— From left to right: disc centre maps of the magnetic and non-magnetic atmosphere line-of-sight velocities. Magnetic component saturates at ±3 km/s and non-magnetic component does it at ±1 km/s.

non-magnetic atmospheres. In this figure it can be seen that there are upflows and downflows. A very prominent feature related with the strong downflows observed is its mainly co-spatial with *strong polarity* patches (black contours).

West region FOV

The LOS velocity distributions for the West region are displayed in Fig. 5.10. The non-magnetic velocity is again characterised by a narrow distribution with a mean value of 2.035±0.003 km/s. This large mean LOS velocity value is due to solar rotation. The projection of solar rotation movement to the LOS direction is maximum at the limb. For the mean heliographic latitude (6.°8) and longitude (75.°8) of the FOV, the expected LOS velocity due to solar rotation profile is ≈1.98 km/s. This value can be calculated using the solar surface differential rotation profile as presented in Snodgrass & Ulrich (1990). Then, the cosinus of the solar longitude gives the projection of this surface motion to the LOS direction. Hence, if this value is subtracted, the distribution is already very close to rest, with an average of 0.06±0.01 km/s.

The magnetic LOS velocity PDF distribution at the West has its distribution centred at 2.065±0.01 km/s. This value is in very close agreement to that of the non-magnetic LOS velocities. There is a common scenario that can explain at the same time the observed magnetic and non-magnetic velocity distributions at the disc centre and at the West limb. In particular, if magnetic features have close to vertical downflows, then this would lead to a redshifted magnetic distribution, as it is seen. At the West however, the projection of this vertical movements to the LOS is minimised and hence, they do not exhibit a clearly different behaviour from the non-magnetic atmosphere. For the mean solar longitude of the West region (75.°8) a vertical 1.730 km/s, given

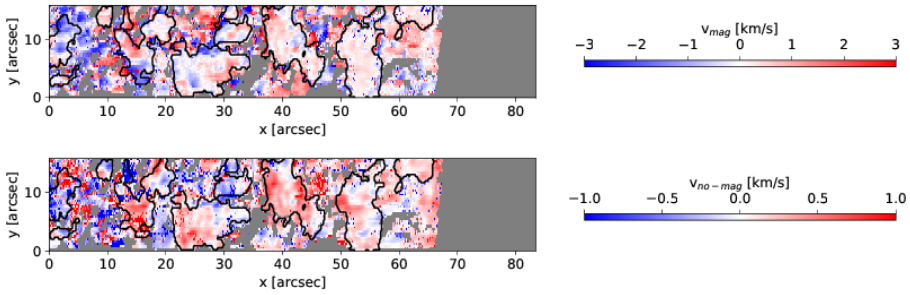

FIGURE 5.12— From top to bottom: magnetic and non-magnetic LOS velocity maps for West limb data. Magnetic component is displayed between ±3 km/s and the non-magnetic one between ±1 km/s.

by the disc centre behaviour, projects to the LOS direction a 0.447 km/s LOS velocity. This can explain the asymmetric magnetic LOS velocity distribution found, whose tail to larger values is more prominent that the one to smaller values. The spatial distribution of these velocities are plotted in Fig. 5.12 together with some examples from the FOV. This time, the *strong polarity* patches (highlighted in Fig. 5.12 with black contours) show weak LOS values of both signs with a slightly predominant red velocities.

North region FOV

The PDF of the non-magnetic LOS velocity at the North region is also given by a narrow distribution, whose mean value is at 0.306±0.001 km/s. When moving to the limb, it is expected that vertical movements decrease their LOS projection, whilst horizontal ones are expected to increase it. For instance, an effect that is already visible in the non-magnetic LOS velocity map (see Fig. 5.13) is the presence of redshifts of $\sim$ 1 km/s over two almost horizontal bands at about 30″ and 60″. Inside these bands, there are blue- and red-shifts of smaller magnitude. This picture is compatible with the presence of supergranulation, where the edges of these cells exhibit strong downflows whose projection to the LOS gives red-shifts. The horizontal movements inside these cells are found to be of the order of a few hundred km/s (Rieutord & Rincon, 2010). These movements are weak enough to be dominated by other plasma motions such as granulation movements. This scenario would naturally lead to the red-shifted mean value observed for the non-magnetic LOS velocity distribution. This situation is also expected for the West region, though the small FOV observed hides the observation of these large scale patterns. The magnetic LOS velocity distribution is broader than the non-magnetic one and its redish tail is dominant above the blue one. This behaviour is similar to that observed at the West limb. Hence the strong downflows observed for disc centre *strong polarity patches* seen close to the limb, project to the LOS direction a smaller value. Hence, there is no bi-modal behaviour close to the limb but an asymmetric magnetic distribution with a more prominent redish tail than the blue one.

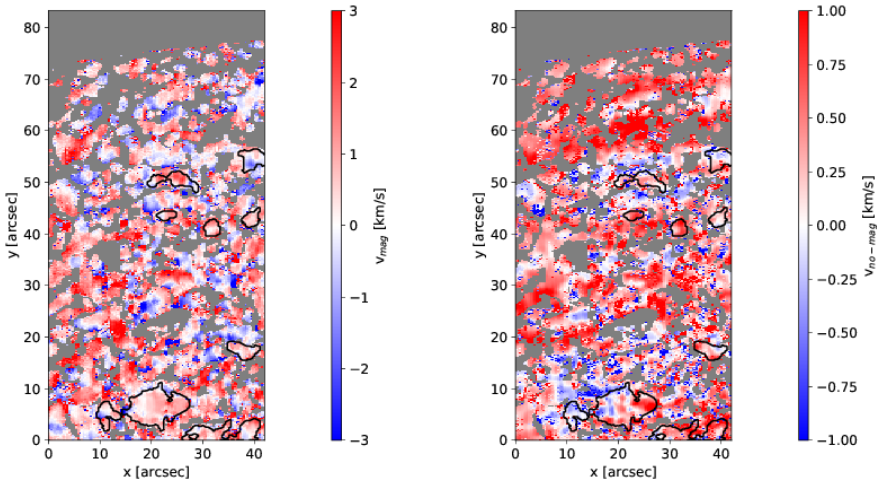

FIGURE 5.13— Same as in Figs. 5.11 and 5.12 but for the North region data.

5.4.3 LOS magnetic field topology

As mentioned in previous section (Sec. 5.3), we restrict ourselves to study the magnetic topology to those pixels that exhibit a magnetic field above a given threshold. This threshold is settled to 500 G at disc centre and 600 G to limb data according to the magnetic field strength above which the Zeeman splitting of the σ components is evident.

Disc centre

Figure 5.14 presents the magnetic field strength, LOS inclination, LOS azimuth, and filling factor PDFs for disc centre. Disc centre magnetic field strength is characterised by a gradual decay of the number of pixels with magnetic field strengths above 500G. These fields are seen to be preferably close to the LOS direction, which at disc centre position is also the vertical to the solar surface. This behaviour is well known to be due to magnetic buoyancy (Spruit, 1976; Parker, 1978). For strong enough magnetic fields, the effect of the magnetic pressure term favours the vertical configuration of these fields. In addition to this properties, these fields have very homogeneous LOS azimuths with no preferred orientation. Finally, the PDF of the filling factor shows a strong preference for small values (below 0.3).

The spatial distribution of these magnitudes over the FOV is presented in Fig. 5.15. In this figure, it can be seen that the spatial distribution is not homogeneous but it forms patchy structures. Moreover, the strongest magnetic fields, (for instance those at x:48″, y:50″, or x:14″, y:70″) are associated with the closer to 180° (0°) LOS inclinations, i.e. the strongest fields are the most vertical ones. Also their filling factors are the biggest ($\sim$ 0.4), around which, the LOS azimuth seems to describe a radial expanding/converging configuration. There is wide agreement that these strong magnetic features are due to the presence of vertical thin magnetic

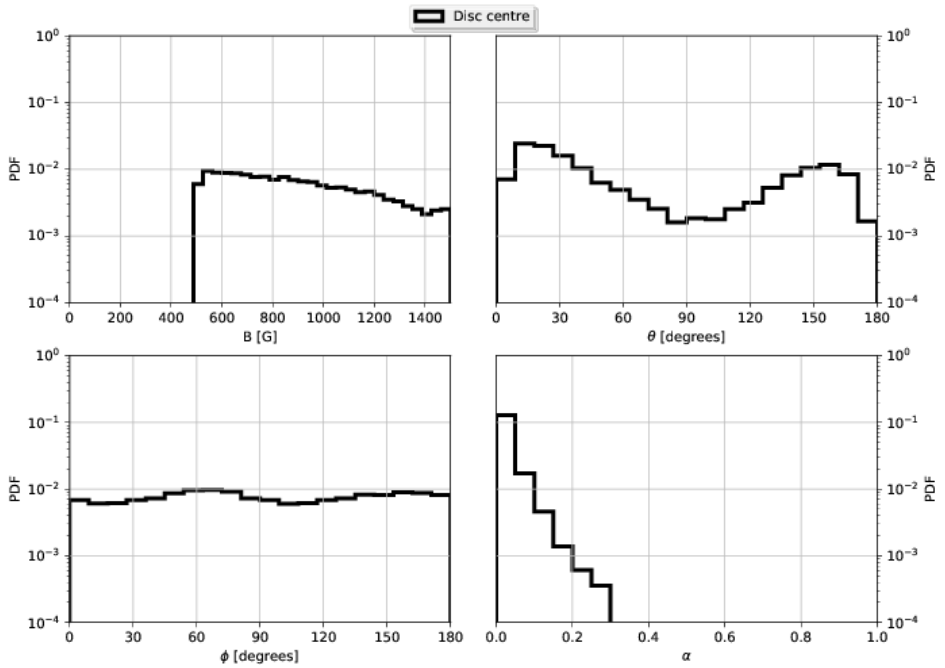

FIGURE 5.14— Top row, from left to right: probability density functions for the LOS magnetic field strength (B) and LOS magnetic field inclination (θ). Bottom row, from left to right: probability density functions for the LOS magnetic field azimuth (ϕ) and LOS magnetic field filling factor (α). Here those pixels of disc centre dataset classified as giving reliable information in the inversion process are represented.

flux tubes (Spruit, 1976; Schüssler, 1990). At the spatial resolution of these observations it is not possible to spatially resolve their size. However, it is possible to check wether the observed magnetic parameters are compatible with these tubes size. Our pixel size is $0\farcs35 \times 0\farcs185$ and the mean filling factor value for this strong features is around of 0.3. Assuming flux tubes with circular sections, these values give a flux tube radius of $\sim$117 km, which is in close agreement with the measured size observed with the highest spatial resolutions (Lagg et al., 2010) and with theory (Schüssler, 1990). The fact that we see large (compared to this few km) magnetic patches can be due to two reasons. On the one hand, the observed structures are blurred by the point spread function of the seeing and of our optical system. This effect can lead to see as a resolved structure, one which is actually below our resolution element. On the other hand, these kG magnetic structures are usually observed in groups rather than individually. The join action of these two effects can explain the fact that we observe these structures covering a large area of the observed FOV.

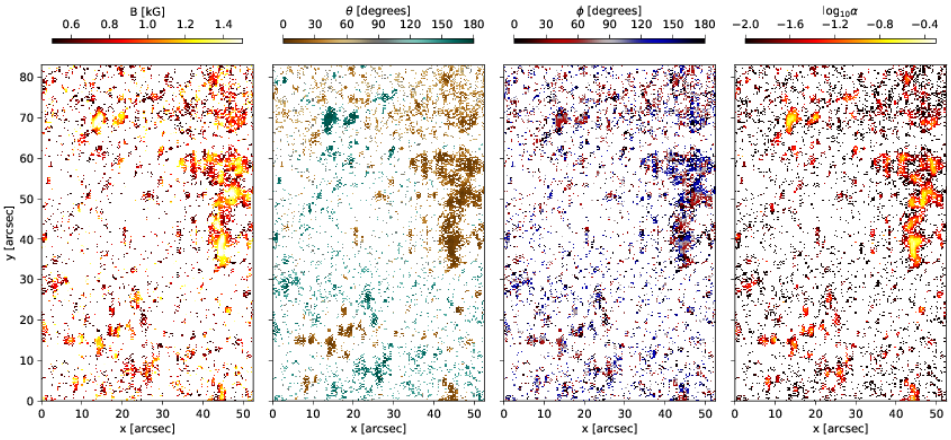

FIGURE 5.15— Disc centre spatial distribution for the reliably inferred magnitudes, from left to right: LOS magnetic field strength (B), LOS magnetic field inclination (θ), LOS magnetic field azimuth (ϕ) and magnetic field filling factor (α).

West region

The West limb LOS magnetic field strength, inclination, azimuth and filling factor probability density functions are shown in Fig. 5.16. The magnetic field strength distribution at West region is similar to that observed at disc centre (grey scale, labelled as "synthetic") with an overall decay from weaker to stronger fields. In this case however, the large fraction of the FOV occupied by strong polarity patches, which are associated (see below) with strong magnetic fields, makes this distribution to have a local maximum around field strengths of 1100 G, which is absent at disc centre.

At this disc position, LOS direction and vertical direction do not match anymore. Hence, the LOS inclination and azimuth are not readily interpreted. This step is properly tackled changing the LOS reference frame to the LRF. This change is subject to the proper resolution of the 180° LOS azimuth ambiguity and it is considered in the following section (Sec. 5.4.4). It is interesting to check the mutual compatibility between the observed LOS inclination and azimuth at the limb data and the distribution observed at disc centre. To that aim we can take the LOS magnetic field inclination and azimuth at the centre of the Sun and project it to any quiet sun region. In particular, to the West limb position. Notice that, at this point, we have not solved the LOS azimuth 180° ambiguity for disc centre position, so we proceed as follows: 1- We do not require spatial coherency. 2- As we have not solved the LOS azimuth 180° ambiguity yet, the assumed LRF distribution is actually affected by this issue for each point. To handle this problem we take one of the two possible LRF azimuth randomly. We consider that this assumption is not strongly relevant in the calculation because, for disc centre, the observed LOS azimuth

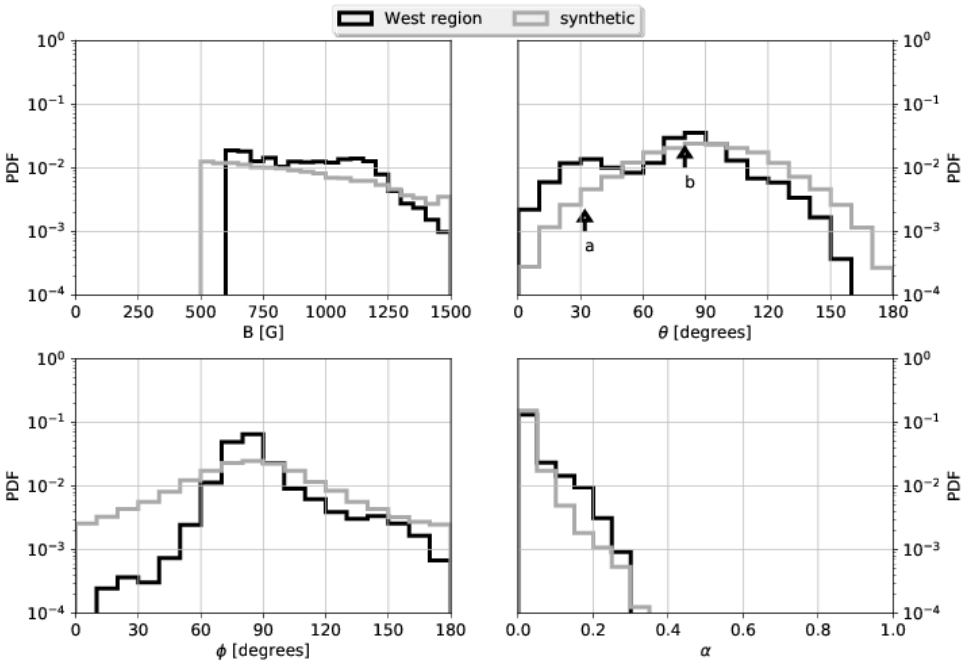

FIGURE 5.16— Dark solid line: West limb probability density function of different magnetic parameters for those pixels considered to be giving reliable inferred parameters. Top row: from left to right: probability density functions for the LOS magnetic field strength (B) and LOS magnetic field inclination (θ). Bottom row: from left to right: probability density functions for the LOS magnetic field azimuth (ϕ) and LOS magnetic field filling factor (α). In grey colour, the same LOS magnetic field magnitudes for a LRF disc-centre-like magnetic topology as would be observed at the West limb positions.

is homogeneous, so from an statistical point of view, there is no reason to prefer one solution or the other. When proceeding this way, we additionally keep the information of the magnetic field strength and filling factor for each magnetic field considered, so that, these parameters distributions can also be compared.

This method only handles with effects due to the magnetic geometrical change when changing the viewing angle, i.e., how a given magnetic field vector at disc centre would be seen at any other disc position. However, there are other effects such as the differences due to the limb effect that are omitted in this study. We do not consider changes in the radiative transfer, the limb darkening, or different pixel size over the solar surface, ... Despite these effects are not considered, this simple exercise gives some insight in the topological agreement between different disc positions topology.

The result of this exercise is overplotted in grey in Fig. 5.16. First of all, the projected dis-

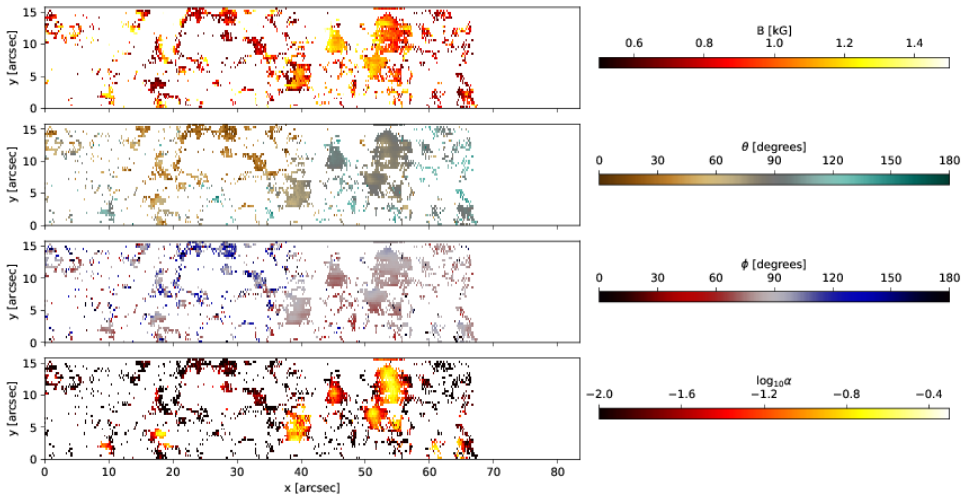

FIGURE 5.17— West limb spatial distribution of from left to right: LOS magnetic field strength (B), LOS magnetic field inclination (θ), LOS magnetic field azimuth (ϕ) and magnetic field filling factor (α). Only those pixels considered to give reliable inverted parameters are presented.

tribution of the field inclination peaks at 90° with broad symmetric tails to 0° and 180°. The peak is associated to the fact that vertical magnetic fields (as are those at disc centre) when observed at a given heliocentric angle, are characterised by LOS inclinations of the same value as the heliocentric angle (or 180°- heliocentric angle).

The observed LOS inclination distribution for the West limb data also has a peak close to 90° but it is slightly shifted to lower values ∼80°. If this peak is due to close to vertical fields (as it is at disc centre), then this offset from 90° to lower values (see arrow *a* in Fig. 5.16) means that there is a dominant polarity. Otherwise, there would be two peaks at symmetric distance around 90°. Since the peak is towards smaller values and assuming it is due to vertical fields (as at disc centre) then, at the LRF there is a dominant positive polarity. Another interesting feature observed at the West limb is a second peak (see arrow *b* in Fig. 5.16) in the LOS inclination distribution at around 30°. These field orientations have no observed counterpart at disc centre, as it is deduced from the shape of the recovered LOS inclination for a disc-centre-like magnetic topology. These bi-modal behaviour is further considered below.

West limb magnetic fields prefer LOS azimuth close to 90°. This LOS azimuth distribution is consistent with the topology seen at the disc centre, i.e. vertically dominated fields, as it can be seen from the also preferred LOS azimuth of 90° for the synthetic distribution obtained after projecting the disc centre fields to the West limb. This is due to the fact that the projection to the sky plane of vertically dominated fields at West limb are aligned in the E-W solar direction.

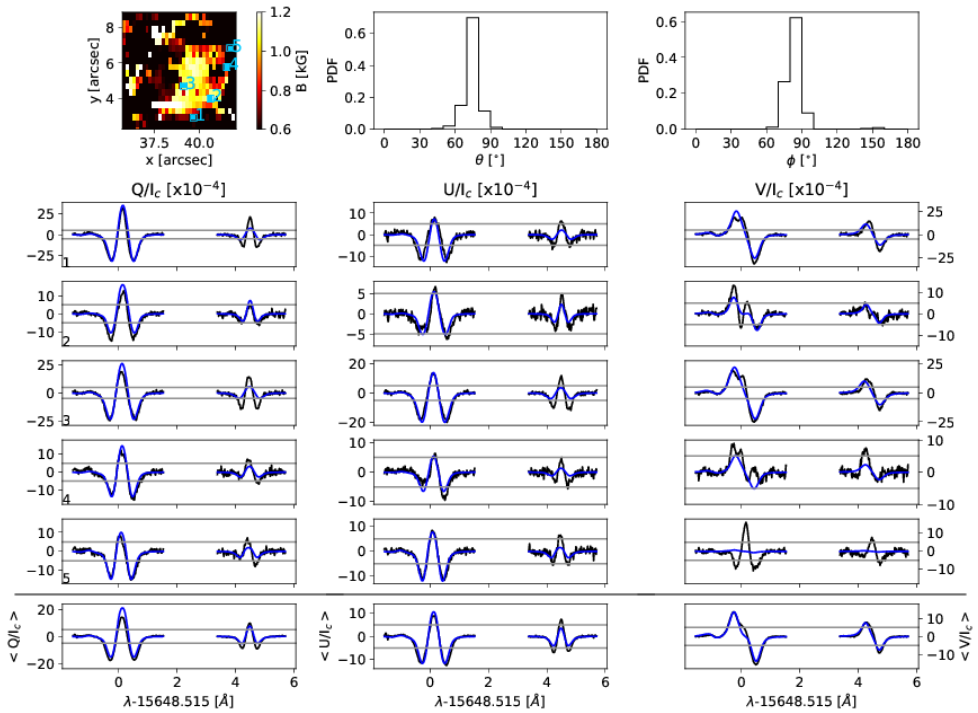

FIGURE 5.18— Top row, from left to right: the magnetic field intensity map of the structure considered, the probability density function of the LOS magnetic field inclination and the LOS magnetic field azimuth probability density function. The panels below, from left to right are: the Stokes Q, U and V observed profiles (dark line) and inversions (blue lines) for the various pixels highlighted on the image. The bottom row shows the observed (black) and inverted (blue) profiles averaged over the whole structure.

The magnetic filling factor distribution at this disc position is slightly different to that at disc centre. For the West limb, the distribution is slightly shifted towards greater values. This is due to the different relative weight of *strong polarity* patches, which are associated to larger filling factors (see below) and, at this disc position, these patches occur more frequently in the West FOV than at disc centre one.

Figure 5.17 shows the spatial distribution of the magnetic parameters. As for the disc centre, the strongest magnetic field strengths are associated with the largest filling factors. At this disc position, the strongest magnetic patches exhibit a decaying magnetic field strength from the side of the structure facing disc centre to limbwards side (see x:54°, y:11° for a very clear example). Furthermore, the magnetic filling factor in such structures is characterised by smaller

values at both sides, the one facing disc centre and the one limbwards. These kind of magnetic features show a LOS azimuth which gradually moves from lower than 90° at the bottom part of the structures (redish colour) to values slightly above 90° in the upper part of the structure (bluish colour).

The magnetism at the West limb shows a sharp difference behaviour when compared to disc centre topology. This is seen when projecting the observed magnetism at disc centre to the West disc position. The clearest feature highlighting this difference is the bi-modal behaviour observed at the LOS magnetic field inclination (marked with arrows *a* and *b*). In order to further explore the reason for such bi-modality, we picked two magnetic structures at the West dataset whose topology resembles that of each modes. First, let start with an example of a typical structure characterised by *b*.

This structure covers an area of $\sim 3'' \times 4''$ and it is characterised by magnetic field strengths from 800 G to 1.2 kG. On the right panels, some typical Stokes Q, U and V profiles are shown. The amplitudes of these profiles are well above the chosen 5σ threshold (marked in grey horizontal lines in the figure), in any of the linear or circular polarisation profiles. Moreover, linear polarisation profiles reach largest amplitudes than those of Stokes V profiles. This picture is hardly seen at disc centre. This sharp change between the observed polarisation Stokes profiles at disc centre and at the West limb can be understood by the change of the viewing angle. If we look at a vertical field at disc centre, it gives large Stokes V amplitudes and very faint linear polarisation profiles. This very same magnetic field seen at the limb however, strongly reduces the amplitudes for Stokes V since the projection to the LOS of a vertical magnetic field close to the limb is very small. In contrast, the component of this magnetic field on the sky-plane is enhanced, giving rise to strong linear polarisation signals, as it is observed. The presence of vertical fields, which are widely observed at disc centre, can explain these fields (see for instance Solanki, 2009, and references therein).

Let consider now an example of a magnetic structure whose topology is representative of mode *a* (Fig. 5.19). In size, this magnetic patch is similar to that of Fig. 5.18, covering $\sim 2'' \times 2''$. This structure also shows Stokes V polarisation signals above our 5σ threshold, reaching amplitudes of the order of 1×10^{-3}. However, there is a clear difference with the structure in Fig. 5.18, i.e. the Stokes linear polarisation signals hardly go above the noise level. It is to be said that, even the weakness of the linear Stokes profiles, the azimuth inferred for the structure is highly aligned in the E-W direction. This situation is not expected if the Stokes linear profiles are pure noise, so this might be indicative of a coherent, though very weak, magnetic field orientation. The average of the linear polarisation profiles should, for a weak but for a similar and coherent behaviour, present a Zeeman-like pattern. This averaged is presented in the last row of Stokes profiles in Fig. 5.19. As it is seen, both Stokes Q and U polarisation profiles have familiar Zeeman shapes and the averaged inversion fits quite well, i.e. the code, even the faintness of the signals, is able to catch this features. From this scenario, it is clear that these fields can not be explained by the presence of a purely vertical structure. However, we wonder what kind of magnetic field topology can explain such an observation.

Of the various scenarios considered, there is one that can potentially explain this situation.

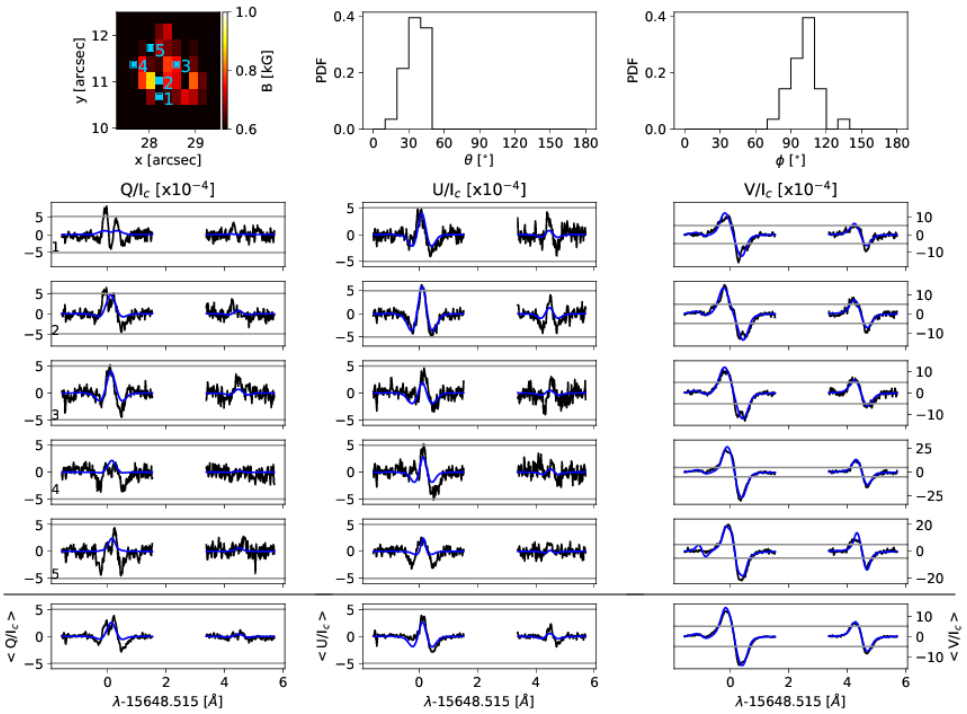

FIGURE 5.19— Same as in Fig. 5.18 but for another structure present in the West limb dataset.

From some years to nowadays, there have been reports of the observations of magnetic loops (Martínez González et al., 2007b; Centeno et al., 2007; Martínez González & Bellot Rubio, 2009; Ishikawa et al., 2010; Martínez González et al., 2010; Gömöry et al., 2010; Wiegelmann et al., 2010; Martínez González et al., 2011; Manso Sainz et al., 2011; Martínez González et al., 2012; Guglielmino et al., 2012; Viticchié, 2012; Gömöry et al., 2013). These structures consist of two feet of opposite polarity that are linked by an arc-like magnetic system, whose size varies from sub-arcsecond to a few seconds of arc. Magnetic loops appear in various shapes and magnetic field strengths and their emergence is not homogeneous nor in time neither in space. When observing at the limbs, the foreshortening strongly reduces our spatial resolution, so, could an unresolved magnetic loop explain an observation such that on Fig. 5.19?

In order to have an insight on the answer, we qualitatively discuss the case of a simplified loop model. In this model, the loop would be given by three magnetic vectors, a, b and c (see left panel in Fig. 5.20), two, verticals and of opposite polarity (a and c), labelled as feet. The third vector (b), labelled as bridge, would be the one connecting both feet. For the sake of simplicity, we consider a loop at the very limb at different configurations. First, the loop is perpendicular

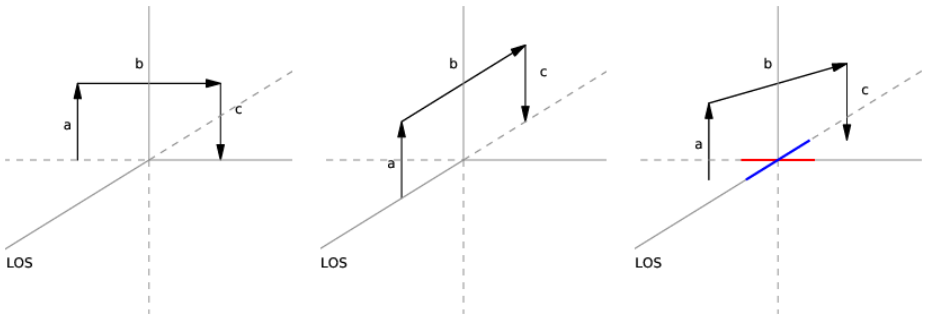

FIGURE 5.20— Schematic draw of three different configurations of a staple-like loop at the very limb of the Sun. From left to right: a loop perpendicular to the LOS, a loop aligned with the LOS and a loop at 45° from the LOS. Red and blue lines in the latter are the perpendicular to LOS and the LOS projections of *b*.

to the LOS (left panel in Fig. 5.20). In such a case, no magnetic field vector would give rise to circular polarisation, as all of them are perpendicular to the LOS. Both feet magnetic vectors (*a* and *c*) give rise to linear polarisation signals in the radial direction. If we set the origin of magnetic azimuth in positive Stokes Q and aligned with the radial direction, then both feet give rise to positive Stokes Q signals. In the other hand, *b* magnetic field, would be perpendicular to the previous case and hence, would give rise to negative Stokes Q signals. So for the particular case of this configuration, an unresolved loop would tend to show no polarimetric signal. Second, another possibility is when the loop is aligned with the LOS (middle panel in Fig. 5.20). In this case, both feet (*a* and *c*) again would give rise to positive Q signals as they are aligned with the radial direction. But now, the bridge (*b*) is along the LOS direction and gives rise to Stokes V polarisation signals (the sign depending if the loop is facing us —positive Stokes V— or not —negative Stokes V—. In this case, the unresolved loop would give rise to both Stokes V and Q, with their amplitudes depending on the heights at which the spectral line used is sensitive to and to the particular configuration of the loop. Finally, we consider an intermediate case, in which the loop is in between the previous two (right panel on Fig. 5.20). In such a case, both feet (*a* and *c*) give, again, linear polarisation signals in the radial direction (positive Stokes Q). However, now, the bridge (*b*) has magnetic component projected to both the LOS and the perpendicular to it, i.e. this time the bridge gives circular and linear polarisation at the same time. The LOS component (blue in the figure) gives Stokes V polarisation signals. The perpendicular to the LOS component (red in the figure) gives rise to negative Stokes Q, as it is in the perpendicular to the radial direction. This way, an intermediate case, gives Stokes V signals (the bridge) and Stokes Q signals, which are given by the contribution of both feet minus the contribution of the linear polarisation signal of the bridge. At this point it is important to remember that VTT polarimetric calibration takes Earth N-S direction as the reference for positive Stokes Q. That is the reason why we observe Stokes Q and U signals for the solar radial direction. The change from Earth to solar reference frame requires taking account the P0 angle that, for the observation date was 23.°88.

The model here considered is very simple. To begin with, the staple-like loop is convenient to have a readily interpretation of the contribution from each part of the loop. More realistic loop shapes (like the ones in Martínez González et al. 2010 or Ishikawa et al. 2010) have to be considered. Furthermore, the above qualitative argument is done at the very limb, though our data covers solar surface areas whose heliocentric angles go down to 70°. In both cases, we expect that the more realistic models would change the relative weights of the contributions from the various loop parts, though not enough to invalidate the general picture here considered. If so, in this scenario it would be possible to reproduce the observed features of structures like the one in Fig. 5.19. First, the presence of circular polarisation signals. Second, the presence of linear polarisation signals, given by the competition of the linear signals coming from the feet and bridge, that could potentially give rise to weak but coherent and preferred linear polarisation signals.

North region

The North region magnetic PDFs in the LOS reference frame are shown in Fig. 5.21. The North region has a lower of strong fields than the disc centre region once this last has been projected. This is consistent with the fact that the fraction of *strong polarity* patches at North region is much smaller than at disc centre and with the fact that the strongest magnetic fields at disc centre are present in these patches.

The LOS inclination distribution is clearly different from that expected for a disc-centre-like magnetic topology. In particular, instead of the smooth distribution of a disc-centre-like case, the North region LOS inclination distribution is characterised by three localised bumps. The one highlighted with b arrow, resembles what one would expect for vertical fields at this disc centre position. As for the West region, this local maximum is shifted from 90° towards smaller values. If these inclinations are associated to vertical magnetic fields (as it is the case at disc centre), then the fact that their inclination is slightly shifted from 90° is the result of a dominant LRF positive polarity. The other two peaks, marked with arrows a and c in Fig. 5.21 share properties between them and with the previously analysed magnetic patches for West region dataset. Further analysis of these fields is performed below.

The LOS azimuth observed (see Fig. 5.21) is strongly concentrated in the N-S solar direction. This direction is naturally obtained for a disc-centre-like topology. It is so because for a mainly vertical distribution, the projection of the LRF vertical to the sky-plane of the magnetic field vector when approaching to the limb, is in the radial direction. Indeed, for the North case, this direction agrees with the solar N-S direction. Notice, however, that this time vertical magnetic fields (those that show a LOS inclination close to 75°) are not the more numerous, as it was the case for the West limb, or as it is expected from the disc centre distribution, i.e. the whole magnetism analysed is aligned in this direction. Finally, the magnetic filling factor is also characterised by small filling factors (≤ 0.1) which slightly increase (~ 0.2) in the strongest magnetic fields, as can be seen in Fig. 5.22.

The North region dataset magnetic parameters spatial distribution are presented in Fig. 5.22. On the one hand, some magnetic patches are consistent with the expected topology from a

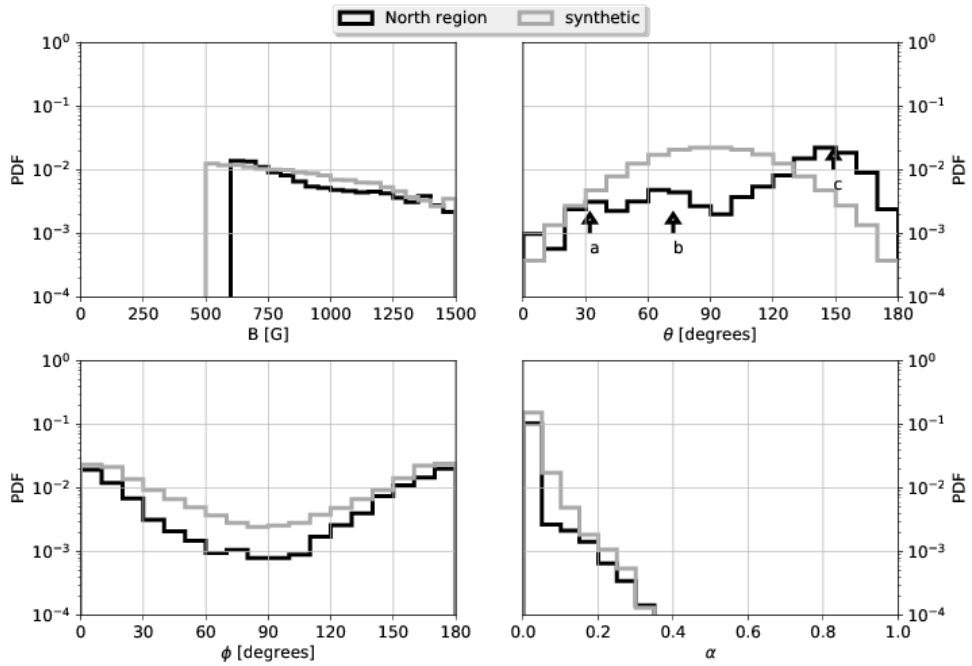

FIGURE 5.21— Dark solid line: North region probability density function of different magnetic quantities: Top row: from left to right: probability density functions for the LOS magnetic field strength (B) and LOS magnetic field inclination (θ). Bottom row: from left to right: probability density functions for the LOS magnetic field azimuth (ϕ) and LOS magnetic field filling factor (α). Only those pixels classified as giving reliable information in the inversion process are presented. In grey colour are the LOS magnetic field parameters expected for the observed disc centre magnetic field topology as it would be seen at the observed North region.

disc-centre-like one. For instance, the strongest magnetic fields are characterised by the largest magnetic filling factors. In this solar disc region, this statement mainly holds for the magnetic structure at x:$\sim$ 20″, y:$\sim$ 7″ (zoomed in in Fig. 5.23). These fields are characterised by LOS inclinations close to $\sim 90^\circ$ (b in Fig. 5.21) and their LOS azimuths are mostly along the N-S direction. On the other hand, and in contrast to the West region, most of the rest of magnetic patches have LOS magnetic field inclinations around 30° and 150° (a and c in Fig. 5.21). A very clear example of this population is the clump of structures observed at x:$\sim$ 10″, y:$\sim$ 30″, part of which is enlarged in Fig. 5.24.

In Fig. 5.23 an example of a magnetic patch with LOS inclinations close to peak b (Fig. 5.21) is presented. The structure has a size of $5'' \times 3''$ and is characterised by strong magnetic fields, ranging from 900 G to 1.5 kG. In this structure, the Stokes Q, U and V profile amplitudes are clearly above the noise level (grey horizontal lines), and as in the case of Fig. 5.18, linear polarisation profiles can reach larger amplitudes than Stokes V profiles. Again, this can be understood

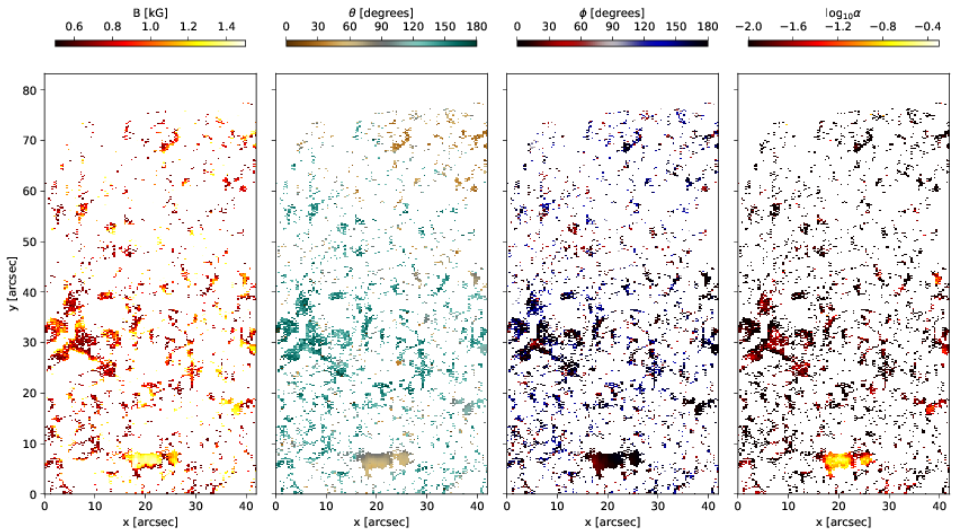

FIGURE 5.22— Spatial distribution at the North region of, from left to right: LOS magnetic field strength (B), LOS magnetic field inclination (θ), LOS magnetic field azimuth (ϕ), LOS magnetic field filling factor (α). The presented results are only for those pixels where the inferred magnetic parameters are considered to give reliable information.

from the change in the viewing angle of vertical fields, that close to the limb, strongly enhance linear polarisation signals.

Figure 5.24 shows an example of an structure of these magnetic fields with LOS inclination at c in Fig. 5.21. Its size is similar to the others considered here, $\sim 3'' \times 4''$ and the magnetic field strengths range from 700 G to 1. kG. Again, these pixels are characterised by Stokes V amplitudes above the noise level whilst linear profiles hardly reach this level. However, and similarly to what it was observed in Fig. 5.19, the azimuth of the whole structure is highly coherent and aligned with the solar radial direction. This structure is also consistent with the presence of unresolved loops.

5.4.4 LRF magnetic field topology

Once we have an idea about the magnetic configuration at the limb data from LOS magnetic field parameters, we now rotate the magnetic field vector in the LOS reference frame to the LRF. This step is not performed over those structures whose topology is compatible with the presence of an unresolved loop because the observed configuration is due to the combination of various underlying fields. The change from LOS to LRF is detailed in Sec. 3.3 and the most

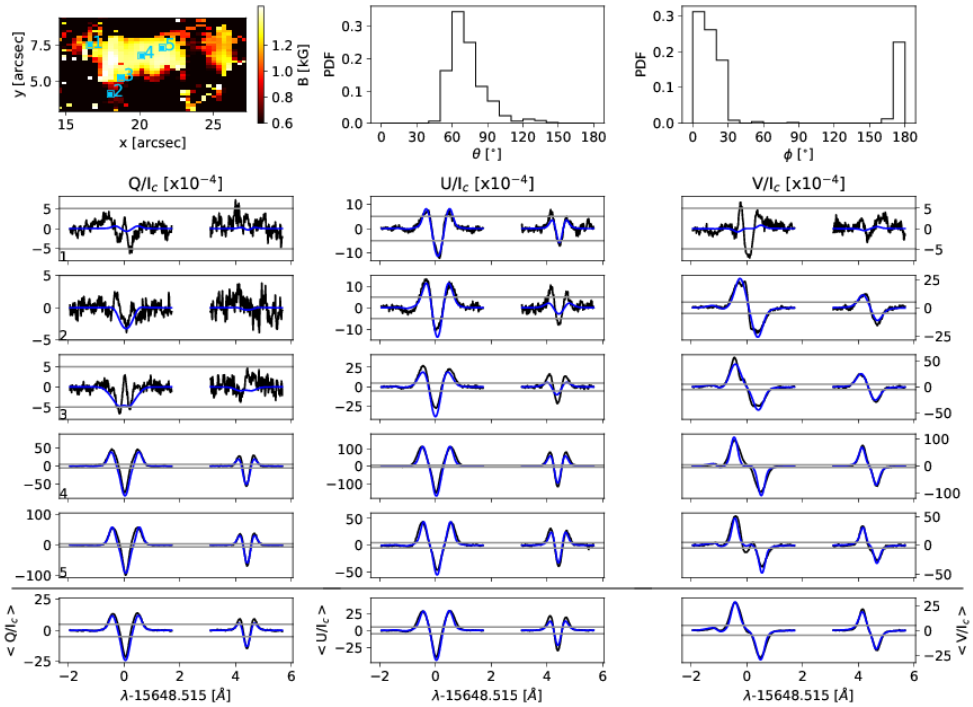

FIGURE 5.23— Same as in Fig. 5.18 but for a structure present in the North limb dataset.

delicate problem resides in solving the 180° ambiguity of the LOS azimuth. The rotation to the LRF is made in two steps, which are detailed below:

- calculate the helioprojected solar longitude and latitude of each point,
- get the two possible LRF configurations for each pixel, associated to the two possible values of the LOS azimuth,
- identify magnetic patches whose structure is assumed to be coherent,
- for each structure, recover the general LRF solution that minimises the difference between the LRF magnetic field with the adjacent LRF configurations inside the structure.

Following this analysis we obtain 8 (7) structures that cover 4.52% (12.21%) of the North (West) limb dataset. Now we have two possible magnetic configurations for each magnetic patch detected (see for instance Fig. 5.25).

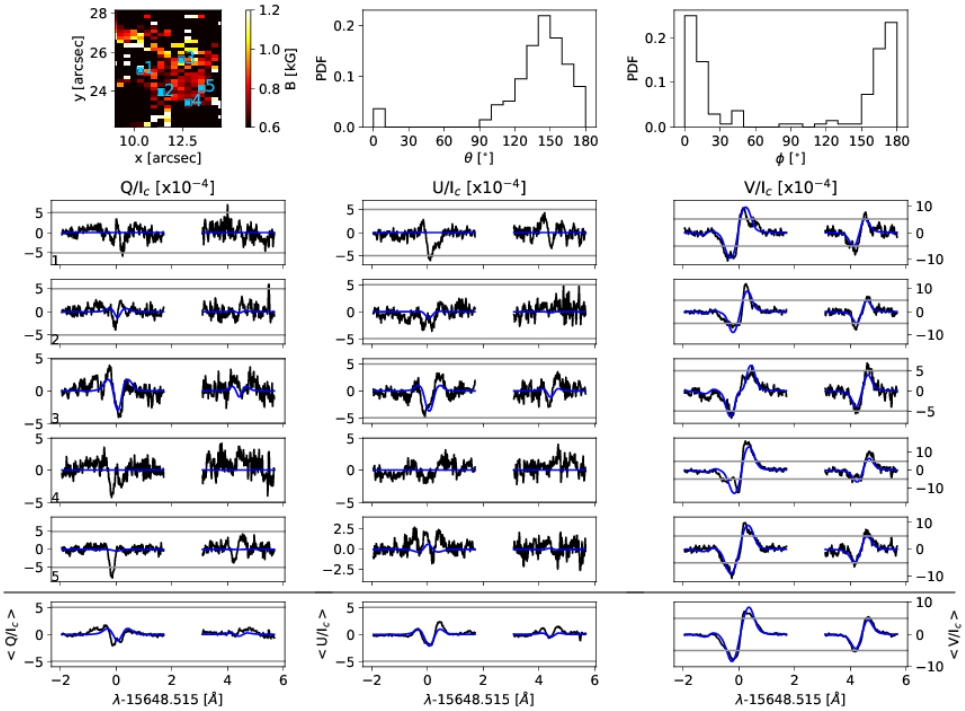

FIGURE 5.24— Same as in Fig. 5.18 but for a different structure to the one in Fig. 5.23 present in the North limb dataset.

The second step is to choose one of the solutions retrieved. To do so we choose as the more feasible structure the one that makes the final LRF azimuth distribution as homogeneous as possible. This is done by looking for the flattest final LRF azimuth distribution.This methodology leads to two final magnetic distributions, the one that is kept as the more likely (hereinafter named as preserved) and the discarded one (hereinafter, discarded).

North region

The LRF inclination and azimuth distributions are presented in Fig. 5.26. The preserved LRF inclination distribution shows vertical fields of both polarities, with dominant positive polarity. This is consistent with the above-mentioned argument about the shift of the LOS inclination distribution to smaller than 90° values. The retrieved LRF azimuth for these vertical fields is homogeneous. It is true that this is the criterion used to choose the "real" 180° LOS azimuth ambiguity solution, however, the important result is that there exist a solution which is compatible with the topology observed at disc centre.

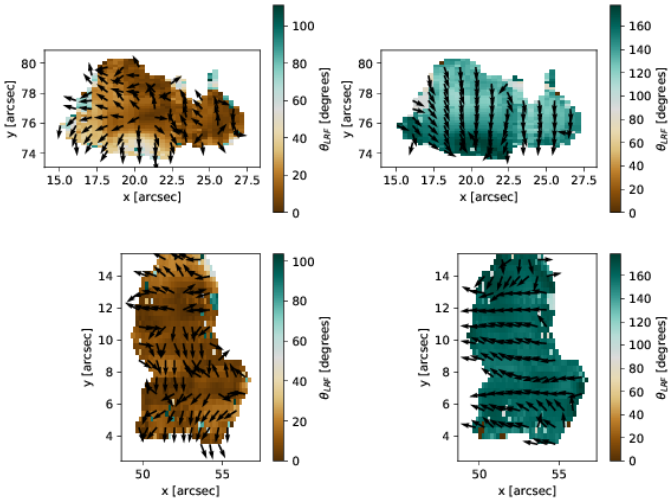

FIGURE 5.25— From top to bottom: two structures taken from the North region dataset and from West region, respectively. The local reference frame magnetic field inclination is in colour scale. Arrows show the local reference magnetic field azimuth. Arrows are plotted for one every three pixels in each direction for the sake of visibility. Each column represents one of the two possible solutions retrieved due to the line-of-sight magnetic field azimuth 180° ambiguity.

The discarded solution LRF azimuth is strongly aligned with the N-S solar direction. The LRF inclination distribution discarded is characterised by a strong preference for LRF inclination at 30° and 150° fields. This discarded topology has a preferred orientation aligned with the solar radial direction and at mid-inclined fields. Since this is a ver singular orientation, for which we found no argument to support, we are confident that the preserved solution is the more likely one.

West region

West limb LRF distributions are presented in Fig: 5.27. The preserved LRF distribution is characterised by a very homogeneous LRF magnetic field azimuth with a vertically dominated LRF inclinations. This topology is consistent with the observed one at disc centre, and the retrieved one for North region, i.e. there exist a coherent scenario that can explain the analysed magnetism topology at the three disc positions.

Similarly to the North case, the discarded solution defines a very singular topology. LRF inclinations are also mid-inclined, with a strong preference for negative polarities and their azimuth is aligned with the solar radial direction.

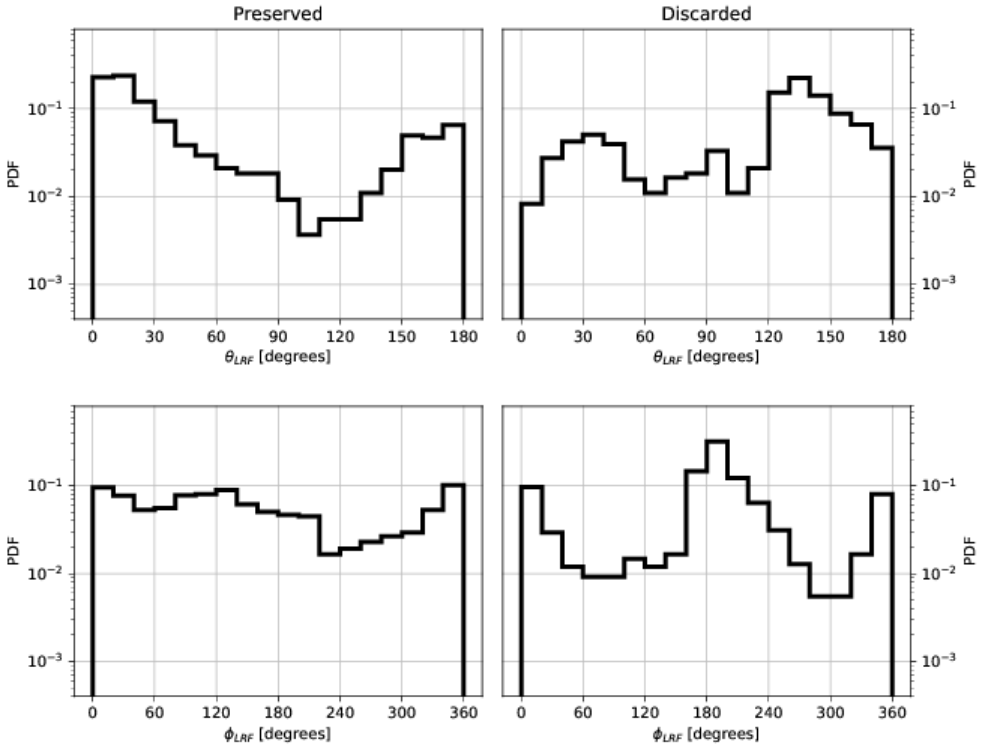

FIGURE 5.26— Left panels, from top to bottom: probability density functions of the preferred local reference frame magnetic field inclination (θ_{LRF}) and azimuth (ϕ_{LRF}) for the North region dataset. Right panels, from top to bottom: probability density functions of the discarded local reference frame magnetic field inclination (θ_{LRF}) and azimuth (ϕ_{LRF}).

5.5 Summary and discussion

- The observed FOVs are pervaded of magnetic signals, up to 80% of the observed area of any polarised Stokes parameter and up to 20% of either Q or U Stokes profiles.

- The amplitudes of the polarimetric signals are very weak, with amplitudes well below 1% of the quiet Sun intensity at disc centre. The strongest amplitudes at disc centre are stronger than those at the limbs and are associated to Stokes V. At the limbs, the strongest signals are associated to any of the Stokes parameters, though they are smaller than the strongest amplitudes at disc centre.

- The detected magnetic signals exhibit in most of the cases (∼70%) regular Stokes V profiles. The rest are found to have one or three lobes and more occasionally four.

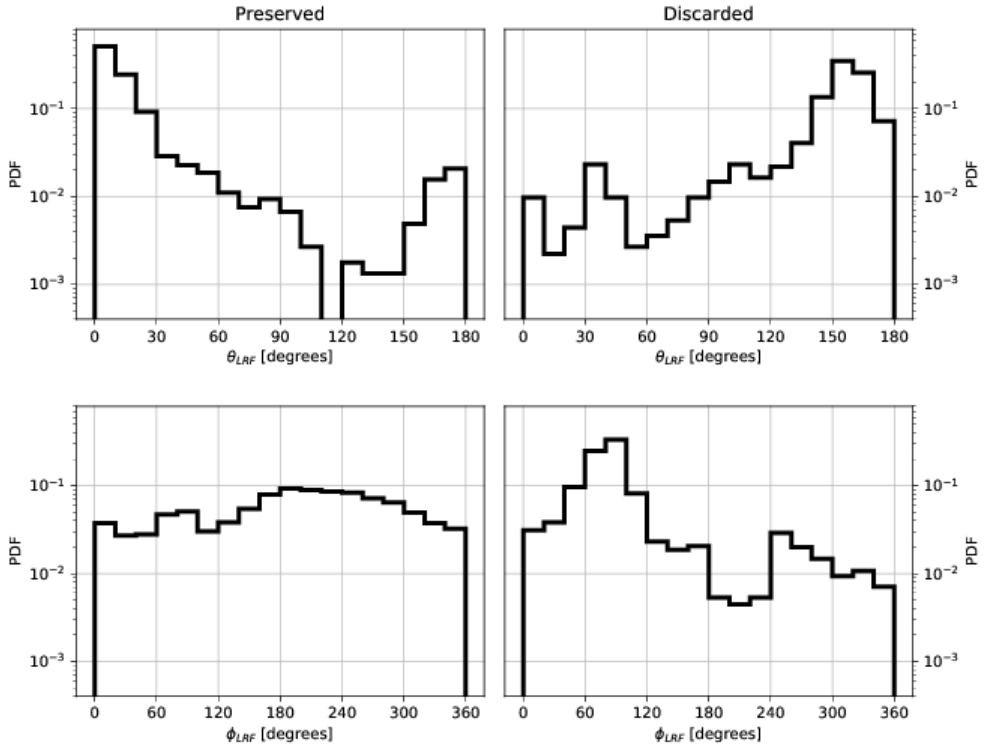

FIGURE 5.27— Left panels, from top to bottom: West region probability density functions of the local reference frame magnetic field inclination (θ_{LRF}) and azimuth (ϕLRF) picked by our 180° LOS azimuth ambiguity method. The same magnitudes, but the discarded ones, are presented in the right panels.

- The amplitude and area asymmetries of the regular Stokes V profiles are broad and show mean positives values at disc centre. This mean values shifts to negatives values when moving to the limbs.
- The FOV mean LOS magnetic flux density at the disc centre and at the West limb is given by strong polarity patches (3.26 Mx/cm^2 and 2.50 Mx/cm^2, respectively). At the North region instead, the polarity identity of the observed region is given by magnetic fields outside strong polarity patches (-1.75 Mx/cm^2).
- The LOS velocities at three discs positions can be explained by a common scenario. The magnetic component LOS velocities show a bi-modal behaviour, with some fields close to rest and other ones with downflows $< v_{LOS} >$ ∼1.73 km/s. When moving to the limb, this second component sharply reduce the projected to LOS component and it is hardly seen as an individual peak, but it is seen as an asymmetric LOS distribution with a more

prominent tail to greater values.

- Only those inverted pixels with magnetic field strengths above 500 (600) G at disc centre (limb) are further studied
- The main properties of the LOS magnetic topology at disc centre are:

  -The magnetic field strength occurrence gradually decreases from the established threshold of 500 G to bigger values.

  -The LOS magnetic field inclination is vertically dominated.

  -The LOS magnetic field azimuth is homogeneous.

  -The magnetic filling factor is dominated by small values (< 0.1) which increase to about 0.4 for the strongest magnetic fields.

- At the limb datasets we found a similar magnetic field topology:

  -The magnetic field strength PDF decays from magnetic field strengths of 600 G towards stronger fields. In addition to this general behaviour, there appears a bump (West limb) or depression (North limb) of magnetic fields at about 1200 G. This local maximum is found to be due to the relative abundance of strong polarity patches: larger than at disc centre for the West and lower than at disc centre for the North dataset.

  -The LOS magnetic field inclinations exhibit a bimodal behaviour when comparing the LOS PDF to that expected at the limb disc positions for a disc-centre-like distribution when only considering the geometrical effects. On the one hand, there are some magnetic fields which are compatible with the topology seen at disc centre under the new viewing angle. On the other hand, there are some magnetic fields whose topology cannot be due to vertical magnetic fields. These magnetic patches are characterised by $\sim 30^\circ$ or $\sim 150^\circ$ LOS inclinations. This inclinations together with their azimuths are compatible with the presence of an unresolved loop.

  -The LOS magnetic field azimuths are strongly aligned with the E-W solar direction.

  -The filling factor distribution exhibits small values with increasing magnetic filling factor for stronger fields.

- In order to change the magnetic fields from LOS to LRF, we look for spatial coherence in those patches whose magnetic field strength is above 600G. In addition, we prevent ourselves from changing to the LRF those structures whose polarimetric signals are compatible with unresolved loops. It is so because these magnetic polarisation signals are due to a mixing of different topology, whose interpretation when changing from LOS to LRF is doubtful. Above this threshold we are confident about the magnetic topology inferred.
- The results at the LRF are characterised by vertical fields and expanding or converging azimuths around them. This component matches the canopy-like scenario, where vertical magnetic fields expand with height exhibiting an halo around them with magnetic field radial expansion or convergence.

From the various parameters observed related with the magnetism at the three different quiet Sun FOVs, we found that just one shows a different behaviour at the North region than at the

quiet Sun at the equatorial limb. It is related with the unbalanced LOS magnetic flux seen at the North region outside *strong polarity patches*, which sets the averaged LOS magnetic flux of the observed area. It is generally accepted that it is the strongest magnetic signals the ones sets the dominant polarity of the polar regions. It is possible that, close to maxima of solar magnetic activity, when these strong magnetic features are the less numerous, the averaged LOS magnetic flux density might not be given by these strong magnetic features. Further observations and analysis is required to discern whether this result is characteristic of the polar regions close to maxima of activity or not. In this sense, the Hinode polar observation program might offer an excelent chance to check the behaviour of the polar magnetism from a minimum to a maximum of activity.

It is worthy to consider the bi-modal behaviour of the magnetic field topology close to the limbs. This bi-modal behaviour has already be seen in Ito et al. (2010); Blanco Rodríguez & Kneer (2010); Jin et al. (2011) and Shiota et al. (2012). They all found that there were some magnetic fields characterised by vertical fields. However, the second component of magnetic fields were found to be preferentially horizontals Ito et al. (2010); Jin et al. (2011), and Shiota et al. (2012) or isotropic Blanco Rodríguez & Kneer (2010). In this study, we also found a bi-modal magnetic behaviour. On the one hand, there are some magnetic fields that are characterised by magnetic field strength ranging from 1 kG to 1.5 kG and whose topology is in agreement with canopy-like structures. According to Ito et al. (2010); Blanco Rodríguez & Kneer (2010); Jin et al. (2011) and Shiota et al. (2012) vertical magnetic fields are the ones that set the dominant polarity of the polar region. In such a case, we have that the area observed is already characterised by the new building up polarity, which is positive. On the other hand, there are some magnetic fields that give rise to a singular topology. This configuration is characterised by LOS inclinations of $\sim 30^{\circ}$ or $\sim 150^{\circ}$ and LOS azimuths along the radial direction. We have qualitatively seen that the presence of unresolved magnetic loops are able to give rise such a preferred orientation.

6

North polar cap in high resolution

In chapter 4 we have studied the long-term evolution of the global magnetic field at solar cycle time scales. In chapter 5, we have performed a magnetic characterisation of polar fields by means of full spectropolarimetry at a moderate spatial resolution. Both approaches to the study of solar polar magnetism lack of high spatial resolution and, in particular for the full spectropolarimetric studies, of large area coverage. This is an important issue since quiet Sun magnetism is known to be populated of small-scale magnetic structures (see de Wijn et al., 2009, for a recent review, and references therein) and, at polar regions, small structures are scattered all over the polar cap surface (Homann et al., 1997; Okunev & Kneer, 2004; Blanco Rodríguez et al., 2007; Tsuneta et al., 2008; Ito et al., 2010; Blanco Rodríguez & Kneer, 2010; Jin et al., 2011; Shiota et al., 2012; Kaithakkal et al., 2013; Quintero Noda et al., 2016). In order to study the poles magnetism with high spatial resolution and a big area coverage we made use of the CRISP instrument installed at the SST. This combination of instrument and telescope allows the highest spatial resolution achievable nowadays for full Stokes spectropolarimetric data. However, the use of visible lines makes us less sensitive to the magnetic field inference by means of Zeeman effect. In this regime, the sensitivity of spectral lines to magnetic field is favoured by increasing wavelength (Sec. 3.1.2).

6.1 Data

The observations took place on 19th August 2015 at the Solar Swedish Telescope (SST; Scharmer et al., 2003) at the Observatorio del Roque de los Muchachos (Spain). At that time the North polar region was well inside the visible disc, allowing the best chance to study its physical properties. Observations made use of the CRisp Imaging Spectro-Polarimeter (CRISP, Scharmer, 2006; Scharmer et al., 2008) in full spectropolarimetric mode. The observations consist on sequential scans of the photospheric FeI 6173 Å and the chromospheric Ca II 8542 Å. In this chapter we only report on the analysis of the photospheric spectral line. The study of the chromospheric spectral line is beyond the scope of this thesis. These lines show a high/moderate sensitivity to magnetic fields with Landé factors 2.5 and 1.1, respectively.

The FeI spectral line was scanned at 20 wavelength positions: from -225 mÅ to +225 mÅ at steps of 25 mÅ and an additional spectral point at the continuum at 525 mÅ from the line

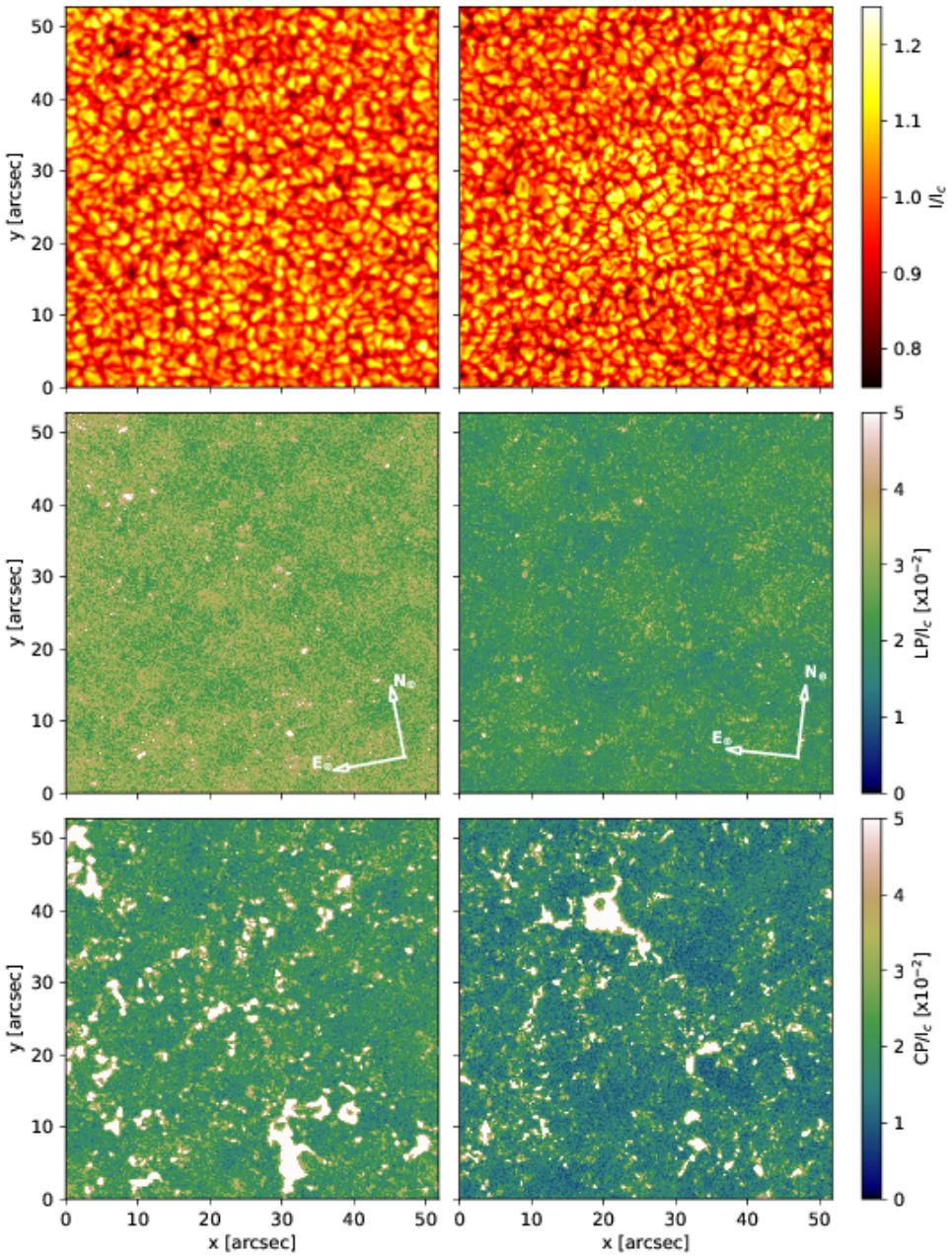

FIGURE 6.1— From top to bottom: Intensity, linear polarisation and circular polarisation maps for the disc centre datasets taken at UT 07:19:01 (left) and at UT 10:21:16 (right). Linear polarisation is given by: $\int_\lambda \sqrt{Q(\lambda)^2 + U(\lambda)^2}\, d\lambda$ and circular polarisation map by: $\int_\lambda \sqrt{V(\lambda)^2}\, d\lambda$.

TABLE 6.1— x ($x_\odot$) and y ($y_\odot$) helioprojected values of the central point of each FOV, the solar latitude ($\lambda_\odot$) and longitude ($l_\odot$) and $\mu = \cos\theta$, where θ is the heliocentric angle. N is the number of repetitions of the scans of both lines at each FOV. $\%_{LIN}$ is the percentage of the FOV that presents linear polarisation signatures above the noise level for the FeI line. $\%_{MAG}$ is the percentage that shows any, linear or circular polarisation above the signal criterion for that spectral line. *Target* is a label to easily identify the FOV of the scan: NP for North pole, EL for East limb and DC for disc centre.

Time (UT)	$x_\odot$ ($''$)	$y_\odot$ ($''$)	$\lambda_\odot$ ($^\circ$)	$l_\odot$ ($^\circ$)	$\mu_\odot$ ($^\circ$)	N	$\%_{LIN}$	$\%_{MAG}$	Target
07:19:01	0.60	0.70	6.86	0.04	1.00	10	0.01	6.45	DC
07:47:05	-915.40	-0.70	1.77	-74.66	0.27	10	0.04	2.85	EL
07:54:59	-883.10	-7.60	2.05	-68.51	0.37	10	0.02	3.95	EL
08:04:09	-14.30	935.80	86.92	-16.28	0.17	10	0.01	1.55	NP
08:12:26	-21.30	892.10	76.74	-5.61	0.34	10	0.17	4.85	NP
08:20:27	-94.00	912.30	79.95	-34.55	0.26	10	0.07	4.25	NP
08:29:31	-124.90	913.90	79.66	-47.13	0.24	10	0.06	3.55	NP
08:38:38	-184.10	908.70	77.36	-62.39	0.22	10	0.07	3.35	NP
08:47:24	72.80	926.30	83.23	40.56	0.21	10	0.04	2.95	NP
08:56:11	32.60	926.30	83.90	18.85	0.22	10	0.02	3.25	NP
09:09:31	131.90	918.20	80.21	54.79	0.21	10	0.05	3.95	NP
09:17:34	193.50	914.30	77.70	73.00	0.18	10	0.06	3.25	NP
09:26:01	198.00	855.70	70.02	37.60	0.38	5	0.17	5.25	NP
09:30:51	175.90	838.30	68.08	29.75	0.43	5	0.26	7.75	NP
09:35:13	109.50	848.50	69.83	19.53	0.43	5	0.34	8.05	NP
09:39:35	57.30	837.60	68.63	9.53	0.47	5	0.16	8.65	NP
09:44:02	-3.00	865.70	72.54	-0.60	0.41	5	0.16	8.05	NP
09:48:24	-76.80	870.80	73.10	-16.16	0.39	5	0.44	9.65	NP
09:52:48	-141.30	885.20	74.73	-34.40	0.33	5	0.16	3.25	NP
09:57:44	-212.30	815.10	65.10	-32.07	0.46	5	0.09	4.75	NP
10:21:16	3.30	-0.20	6.80	0.20	1.00	10	0.01	7.85	DC

core. The 0 mÅ reference is the minimum position of the spectral line as measured at the etalon calibration process at the morning (UT 07:10). At each wavelength position four modulated states of the light were taken in order to recover the four Stokes parameters for each wavelength. Each of these four measurements at each wavelength position was repeated twelve times. The integration time for each image was close to 18 ms, and together with the 17 ms reading time, this spectral line was scanned in ∼32 seconds. This type of calibration, together with the non correction of the Earth rotation at Canary Islands latitude, involves up to 410 m/s uncertainty (as calculated following Plaskett, 1952). Since the calibration was done at the beginning of the morning, an increasing reddening is obtained until close to noon.

The scan of this photospheric line together with the scanning of Ca II 8542 Å spectral line, which took ∼16 seconds, gave a sequential scanning cadence of ∼50 seconds. At each disc position we repeated this scanning setup between 5 and 10 times as it is detailed in Tab. 6.1.

The excellent seeing conditions together with the use of the adaptive optics system (which is an

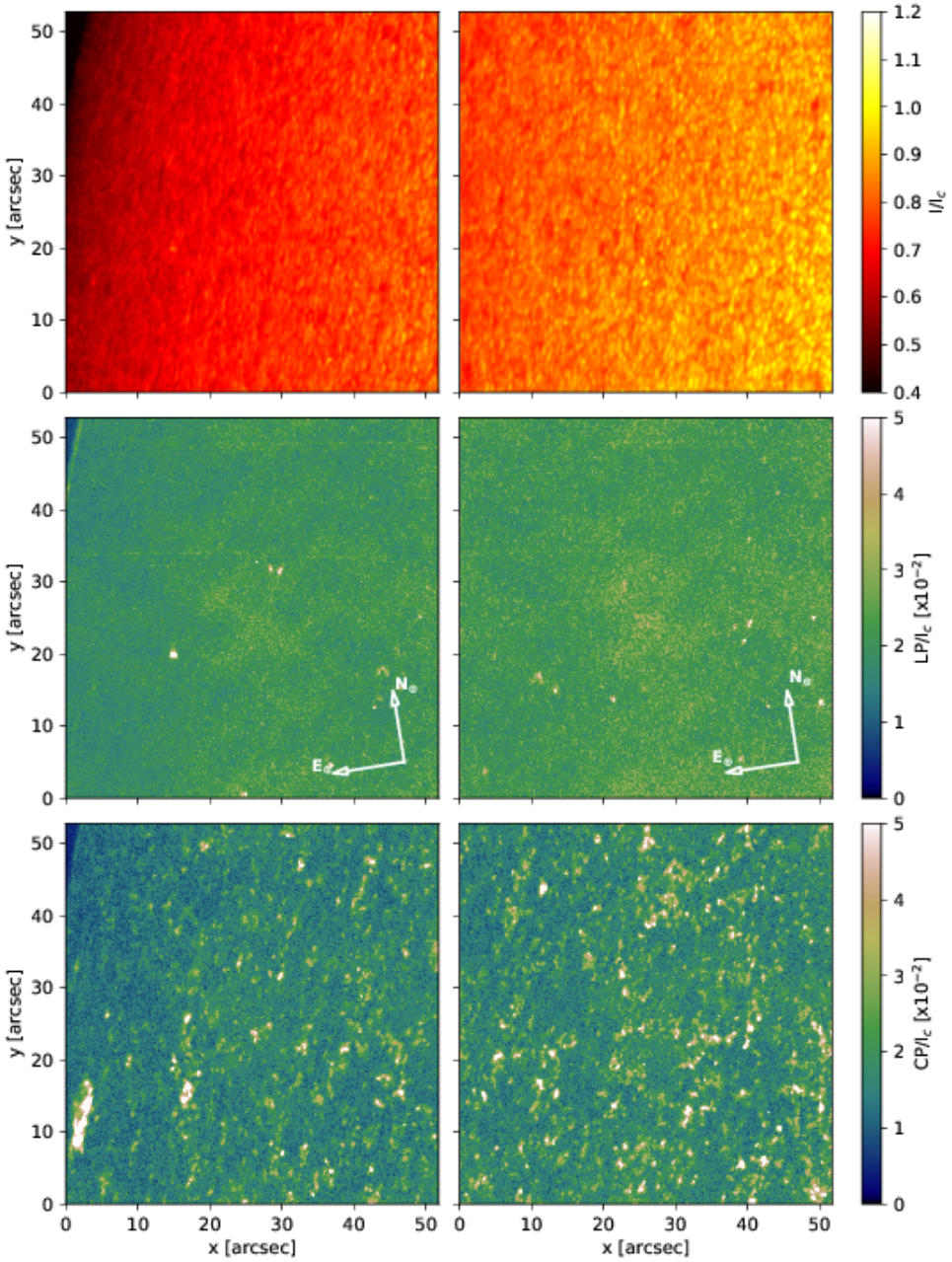

FIGURE 6.2— Same kind of representantion as in Fig. 6.1 for two scans taken at the East limb: at UT 07:47:05 (left) and at UT 07:54:59 (right).

update of the previous one, Scharmer et al., 2003), allowed a big coverage of the North polar region (as seen in Fig. 6.3) and of quiet Sun regions at disc centre (Fig. 6.1) and at the East limb with high spatial resolution (Fig. 6.2).

The reduction of the data is performed using the CRISPRED pipeline (de la Cruz Rodríguez et al., 2013). The standard reduction involves image restoration by means of the Multi-Object Multi-Frame Blind Deconvolution (MOMFBD; van Noort et al., 2005). However, we prefer to use a de-stretching module (kindly implemented by de la Cruz Rodriguez). This is so since the polarisation signals expected at quiet Sun regions are very weak and image restoration techniques increase the noise. This way, the observations do not reach the diffraction limit of the telescope ($0\farcs12$) but they have a spatial resolution at $0\farcs35$ as retrieved from the two-dimensional Fourier power spectrum. In this situation, the original pixel size involves a spatial oversample. In order to correct for this and at the same time increase the signal-to-noise ratio, a binning of three by three pixels is performed. The original image scale is $0\farcs059$/px which, after binning, results in a final pixel size of $0\farcs177$. Some additional steps to the standard reduction are done as detailed in Sec. 2.3.3.

After the reduction process, the polarimetric sensitivity, as derived from the standard deviation of the Stokes Q, U and V parameters at the continuum point, is $\sigma = 1. \times 10^{-3}\, I_c$. The binning process increases this sensitivity giving $\sigma = 4. \times 10^{-4}\, I_c$. We consider that a magnetic signature is detected when any of the Stokes polarised parameters exhibits a wavelength point above 3σ. The forthcoming analysis is performed only over those pixels classified as "magnetic". Under this selection criterion, 5.17% of the observed area is magnetic with only 0.12% of the FOV exhibiting at least linear polarisation signatures. Table 6.1 details the percentages for each FOV.

6.1.1 Stokes profiles amplitudes

For those pixels that present polarisation signals over the 3σ threshold, Fig. 6.4 presents the probability density functions of the Stokes profile amplitudes. Disc centre (middle panel) has a clearly dominant Stokes V distribution, i.e., most of the polarimetric signals are detected by the presence of Stokes V profiles (see for instance Tab. 6.1). The Stokes V profiles amplitude distribution is dominated by small amplitudes, with 91.86% of the profiles with a maximum amplitude below 1% I_c. Yet, at disc centre the Stokes V distribution exhibits a large tail to higher amplitude values reaching a maximum of about 8% I_c. The linear Stokes profiles amplitude are similar to Stokes Q and U with very low amplitudes, hardly reaching 1% of the quiet Sun continuum intensity.

At the West region, Stokes V profiles show the largest amplitudes. The fraction of magnetic pixels with circular polarisation is 99.90%, i.e. almost all the polarised signals are detected by means of circular signatures. However, in comparison to disc centre, the maximum Stokes V profile amplitude found is about 1% of the quiet Sun continuum intensity. Another difference with the disc centre distribution is that the linear amplitude distribution reaches also 1% of the quiet Sun continuum intensity. Furthermore, at this disc position, the linear polarisation distributions are not similar anymore and Stokes Q dominates above Stokes U. This might be a consequence of the magnetic field topology. A magnetic field topology close to a vertical dis-

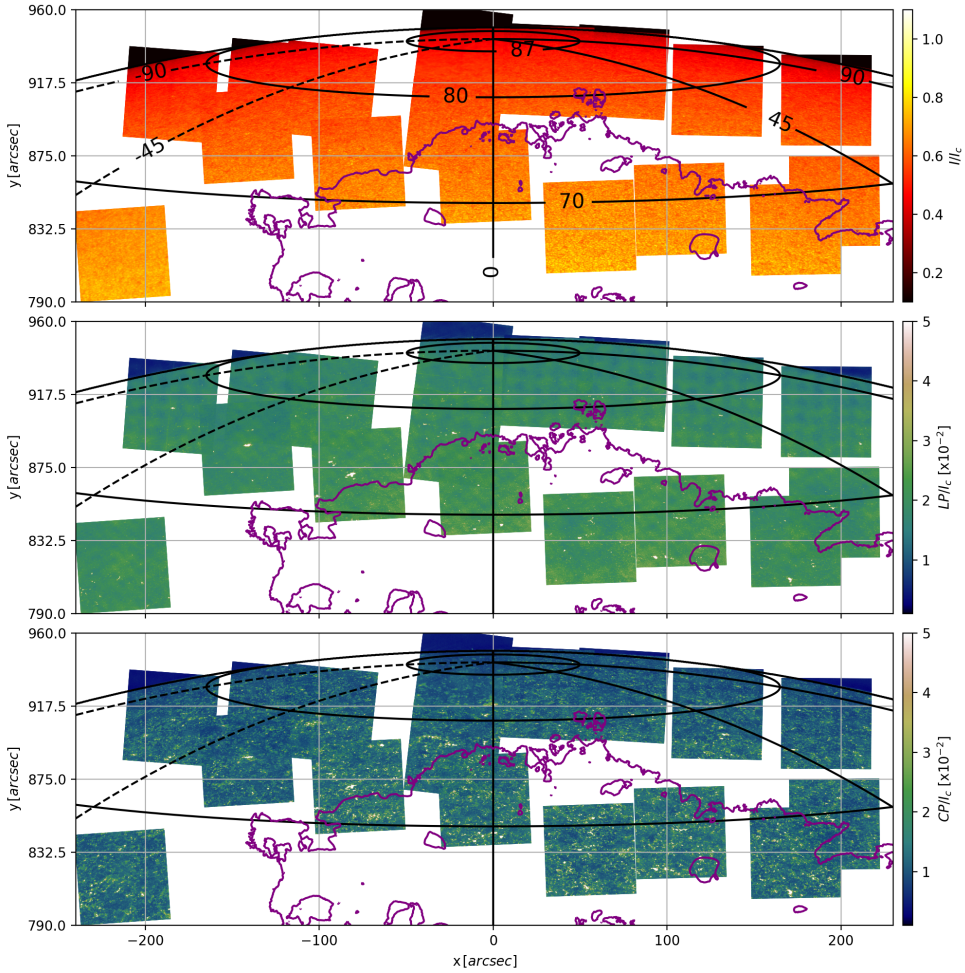

FIGURE 6.3— Mosaic of the North polar region with the 17 scans taken. The continuum intensity is shown in the upper panel, the linear polarisation map in the middle one and the circular polarisation map in the bottom. The purple contour depicts the position of a coronal hole as estimated from the SDO/AIA 193 Å intensitygram.

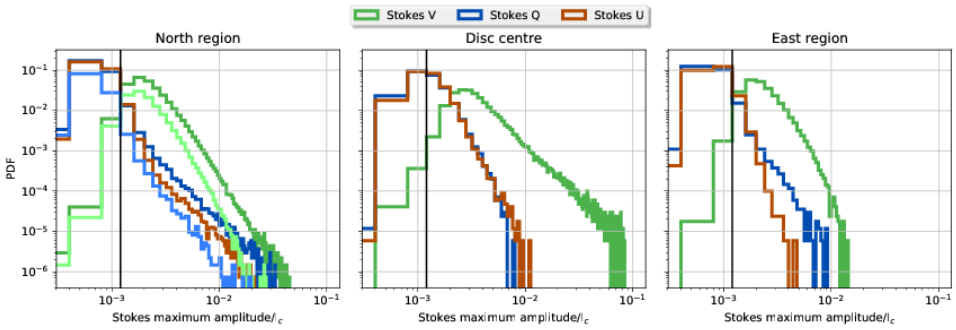

FIGURE 6.4— From left to right: Stokes amplitude probability density functions for the North, disc centre and East regions, respectively. Stokes V is in solid green, Stokes Q in solid blue and Stokes U in solid brown. For the North region case, two additional distributions are included, light green is for the Stokes V amplitude probability density functions above solar heliocentric angles of 70°. Solid light blue is the Stokes Q probability density function above that same heliocentric angle.

tribution favours a magnetic field vector projection in the solar radial direction, which for an East-limb region is along the E-W direction (90°-270°).

The North region has similar characteristics to the East region. However, at this disc position, observations reached heliocentric angles well below those for the East region and so, the tails for the probability density functions are enhanced. In order to support this statement, Fig. 6.4 includes light grey and dark grey solid lines highlighting the probability density functions for the Stokes V maximum amplitudes and Stokes Q maximum amplitudes, respectively. These distributions are restricted to those pixels with heliocentric angles above 70°. The comparison of these two distributions with those observed at the East region show a good agreement.

In summary, most of the observed polarimetric signals are detected by the presence of Stokes V signatures. When moving to the limb, Stokes V maximum amplitudes are reduced whilst linear polarisation amplitudes increased their largest values, yet in a similar way for both limb datasets. This property makes us suspect that this behaviour comes from projection effects.

The comparison of these amplitude distributions with those observed at the VTT show some similarities and some differences. First, in both observations, it is found that, at disc centre, Stokes Q and U amplitudes are characterised by much smaller amplitudes than Stokes V profiles. This situation changes when moving to the limbs. At both limb datasets, the amplitudes of Stokes Q and U are, in general, smaller than Stokes V amplitudes and the largest amplitudes reached by Stokes Q, U and V profiles are similar. The clearest difference between the results at the SST and at the VTT resides in the value of the amplitudes. At the VTT, the largest amplitudes for Stokes V are found at disc centre with up to 1.5% I_c. This same amplitudes are reached for Stokes Q and U at the limbs. At the SST we found a similar situation. Stokes V amplitudes at disc centre reaches the maximum amplitude values up to 8% I_c. Again, maximum

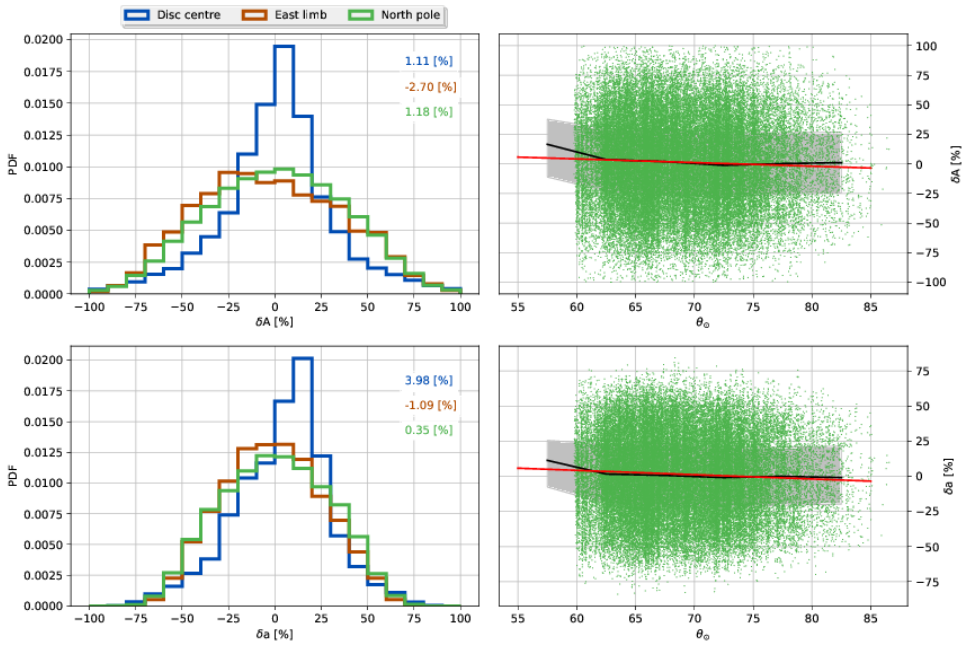

FIGURE 6.5— Left column, from top to bottom: Stokes V profile area and amplitude asymmetry probability density functions. In blue the ones for disc centre, in brown the ones for the East limb and in green for the North region. The values at the top-right present the mean value of the distribution. Right panels, from top to bottom: latitudinal dependence of the area and amplitude Stokes V profile asymmetries. Grey shadow highlights the area between the 25th and 75th percentile, whilst dark solid line is for the 50th percentile. Red line stands for a least-square fit to a first order polynomial.

amplitudes of Stokes Q and U are found at limb datasets, reaching up to 4% I_c.

6.1.2 Stokes V asymmetries

Another interesting feature is the presence of asymmetries in the Stokes V profiles. This property is sensitive to gradients of the magnetic field and velocity along the LOS. Hence differences in the magnetic field topology at the low latitude quiet Sun and high latitude quiet Sun may leave some imprints on the Stokes profiles. In particular, in the asymmetries of Stokes V profiles.

The left column of Fig. 6.5 presents the histograms of the area (top) and amplitude (bottom) asymmetries for the data at the disc centre, East limb, and North polar region. Disc centre area asymmetries are characterised by a narrow distribution with a mean value of 1.11% with quite symmetric long tails. At the East limb, the area asymmetry distribution is broader than at disc centre and its mean value is -2.70%. If we assume that both underlying magnetic field

topologies are equivalent, then this difference has to come from projection effects (either from limb effect —including radiative transfer effects— or from geometrical changes).

The North polar region is also characterised by a broad area asymmetry distribution, but for this region, the distribution is centred at 1.18%, quite close to the value at disc centre. The projection effects at the East and at the North regions must be the same and the difference between these two distributions cannot be due to this effect. An important point to take care of in the comparison between North and East limb is the fact that the area covered at the North polar region is much larger than that at the East limb. This means that the heliocentric angles involved in the North region cover a wider range than those at the East limb. Moreover, the North region distribution is dominated by the smaller heliocentric angles, since the smaller the heliocentric angle the larger the number of identified "magnetic" pixels. This dependence is already seen in the right column of Fig. 6.5. The scatter plot shows the latitudinal dependence of the area asymmetry with solar latitude for the North solar region. The red line is the least-square fitting of a first order polynomial to the whole distribution. It is observed that the area asymmetry distribution decreases with increasing latitude and, actually, it changes its sign above $\theta_\odot \sim 75°$.

A very similar situation is found for the amplitude asymmetry (lower panels), where the disc centre distribution is characterised by a positive (3.98%) mean value and a broader than disc centre distribution. This time, the negative tail is clearly broader than the positive one, leading to an asymmetric distribution. At the East limb, the amplitude asymmetry is found to be characterised by a broader and symmetric distribution with a negative (-1.09%) mean value. North polar region is also characterised by a broader than disc centre amplitude distribution like the East limb, but its mean value (0.35%) is something in between that of East limb and the one of disc centre. In order to see if this difference comes from the fact that the heliocentric angles covered at the North extend to smaller values than those covered at the East, we consider the latitudinal dependence of these magnitudes (right panels of Fig. 6.5). The trend of both, the area (top-right panel) and the amplitude (bottom-right panel) asymmetry is found to move from a positive value for lower latitudes (below $\theta_\odot \sim 60°$) to negative ones above $\theta_\odot \sim 70°$. This point can be further checked from the mean area and amplitude distributions for the North region, but restricted to the heliocentric angles observed at the East limb: -0.33 and -0.61, respectively.

This behaviour in the mean value distribution of the amplitude and area asymmetries from a positive to lower mean values with the heliocentric angle, even to negative values, is consistent with the results obtained in the previous chapter and the reported results for other visible (Stenflo et al., 1987b) and infrared spectral lines (Stenflo et al., 1987a). We have already seen that this effect was reproduced by Buente et al. (1993) for vertical thin tubes. As it was the case in the previous chapter, the shift of the mean value is seen for both limb datasets, discarding polar singular magnetic properties concerning these parameters.

6.2 Methods: inversion of the data

As overviewed in Chapter 3, the process from Stokes vector profiles to physical parameters is performed by means of the so-called inversion methods. In particular, we use the SIR code in order to handle this step. However, it is necessary to supply a model atmosphere as well as the parameters to be perturbed in order to fit the observations.

We consider each resolution element as the combination of two atmospheres. The first one is magnetic and its free parameters are the temperature (with up to five nodes), and height independent LOS velocity, microturbulent velocity, magnetic field strength, inclination and azimuth. The second component is non-magnetised and its free parameters are the LOS velocity and microturbulent velocity. The temperature is fixed to be the same for both magnetic and non-magnetic atmospheres. The filling factor, which gives the relative weight of each of the previous components, is also set as a free parameter. This two-component model is accompanied by the theoretical CRISP spectral transmission profile. This profile also carries the information of the wavelength shift due to imperfections in the etalons (see Sec. 2.3.3). This profile is calculated with dedicated software given by the instrument team. The two model atmospheres strategy is necessary to reproduce the presence of differential LOS velocities between the Stokes I and Stokes V profiles. In addition, the different microturbulent velocities are added to fit the width of Stokes I profile and the width of Stokes Q, U and V profiles.

This two-component model cannot reproduce the presence of asymmetric Stokes Q, U and V profiles. These features are indicative of gradients of velocity and/or magnetic field along the LOS. In the ideal case of a constant magnetic field with a constant LOS velocity, Stokes Q and U profiles are symmetric and Stokes V profiles are antisymmetric. We have already seen that this is not the case for our data; however, a constant LOS velocity and constant magnetic field along LOS inversion model is able to retrieve an average estimation of this LOS variation (Westendorp Plaza et al., 1998). Another case to take care of is the presence of so strong gradients that one of the lobes of Stokes V profile is suppressed. Single-lobed Stokes V profiles are defined when only one of the lobes of Stokes V profile is above the 3σ threshold. This happens to $\sim$1% of the pixels with polarimetric signals. In this situation, the inversion strategy here proposed leads to inaccurate results so single-lobed Stokes V profiles are discarded in the forthcoming analysis. The various steps given to settle this inversion strategy are exemplified in Fig. 6.6.

Each pixel is inverted 50 times with initial random LOS velocity, microturbulent velocity, and magnetic field strength, inclination, and azimuth. The initial guess temperature stratification is that of the VALC semi-empirical model atmosphere (Vernazza et al., 1981). Initial magnetic field strength values are taken between 0 G and 1000 G whilst inclination values are given for the polarity of the field as determined from the sign of the Stokes V profile. The initialisations of LOS velocities take values in between $\pm$ 2 km/s and that of microturbulent velocities are between 0 km/s and 2 km/s. The result of the inversion is taken to be the one with the best χ^2.

The inversion process requires an additional point to be aware of. It has been shown that when the magnetic field strength is not strong enough, the inversion is not sensitive to magnetic field strength, magnetic field inclination and filling factor independently, but it fits the magnetic flux

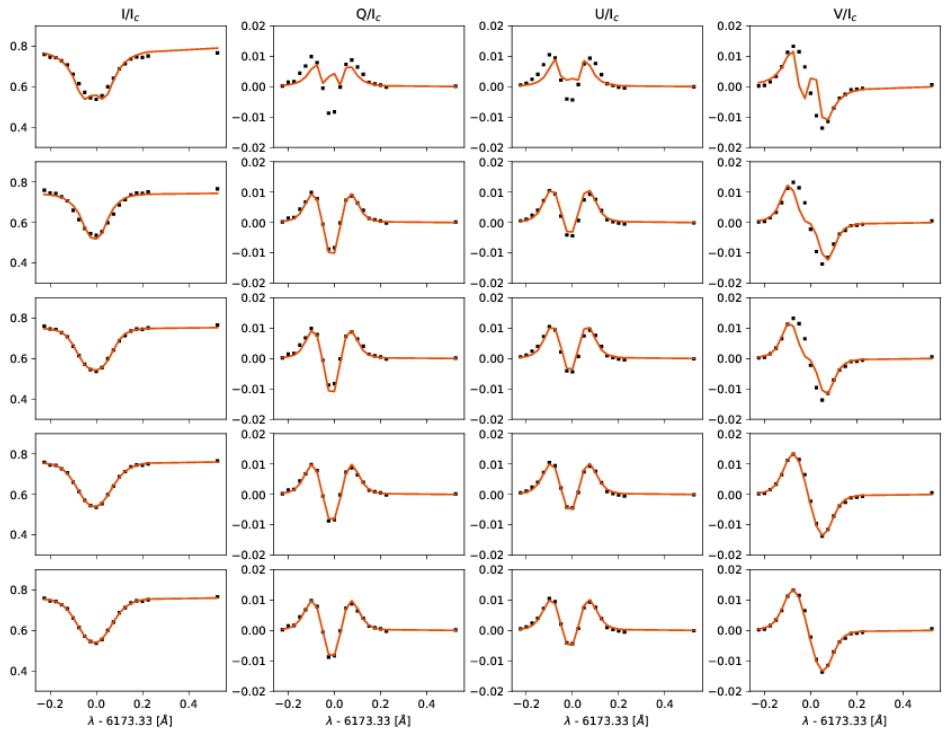

FIGURE 6.6— From left to right: Stokes I, Q, U and V profiles of a pixel observed at the North region. In black square marks are the observations. In solid brown the best inversion result of several attempts. From top to bottom, the inversion strategy is changed from the most simple one (top) to the most complex one (bottom). The simplest inversion model proposed (top row) is a unique atmosphere, which is magnetic (magnetic field strength, inclination and azimuth are allowed to vary) and with additional free parameters in LOS velocity and temperature (with 5 nodes). This first guess shows two evident problems: 1-the presence of differential LOS velocities between the Stokes I and Stokes V profiles and 2-the inability to fit the width of Stokes I profile. The former is coped adding a second model atmosphere, which is non magnetic, and whose LOS velocity can be different to that of the magnetic atmosphere (second row). The temperature stratification is fixed the same for both atmospheres, since the tests with different temperature stratifications do not improve the fit (last row). In order to handle the latter, we add the microturbulent velocity to the free parameters to the second non-magnetic atmosphere (third row). This model however still lacks of the proper width of Stokes Q, U and V profiles. This is solved adding the microturbulent velocity of the magnetic atmosphere to the free parameters (fourth row).

$\Phi = \alpha\, B\, \cos\theta$, where α is the filling factor, B the magnetic field strength and θ the magnetic field inclination (Asensio Ramos et al., 2007). This restriction is proved in this work as follows. In each pixel we performed additional inversions for different and fixed values of the magnetic field inclination (10°, 20°, 30°, 40°, 50°, 60°, 70°, 80° for positive polarities or 170°, 160°, 150°, 140°, 130°, 120°, 110°, 100° for negative ones). This inversion has only three free parameters: the filling factor, the magnetic field strength and the microturbulent velocity of the magnetic component. The rest of the parameters are set from the first inversion. If the χ^2 value for the

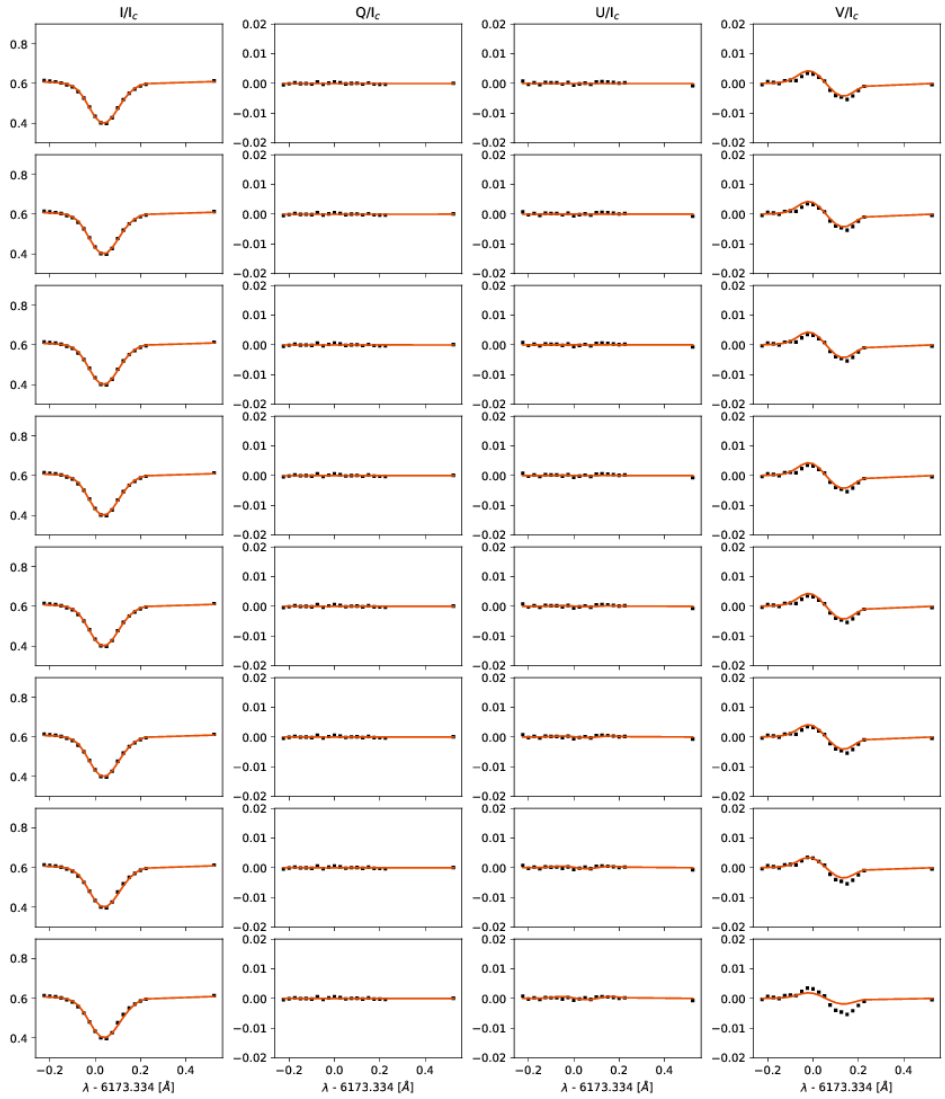

FIGURE 6.7— From left to right: Stokes I, Q, U and V profiles of a pixel of the North region. Solid brown line stands for the best fit in the inversion, black square marks represent the observations. From top to bottom, the inversion are done for fixed line-of-sight inclinations: 10°, 20°, 30°, 40°, 50°, 60°, 70°, and 80°

supplied inclinations does not vary more than a given threshold, then the inversion is considered to be coupled between magnetic field strength, LOS magnetic field inclination and filling factor. For these pixels, the inverted parameter is already the magnetic flux (Φ). Otherwise the inversion is considered to be sensitive to the magnetic field strength, magnetic field inclination and filling factor independently.

The threshold between these two regimes is settled from the behaviour of the χ^2 for the various inclinations and for each of the Stokes parameters. To do so, we look at slope of the χ^2 for each Stokes parameter in the inversions for the fixed inclinations between 10°-30° (170°-150°), 40°-60° (140°-120°) and 60°-80° (120°-100°). For each angle range, we take the maximum slope value of the Stokes parameters, i.e. in this step we check if any of the Stokes parameters shows sensitivity to the LOS magnetic field inclination in each range. After this step, we have three slope values for the χ^2, one for each inclination range. Finally, if the minimum value of these three values is above a given threshold, then the inversion is said to be sensitive to magnetic field strength, magnetic field inclination and filling factor individually. Otherwise the inversion is consider to be sensitive only to magnetic flux. In this step we check if the inversions are really sensitive to the whole range inclination between 10° to 80° (170° to 100°). This is exemplified in Figs. 6.7 and 6.8.

In Fig. 6.7 an example of a pixel in which the magnitude inverted is Φ. It can be seen that the fit for inclinations from 10° to 70° is equally good, and only for an inclination of 80° the fit of Stokes Q, U and V really worsen. In this case, the slope for the ranges 10°-30° and 40°-60° are flat, i.e. a LOS magnetic field inclination of 10° and another of 60° is equally good. It is for LOS magnetic field inclinations between 60°-80° that the χ^2 worsen. This is the reason why we require that the three LOS magnetic field inclination ranges, independently, show a χ^2 variation in at least one of the Stokes parameters. Figure 6.8 is an example of the opposite situation. In this case, the four Stokes parameters vary their χ^2 for the various LOS magnetic field inclinations considered, i.e. we can be confident that the inversion is sensitive to the LOS magnetic field inclination, and hence, to the topology of the magnetic field.

6.3 Analysis

6.3.1 LOS velocities

After the inversion of the pixels with polarimetric signals above the 3σ threshold, some physical magnitudes of interest are available. The LOS velocity is a well constrained quantity, hence we can analyse its properties in the whole inverted pixels. The LOS velocities of both atmospheres used in the inversion are depicted in Fig. 6.9 for the three disc positions. We previously mentioned that we expect a reddening with time due to the Earth rotation since the zero wavelength calibration of the spectral line centre position was done at the beginning of the morning. In order to subtract this variation, we followed Plaskett (1952) to calculate time variation of the Earth rotation velocity compared to the Sun of observatory latitude ($\lambda = 28^\circ\,45'\,25''$) and subtract it.

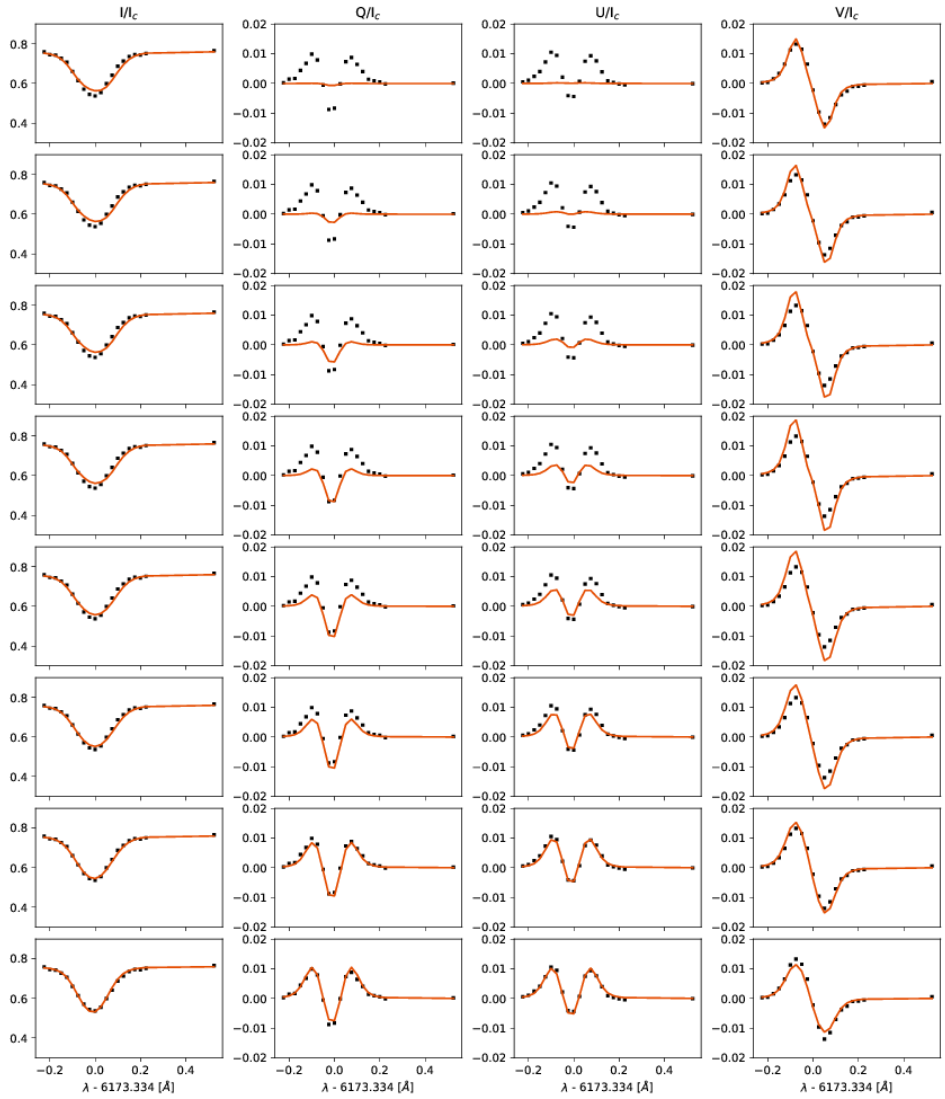

FIGURE 6.8— Same type of representation as in Fig. 6.7 for another pixel of the North region.

Disc centre FOV:

The non-magnetic velocities at disc centre (mid panel) are characterised by a symmetric distri-

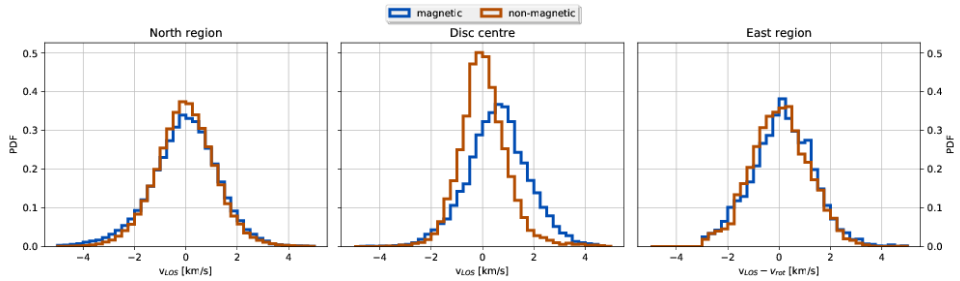

FIGURE 6.9— From left to right: probability density functions of the LOS velocities for the magnetic, non-magnetic and the difference between the previous two. North region results are in blue, East region in brown and disc centre in blue colours.

bution with a mean value of 0.00 km/s and a width of 0.83 km/s. In contrast, the magnetic component distribution is clearly dominated by downflows, with a mean value of 0.61 km/s and a width of 1.17 km/s. This positive mean value of the magnetic component is usual and was already found at the VTT and also in the bibliography (Khomenko et al., 2003, and references therein). In this scenario, magnetic fields are dragged by granular motions to intergranules and the edges of supergranules where they coalesce or annihilate with other magnetic fields. Hence, it is usually observed that QS magnetic fields are preferentially concentrated around these solar surface areas, though the distribution shows large tails to positive and more negative values. This same argument should be valid for the non-magnetic component. However, since we do not post-process the data with image reconstruction techniques we can expect that the non-magnetic atmosphere includes additional effects, for instance, stray-light due to seeing. This effect can potentially erase velocity information mixing intergranular profiles (downflows) with surrounding granular light (upflows).

East limb FOV:

At the East limb (right panel), the non-magnetic LOS velocity distribution has a mean value of -1.92 km/s and 1.11 km/s width. This huge value is associated to the solar surface rotation velocity. For the mean latitude of the observed area $< \lambda_\odot >= -0.13°$ and its mean longitude $< l_\odot >= -71.18°$ the rotation velocity is -1.96 km/s, in close agreement with the mean value found for the non-magnetic velocity distribution. The magnetic distribution is in very good agreement with the non-magnetic one, with no clear difference between the magnetic and non-magnetic component nor in mean value: -1.84 km/s nor the width: 1.17 km/s. If we assume that at this disc region, the velocity field is the same than at disc centre, then the magnetic component would be characterised by close to vertical downflows. These vertical movements strongly reduced their projection to the LOS and hence, when looking at the East limb, the relative velocity between the magnetic and non-magnetic components is reduced significantly.

North limb FOV:

The North region data (left panel) shows a very similar behaviour to that seen at the East region. Both the magnetic and non-magnetic components are characterised by distributions centred at 0, -0.03 km/s for the magnetic component and -0.007 for the non-magnetic one and a width of 1.24 km/s and 1.11 km/s, respectively. LOS velocities thus do not show any singular behaviour at polar region when compared to quiet Sun at equatorial limbs.

These results for the LOS velocities are slightly different than those found at the VTT. At the VTT, the North region exhibited a non-magnetic LOS velocity mean value slightly positive and the magnetic component was even a bit more red-shifted. In principle, the area covered with the SST is much larger than that reached at the VTT, even for the disc centre and equatorial quiet Sun. Hence, we expect to be less sensitive to local effects in this last study. From this datasets, we found a common scenario that can explain the observed properties at the three disc positions, leaving the further understanding of the results found at the VTT data for future IR observations of larger areas.

6.3.2 LOS magnetic flux

The LOS magnetic flux density (Φ) is another physical property that is well constrained from observations. Figure 6.10 shows the probability density functions of Φ for the three fields-of-view. The three observed disc regions has a polarity imbalance (top row), which is positive for the North region, with mean value: 0.359 Mx/cm^2 and negative for disc centre and East region with -4.396 Mx/cm^2 and -1.279 Mx/cm^2, respectively. The LOS magnetic flux density at disc centre exhibits a very broad tail to strong LOS magnetic fluxes, with a clearly positive dominant one. At the limbs these tails reach lower LOS magnetic flux values. Similarly to the case of the amplitude of Stokes profiles, at the East region, the distribution reaches lower maximum LOS magnetic fluxes than at the North one. As before, this is due to the fact that at the North disc position, the observed heliocentric angles are well below those observed at the East limb. If we restrict the North region to those heliocentric angles covered at the East one, (top-left panel in grey lines), the distribution resembles more that at the East. If we look at Fig. 4.3 we can see that the mean LOS magnetic flux of the polar region matches that of the new building up polarity, i.e. the polar region has already changed its polarity. An interesting point here is that, if the calculation of the mean LOS magnetic flux value is performed for solar latitudes above 70°, then $< \Phi >= -0.151$ Mx/cm^2, which is close to show no dominant polarity or even, the polarmost area exhibit yet the opposite polarity. This is consistent with the global picture where polar regions change their polarity with incoming opposite polarity from low/mid latitudes. Hence, for these observations, which date close to the polar region polarity reversal, a partial polarity change is feasible.

In Fig. 6.10 we show the contribution to the total LOS magnetic flux density of polarity patches that are classified as *strong polarity* patches or for the rest of the surface. In order to get a magnetic patch classified as *strong polarity* we proceed as follows:

1. identify those patches that present polarisation signals above 0.5% I_c,

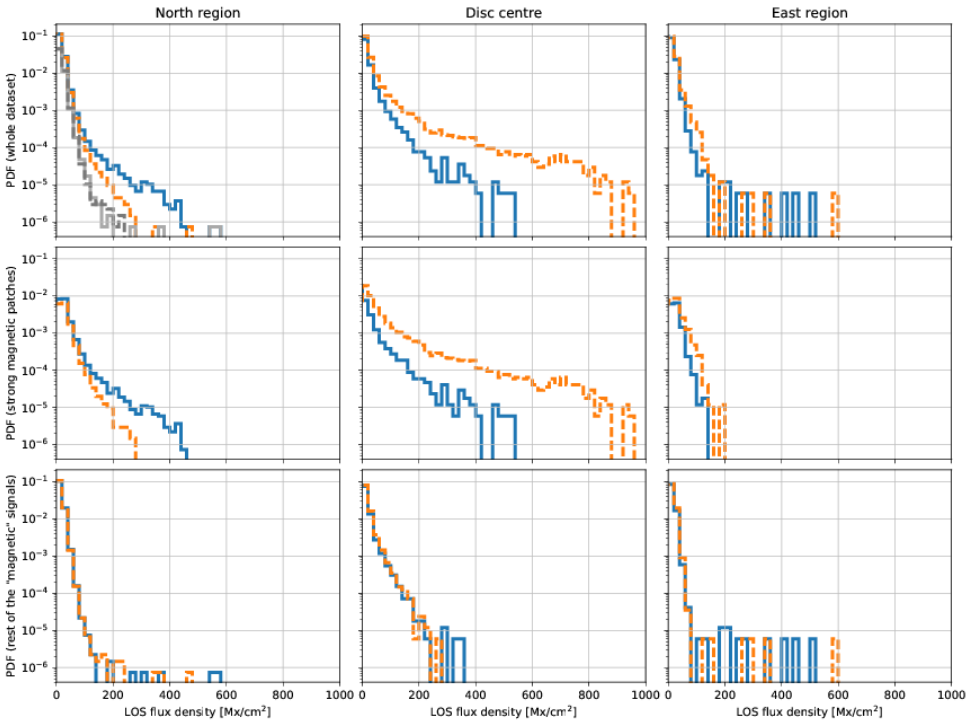

FIGURE 6.10— Top row, from left to right: line-of-sight magnetic flux probability density functions for North region, disc centre and East limb data. In solid blue, the positive tail is presented. The negative one is folded to positive values in orange dashed line. Middle panels follow the same representation for *strong polarity* patches (see text for their definition) and bottom panels for the rest of the magnetic signals. Top-left panel additionally includes two grey lines to show the line-of-sight magnetic flux above solar latitudes of 70°.

2. get patches with polarimetric signals above 3σ, and
3. finally, those structures in step 2 that harbour in their interior patches identified in step 1 are classified as *strong polarity* patches

This way we found that 1.26%, 4.77% and 1.08% of the magnetic signals of the North, disc centre and East regions, respectively are associated to *strong polarity* patches. They settle the dominant polarity of each region (middle row), though they represent a minority of the various FOVs observed. This result is different to that found from the VTT data analysis where we found that the North region polarity was due to the rest of magnetic signals instead of coming from *strong polarity* patches. This might be due to the fact that the observations at the VTT were performed during the reversal of the polar region polarity. In contrast, when taking this data, the new polarity of polar regions was already building up.

6.3.3 LOS magnetic topology

Hereinafter, only those pixels whose inversion in which the magnetic field strength, LOS magnetic field inclination and filling factor are reliably inferred are considered. Those pixels are selected depending on the behaviour of the χ^2 for fixed inclination inversions as detailed in Sec. 6.2. Even when these pixels have passed this test, we have found that the magnetic field strength, filling factor and microturbulent velocity can still be coupled.

In order to check whether the inferred magnetic field strength is determined independently of the filling factor or if they are coupled we performed an additional test. In this second test, we fixed the magnetic field strength to 100, 300, 500, 700, 900, 1100, and 1300 G. The free parameters of the inversion are the microturbulent velocity of the magnetic component, the LOS magnetic field inclination, the LOS magnetic field azimuth, and the filling factor. Two examples of fits after following such procedure are shown in Figs. 6.11 and 6.12. The figures show the best of 50 attempted inversions for, from top to bottom, 100, 300, 500, 700, 900, 1100, and 1300 G. Figure 6.11 presents a case in which the best fit to the observed Stokes profiles is clearly sensitive to the forced magnetic field strength. This means that the inversion of such a pixel is sensitive to the magnetic field strength determination. Surprisingly, Fig. 6.12 shows that as long as the imposed magnetic field strength is above 100 G and below 1100 G, the best fit for each magnetic field strength value is equivalent. Hence, the inferred strength is valid for an extremely wide variety of values. This large magnetic field strength range is allowed by the action of the filling factor and the microturbulent velocity. The filling factor increases as the forced magnetic field strength values is decreased, moving from 0.20 for 900 G to 0.85 for 300 G. In addition, the microturbulent velocity also increases from 1.58 km/s at 900 G to 1.83 km/s at 300 G inversion. Martínez González et al. (2006) already found that when Zeeman splitting is of the order or smaller than the Doppler width, the determination of the magnetic field strength might be affected by small variations of the temperature (role played by microturbulent in our test), i.e. the effect of small variations of Temperature has similar influence on Stokes profiles as variations of magnetic field. It is to be notice that even when the magnetic field strength is so poorly determined, the LOS inclination varies in a relatively narrow range of values ($66^\circ \pm 4$).

As most of the pixels (93%) that passed the test concerning their inclination reliability has a magnetic field strength poorly determined, in the forthcoming analysis, we restrict ourselves to the magnetic field inclination and azimuth.

Disc centre FOV:

Figure 6.13 presents the probability density functions for the LOS inclination, and azimuth (between 0° and 180°) for the disc centre region.

The LOS magnetic field inclination at disc centre is characterised by a polarity imbalance, with a dominant negative polarity. This was already seen in the LOS magnetic field flux density distribution (Fig. 6.10) and it is associated to the presence of strong magnetic patches of this polarity. These strong fields have inclinations close to the LOS ($\sim 180^\circ$). The LOS magnetic field inclination distribution is characterised by a preference for horizontal fields ($\theta_{LOS} \sim 90^\circ$). The magnetic fields analysed in Fig. 6.13 are derived from those polarimetric signals that show

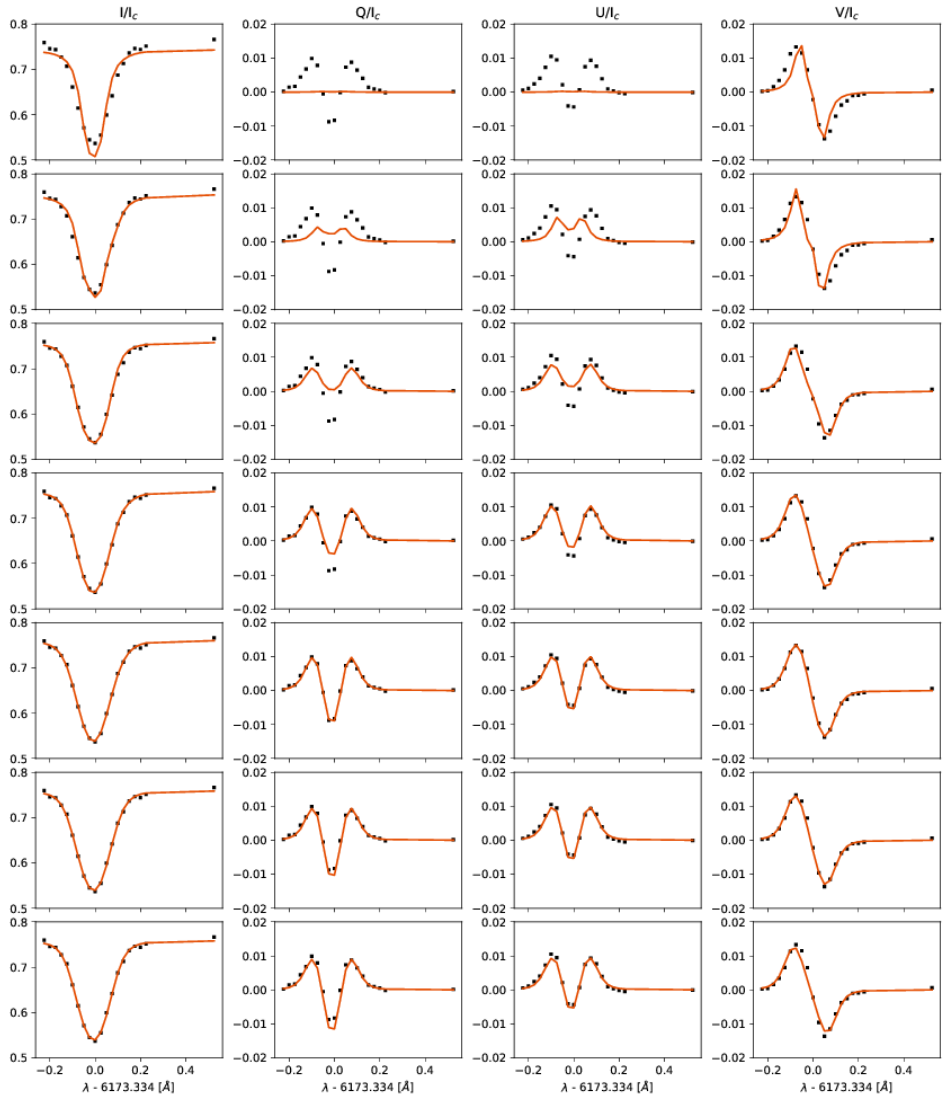

FIGURE 6.11— From left to right: Stokes I, Q, U and V profiles for a North region pixel. Observed profiles are plotted with black square marks. Best inversion profiles are in brown. From top to bottom: inversions performed at fixed magnetic field strength values of: 100, 300, 500, 700, 900, 1100, and 1300 G.

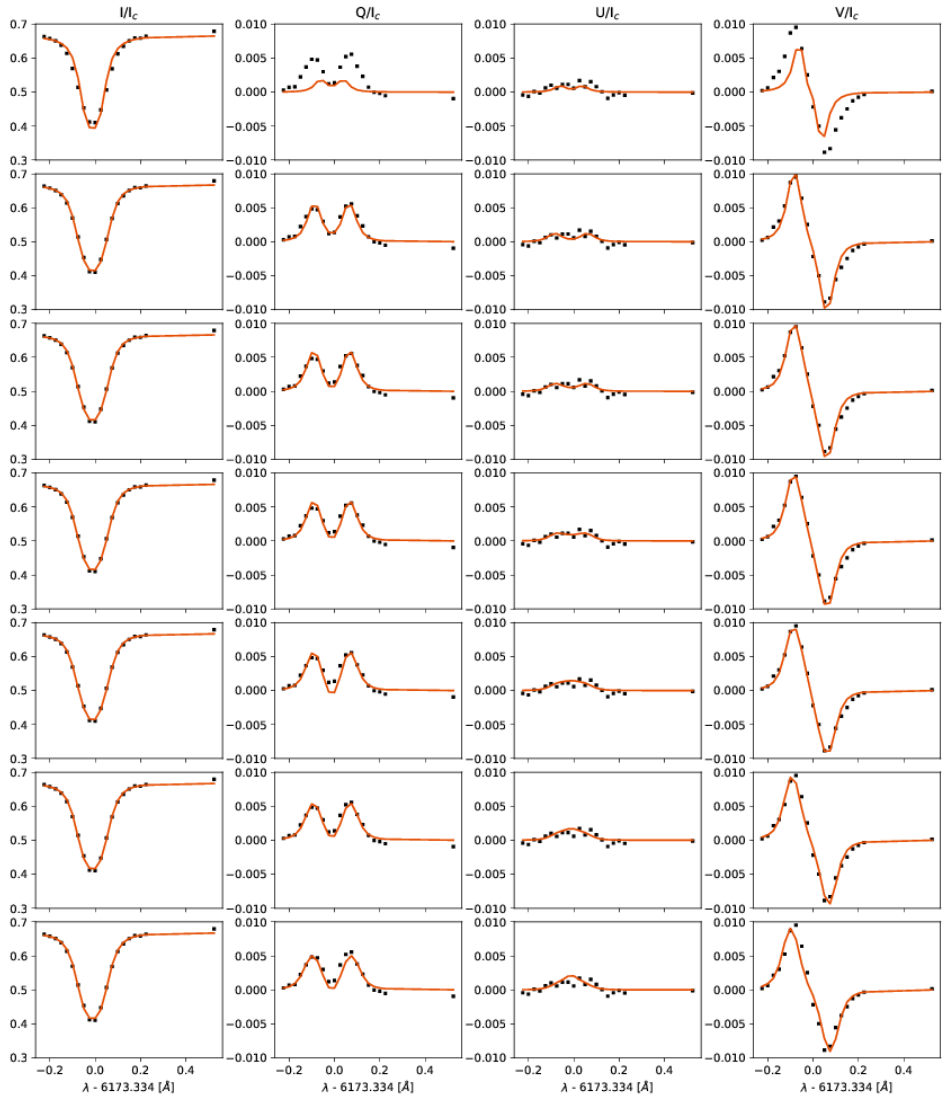

FIGURE 6.12— Same representation as in Fig. 6.11 for another case of the North region.

sensitivity to the LOS inclination. This criterion is fulfilled at this disc position when: 1- Linear polarisation is present. This property strongly limits the allowed LOS magnetic inclinations that

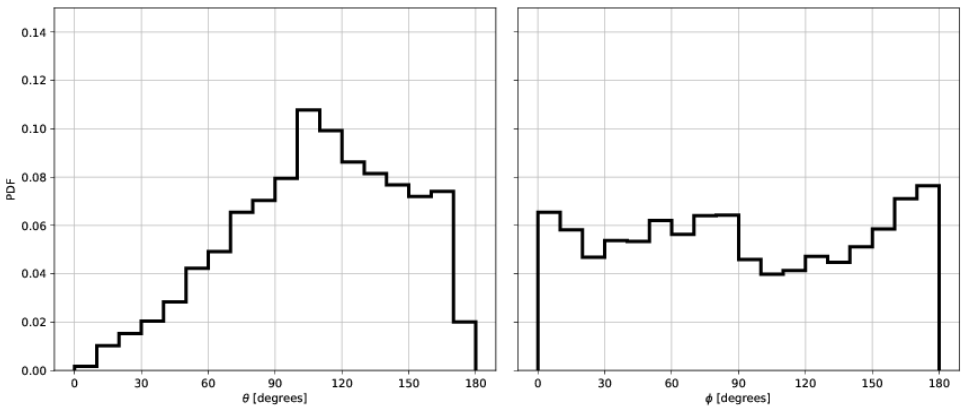

FIGURE 6.13— From left to right: probability density functions of the line-of-sight magnetic field inclination and azimuth of the disc centre dataset.

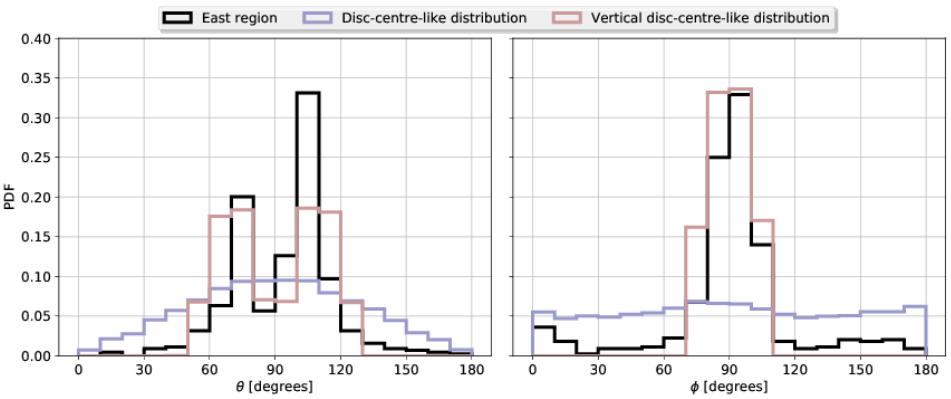

FIGURE 6.14— In solid black and from left to right: probability density functions of the line-of-sight magnetic field inclination and azimuth of the east region dataset. In blue, there is the observed disc centre magnetic field topology as it would be seen at the East region when taking into account geometrical effects. Red solid lines correspond to a subset (vertical fields) of the observed disc centre magnetic field topology.

is recovered. 2- Very strong fields, which tend to orientate along the LOS and where the Zeeman splitting of the sigma components is the most relevant feature in the inversion. This point could potentially bias our analysed magnetic distributions to horizontal fields (that give rise to linear signals) and to the strongest magnetic signals (that give rise to full Zeeman splitting), which at this disc position are usually vertical.

The last magnetic parameter for this disc position is the LOS magnetic field azimuth, whose probability density function is almost uniform.

Limb FOVs:

East region magnetic distributions are presented in Fig. 6.14. Figure 6.15 shows those corresponding to the North dataset.

As at the VTT, once the observed FOV is far from disc centre, the LOS reference frame does not match that of the local reference frame and hence, the LOS magnetic field inclination and azimuth can not be interpreted directly. As in the previous chapter, and in order to figure out some properties of the observed magnetic fields without changing the observed magnitudes to the LRF, we follow the same strategy as before. In this method, we use the disc-centre observed topology as reference. In particular, for that of the observed East (North) area. Knowing the LRF topology and the coordinates of every pixel on the disc, we can build the equivalent LOS topology that would be observed for a disc-centre-like distribution. This is shown in Fig. 6.14 (6.15) in blue. It is clear that the observed distributions at the East do not agree with those observed at disc centre. In contrast to the smooth LOS inclination expected from disc centre data, the one at the East limb shows two clear peaks at 75° and 105°. These values are close to the heliocentric angle of the observed area. Since vertical fields are expected to show this LOS inclinations, we select a subset of the fields inferred at disc centre. This selection is done for magnetic fields with inclinations below 15° or above 165°. The result is shown in red in Fig. 6.14 and Fig. 6.15 and this time the agreement between the expected distribution for vertical fields at disc centre and the observed ones is good. Furthermore, this set of close to vertical fields also reproduce the observed LOS magnetic azimuth distribution. The observed LOS magnetic field topology at limb datasets resembles quite well what one would expect from the subset of vertical fields of the disc centre distribution. It has to be noticed that at limb regions, the pixels that pass the reliability test (and the ones studied above) are characterised by strong linear Stokes signals. This scenario strongly bias our observed magnetic field topology to found vertical fields, since we need strong linear polarisation signals to be able to infer a reliable LOS magnetic field inclination.

6.3.4 LRF magnetic topology

For a proper comparison between the limb data and the one at disc centre it is convenient to turn to the LRF. To do so, we followed the same method detailed in Sec. 3.3. To that aim, we identify several magnetic structures where the LOS magnetic field azimuth and inclination are reliably inferred. In the LOS reference frame the 180° LOS azimuth ambiguity entails two possible solutions for each structure (assuming the magnetic field vector is smooth in the structure). Figure 6.16 presents two examples of LRF inclinations and azimuths retrieved for two structures at the North and two more at the East regions. The first point to bear in mind is that both solutions for the whole set of structures are physically feasible, i.e. we cannot discard any solution by inconsistent morphology. Hence, in order to pick one of the two possible morphologies for each structure, we demand that the final LRF azimuth (ϕ) distribution, given by the whole set of structures identified, at each disc position is as flat as possible. This criterion is based on

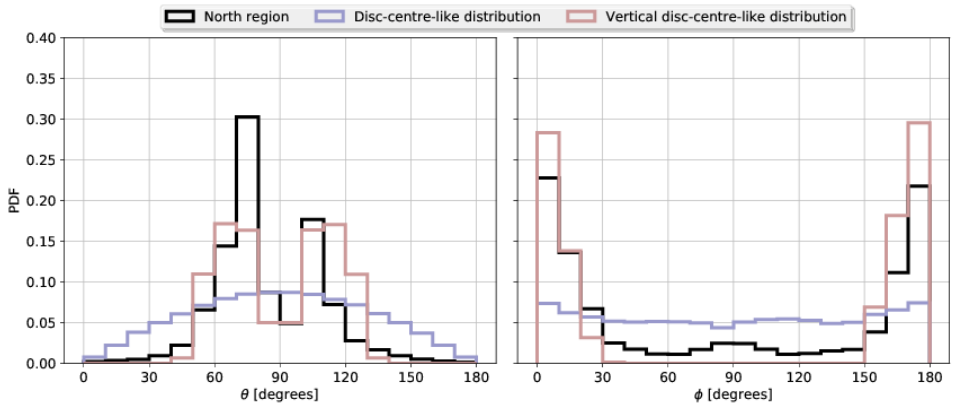

FIGURE 6.15— North region line-of-sight magnetic field topology following the same representation as in Fig. 6.14.

the azimuth distribution inferred at the disc centre, and since we found no argument to have a preferred magnetic field orientation. This way, the retrieved topology (and the discarded one) is shown in Figs. 6.17 and 6.18.

Both East and North quiet Sun regions are compatible with a flat LRF azimuth distribution. In such a scenario, the LRF inclination is characterised by vertical distributions of mixed polarities. The discarded solution for the North pole quiet Sun has LRF inclinations around 45° and the equivalent negative field 135°. These fields are aligned along the N-S solar meridian. A similar scenario is found at the East limb quiet Sun though at this disc position, the magnetic fields are aligned with the E-W solar parallel. Such a magnetic field configuration constitute a very specific topology which is disc position dependent and aligned with the radial direction. This fact together with the absence of this magnetic field configuration at disc centre quiet Sun, leads us to reject these solutions.

In the general scenario, the reversal of the polar region dominant polarity takes place by the incoming polarity from lower latitudes. This incoming polarity carries a preferred polarity given by that of the following part of active regions. This polarity is of opposite sign to that of the polar regions and hence, it supplies flux that cancels the previous dominant polarity and afterwards, builds up the new dominant polarity of the polar region. Since our data was taken close to a polarity reversal and the polar area covered is large enough, we look at the LRF polarity distribution with latitude.

In Fig. 6.19, we explore the polarity distribution over the covered North polar area. LRF positive polarities are shown in blue, whilst negative ones are in brown. In the scatter plot, it can be seen that blue patches dominate at lower latitudes. This conclusion is better shown by the histogram on the left, with the PDF of positive and negative distributions with latitude. It is

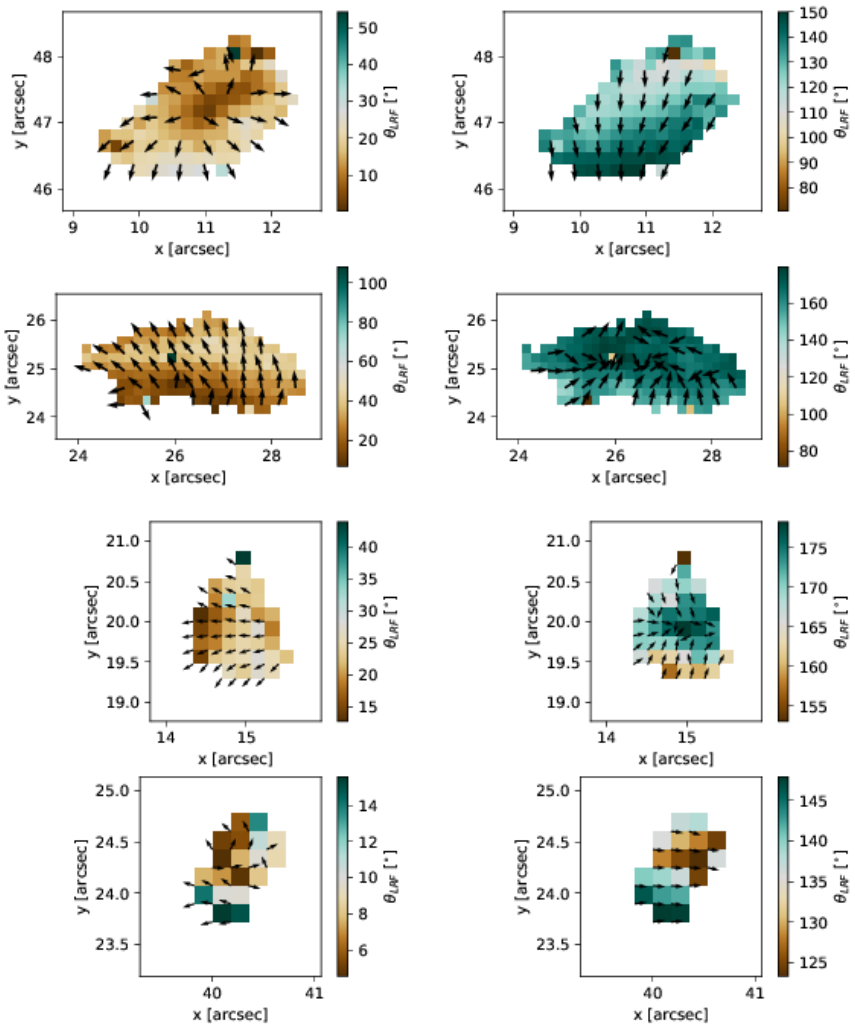

FIGURE 6.16— From top to bottom: four magnetic structures with the two possible solutions retrieved when changing from LOS to LRF (left and right). In color scale the LRF magnetic field inclination is shown and arrows represent the LRF azimuth. The two upper structures correspond to the polar region and the other two to the East region.

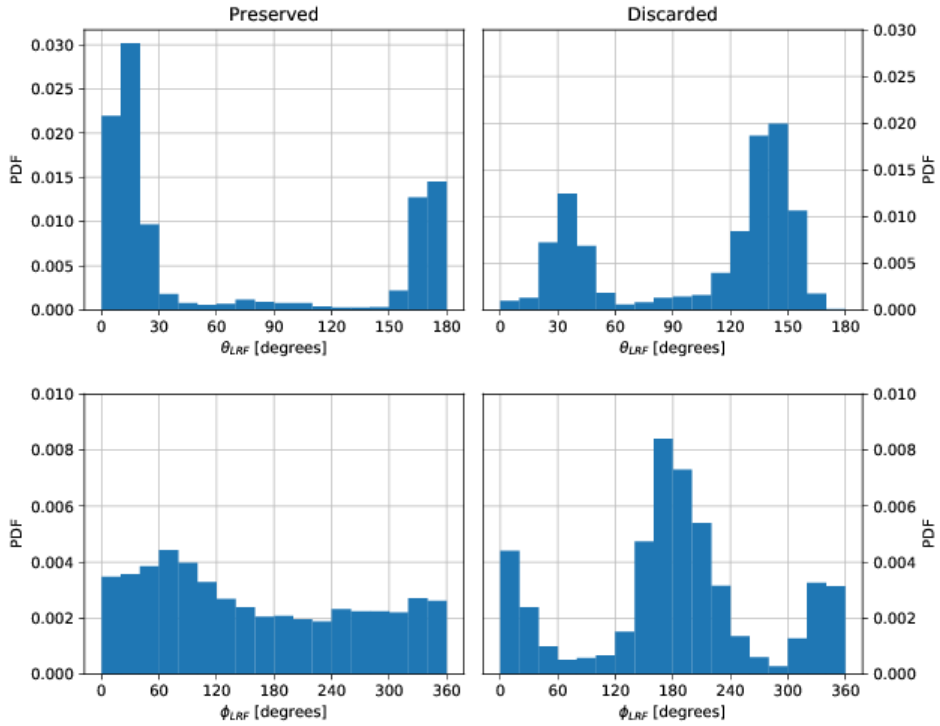

FIGURE 6.17— Left panels, from top to bottom: North region local reference magnetic field inclination and azimuth probability density functions that are to be preferred after the line-of-sight to local reference frame method. Right panels: discarded solution.

clear that the LRF negative and positive polarities above latitude 70° are quite balanced, whilst the positive polarity is more dominant at lower latitudes.

Another question that can be further explored is whether this dominant polarity comes from the largest magnetic concentrations or the whole distribution shows this imbalance. To do so, we calculate the total LRF flux of each of the 274 magnetic patches identified at the North polar region. This magnitude is the result of the magnetic flux density previously introduced ($\Phi = \alpha\, B\, \cos\theta$) times the pixel area and integrated over the whole patch. In order to calculate the pixel area it has to be taken into account that limb observations are affected by foreshortening effect. The resulting magnitude is the magnetic flux of the structure, whose decimal logarithm is shown in Fig. 6.20. Most of the patches are characterised by magnetic fluxes between 10^{17} and $10^{18.5}$ Mx, with small tails towards smaller and larger values. Concerning the contributors to the polarity, we see that above 10^{17} Mx, the distribution is completely dominated by positive patches. This

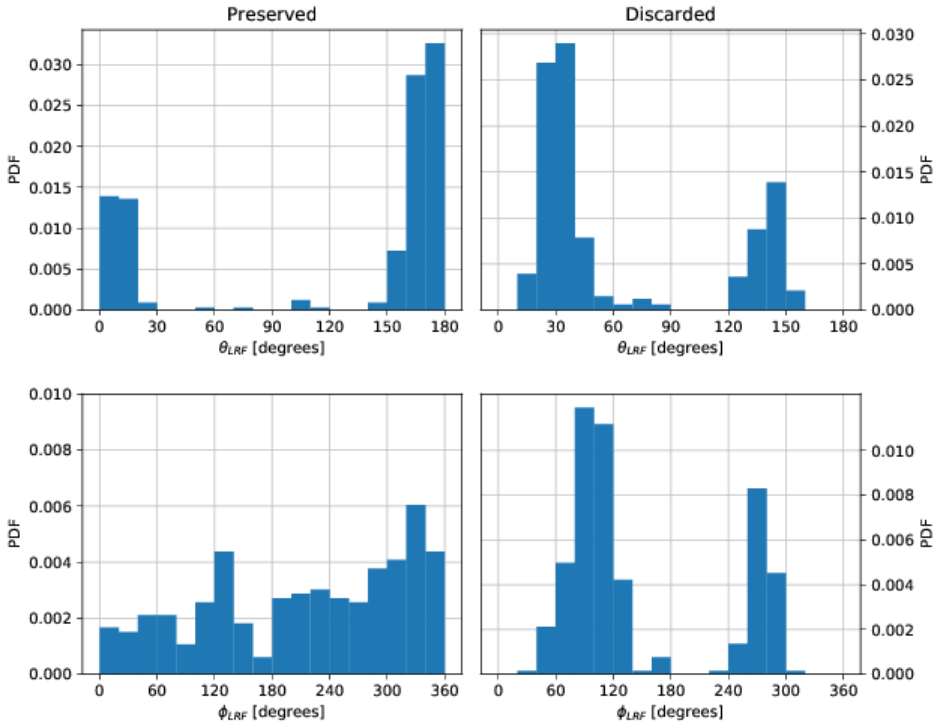

FIGURE 6.18— Left column, from top to bottom: prefered local reference frame magnetic field inclination and azimuth at the East region by our LOS to local reference frame method. Right column, from top to bottom: discarded East limb data probability density functions.

is in agreement with the results by Shiota et al. (2012), who found that the magnetic patches with magnetic flux above 10^{17} Mx are the main agents of the dominant polarity of the polar region, and the ones whose population vary with the solar cycle.

6.4 Summary of the results and discussion

- The observed FOVs show magnetic signals in ∼6% of the observed area of any polarised Stokes parameter and only to ∼0.5% of either Q or U Stokes profiles. This signals are seen in patches of a few arcseconds.
- The amplitudes of the polarimetric signals are weak, though the maximum amplitudes reach almost 10% of the quiet Sun intensity at disc centre. The strongest amplitudes at disc centre are stronger than those at the limbs and are associated to Stokes V. At the

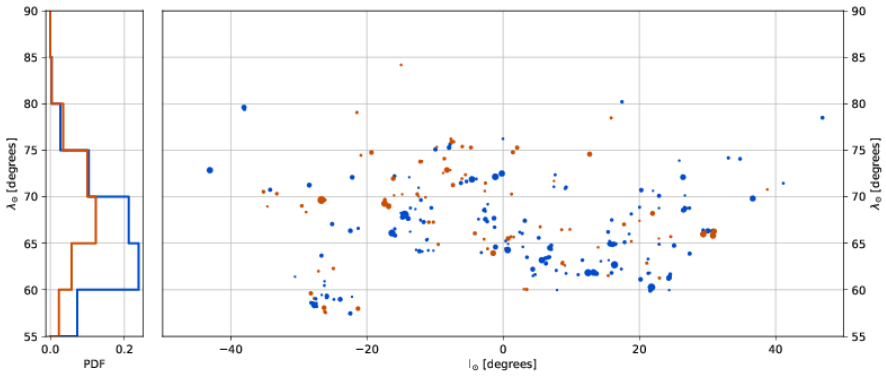

FIGURE 6.19— Right panel: solar heliospheric longitude and latitude distribution of the local reference magnetic flux for the magnetic patches found at the North region dataset. Blue colour stands for positive (outgoing from the Sun) magnetic fields. Negative (ingoing to the Sun) magnetic fields are plotted in brown. Left panel: probability density functions with solar latitude of the local reference frame magnetic flux found for the various magnetic patches. Colour code is preserved for the sake of clarity.

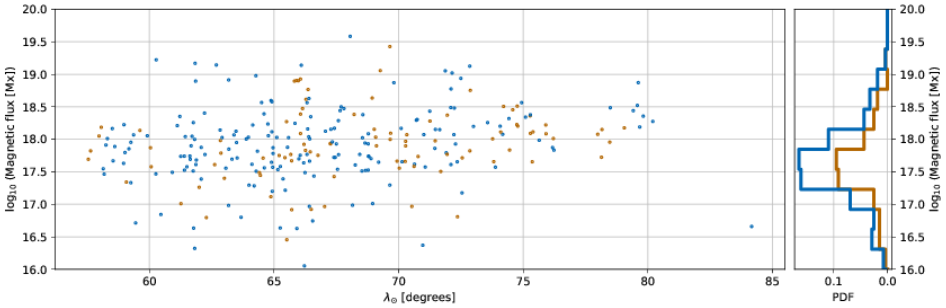

FIGURE 6.20— Left panel: local reference frame magnetic flux dependence with heliospheric latitude for the polar region dataset. Blue colour stands for positive flux (outgoing the solar surface) and brown for negatives values. Right panel: local reference frame probability density functions. Colour code is preserved for the sake of clarity.

limbs, the strongest signals are associated to any of the Stokes parameters, though they are smaller than the strongest amplitudes at disc centre. This situation, except for the amplitudes values, is much the same as at the VTT.

- The amplitude and area asymmetries of the regular Stokes V profiles are broad and show mean positives values at disc centre. This mean values shifts to negatives values when moving to the limbs. This behaviour is again similar to that observed at the VTT.

- The FOV mean LOS magnetic flux density at the three disc positions is given by strong polarity patches and it is found to be -4.396 Mx/cm^2 for disc centre, 0.359 Mx/cm^2 for North region, and -1.279 Mx/cm^2 for the East limb. This time, this situation is different from that at the VTT where we found that at the North polar region the mean LOS magnetic flux density was set by the non-*strong polarity* patches. Whether this is due to the limited area coverage of VTT observations or if its something proper of the polar region requires of more observational effort.

- The LOS velocities found are consistent with the same picture found at the VTT. However, the values of the LOS downflows of the magnetic component at the SST are $\sim$ 600 m/s and at the VTT, $\sim$ 1.7 km/s

- The magnetic field topology is analysed over those inversions that show sensitivity to the LOS inclination. The magnetic field strength and filling factor, however, are very poorly determined for most of the magnetic fields and hence, they are not analysed.

- The main properties of the LOS magnetic topology at disc centre are:

  -The LOS magnetic field inclination shows many horizontal fields whose occurrence decreases to more vertical fields.

  -The LOS magnetic field azimuth is homogeneous.

- At the East limb, the main LOS magnetic field properties are:

  -The LOS magnetic field inclinations are strongly concentrated around the mean heliocentric angle and around 180-$\theta_\odot$. This is symptomatic of a vertically dominated distribution, as it is checked by choosing a subset of vertical fields from disc centre.

  -The LOS magnetic field azimuths are strongly aligned with the E-W solar direction.

- At the North limb, a similar situation to that on the East limb is observed:

  -The LOS magnetic field inclinations are characterised by a distribution with two strongly preferred inclination values. This values matched the mean heliocentric angle and around 180-$< \theta_\odot >$

  -The LOS magnetic field azimuth aligns with N-S direction.

- In order to change the magnetic fields from LOS to LRF, we look for spatial coherence in those patches whose magnetic fields show sensitivity to the LOS inclination.

- The results at the LRF are characterised by vertical fields and expanding or converging azimuths around them. This component matches the canopy-like scenario, where vertical magnetic fields expand with height exhibiting an halo around them with magnetic field radial expansion or convergence.

We found that the magnetic fields for which, a topology can be retrieved are characterised by vertical fields. These fields are in agreement with one of the components found at the infrarred study of the previous chapter, the study of Quintero Noda et al. (2016) and with one of the components found by Ito et al. (2010); Blanco Rodríguez & Kneer (2010); Jin et al. (2011) and Shiota et al. (2012). At the previous chapter we observed a bi-modal behaviour for the magnetic

fields above 600 G. In order to check whether the observed polarisation signals at the visible wavelength is compatible with those at the infrarred ones, we have looked at the profiles for which a topology could not reliably inferred. We found that these magnetic fields that share topological characteristics to the non-vertical fields found at the infrarred. First, their magnetic field strength is strong enough to show Zeeman splitting at 15648 Å but have a magnetic field strength below 1000 G. Hence, this is compatible with the fact that at 6173 Å we can not determine the magnetic field strength. Second, at the infarred, these non-vertical fields were characterised by weak linear polarised signals. This property is also shared by the fields inferred from the visible study whose topology has not been addressed. However, at the visible, the observed spectral line's Zeeman to Doppler width is much lower than at the infrarred (remind the linear dependence of this ratio with wavelength). Hence, these fields discarded from the magnetic field analysis could be the visible the counterpart of the non-vertical fields seen at infrarred wavelengths.

For the subset of magnetic fields observed at the visible whose topology is retrieved, we obtained the LRF topology and calculate the magnetic flux associated to each magnetic structure. We have found that the magnetic patches that carry the polarity imbalance at the North region is given by the magnetic patches with LRF magnetic flux above 10^{17} Mx. The distribution of the magnetic structures over the North polar region is so that the polarity imbalance takes place below solar latitude of 70°. Hence, we have found that:

1. the largest magnetic concentrations are the ones that give the LRF polarity sign of the polar region and
2. these structures are localised in latitudes below 70°.

This picture is consistent with that found by Shiota et al. (2012), who found that the largest magnetic patches are the ones that give the polarity identity of the polar region. In addition, it is found that during and after a polar region polarity reversal, the new building flux arrives to the polar regions from lower latitudes (Benevolenskaya, 2004). This would explain why the polarity imbalance observed is concentrated below 70°.

7

Conclusions

In this thesis we have studied the photospheric magnetism at solar polar regions. This objective was accomplished by means of different spectropolarimetric observations aiming to characterise both, the temporal behaviour of the polar region magnetism and the high-resolution and high magnetic sensitivity characterisation of their magnetism. To do so, two main strategies are followed. On the one hand, the long term study requires of very long (several years) observations. In this sense, the SDO satellite is an excellent candidate, as one of the onboard instrument, HMI, has been recording data since 2010 systematically and for the whole disc. On the other hand, the study of the topology requires at the same time of high resolution and high polarimetric sensitivity. To tackle this second target, we access to full Stokes spectropolarimetric observations in two different facilities: 1- the TIP-II instrument installed at the VTT that offers near infrared observations, and 2- the CRISP instrument at the SST, that allow high sensitivity spectropolarimetric observations as well as large FOVs.

The analysis of the mean LOS magnetic field component averaged over longitudes at the polar regions exhibit the expected behaviour as the Sun undergoes a solar maximum magnetic activity. During this time, polar regions show a progressive magnetic field strength decay as the Sun gets closer to the maximum. They reverse their polarity during the maximum and start building up their new dominant magnetic polarity, which gives their magnetic identity until next solar maximum. In addition to this global behaviour, we found an unexpected oscillatory and weak magnetic signal along most of the time series and when each polar region is better observed.

Interestingly, this signal is not only observed at polar regions but it is present allover the solar surface during the whole time series. The Fourier analysis shows a clear concentration of power at the solar rotation frequency at each latitude, i.e., the periodicity traces the solar differential rotation, hence confirming the solar origin of the signal. A natural candidate for such an oscillation are active regions, since, at a given time, their distribution within the activity belt is not axisymmetric. However, the study of the mean LOS magnetic field component due to active regions, show no concentration of Fourier power at solar rotation frequencies. This is due to the fact that they emerge at the solar surface in an incoherent way. Hence, the phase coherency, at much larger timescales than their lifetimes (from weeks to few months) , like the

ones here studied is lost. This is the reason that active regions do not concentrate Fourier power at solar rotation frequencies. This result points to a large-scale, long-term candidate, whose coherency is long enough to produce such an oscillation. One such candidate is the presence of non-axisymmetric components of the global magnetic field. This scenario is further considered with a very simple model in which the global magnetic field is an inclined dipole. The model includes the measured solar rotation profile and considers the Earth orbit inclination. With such a model, we can reproduce some global properties of the oscillation when the inclination of the dipolar and rotation axes are between 21° and 40°. There are previous reports of magnetic tilt angles with respect to the solar rotation axis at higher layers of the solar atmosphere (Hundhausen, 1977) but, to the best of our knowledge, its the first observation pointing to such a tilt at photospheric layers.

This study allows the long-term characterisation of the polar regions magnetism, however, more magnetic sensitivity is needed for a complete characterisation of the magnetic field topology. This step has been further consider from two different points of view.

We use TIP-II at VTT to observe at infrared wavelengths, which allow the analysis of the weakest magnetic signals thanks to the higher Zeeman sensitivity of this spectral wavelength. We have found that most of the observed area show polarimetric signals. However, we can not reliably retrieve the magnetic topology from all of them. We only consider those fields that produce a Zeeman splitting larger than the Doppler width. We then consider only these pixels with magnetic field strength larger than 600 G. This requirement ensures a proper determination of the magnetic field strength, and thus, it breaks the possible degeneracy with inclination and filling factor.

In this analysis we found a bi-modal behaviour. On the one hand, some of these fields, are characterised by strong ($\sim$ 1100 G) fields whose topology is consistent with vertical fields. Moreover, when retrieving the local reference frame topology, the previous properties are confirmed and we found that they match the canopy-like structures. These structures are characterised by a core of strong vertical fields around which, the magnetic fields expand or coalescence radially. On the other hand, for the rest of magnetic fields that are above 600 G we can say that they cannot be due to individual magnetic field structures of vertical fields. It is so because the amplitudes for such a configuration presents linear polarisation signals well above the ones we see for these fields. However we have qualitatively seen that, the presence of unresolved magnetic field loops, might be able to explain these second component.

The CRISP instrument installed at the SST allows a much better area coverage of the poles with higher spatial resolution but more moderate polarimetric sensitivity. As before, we analyse only those pixels where the magnetic field vector information can be unambiguously retrieved. Since the Zeeman splitting in the visible is smaller than in the infarred, we can not use the magnetic field strength as a sufficient condition to find those pixels where the magnetic field is uniquely retrieved. However, we use a criterion based on the behaviour of the model fit to observations for fix magnetic field configurations. For this subset of pixels we found that they are characterised by vertical fields with a canopy-like morphology, i.e. they are consistent with the vertical fields found at the VTT.

The large North region coverage shows that these magnetic fields are concentrated in patches scattered allover the surface. The total LRF flux going through the solar surface in these patches ranges from 10^{16} Mx to $10^{19.7}$ Mx, i.e. we do not reached as weak structures as Shiota et al. (2012), who reaches 10^{15} Mx. Yet, we found that the dominant polarity is settled by patches with fluxes above 10^{17} Mx, in agreement with what they found. Moreover, we found that North polar region above 70° latitude is in polarity balance. It is below this limit where the positive polarity clearly dominates above the negative polarity. This picture is consistent with the accepted landscape where the new polarity is transported from the flux supply coming from decaying active regions at lower latitudes. The active region decay supplies magnetic flux to the surroundings and the one dragged to higher latitudes is characterised by a preferred polarity —that of the following part of the decaying active region—.

Apart from these fields for which we retrieved the magnetic field topology, this visible study show several polarimetric signals scattered all over the solar surface for which we cannot accurately determined their topology. However, in order to see whether the qualitative scenario used to explain the non-vertical fields of the VTT, we consider the mean polarimetric signals for each patch. This way, even when the visible spectral range has lower polarimetric sensitivity, if the whole structure has tiny but coherent azimuth, might show similar polarimetric properties. From several structures, we found that a few of them do show very weak linear polarisation signals pointing in the radial direction. Hence, this structures might be the visible counterpart of the non-vertical magnetic field observed at the infrarred.

In conclusion, we have performed a deep study of the polar magnetism finding that, in general, the picture inferred from the work here presented is in agreement with the general landscape already available from previous studies about the solar polar regions magnetism. This way, we have seen that the polar region behaviour is as was expected for during the period covered by the observations. We have also performed an analysis of the magnetic topology at the polar regions close to a maximum of activity, phase of the cycle for which not such a study had been done yet. Finally we have additionally found an exiting magnetic signal present all over the surface which could be associated to the presence of an axisymmetric component in the global magnetic field.

In our study of the polar magnetism we have confirmed previous findings and some of our results are in agreement with the general landscape of the global magnetism. In particular we find that the sign of the polar caps is determined by vertical kG fields found in small patches with canopy-like topology. But more interestingly, we have identified a new populations of fields whose topology is not compatible with vertical fields. Aside from a detailed study of the polar magnetism, we have looked at this magnetism from a global scale perspective. In agreement with previous studies we have found that the magnetic strength of the polar regions followed a progressive weakening when elapsing to the maximum of activity. Then both poles reversed their dominant polarity and started to build up the new one. Finally, we have discovered a weak magnetic signal present all over the surface which could be associated to the presence of an axisymmetric component in the global magnetic field. This result has implications in the theory of generation of solar magnetism since up to now, global magnetic field non-axisymmetric

configurations are recovered for short periods of time.

A

Inversions with two magnetic atmospheres

At the beginning of the chapter we have analysed Stokes V profile asymmetries and Stokes V profile shapes (see Sec. 5.2.2). Asymmetries or multi-lobed profiles are features that the model proposed (one magnetic atmosphere with all parameters constant in height except for the temperature) could not reproduce. In this section we slightly increase the complexity of the model used to reproduce some features of the observed Stokes spectra. In particular, we consider now that each Stokes spectrum is the result of the presence of two different magnetic atmospheres (with all the parameters constant in height but the temperature) and a given non-magnetic stray-light profile that occupies 30% of the pixel. For a more detailed description of the model, the reader is referred to Sec. 5.3.

The comparison of the various magnetic parameters recovered from the two different inversion strategies is presented in Fig. A.1. The comparison of the magnetic component retrieved with the one magnetic component inversion and the minor component inferred from the two magnetic component inversion show good agreement for both, the magnetic field strength and LOS inclination. The minor component LOS azimuth retrieved with the two magnetic atmospheres is slightly noisier but is in good agreement with that from the one magnetic inversion. The filling factor (right panels) show less agreement. This can be due to two reasons. The first one is that a fraction of the pixel is occupied by the stray light factor. Hence, for the same magnetic field, it is expected that the filling factor of the two magnetic atmosphere is larger, since the *pixel size* available is smaller. The second one is that, if the magnetic field strength is no larger than the Doppler width, then we might retrieve the LOS magnetic flux density instead of the filling factor independently. The major component of the two magnetic atmospheres inversion shows a completely different behaviour, characterised by very weak fields, LOS inclinations close to 90° and huge filling factors. Hence, we have that the major component retrieves similar results to the magnetic component of the single magnetic inversion. Since the minor component is characterised by very small magnetic fields, the magnetism analysed in this thesis (above 600 G at the limbs) is characterised similarly by the magnetic component of the one magnetic inversion or by the major component in the case of a two magnetic atmospheres inversion.

The inversion strategy with two magnetic atmospheres is able to reproduce more than one lobe

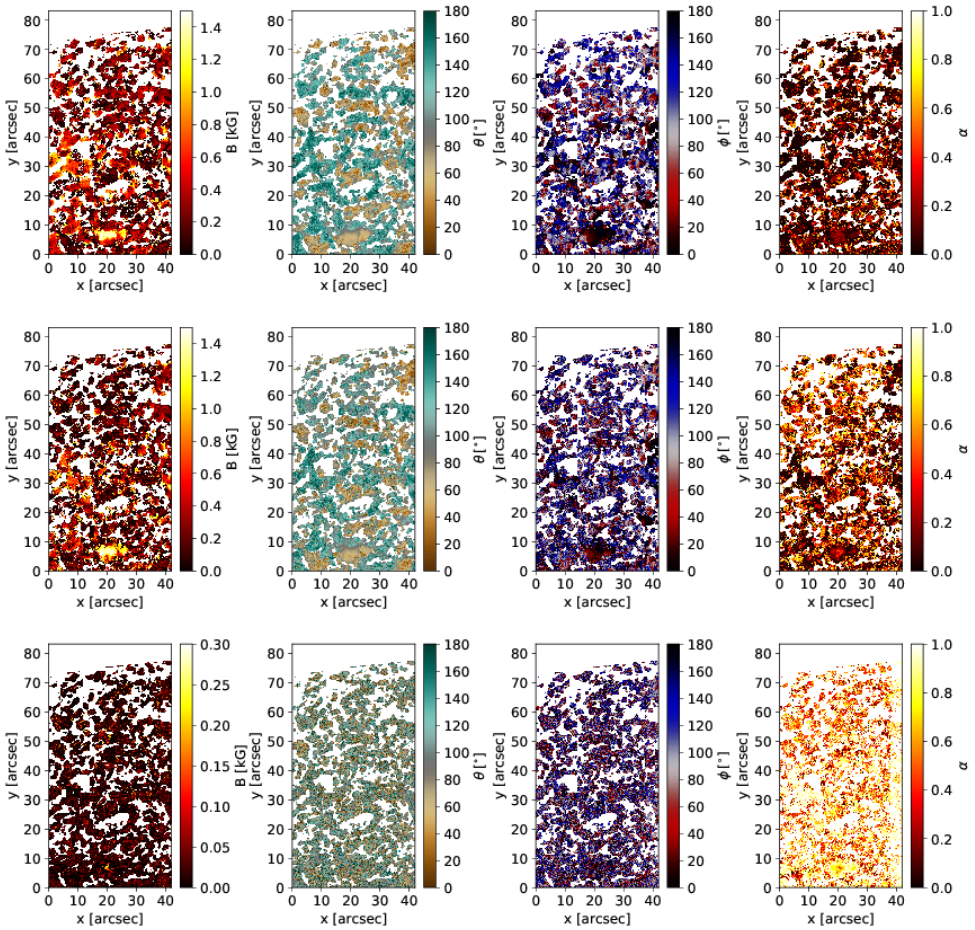

FIGURE A.1— From left to right: LOS magnetic field strength, inclination, azimuth and filling factor maps for the North region data. The results for the one magnetic atmosphere inversion are in the top row, the major component of the inversion with two magnetic atmospheres are presented in middle row and the minor component results for this second inversion strategy are in bottom row .

profiles (see for instance Fig. 5.7) and profiles with amplitude asymmetries. In Fig. A.2 we show the probability density functions of amplitude asymmetry found for the observed, for the one magnetic inversion and for the two magnetic atmosphere inversion. It can be seen, that the latter partially reproduces the observed distribution. The two magnetic inversion strategy is also able to improve the inversion of those pixels where the LOS velocity of the linear profiles is

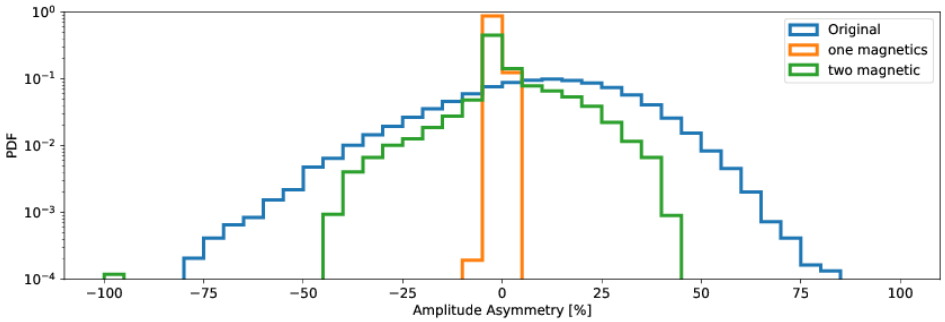

FIGURE A.2— Blue line: the amplitude asymmetry distribution of the observed Stokes V profiles. Orange line: the amplitude asymmetry distribution of the synthetic Stokes V profiles of the inversion with one magnetic atmosphere. Green line: the amplitude asymmetry distribution of the synthetic Stokes V profiles with two magnetic inversions.

different to that of the circular polarisation profiles. Thus this strategy leads to an improvement of the reduced chi-squared for most of the FOV: 51%, 54% and 46% for the North, disc centre and West datasets, respectively. In a 38%, 37% and 34% of the cases, the two magnetic inversion reaches a fit a 10% than that by the single magnetic inversion. However, the magnetic properties inferred by the simplest inversion with only one magnetic atmosphere is in quite well agreement with the information encoded in the minor component of the two magnetic atmospheres inversion. Hence for the cases considered in this thesis, the one magnetic inversion strategy is enough

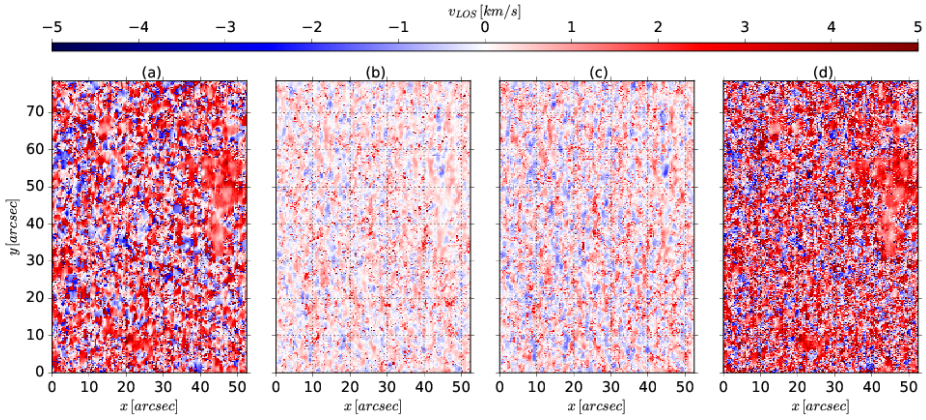

FIGURE A.3— LOS velocities for the magnetic (a) and non-magnetic (b) atmospheres of the inversion where this two atmospheres share every pixel. Panels c and d depict the LOS velocities of the major and minor components of the two magnetic components inversion. The data is for disc centre position. .

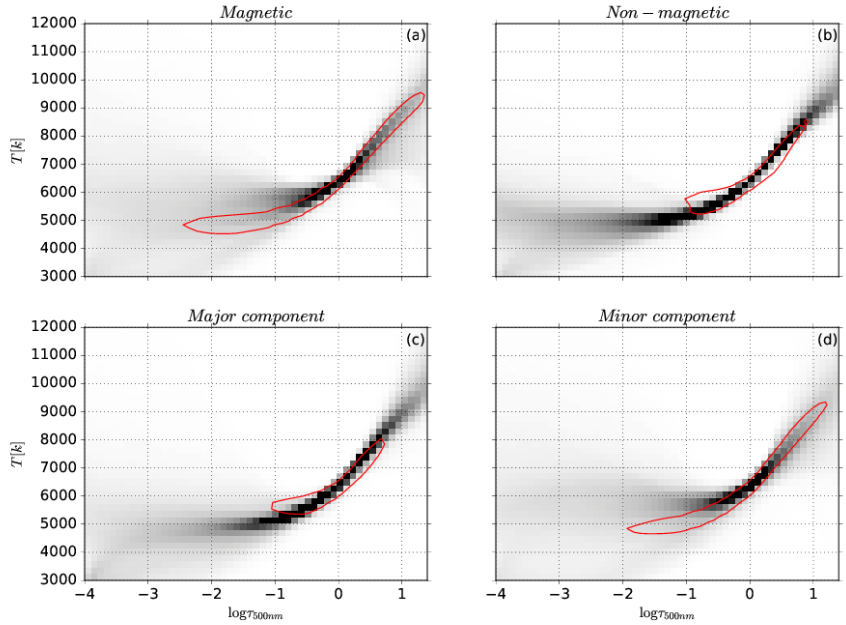

FIGURE A.4— Temperature stratification with $\log \tau_{500}$ the disc centre dataset. Panels *a* and *b* show the magnetic and non-magnetic atmospheres of the simplest inversion strategy, respectively. Red contour shows the first quartile of the other atmosphere distribution. The same representation is used to display the temperature density plots for the two magnetic atmospheres of the more complex inversion strategy: the major component in *c* and the minor one at *d* .

when analysing their global properties. It is so because the one magnetic strategy and the two magnetic one retrieves similar information and the single magnetic one is easier to interpret.

The comparison of the LOS velocities recovered from the two different inversion strategies points in this same direction. This comparison is shown in Fig. A.3. The LOS velocities for the four atmosphere components are depicted: panel *a* is the magnetic atmosphere of the inversion with only one magnetic atmosphere, *b* is the non-magnetic atmosphere, *c* is the major atmosphere of the two magnetic components inversion, and *d* is the minor component. It is clear that, as in the case of the magnetic parameters, the magnetic atmosphere of the simplest inversion strategy resembles well with the minor component of the two magnetic atmospheres inversion strategy. It is also seen that the non-magnetic and the major atmospheres are also very similar. Again it is seen that the magnetic atmosphere of the simplest inversion is able to catch most of the magnetic information.

This same situation is seen in the temperature distributions of the atmospheres for each inversion strategy. This conclusion can be reached with Fig. A.4, where the temperature density plots of the disc centre inversions are presented. The temperatures recovered for the magnetic atmosphere of the simplest inversion are very similar to that obtained for the minor component of the two magnetic atmospheres inversion, i.e. the one that exhibits similar magnetic and dynamic properties. In both cases, these atmospheres are characterised by a hotter plasma above the $\tau_{500} = -0.8$ nm than that inferred for the non-magnetic. Below $\tau_{500} = 1$ the temperature of the magnetic atmosphere of the simplest inversion and that of the minor component of the two magnetic atmospheres, is found to be slightly cooler than the other atmosphere sharing the pixel. In addition, both the non-magnetic component and the major component show a more coherent temperature behaviour through a wider $\log \tau$ range. This is observed in the higher density compared to the other component temperature stratifications from $\log \tau = -2$ to $\log \tau = 1$.

We feel confident on the results of the analysis from the simplest inversion since it seems that the major properties of the physical parameters are not strongly distorted and the interpretation is much simpler.

Bibliography

Allende Prieto, C., Asplund, M., & Fabiani Bendicho, P. 2004, A&A, 423, 1109

Asensio Ramos, A. 2009, ApJ, 701, 1032

Asensio Ramos, A., Martínez González, M. J., & Rubiño-Martín, J. A. 2007, A&A, 476, 959

Babcock, H. D. 1959, ApJ, 130, 364

Babcock, H. W. 1961, ApJ, 133, 572

Babcock, H. W., & Babcock, H. D. 1952, PASP, 64, 282

—. 1955, ApJ, 121, 349

Bahcall, J. N. 1969, Scientific American, 221, 28

Beck, C., Rezaei, R., & Fabbian, D. 2011, A&A, 535, A129

Benevolenskaya, E. E. 2004, A&A, 428, L5

Berdyugina, S. V., & Fluri, D. M. 2004, A&A, 417, 775

Bianda, M., Ramelli, R., Gisler, D., & Stenflo, J. O. 2014, in Astronomical Society of the Pacific Conference Series, Vol. 489, Solar Polarization 7, ed. K. N. Nagendra, J. O. Stenflo, Q. Qu, & M. Samooprna, 167

Blanco Rodríguez, J., & Kneer, F. 2010, A&A, 509, A92

Blanco Rodríguez, J., Okunev, O. V., Puschmann, K. G., Kneer, F., & Sánchez-Andrade Nuño, B. 2007, A&A, 474, 251

Bommier, V., Derouich, M., Landi Degl'Innocenti, E., Molodij, G., & Sahal-Bréchot, S. 2005, A&A, 432, 295

Born, M., & Wolf, E. 1999, Principles of optics : electromagnetic theory of propagation, interference and diffraction of light

Borrero, J. M., & Kobel, P. 2013, A&A, 550, A98

Bruno, R., Burlaga, L. F., & Hundhausen, A. J. 1982, JGR, 87, 10339

Buehler, D., Lagg, A., & Solanki, S. K. 2013, A&A, 555, A33

Buente, M., Solanki, S. K., & Steiner, O. 1993, A&A, 268, 736

Centeno, R., et al. 2007, ApJL, 666, L137

Charbonneau, P. 2010, Living Reviews in Solar Physics, 7, 3

Collados, M. 1999, in Astronomical Society of the Pacific Conference Series, Vol. 184, Third Advances in Solar Physics Euroconference: Magnetic Fields and Oscillations, ed. B. Schmieder, A. Hofmann, & J. Staude, 3–22

Collados, M., Lagg, A., Díaz Garcí A, J. J., Hernández Suárez, E., López López, R., Páez Mañá, E., & Solanki, S. K. 2007, in Astronomical Society of the Pacific Conference Series, Vol. 368, The Physics of Chromospheric Plasmas, ed. P. Heinzel, I. Dorotovič, & R. J. Rutten, Heinzel

de la Cruz Rodríguez, J., Löfdahl, M. G., Sütterlin, P., Hillberg, T., & Rouppe van der Voort, L. 2015, A&A, 573, A40

de la Cruz Rodríguez, J., Rouppe van der Voort, L., Socas-Navarro, H., & van Noort, M. 2013, A&A, 556, A115

de Wijn, A. G., Stenflo, J. O., Solanki, S. K., & Tsuneta, S. 2009, SSRv, 144, 275

del Toro Iniesta, J. C., & Ruiz Cobo, B. 2016, Living Reviews in Solar Physics, 13, 4

Derouich, M., Bommier, V., Malherbe, J. M., & Landi Degl'Innocenti, E. 2006, A&A, 457, 1047

Doerr, H.-P. 2015, PhD thesis, University of Freiburg

Domingo, V. 1995, in ESA Special Publication, Vol. 376, Helioseismology, 3

Domingo, V., Fleck, B., & Poland, A. I. 1995a, SSRv, 72, 81

—. 1995b, SoPh, 162, 1

Domínguez Cerdeña, I., Sánchez Almeida, J., & Kneer, F. 2003, A&A, 407, 741

Ermolli, I., Berrilli, F., & Florio, A. 2003, A&A, 412, 857

Ermolli, I., et al. 2013, Atmospheric Chemistry & Physics, 13, 3945

Faurobert, M., Arnaud, J., Vigneau, J., & Frisch, H. 2001, A&A, 378, 627

Faurobert, M., & Ricort, G. 2015, A&A, 582, A95

Faurobert-Scholl, M., Feautrier, N., Machefert, F., Petrovay, K., & Spielfiedel, A. 1995, A&A, 298, 289

Ferrario, L., Melatos, A., & Zrake, J. 2015, SSRv, 191, 77

Foreman-Mackey, D., Hogg, D. W., Lang, D., & Goodman, J. 2013, PASP, 125, 306

Gömöry, P., Balthasar, H., & Puschmann, K. G. 2013, A&A, 556, A7

Gömöry, P., Beck, C., Balthasar, H., Rybák, J., Kučera, A., Koza, J., & Wöhl, H. 2010, A&A, 511, A14

Gošić, M., Bellot Rubio, L. R., del Toro Iniesta, J. C., Orozco Suárez, D., & Katsukawa, Y. 2016, ApJ, 820, 35

Grossmann-Doerth, U., Keller, C. U., & Schuessler, M. 1996, A&A, 315, 610

Guglielmino, S. L., et al. 2012, ApJ, 745, 160

Hale, G. E. 1908, ApJ, 28, 315

—. 1913, ApJ, 38, 27

Hale, G. E., Ellerman, F., Nicholson, S. B., & Joy, A. H. 1919, ApJ, 49, 153

Hale, G. E., & Nicholson, S. B. 1925, ApJ, 62, 270

Hale, G. E., Seares, F. H., van Maanen, A., & Ellerman, F. 1918, ApJ, 47, 206

Hathaway, D. H. 1996, ApJ, 460, 1027

Hoeksema, J. T. 1991, in BAAS, Vol. 23, Bulletin of the American Astronomical Society, 679–683

Homann, T., Kneer, F., & Makarov, V. I. 1997, SoPh, 175, 81

Howard, R., & Labonte, B. J. 1981, SoPh, 74, 131

Hundhausen, A. J. 1977, in Coronal Holes and High Speed Wind Streams, ed. J. B. Zirker, 225–329

Ishikawa, R., Tsuneta, S., & Jurčák, J. 2010, ApJ, 713, 1310

Ito, H., Tsuneta, S., Shiota, D., Tokumaru, M., & Fujiki, K. 2010, ApJ, 719, 131

Jin, C. L., Wang, J. X., Song, Q., & Zhao, H. 2011, ApJ, 731, 37

Kaithakkal, A. J., Suematsu, Y., Kubo, M., Iida, Y., Shiota, D., & Tsuneta, S. 2015, ApJ, 799, 139

Kaithakkal, A. J., Suematsu, Y., Kubo, M., Shiota, D., & Tsuneta, S. 2013, ApJ, 776, 122

Keller, C. U., Deubner, F.-L., Egger, U., Fleck, B., & Povel, H. P. 1994, A&A, 286, 626

Khomenko, E. V., Collados, M., Solanki, S. K., Lagg, A., & Trujillo Bueno, J. 2003, A&A, 408, 1115

Kiselman, D., Pereira, T. M. D., Gustafsson, B., Asplund, M., Meléndez, J., & Langhans, K. 2011, A&A, 535, A14

Kleint, L., Berdyugina, S. V., Shapiro, A. I., & Bianda, M. 2010, A&A, 524, A37

Kleint, L., Shapiro, A. I., Berdyugina, S. V., & Bianda, M. 2011, A&A, 536, A47

Kosugi, T., et al. 2007, SoPh, 243, 3

Krivova, N. A., & Solanki, S. K. 2004, A&A, 417, 1125

Lagg, A., et al. 2010, ApJL, 723, L164

Landi Degl'Innocenti, E., & Landolfi, M., eds. 2004, Astrophysics and Space Science Library, Vol. 307, Polarization in Spectral Lines

Leighton, R. B., Noyes, R. W., & Simon, G. W. 1962, ApJ, 135, 474

Lemen, J. R., et al. 2012, SoPh, 275, 17

Lin, H. 1995, ApJ, 446, 421

Lin, H., & Rimmele, T. 1999, ApJ, 514, 448

Lin, H., Varsik, J., & Zirin, H. 1994, SoPh, 155, 243

Lites, B., et al. 2007, PASJ, 59, S571

Lites, B. W., Centeno, R., & McIntosh, S. W. 2014, PASJ, 66, S4

Lites, B. W., et al. 2008, ApJ, 672, 1237

—. 2013, SoPh, 283, 579

Liu, Y., et al. 2012, SoPh, 279, 295

Livingston, W., & Harvey, J. 1971, in IAU Symposium, Vol. 43, Solar Magnetic Fields, ed. R. Howard, 51

Livingston, W., & Wallace, L. 1991, An atlas of the solar spectrum in the infrared from 1850 to 9000 cm-1 (1.1 to 5.4 micrometer)

Loève, M. M. 1955, M. M., Probability Theory (Princeton: Van Nostrand Company)

Makarov, V. I., & Makarova, V. V. 1996, SoPh, 163, 267

Manso Sainz, R., Martínez González, M. J., & Asensio Ramos, A. 2011, A&A, 531, L9

Martínez González, M. J., Asensio Ramos, A., Carroll, T. A., Kopf, M., Ramírez Vélez, J. C., & Semel, M. 2008, A&A, 486, 637

Martínez González, M. J., & Bellot Rubio, L. R. 2009, ApJ, 700, 1391

Martínez González, M. J., Collados, M., & Ruiz Cobo, B. 2006, A&A, 456, 1159

Martínez González, M. J., Collados, M., & Ruiz Cobo, B. 2007a, in Modern solar facilities - advanced solar science, ed. F. Kneer, K. G. Puschmann, & A. D. Wittmann, 157

Martínez González, M. J., Collados, M., Ruiz Cobo, B., & Solanki, S. K. 2007b, A&A, 469, L39

Martínez González, M. J., Manso Sainz, R., Asensio Ramos, A., & Bellot Rubio, L. R. 2010, ApJL, 714, L94

Martínez González, M. J., Manso Sainz, R., Asensio Ramos, A., & Hijano, E. 2012, ApJ, 755, 175

Martínez González, M. J., et al. 2011, ApJL, 730, L37

McIntosh, S. W., Leamon, R. J., Hock, R. A., Rast, M. P., & Ulrich, R. K. 2011, ApJL, 730, L3

Metcalf, T. R., et al. 2006, SoPh, 237, 267

Müller, D., Marsden, R. G., St. Cyr, O. C., & Gilbert, H. R. 2013, SoPh, 285, 25

Neckel, H. 1984, SSRv, 38, 187

Noyes, R. W., & Leighton, R. B. 1963, ApJ, 138, 631

Okunev, O. V., & Kneer, F. 2004, A&A, 425, 321

Orozco Suárez, D., et al. 2007a, ApJL, 670, L61

—. 2007b, PASJ, 59, S837

Ortiz, A., Bellot Rubio, L. R., Hansteen, V. H., de la Cruz Rodríguez, J., & Rouppe van der Voort, L. 2014, ApJ, 781, 126

Ortiz, A., Domingo, V., Sanahuja, B., & Solanki, S. K. 2002, in ESA Special Publication, Vol. 508, From Solar Min to Max: Half a Solar Cycle with SOHO, ed. A. Wilson, 185–188

Parker, E. N. 1978, ApJ, 221, 368

Pesnell, W. D., Thompson, B. J., & Chamberlin, P. C. 2012, SoPh, 275, 3

Plaskett, H. H. 1952, MNRAS, 112, 414

Quintero Noda, C., Asensio Ramos, A., Orozco Suárez, D., & Ruiz Cobo, B. 2015, A&A, 579, A3

Quintero Noda, C., Suematsu, Y., Ruiz Cobo, B., Shimizu, T., & Asensio Ramos, A. 2016, MNRAS, 460, 956

Rees, D. E., & Semel, M. D. 1979, A&A, 74, 1

Rieutord, M., & Rincon, F. 2010, Living Reviews in Solar Physics, 7, 2

Ruiz Cobo, B., & Asensio Ramos, A. 2013, A&A, 549, L4

Ruiz Cobo, B., & del Toro Iniesta, J. C. 1992, ApJ, 398, 375

Sánchez Almeida, J., & Lites, B. W. 2000, ApJ, 532, 1215

Scharmer, G., Owner-Petersen, M., Korhonen, T., & Title, A. 1999, in Astronomical Society of the Pacific Conference Series, Vol. 183, High Resolution Solar Physics: Theory, Observations, and Techniques, ed. T. R. Rimmele, K. S. Balasubramaniam, & R. R. Radick, 157

Scharmer, G. B. 2006, A&A, 447, 1111

Scharmer, G. B., Bjelksjo, K., Korhonen, T. K., Lindberg, B., & Petterson, B. 2003, in SPIE, Vol. 4853, Innovative Telescopes and Instrumentation for Solar Astrophysics, ed. S. L. Keil & S. V. Avakyan, 341–350

Scharmer, G. B., et al. 2008, ApJL, 689, L69

Scherrer, P. H., et al. 1995, SoPh, 162, 129

—. 2012, SoPh, 275, 207

Schlichenmaier, R., & Collados, M. 2002, A&A, 381, 668

Schou, J., et al. 2012, SoPh, 275, 229

Schrijver, C. J., & Harvey, K. L. 1994, SoPh, 150, 1

Schroeter, E. H., Soltau, D., & Wiehr, E. 1985, Vistas in Astronomy, 28, 519

Schüssler, M. 1990, in IAU Symposium, Vol. 138, Solar Photosphere: Structure, Convection, and Magnetic Fields, ed. J. O. Stenflo, 161

Seares, F. H. 1917, PASP, 29, 155

Seares, F. H., van Maanen, A., & Ellerman, F. 1918, in Publications of the American Astronomical Society, Vol. 3, Publications of the American Astronomical Society, 330

Semel, M. 1967, Annales d'Astrophysique, 30, 513

Severny, A. B. 1971, in IAU Symposium, Vol. 43, Solar Magnetic Fields, ed. R. Howard, 675

Sheeley, Jr., N. R. 1964, ApJ, 140, 731

—. 2008, ApJ, 680, 1553

Shiota, D., Tsuneta, S., Shimojo, M., Sako, N., Orozco Suárez, D., & Ishikawa, R. 2012, ApJ, 753, 157

Sigwarth, M., Balasubramaniam, K. S., Knölker, M., & Schmidt, W. 1999, A&A, 349, 941

Simon, G. W., & Leighton, R. B. 1964, ApJ, 140, 1120

Skumanich, A., & López Ariste, A. 2002, ApJ, 570, 379

Snodgrass, H. B., & Ulrich, R. K. 1990, ApJ, 351, 309

Snyder, C. W., Neugebauer, M., & Rao, U. R. 1963, International Cosmic Ray Conference, 1, 185

Socas-Navarro, H., Martínez Pillet, V., & Lites, B. W. 2004, ApJ, 611, 1139

Socas-Navarro, H., & Sánchez Almeida, J. 2002, ApJ, 565, 1323

Solanki, S. K. 2009, in Astronomical Society of the Pacific Conference Series, Vol. 405, Solar Polarization 5: In Honor of Jan Stenflo, ed. S. V. Berdyugina, K. N. Nagendra, & R. Ramelli, 135

Solanki, S. K., & Stenflo, J. O. 1984, A&A, 140, 185

Spruit, H. C. 1976, SoPh, 50, 269

Spruit, H. C., & Roberts, B. 1983, Natur, 304, 401

Staiger, J. 2012, in Astronomical Society of the Pacific Conference Series, Vol. 463, Second ATST-EAST Meeting: Magnetic Fields from the Photosphere to the Corona., ed. T. R. Rimmele, A. Tritschler, F. Wöger, M. Collados Vera, H. Socas-Navarro, R. Schlichenmaier, M. Carlsson, T. Berger, A. Cadavid, P. R. Gilbert, P. R. Goode, & M. Knölker, 445

Stenflo, J. O. 1970, SoPh, 13, 42

—. 1973, SoPh, 32, 41

—. 1982, SoPh, 80, 209

Stenflo, J. O. 2003, in Astronomical Society of the Pacific Conference Series, Vol. 307, Solar Polarization, ed. J. Trujillo-Bueno & J. Sanchez Almeida, 385

—. 2010, A&A, 517, A37

Stenflo, J. O., & Harvey, J. W. 1985, SoPh, 95, 99

Stenflo, J. O., Keller, C. U., & Gandorfer, A. 1998, A&A, 329, 319

Stenflo, J. O., Solanki, S. K., & Harvey, J. W. 1987a, A&A, 171, 305

—. 1987b, A&A, 173, 167

Svalgaard, L., Duvall, Jr., T. L., & Scherrer, P. H. 1978, SoPh, 58, 225

Svalgaard, L., & Kamide, Y. 2013, ApJ, 763, 23

Tanaka, Y. 1964, PASJ, 16, 336

Tang, F., & Wang, H. 1991, SoPh, 132, 247

Tritschler, A., Schmidt, W., Langhans, K., & Kentischer, T. 2002, SoPh, 211, 17

Trujillo Bueno, J., Shchukina, N., & Asensio Ramos, A. 2004, Natur, 430, 326

Tsuneta, S., et al. 2008, ApJ, 688, 1374

van de Hulst, H. C. 1953, The Chromosphere and the Corona, ed. G. P. Kuiper, 207

van Driel-Gesztelyi, L., & Green, L. M. 2015, Living Reviews in Solar Physics, 12, 1

van Noort, M., Rouppe van der Voort, L., & Löfdahl, M. G. 2005, SoPh, 228, 191

Varsik, J., Durrant, C. J., Turner, J., & Wilson, P. R. 2002, SoPh, 205, 231

Vernazza, J. E., Avrett, E. H., & Loeser, R. 1981, ApJS, 45, 635

Viticchié, B. 2012, ApJL, 747, L36

von der Luehe, O., Berkefeld, T., & Soltau, D. 2002, in SPIE, Vol. 4538, Optics in Atmospheric Propagation and Adaptive Systems IV, ed. A. Kohnle, J. D. Gonglewski, & T. J. Schmugge, 197–204

Waldmeier, M. 1955, ZAP, 38, 37

Westendorp Plaza, C., del Toro Iniesta, J. C., Ruiz Cobo, B., Martínez Pillet, V., Lites, B. W., & Skumanich, A. 1998, ApJ, 494, 453

Wiegelmann, T., et al. 2010, ApJL, 723, L185

Woods, T. N., et al. 2012, SoPh, 275, 115

Yeo, K. L., Krivova, N. A., Solanki, S. K., & Glassmeier, K. H. 2014, A&A, 570, A85

Zeeman, P. 1897, ApJ, 5, 332

Zhou, G. P., Wang, J. X., & Jin, C. L. 2010, SoPh, 267, 63

Zirin, H. 1985, Australian Journal of Physics, 38, 961

Acknowledgments

The work here presented has been carried out in the *Instituto de Astrofísica de Canarias* and the *Universidad de La Laguna*. This thesis has made use of data coming from three different facilities. First, HMI data was used by courtesy of NASA/SDO and science teams, for which, I would like to express them my gratitude. Second, I thankful to the *Astrophysikalisches Institut Potsdam*, the *Kiepenheuer-Institut fr Sonnenphysik* and the *Max-Planck-Institut fr Sonnensystemforschung* that made possible the observations performed at the Vacuum Tower Telescope at the Spanish *Observatorio del Teide* of the *Instituto de Astrofísica de Canarias*. Finally, I would like to express my gratitude to the Institute for Solar Physics of the Royal Swedish Academy of Sciences for operating the Solar Swedish Telescope at the Spanish *Observatorio del Roque de los Muchachos* of the *Instituto de Astrofísica de Canarias*. I am also very grateful to Stockholm university for the two weeks stay I spent there and to all the people there that made the stay so charm and worthy.

I would like to thanks Manolo and Marian for being so fantastic supervisors. For their continuous support and advice, for their always open doors for my doubts, for so wonderful time and teaching at the *Observatorio del Teide* and for so many wonderful experiences, I will always be so grateful for.

Because of their active help in the thesis I would like to thanks Andrés, who has always had time to give me useful advices and for having so nice discussions. I would also like to thanks Jaime for his wisdom advice in the setup of the observations of the CRISP instrument and the posterior reduction. I am so grateful to Basilio, who has give me so many good advices along these years. I would like to express my gratitude to Luis and, specially Sara, who guided me on my first steps with CRISP data. I am thanks to Antonio Dorta, who has always help me so much with HTCondor.

Finally I would like to express my most sincere grateful to my parents and brother, without whose support and care this would not have been possible. I am thanks to my friends who has always cared about me and make me spent so nice time. Finally, to Ana Belén, *the pidgeon*, without whose support, this thesis would have not been possible.